UNIVERSITÄT AUGSBURG

DISSERTATION

Photoluminescence quantum efficiency investigations on thin film light-emitting diodes during electrical operation

---

von

Manuel ENGELMAYER

zur Erlangung des
Doktorgrades der Naturwissenschaften
(Dr. rer. nat.)

eingereicht an der
Mathematisch-Naturwissenschaftlich-Technischen Fakultät
der Universität Augsburg

Augsburg, März 2022

Universität
Augsburg
University

1. Gutachter:	Prof. Dr. Wolfgang BRÜTTING
2. Gutachter:	Prof. Dr. Achim WIXFORTH

Datum der mündlichen Prüfung: 31.05.2022

Contents

1. Introduction **1**

I. Basic concepts **3**

2. Thin film light-emitting diodes **5**
- 2.1. Introduction to organic semiconductors . . . 5
- 2.2. Excitonic properties of organic semiconductors . . . 9
- 2.3. Electrical operation . . . 12
- 2.4. Light emission from an optical cavity . . . 16
- 2.5. Molecular orientation in organic thin films . . . 19
- 2.6. External quantum efficiency . . . 21

3. Experimental methods **23**
- 3.1. Atomic force microscopy . . . 23
- 3.2. jVL & EQE determination . . . 25
- 3.3. Impedance spectroscopy . . . 27
- 3.4. Time resolved photoluminescence spectroscopy . . . 28
- 3.5. PLQE measurements in thin film LEDs under operation . . . 31
- 3.6. Device fabrication . . . 39

II. Organic light-emitting diodes **41**

4. Theoretical description of organic light emission **43**
- 4.1. Organic emitters . . . 43
  - 4.1.1. Phosphorescent emitters . . . 43
  - 4.1.2. Thermally activated delayed fluorescence . . . 45
- 4.2. Efficiency loss mechanisms in organic light-emitting diodes . . . 46
  - 4.2.1. Triplet-Triplet-Annihilation . . . 47
  - 4.2.2. Triplet-Polaron Quenching . . . 48

5. Optical and electrical characterization of polar OLEDs 51
5.1. Investigations on polar hole transporting material OLEDs 52
5.1.1. Phosphorescent OLEDs 52
5.1.2. TADF OLEDs 65
5.1.3. Discussion 72
5.2. Investigations on polar electron transporting material OLEDs 78
5.2.1. Unpolar host OLEDs 79
5.2.2. Polar host OLEDs 82

III. Quantum dot light-emitting diodes 89

6. Basics of QD light-emitting diodes 91
6.1. Theoretical backgrounds of colloidal quantum dots 91
6.1.1. Introduction to nanocrystal emitters 92
6.1.2. Quantum confinement effect 93
6.1.3. QD band structure engineering 96
6.1.4. Device architecture of QDLEDs 97
6.1.5. State of the art 100
6.2. Efficiency loss mechanisms in quantum dot light emitting diodes 103
6.2.1. Trap assisted recombination 103
6.2.2. Electric field quenching 104
6.2.3. Auger quenching 108
6.2.4. The ABC-model of efficiency losses in QDLEDs 110
6.3. Introduction to nanocrystal synthesis 113

7. Characterization of QDLEDs 115
7.1. Physical properties of QDs 117
7.1.1. Morphology of QD films and device stability 117
7.1.2. Photoluminescence spectroscopy 120
7.2. PLQE determination of QDLEDs during electrical operation 123
7.2.1. Electric field effects on the QD performance 124
7.2.2. Current induced quenching in QDLEDs 129
7.3. Charging of QDLEDs 135

IV. Summary and Outlook 145

A. Appendix 151

CHAPTER 1

Introduction

In the first week of 2022, a new type of display technology called QD-OLED was presented on the Consumer Electronics Show (CES2022) in Las Vegas by *Samsung*. This type of display combines the advantages of two previously established technologies, Quantum Dot (QD)- and Organic Light-Emitting Diode (OLED)-based displays. While formerly the QDs were used on LCD panels in order to convert the blue backlight into red or green emission respectively, in the new QD-OLED, the backlight is replaced by an OLED. This segmented blue OLED backlight can be switched individually for each pixel, where the photons either pass a QD-based color conversion layer or a scattering layer for unchanged blue emission. This results in the displays featuring high contrast values, high brightnesses, better color purities, fast reaction times, large viewing angle stabilities, low power consumption and overcoming of the burn-in effect which affected OLED screens in the past. All of these advantages are however strongly coupled to the two single components' individual performances. The work presented in this thesis accordingly will focus on both thin film Light-Emitting Diodes (LEDs) comprising either organic or inorganic QD emitters.

Since the first efficient OLED was built in 1987 by Tang and VanSlyke, a multitude of improvements have been applied to push the achievable efficiencies of such devices higher and higher [1]. For instance, a better understanding of light-generation processes, the interplay between additional thin films, injection barriers and outcoupling issues have helped increasing the overall OLED efficiencies. The underlying principle of a light-emitting organic layer sandwiched between two charge supplying layers however is still unchanged to this day. The first part of this thesis will cover investigations on OLEDs with both phosphorescent and Thermally Activated Delayed Fluorescence (TADF) emitters. Particular focus will be set on the influence of implemented polar layers – as electron- or hole transporting layers or as host matrix for emissive dye molecules – on the emitter efficiency both under electrical operation as well as below the luminance turn-on.

Subsequently, investigations on QDLEDs will be described. Here, the working principle of an OLED was kept while the emitting organic layer is replaced by inorganic colloidal QDs. This technique was developed by Alivisatos *et. al* in 1992, where Cadmium selenide (CdSe)-based Nanocrystals (NC) were used to electrically generate luminance [2]. Although CdSe has been the state-of-the-art material for most of the respective research since then, applications in consumer end products face the problem of the high toxicity of Cd-based compounds. Therefore, throughout this thesis, exclusively Indium Phosphide (InP)-based QDs were used. Furthermore, all QDs were deposited from solution, which shows the low-cost potential for future industrial applications. The focus in this part of the thesis will be set on the determination of dominant efficiency loss processes under different operational conditions. Most notably high operational biases, which are needed to achieve high luminances, lead to a reduced LED efficiency. This is generally called *Roll-Off*, but a multitude of effects can be the reason for its occurance. Therefore, determination of dominant loss mechanisms under different conditions is a most crucial step on the path to improved next generation technologies.

In order to determine the described loss mechanisms and optical efficiencies during operation of both organic and QD emitters, a field dependent Photoluminescence Quantum Efficiency (PLQE) measurement setup was built. It allows to operate arbitrary devices under different electrical conditions while simultaneously detecting the emitter PLQE. This allows to *in-situ* investigate on efficiency reducing effects while excluding external effects coming from, for instance, adjacent charge transporting layers or charge imbalance issues, which would affect the overall device efficiency. The experimental setup is based on a reference experiment from the literature but was adapted, optimized and validated for the work to be done in this thesis [3].

Part I.

Basic concepts

CHAPTER 2

Thin film light-emitting diodes

The first part of this thesis will cover the basic theoretical backgrounds necessary to understand the working principles of thin film LEDs. They will mostly be described at the example of organic LEDs, meaning that the light generation comes from organic molecules. Later, nanocrystal emitters will replace their organic counterparts, the thin film device working principles will mostly stay the same however. Therefore, the theoretical basics described in this part of the thesis will be valid for both organic and inorganic thin film LEDs, although mostly OLEDs are being referred to.

2.1. Introduction to organic semiconductors

Organic chemistry is generally considered to revolve around the physical and chemical properties of carbon compounds [4, 5]. The term *Organic Semiconductors (OSC)* therefore describes a fraction of carbon based materials, which can be used in the respective electronic applications. In this thesis, only the field of OLEDs was worked on, therefore only materials with interactions with light in the visible range of the electromagnetic spectrum come into play. Note, that there are of course also other fields of interest like, for instance, the topic of organic photovoltaics, which is one potential way to overcome today's energy challenges.

All types of semiconductors, and therefore also OSC, have to be electrically conductive under the right circumstances. In order to explain the conductive behaviour of this material class, a look onto one of the simplest carbon compounds of ethene in figure 2.1 can be helpful.

Carbon in its base form has an atomic number of 6 and is therefore in the electronic ground state of $1s^2 2s^2 2p^2$. Combining two carbon atoms to a molecule will then lead to a hybridisation of the $2s$ and $2p$ orbitals. If the carbon has only three adjacent atoms to bond to, the hybridization eventually will be of the kind sp^2 meaning that the s and

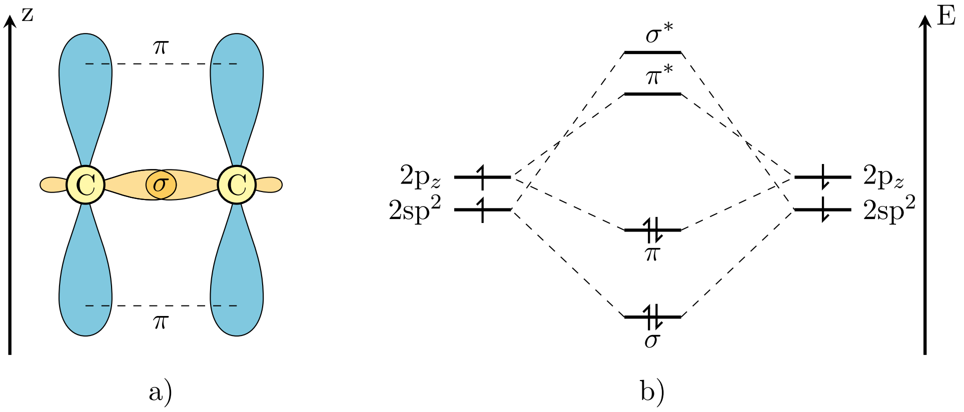

Figure 2.1.: a) Schematic depiction of the carbon-carbon bond in an ethene molecule with the double bond consisting of each one σ- and π-type bond. Hydrogen atoms and C-H-bonds are omitted.
b) Energy level diagram of the two atomic and the molecular orbitals. The lowest energy transition would be from the π to the π^* orbital.

two p-orbitals (p_x, p_y) will form the hybrid orbitals shown in figure 2.1 on the left. Note that the blue vertical orbitals are the p_z orbitals, while only a single sp^2 hybrid orbital is drawn in orange color. The other two sp^2 orbitals would then form the bonds between additional atoms like hydrogen in the case of pure ethene.
While forming a molecular bond, the two carbon atoms overlap with their respective atomic orbitals and form molecular orbitals. In this particular case, the two p_z and two sp^2 orbitals form two binding, σ and π, and two anti-bonding, σ^* and π^*, molecular orbitals. Since with this particular electronic configuration, all binding orbitals are filled with electrons and the anti-binding orbitals are empty, the overall electronic molecular energy is lower than the atomic energy, so that the molecular bond minimizes the system's total energy and the molecule is stable. Also note, that due to complete filling of orbitals, in a simplified picture also the respective Density of States (DOS) for charge carrier transport is filled. Therefore OSC typically are considered insulators. Only upon introduction of charges via injection, doping or photoexcitation, mobile charge carriers are imported into the system and the respective material becomes conductive. Again, note that charge transport in organic solids does usually not occur via band transport, but via incoherent hopping between localized states [6–10].

As can be seen on the right of figure 2.1, the frontier orbitals, meaning the Highest Occupied Molecular Orbital (HOMO) and Lowest Unoccupied Molecular Orbital (LUMO), are located in the π- and π^*-orbital for ethene, respectively [11]. The energy gap is therefore defined by the energetic difference between these two orbitals. Extending this model of two bound carbon atoms into larger molecules leads to longer, potentially cyclic, aliphatic chains. If this carbon chain consists of exclusively alternating single-and double bonds in the chain, the compound in fact is a planar molecule with the mentioned σ-orbitals connecting the carbon nuclei. However, the nominally alternating π bonds above and below the nuclei-plane form a conjugated π-electron system, where the respective π-electrons of all carbon atoms in the chain are delocalized. This leads to a higher stability in the special case of aromatic compounds but generally influences the electronic properties of the material. The size of the π-electron system inversely affects the size of the energy gap, meaning a large molecular size generally leads to a smaller gap. Similarly, substitution of carbon atoms by atoms with a different number of valence electrons (like Nitrogen) changes the electronic properties of the compound and can easily be attributed towards a change in electronic and therefore electrical properties. By adjusting the size of the delocalized π-electron system and the chemical composition of a compound, the electronic properties can therefore be tuned towards e.g. improved electron or hole conductance. The use of various such materials adjacent to each other thereby allows the design of (opto-)electronic devices, as will be explained in section 2.3 of this dissertation.

Another property that changes with the size of the π-electron system is obviously the molecular size and weight. This leads to a change in phase from the smallest organic hydrocarbon of ethene (C_2H_4) being a gas at room temperature to larger molecules like benzene or toluene (C_6H_6, C_7H_8) being liquids and even larger molecules like anthracene ($C_{14}H_{10}$) being solids, which even tend to crystallize [12]. Traditionally, most of the materials used in OSC devices come from the group of these so called *small molecules* in amorphous or crystalline films, however it is also possible to use *polymers* in devices. During the course of this work, both small molecules as well as polymers will be used. As the focus point of this work is not set on these layers, however, only a short overview over the different material classes shall be given here. More detailed information can be found in references [13–19].

Small molecules have a lower weight compared to the polymeric semiconducting materials. This enables film deposition by thermal evaporation, which is not possible for polymers. However, for small molecules, the formation of organic crystals is possible, which in turn can be detrimental for the application in devices, if for example the film morphology changes with ongoing degree of crystallization. Typical chemical structures for small molecules and polymers can be found in figure 2.2.
Polymers on the other hand usually consist of a conjugated carbon backbone with additional sidechains to alter the electronic properties. The long polymeric chains in a film are then intertwined with each other, which leads to a higher mechanical film stability. Because of this, thermal evaporation is commonly not possible without chemical decomposition and solution based techniques like spincoating, roll-to-roll processes, spray- or dip coating or various printing methods have to be applied for this material class. This in turn leads to (industrially) low processing costs and easy scalability. One disadvantage of polymers is, however, that the synthesis of complex polymers needs careful catalysis in order to obtain high purity materials, which can in turn complicate the synthesis process and increase the overall costs again. Also, the layer formation, which is a crucial

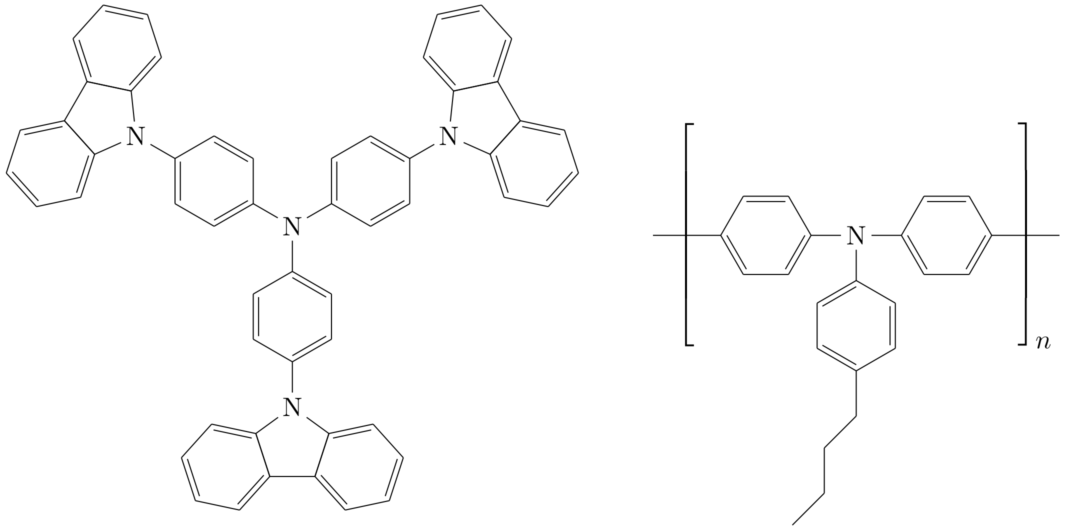

a) TCTA

b) pTPD

Figure 2.2.: Chemical structure formula of a small molecule (a) and polymer (b). Both materials were used during the course of this thesis as hole transporting materials.

point in thin film devices, can turn out to be difficult and the relevant parameters for the respective solution processing method of choice have to be chosen carefully. These parameters include the viscosity of the solution, the ratio of solvent to deposition material, potential additives or additional solvents might have to be added or the processing environment might have to be adapted by e.g. adjusting the processing temperature distribution in order to properly control e.g. the drying process.

2.2. Excitonic properties of organic semiconductors

Excitons in organic and inorganic semiconductors

Excitons are quasiparticles in an insulator or semiconductor consisting of an electron and a hole [20]. These two charge carriers are bound by the Coulombic force due to their contrary electrical charge. The resulting binding energy E_B can be expressed by equation 2.1:

$$E_B = \frac{e^2}{4\pi\epsilon\epsilon_0 r_E} \tag{2.1}$$

The Coulomb radius r_C, which is the distance of an electron and a hole if the binding energy exactly equals the thermal energy, can be given by:

$$E_B = E_{thermal} \longleftrightarrow r_C = \frac{e^2}{4\pi\epsilon\epsilon_0 k_B T} \tag{2.2}$$

With the elementary charge e, the electron-hole distance r_E, the Boltzmann constant k_B and the relative and vacuum permittivity ϵ and ϵ_0, respectively. Considering typical values for OSC for ϵ (3.5) [14] and r_E in the order of a molecular size (1 nm), the resulting binding energy E_B is roughly 0.4 eV. Additionally, the Coulomb radius r_C of an exciton at room temperature (295K) equals slightly more than 16 nm. This clearly demonstrates two points typical for OSC:

- The exciton Coulomb radius is the distance where the attractive Coulomb force in an organic solid starts to draw together the two charge carriers. A Coulomb radius of a few tens of nm is a quite large distance compared to the intermolecular distances of only a few nm. That effectively means, that diffusing charge carriers can rather easily recombine in organic solids.
- With an exciton binding energy of a few hundreds of meV, the room temperature thermal energy is nowhere close to being able to overcome this potential. Therefore bound electron-hole pairs in OSC tend to stay together rather than dissociate as free charge carriers.

The consequence of these points is that for processes that rely on diffusion to generate excitons, like it is the case for OLEDs, OSC are ideally suited. Especially considering typical layer thicknesses of emissive layers in OLEDs being 10 to 20 nm, one can easily understand why the charge carriers, upon entering the layer, quickly form excitons. For processes, that rely on diffusion to separate the charge carriers however, like charge separation in solar cells, this brings challenges that need to be overcome in order to generate efficient devices.

Comparing these values to their respective inorganic semiconductor counterparts of $E_{B,inorg.} \approx 5\,\text{meV}$ and $r_{E,inorg.} \approx 10\,\text{nm}$ shows the inherent differences between excitonic properties of organic and inorganic semiconductors [14]. Thereby, the excitons occurring in organic materials are called *Frenkel excitons* while inorganic excitons are

labelled *Wannier excitons* [15, 21].
While the binding energy of closely bound excitons in OSC can be described by equation 2.1, inorganic Wannier excitons typically can be approximated by the analogy of an electron in a hydrogen atom, since the effective hole mass is typically larger than the respective effective electron mass. The respective energy can be given as

$$E = \frac{\mu}{m_0 \epsilon^2} R_y n^{-2} \tag{2.3}$$

with the reduced electron and hole mass $\mu = m_e m_h/(m_e + m_h)$, the Rydberg energy R_y, the permittivity ϵ and electron mass m_0 [22].
Note that most of differences between organic and inorganic semiconductors arise from the difference in their atomic and molecular structure. While inorganic semiconductors usually form crystals where the atoms are mostly covalently bound to each other, the intermolecular bonding in OSC is based on the much weaker *Van-der-Waals* force. Due to this striking difference, charge carrier transport works differently in the two semiconductor classes with band transport in inorganic and hopping transport in OSC being the mostly dominant process at room temperature. Also, the dielectric screening is higher in inorganic solids, as is expressed by a typically much higher ϵ of around 11. This, of course, also partly explains the above mentioned differences in r_C and E_B.
More details about the aforementioned processes can be readily found in the literature [5, 14, 15].

Spin states of excitons

For an organic molecule to interact with light, electronic transitions between different energy levels are necessary. These transitions have to be allowed from a quantum-mechanical point of view, which in turn means that the spins of the involved excitons need to be accounted for. Note that this is of course true for both light absorption and light emission in an organic emitter.

Defining electronic states as spin up ↑ ($s = 1/2$, $m_s = 1/2$) and spin down ↓ ($s = 1/2$, $m_s = -1/2$), the resulting system total quantum numbers S and M_s, defined as the sum of charge carrier individual quantum numbers, can be in one of four possible combinations:

$$\begin{aligned} S_n &= \frac{1}{\sqrt{2}} \left(|\uparrow\downarrow\rangle - |\downarrow\uparrow\rangle \right) && S = 0,\ \ M_s = 0 \\ T_n &= \begin{cases} |\uparrow\uparrow\rangle & S = 1,\ \ M_s = 1 \\ \frac{1}{\sqrt{2}} \left(|\uparrow\downarrow\rangle + |\downarrow\uparrow\rangle \right) & S = 1,\ \ M_s = 0 \\ |\downarrow\downarrow\rangle & S = 1,\ \ M_s = -1 \end{cases} \end{aligned} \tag{2.4}$$

The four combinations of ↑ and ↓ for a two particle system result in different quantum numbers for the respective final state. If both S and M_s are zero, then the exciton state is called *Singlet* S_n according to the multiplicity rule of $2S+1$. Correspondingly, the multiplicity for the other states with $S=1$ is three, which is why these states are called *Triplets* T_n with magnetic quantum numbers of $M_S=\{1,0,-1\}$. The index n indicates the energetically different states, where $n=0$ indicates the ground state, $n=1$ the first excited state and so on. Note that a triplet ground state T_0 typically does not exist.

The theoretical description of optical transitions needs a closer look at the quantum mechanical processes involved, which are described in more detail in e.g.[14]. Looking at optical transitions between different energy states, a number of factors need to be taken into account. *Fermi's golden rule* states, that in order for a transition to happen, the respective rate of the transition from initial to final state k_{if} has to be non-zero:

$$k_{if}=\frac{2\pi}{\hbar}\left|\langle\psi_f|\,\widehat{H'}\,|\psi_i\rangle\right|^2\rho(E_f) \tag{2.5}$$

The excitation is considered through a small perturbing Hamiltonian $\widehat{H'}$, $\rho(E_f)$ is the density of final states and ψ_i and ψ_f are the initial and final state wavefunctions.
Assuming the electron- and atomic nuclei movement do not influence each other (*Born-Oppenheimer Approximation*), equation 2.5 can be expressed as

$$k_{if}=\frac{2\pi}{\hbar}\rho\left|\langle\psi_{el,f}|\,e\hat{r}\,|\psi_{el,i}\rangle\right|^2\cdot\left|\langle\psi_{vib,f}|\psi_{vib,i}\rangle\right|^2\cdot\left|\langle\psi_{spin,f}|\psi_{spin,i}\rangle\right|^2 \tag{2.6}$$

with the help of the dipole operator $e\hat{r}$ and the assumption of $\psi_{total}=\psi_{Electronic}\cdot\psi_{Vib}\cdot\psi_{Spin}$. For this line of argumentation, only the last of the three terms in equation 2.6 shall be considered. The so called *spin-factor* can only take the two values of either 0 or 1, in case the spins of the initial and final state are different from each other or identical, respectively. Looking back at the argumentation to the possible combinations of electron spins from above, this now means that any transition, that has a non-zero transition rate k_{if}, needs to have identical spins in both states. Therefore, only transitions from singlet to singlet states or triplet to triplet states are spin-allowed, while any transition from singlet to triplet or vice versa is not allowed. The optical transition from S_0 to S_1 is commonly called *Absorption*, while the release of a photon is then called *Fluorescence*. Direct photon absorption into a triplet state is therefore not observed, since the energetically lowest state usually is a singlet state. Note that there are other processes and transitions happening in actual OLED materials, which will be covered in section 4 of this thesis.

2.3. Electrical operation

Working principle and device layout

An OLED is an electrically driven device that emits light upon electrical excitation. The energy therefore does not come from an optical exciation as shown in the theoretical background so far, but comes from an external source. The most simple device layout of an OLED consists of a single suitable organic thin film sandwiched between two electrodes. However, already the first efficient thin film electroluminescent OLED built by Tang and Van Slyke [1] in 1987 consisted of a bilayer structure. Therefore, the working principle of a model OLED shall be explained at the case of a more complex structure similar to the structures actually used during the course of this work, as is shown in figure 2.3.

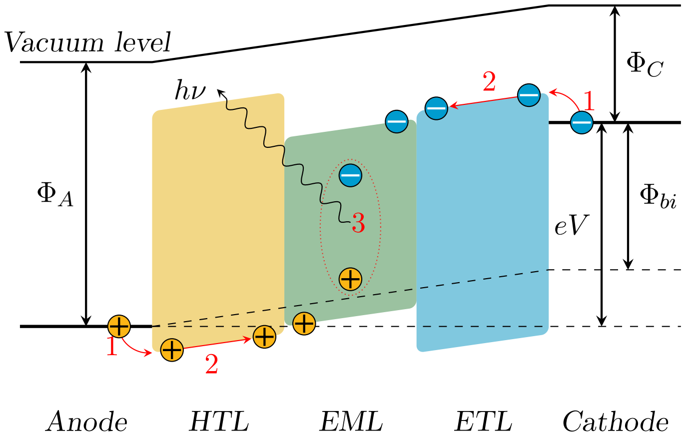

Figure 2.3.: Schematic energy band diagram of an OLED under operation with an externally applied voltage V. The charge carriers are being injected into the charge transport layers (1). Then the charge transport in the respective layers brings the charge carriers towards the respective EML interface (2). Electrons are transported via the ETL LUMO, holes are transported via the HTL HOMO. Upon entering the EML, the charges form excitons (3), which can decay radiatively under emission of a photon, labelled as $h\nu$ in the graph.
The electrode workfunctions are labelled with Φ_A and Φ_C for the anode and cathode, respectively. The potential difference between the two workfunctions results in a built-in potential Φ_{bi}. If the externally applied voltage is too low, so that $eV < \Phi_{bi}$, no charge injection into the device can occur and no luminescence can be expected. The image was adapted from [18, 23]

Here, an OLED consisting of five different layers can be seen. The goal of the device design is to have excitons in the Emitting Layer (EML) that can decay radiatively and emit photons. The necessary charge carriers, electrons and holes, will be injected from the respective electrodes into the adjacent Charge Transport Layer (CTL). The charge injection process itself will not be explained in detail here, as the underlying physics are highly dependent on the involved materials and conditions. These physical processes rely on tunneling (*Fowler-Nordheim tunneling* [24]) or thermal activation (*Richardson-Schottky thermionic emission*) [14]. It is important to note, that even in those models, not all preconditions like the disorder in organic solids are accounted for.

After injection into the CTLs, the charge carriers drift, driven by the interplay of external and internal electric fields, towards the interface of CTL and EML. The two CTL layers usually consist of different materials, adapted to the respective charge carrier transport. They are therefore most commonly labelled Hole Transport Layer (HTL) and Electron transport layer (ETL), respectively. If no additional potential barriers are present between the CTLs and the EML, the charges can move into the EML, where they ideally form excitons. The excitons then have a certain excited state lifetime τ and decay accordingly under photon emission. The big advantage of a dedicated EML over a simple mono- or bilayer device is, that the EML material can be designed suitably for the specific device. With proper energy level alignment of the EML and ETL HOMOs and EML and HTL LUMOs, the charge carriers can be confined in the EML. This in turn increases the OLED efficiency as will be explained later in more detail [25].

Additionally, the EML can be used as a host material for a luminescent dye, which allows to tune the macroscopic layer properties like conductivity or refractive index while separately adjusting the emissive species properties like the emission wavelength. Also, this method reduces the overall concentration of dye molecules, which can be adventegous for the device efficiency as will be explained in detail later in this thesis as well. These systems then typically are referred to as *guest-host systems*.

The generated photon will then exit the device typically through a transparent Indium tin oxide (ITO) electrode.

Current-Voltage Characteristics in organic light emitting diodes

Light generation in OLEDs takes place upon electrical excitation. Therefore any applied forward voltage V will result in a device current j, which yields valuable information about the physical properties of the respective device. As already mentioned above, OLEDs typically have a built-in potential Φ_{bi} due to the difference in workfunctions of the two electrode materials. The resulting unbiased band bending needs to be compensated for in order to inject charge carriers into the active layers. Therefore, the current below V_{bi} is not governed by actual diode current, but rather by leakage currents between the electrodes by for example lateral conductivity of some layers. As this current is usually only dependent on the resistance of these layers, it is considered *Ohmic* in its behaviour. The current is therefore given by

$$j = en\mu\frac{V}{d} \tag{2.7}$$

with the elementary charge e, the charge carrier density n, the charge carrier mobility μ and the device thickness d. This bias regime is marked in yellow with *a)* in figure 2.4.

Exceeding V_{bi}, the charge carriers can be injected into the CTLs and the actual diode current can begin to flow. The first comprehensive description of the current densities in *pn-junctions* and *pn-transistors* was published in 1949 and describes the dependence of the LED current to voltage in dependence of the temperature and a diode ideality factor n, that can give insights into the underlying recombination and transport processes involved during device operation [26]:

$$j = j_0 \left[\exp\left(\frac{eV}{nk_BT} \right) - 1 \right] \tag{2.8}$$

The respective exponential bias regime is depicted in green color in figure 2.4 and its onset ideally marks the luminance onset as well (not shown in the graph). In an ideal device, the built in and the turn on voltage are therefore identical. Note however, that equation 2.8 treats the OLED as a simple pn-junction, which is a strongly simplified view. Therefore further theoretical considerations have to be taken into account in order to quantiatively model the diode current, which will however not be covered in this thesis. For more details see for instance [18, 27].

The last, blue regime in figure 2.4 finally represents the transport limited regime in a jV-characteristic. Depending on the materials used in the respective OLED, different

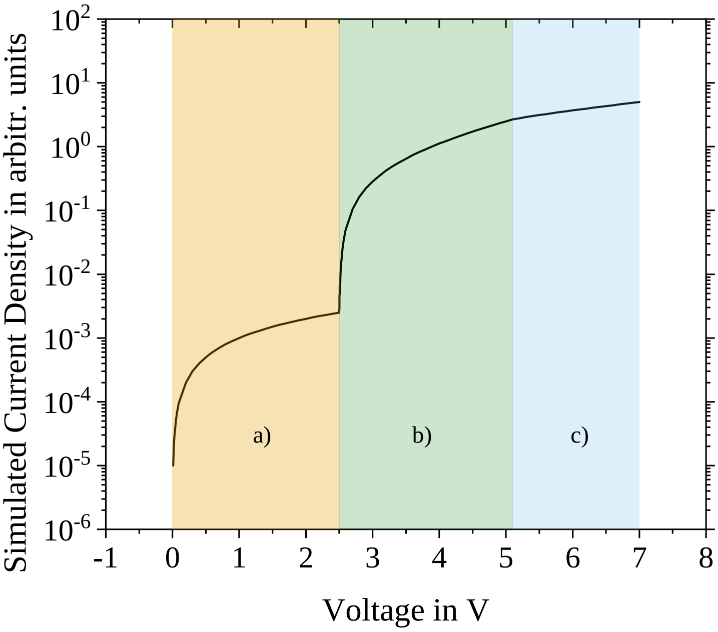

Figure 2.4.: Simulated Current-Voltage characteristics of an OLED. The three shaded areas correspond to the respective current regimes. Below the simulated V_{bi} of 2.5V, the current is goverened by Ohm's Law (a)), the exponential curve can be seen up until ca. 5.2V (b)) whereafter the current limitation of SCLC comes into play(c)).

mechanisms can apply. The most common processes leading to a current limitation are Space Charge Limited Current (SCLC) and Trap Charge Limited Current (TCLC).
SCLC occurs if certain preconditions in a biased OSC are met. The theoretical description is taken from [14, 15] and is based on a trap free OSC sandwiched between two non injection limited electrodes. This ensures that the electrodes always supply enough charge carriers so that the actual current limitation comes from the organic itself and all present charge carriers Q can be assumed to be equal to the number of injected charge carriers Q_{inj}. Furthermore, the model assumes unipolar charge transport, a homogenous electric field distribution across the observed layer and a homogenous organic layer itself while diffusion currents in general will be neglected. This last point in particular can lead to problems in the interpretation of measurement data, if the transition into the SCLC regime is close to the built-in voltage V_{bi}.
The general starting point for the description of the current density is given here:

$$j_{SC} = \frac{Q}{A \cdot d} \cdot \nu = \mu \frac{V}{Ad^2} \tag{2.9}$$

Taking into account the maximum capacitance in an insulator

$$C = \frac{Q}{V} = \epsilon \epsilon_0 \frac{A}{d}, \tag{2.10}$$

the limiting current current then calculates to

$$j_{SCLC} = \mu \epsilon \epsilon_0 \frac{V^2}{d^3} \tag{2.11}$$

This equation neglects however, that the space charges in the insulator affect the electric field distribution inside the layer. Due to this, the equation has to be adapted by a factor yielding the *Mott-Gurney equation* for field independent charge carrier mobilites [28]:

$$j_{SCLC} = \frac{9}{8} \mu \epsilon \epsilon_0 \frac{V^2}{d^3} \tag{2.12}$$

The model of SCLC in general gives an idea about how much current of only one charge carrier type the OSC can sustain and therefore serves as an upper limit for the maximum current. Introducing traps into the system will change the above equation depending on the magnitude and shape of the trap density. For a general case of exponentially distributed traps in the energy space, the overall device limiting current j_{TCLC} can be described as follows [29, 30]:

$$j_{TCLC} = e \mu N_c \left(\frac{2l+1}{l+1} \right)^{l+1} \left(\frac{l}{l+1} \cdot \frac{\epsilon}{q N_t} \right)^l \frac{V^{l+1}}{d^{2l+1}} \tag{2.13}$$

with $l = E_t / k_B T$, the trap depth E_t and the respective charge carrier and trap densities N_c and N_t. Note that for the case of no or only shallow traps that are already completely filled at low currents ($l = 1$), the proportionality of $j \propto V^2/d^3$ is identical to the case displayed in equation 2.12. Similarly, for $l = 0$, the proportionality of $j \propto V/d$ is identical to equation 2.7. For the simulation of the blue shaded area in figure 2.4, an arbitrary $j \propto V^2$ dependence was assumed.

2.4. Light emission from an optical cavity

The following section will cover the optical simulation of OLED emission in a simulated stack. The comprehensive derivation of the involved backgrounds can be found in [23, 31–34]. Only the qualitative description and results will be quoted here.

Outcoupling of optical modes

So far, the light emission process was treated as if the only relevant factors regarding the respective processes in OLEDs are the charge carrier transport to generate excitons and the energy levels of the EML or doped dye, respectively, that determines the emission color. However, OLEDs are complex devices, where a (multi-)layered structure is applied. As already mentioned earlier, a typical OLED consists of one reflecting and one transparent electrode with the organic layer stack inbetween them. Due to the comparably low electrical conductivity of organic semiconductors, these layers typically are below 1 µm thin in total. This brings the overall device thickness into the range of the wavelength of the emitted light, so that optical effects inside the cavity alter the emissive properties of the OLED. Assuming isotropical emission in the organic layers, the photons can be coupled to different optical modes as can be seen in figure 2.5.

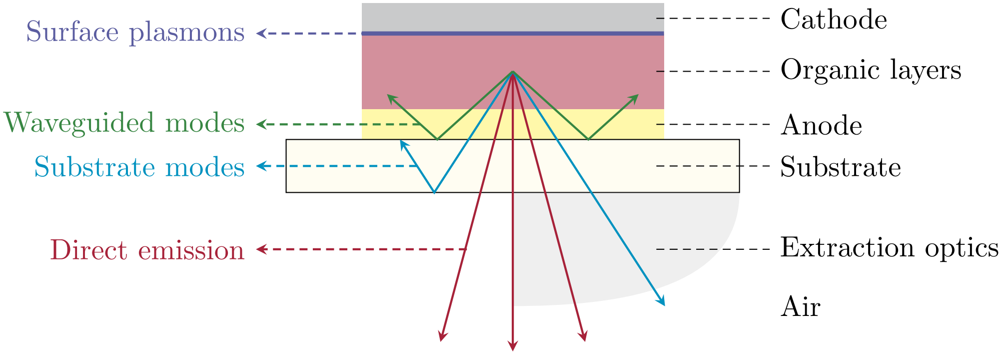

Figure 2.5.: Schematic depiction of the various optical modes in a simplified OLED. The image was redrawn from [35]. The right half of the OLED shows the use of additional extraction optics, that can be used to enhance the OLED efficiency by outcoupling the formerly trapped substrate modes.

Depending on the emission angle after radiative exciton relaxation, the photon can be reflected at the various interfaces in the OLED stack:

- If the emission happens perpendicular to the substrate surface or only barely deviates from that angle, the generated photons can leave the device into the surrounding air. This is the desired outcome, as the light can be used for external applications then.
- At higher emission angles, the light will not be able to cross the substrate-air

surface. Here a strong change in the refractive index of the respective medium takes place, so that according to *Snell's Law*, no transition into air is possible. This behaviour is called *Total Internal Reflection* and starts at a critical angle of θ_c perpendicular to the substrate surface of:

$$\theta_c = \arcsin \frac{n_2}{n_1} \tag{2.14}$$

with n_1 and n_2 being the refractive indices of the substrate and air, respectively. These modes are called *Substrate Modes* and can be harvested by the application of a suitable extraction layer. Different approaches have been made to extract these modes, which in turn significantly enhances the overall device performance. Possible ways to extract these modes are the use of macroextractors like microlenses on top of the substrate, nanoparticle external extraction layers or a roughening of the substrate-air surface [36, 37].

- Similarly, the photons can already be trapped at even higher emission angles at the interface between anode and substrate. For simplicities sake, the refractive index of both anode material and organic layers is assumed to be identical here. Again, total internal reflection between the layers with different refractive indices will leave a fraction of the light incapable of leaving the device. The usage of suitable extraction techniques can increase the overall device efficiency, this time however, the additional extraction layer needs to be between substrate and organic layers. This needs more careful device processing, but can also lead to a higher efficiency enhancement compared to the aforementioned external extraction techniques [38, 39].

- Finally, photons can also couple to surface plasmon polaritons at the cathode-organic interface. This effect is highly dependent on the distance between the emissive layer and the metal surface. Therefore this effect can be minimized by using a suitably thick organic transport layer inbetween [40, 41].

Influencing the radiative rate

Using a classical oscillating dipole model to explain the light emission of luminescent molecules, the interference effects of the initially emitted photon with reflected photons from the metal interface quickly become clear, as the electromagnetic radiation interacts with the emitter itself. This becomes an important fact to consider, as OLEDs typically feature one highly reflective metal electrode, which turns the layer stack into a micro-cavity. Therefore, this cavity not only influences the amount of outcoupled light as was explained above, but also influences the radiative decay rate through interference. This effect is called *Purcell effect* and can be described by the following equations.

Generally, the internal quantum efficiency q of an emissive species in an infinite bulk can be described by the ratio of radiative k_r and non-radiative k_{nr} decay rates. The sum of radiative and non-radiative rates equals the overall decay rate and can be inverted to find the system's excited state lifetime τ.

$$\tau^{-1} = k_r + \sum_i k_{nr,i} \tag{2.15}$$

$$q = \frac{k_r}{k_r + \sum\limits_i k_{nr,i}} = \tau k_r \tag{2.16}$$

Taking the cavity into account instead of the condition of infinite bulk, this formula changes to

$$q_{eff} = \frac{F \cdot k_r}{F \cdot k_r + \sum\limits_i k_{nr,i}} \tag{2.17}$$

with the *Purcell factor* F. Furthermore, it can be shown, that the effective and internal quantum efficiencies can be put into relation

$$\frac{q_{eff}}{q} = \frac{F}{(1-q) + qF} \iff q_{eff}(F, q) = \frac{qF}{(1-q) + qF} \tag{2.18}$$

which clearly shows that the effective quantum efficiency of an emitter is a function of the cavity, expressed by F, and its own internal quantum efficiency q [42]. Note, that F can be larger as well as smaller than unity depending on the respective layer stack used. This relation can be used to simulate the total output power of OLEDs with different Purcell factors and internal quantum efficiencies or can in turn yield information about internal qantum efficiency of experimental samples where the cavity is known.

2.5. Molecular orientation in organic thin films

In section 2.3 of this thesis, the (multi-)layered structure of OLEDs and their working principle was explained. While the simplified description of the device stack as a number of homogenous layers is helpful to explain a lot of effects, it is not sufficient to explain the origin of interfacial charges in the device.
Considering the case of small molecules as building blocks for the layers in general, the molecular properties have to be considered when trying to understand the macroscopic thin film- and overall device properties. A lot of the commonly used materials in OLEDs are anisotropic in shape and therefore in their optoelectronic properties. This can typically be seen in film both by optical as well as electrical measurements. The optical effect will not be covered in the experimental part of this thesis, so the theoretical basics will be only shortly mentioned here.

The direction of any emitted photon from an emissive molecule is governed by the molecular Transition Dipole Moment (TDM). The TDM in turn is defined by the molecular frontier orbitals (HOMO/LUMO) and thereby coupled to the molecular geometry. This means, that a preferential alignment of molecules in a film leads to a non-isotropic photon generation in this film. This can be used to purposely alter the distribution of energy into different optical modes as was explained earlier. As was shown in section 2.4, only a fraction of the generated light that is emitted below a critical angle with respect to the sample surface can leave the device. Aligning the majority of TDMs and therefore molecules in parallel to the substrate will therefore strongly increase the outcoupled light. This technique has been found to be a major factor for the design of modern OLEDs and is crucial for the design of highly efficient devices [43, 44]. The TDM alignment can be influenced by the used molecule for guest and hosts in the respective systems as well as the processing conditions during film deposition. The measurement can be done via angular dependent photoluminescence spectroscopy or back focal plane imaging [45].

Additionally, preferential alignment of molecules in a film can lead to more than optical outcoupling effects. In fact, if the molecule has a significant Permanent Dipole Moment (PDM), the PDMs of single molecules add up in a macroscopic film and can alter the electrical properties of said film. This so called Spontaneous Orientation Polarization (SOP) of the molecules therefore can lead to the formation of a sheet charge at the interface between two adjacent layers with the respective countercharge at the opposite interface. The total film polarization P_0 parallel to the film normal direction can then be expressed via the angle θ_i between PDM and surface normal direction, the molecular PDM p and the film volume L by :

$$P_0 = \frac{p \sum_i cos\theta_i}{L} = p\langle cos\theta \rangle n \tag{2.19}$$

with the film density n and average orientation $\langle cos\theta \rangle$ [46]. The respective electric field

V_s formed by this polarization can furthermore be calculated by

$$V_s = \int_0^d \frac{P_0}{\epsilon\epsilon_0} dz = \frac{p\langle cos\theta\rangle n \cdot d}{\epsilon\epsilon_0} \tag{2.20}$$

with P_0 being parallel to the substrate normal in z-direction, the film thickness d and the vacuum and relative permittivities ϵ_0 and ϵ, respectively.

The resulting surface potential can, depending on the film deposition conditions, composition and thickness, reach significant magnitudes. A prominent example for this is the study published in [47], where a potential of 28 V was found upon deposition of 560nm of Tris-(8-hydroxychinolin)-aluminium (Alq_3) on a gold substrate, which is why the term Giant Surface Potential (GSP) was formed. This GSP is nowadays found in films of many polar organic materials and can be influenced by a variety of processing parameters [48]. It shall be noted, that these interfacial charges can heavily influence the electrical performance of an OLED, as the interface charges for example might be responsible for an accelerated or attenuated charge injection from the adjacent layers [49].
Therefore, it is crucial to analyze any experimental data gained from OLEDs with respect to the presence or absence of interfacial charges. One common phenomenon during device operation is the accumulation of charges at biases below the actual turn on voltage V_{bi}. This can in turn significantly influence the emissive species efficiency, as was shown recently for phosphorescent OLEDs [50]. As soon as only one charge carrier type can be injected into the organic device, which cannot leave the device again, the charges accumulate at an interface. With the proper alignment of interfacial charge, this is acclerated to counteract the charge built up by SOP. The so far only space charge-like interfacial charge will therefore be countered by real charge carriers. This will therefore significantly increase the charge carrier density at and close to the interface, which will influence, among other things, exciton quenching processes which are sensitive to it. The details of such quenching processes will be covered later in this thesis in sections 4.2 and 6.2.

To shortly summarize this topic, one can say that a preferred alignment of molecules in films of OLEDs, which possess a PDM, can influence both the electrical device performance with respect to charge transport or injection mechanisms as well as the emissive species' efficiency. Furthermore preferential dipole alignment can affect the outcoupling factor via influencing the emission angle of emitted photons.

2.6. External quantum efficiency

One of the most important figure of merits regarding OLEDs is the External Quantum Efficiency (EQE) η_{EQE}. The EQE determines the efficiency of an OLED under electrical operation and is generally defined by the fraction of harvested photons per injected charge carriers:

$$\eta_{EQE} = \frac{\dot{n}_{photons}}{\dot{n}_{electrons}} \tag{2.21}$$

While both of these quantities can be measured relatively easily as will be shown in section 3.2 of this thesis, the physics of the involved processes can be quite complex depending on the respective layer stack. It is therefore common to split the total EQE into several subfactors influencing the overall emission [23, 25]:

$$\eta_{EQE} = \gamma \cdot q_{Exc} \cdot q_{eff} \cdot \eta_{out} \tag{2.22}$$

- γ hereby specifies the so called *Charge Balance Factor*. In figure 2.3, the working principle of an OLED under electrical operation is shown. In this figure, the ideal case of perfect charge balance was silently assumed. In reality however, the energy levels of all involved layers in the stack have to be carefully adjusted to each other. Otherwise, an injected hole can potentially pass right through the EML and ETL into the cathode without ever forming an exciton. Similarly, electrons can move through the EML and HTL towards the anode.
  It is therefore crucial to insert suitable barriers or even dedicated blocking layers for holes and electrons, respectively, in order to enable efficient exciton formation in an OLED.
  Note that perfect charge balance ($\gamma = 1$) is typically not reached in real devices immediately upon turn on as the injection of one charge carrier type is typically faster than the other's. This leads to an increase in EQE at low current densities before the efficiency limiting processes mentioned below come into play.
  γ is mostly influenced by the stack design via the layers' injection and transport properties for the respective charge carriers.

- q_{Exc} is the radiative exciton fraction. It determines the fraction of electrically generated excitons that can actually emit light radiatively. As was shown in equation 2.4, in first generation OLEDs, two charge carriers can form an exciton with four different spin states, where three triplet- and one singlet state emerges. Only the singlet state can decay through the emission of a photon back to the ground state, so that statistically, three out of four charge carriers form nonradiative excitons in this particular material class. q_{Exc} would therefore be 0.25.
  Note that this value can be changed by choosing different materials as emissive species. More details about this topic can be found in section 4 of this thesis.

- q_{eff} is the effective quantum efficiency. While q_{Exc} describes the fraction of excitons that can decay radiatively, q_{eff} describes the fraction of excitons that actually do emit radiatively. In other words, q_{eff} describes the relationship of radiative and non-radiative decay rates. Note that this factor is obviously dependent on the emitter itself, however external influences can significantly alter it as well. It was shown earlier in equation 2.17, that the *Purcell Factor F* arising from the OLED microcavity can influence it. Furthermore, the effective quantum efficiency can be quenched by different means like an applied electric field or the charge carrier density in the emitter vicinity. More details about several selected quenching processes can be found in sections 4.2 and 6.2.

- η_{Out} is the outcoupling factor. As was already mentioned in section 2.4 of this thesis, only a fraction of the actually generated photons in an OLED can leave the device to be used in applications. The rest of the photons can be coupled to substrate- or waveguided modes, can transfer its energy at the metal interface by interacting with surface plasmons or can be reabsorbed by any of the layers. A simple and rough estimate for the outcoupling factor without any particular effort to enhance it, can be made by

  $$\eta_{Out} \approx \frac{1}{2n^2} \tag{2.23}$$

  with n being the refractive index of the organic layers. Even if all the forementioned factors can be brought to unity, only the outcoupling factor by itself can therefore significantly limit the OLED performance. Assuming a typical refractive index of organic layers of roughly $n \approx 1.8$, η_{Out} yields only around 15% [42, 51]. Evidently, this factor needs to be respected when designing modern high efficiency OLEDs. Typical ways to improve η_{Out} are the optimization of the respective stack design, application of extracting optics like micro lenses or extraction layers, or the preferential alignment of emitter molecules in the films to increase the overall outcoupled light.

CHAPTER 3

Experimental methods

3.1. Atomic force microscopy

When using any kind of nanoparticle system in thin film applications, one major issue to focus on is the film formation of the particles. To characterize these films, a Bruker Dimension Icon Atomic Force Microscopy (AFM) system was used. All shown measurements were done under ambient conditions using the Bruker-developed ScanAsyst-Mode, which is based on their PeakForce®-technique.

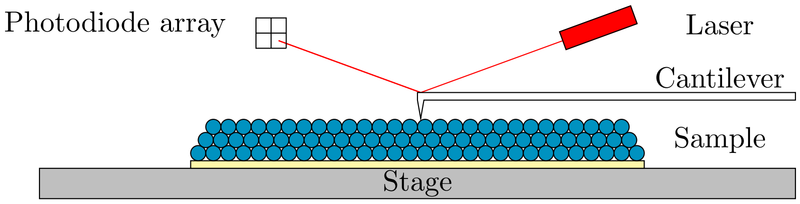

Figure 3.1.: Schematic drawing of the used AFM

As can be seen in figure 3.1, during an AFM measurement, the sample is located on a xy-stage and will be scanned across by the cantilever with the attached silicon nitride tip. On the backside of the cantilever, a laser beam will be reflected and sent towards a sectioned photodiode array. Oscillations of the cantilever can then be recorded using this photodiode signal.

In the ScanAsyst-mode, the cantilever is being oscillated well below its resonance frequency and the AFM tip is actually in contact with the sample surface. The contact force however is controlled to be always below 200 pN, which typically is low enough to neither damage the sample surface nor the tip. Going from one tap to the next, the interaction force of the cantilever and sample surface is being recorded and the system automatically adapts the cantilever feeback for the subsequent tap in order to assure the low contact force. These feedback adaptions then can be translated into the topographical information of the sample.

One big advantage of this measurement mode with respect to typical tapping mode measurements is that the contact force is so low that there is no damage done to the tip or sample. However also compared to classical non-contact AFM methods / dynamic force microscopy, the eventually possible resolution is higher with the Peakforce technique as the system adapts its parameters at every single tap. This in turn improves the signal-to-noise ratio of the measurement. More information about the PeakForce-technique and the ScanAsyst mode can be found with the manufacturer [52, 53].

3.2. jVL & EQE determination

A central method of characterization for OLEDs is the measurement of Current-Voltage-Luminance (jVL) characteristics. As can be seen in figure 3.2, the sample is placed on an immovable stage inside of an enclosed box with a non-reflecting inner surface. The stage includes connectors to electrically power the device which are adapted to the sample design used in the group. Note that this measurement box was located inside of a N_2-glovebox, so no further processing steps inbetween sample fabrication and characterization had to be taken.

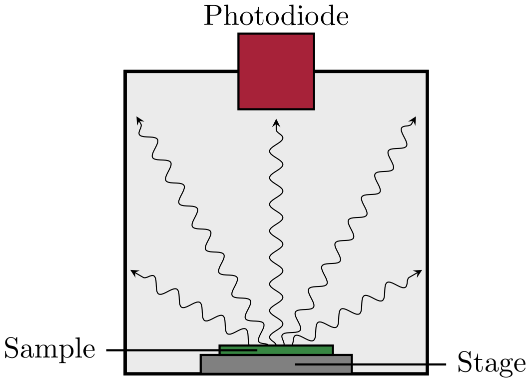

Figure 3.2.: Schematic drawing of the jVL measurement setup

An automated labview program controls the Source Measure Unit (SMU) to sweep the applied voltage in a given voltage regime with a specified step size. The powered OLED will then respond to the bias with a respective current and potentially luminance. The luminance will be filtered through a photopic color filter and be detected by a photodiode. The generated photocurrent will then also be recorded by the aforementioned Keithley2612B DualChannel SMU.

The mathematical transformation of the recorded photocurrent into the respective luminance in the unit of $\mathrm{cd\,m^{-2}}$ and from this point calculating the device EQE is dependent on the experimental setup geometry and sensitivity. Therefore parameters like the distance between the sample and photodiode, the pixel and photodiode size and the spectral sensitivity of the photodiode need to be well known. Assuming lambertian emission, the luminance L can be considered proportional to the photodiode current I_p.

$$L \propto I_p \tag{3.1}$$

The EQE is furthermore defined as the number of emitted photons of an OLED divided by the number of injected electrons and is shown in equation 3.2.

$$\eta_{EQE} = \frac{n_{emitted\,photons}}{n_{injected\,electrons}} = C \cdot \frac{L}{j} \tag{3.2}$$

Experimentally, the EQE can therefore be calculated by dividing the photodiode current by the sample current and multiplying the result with a constant prefactor C. Note that C is dependent on the experimental setup and the emission spectrum of the OLED. More details for the respective calculations of L and η_{EQE} can be found in ref. [54–58]

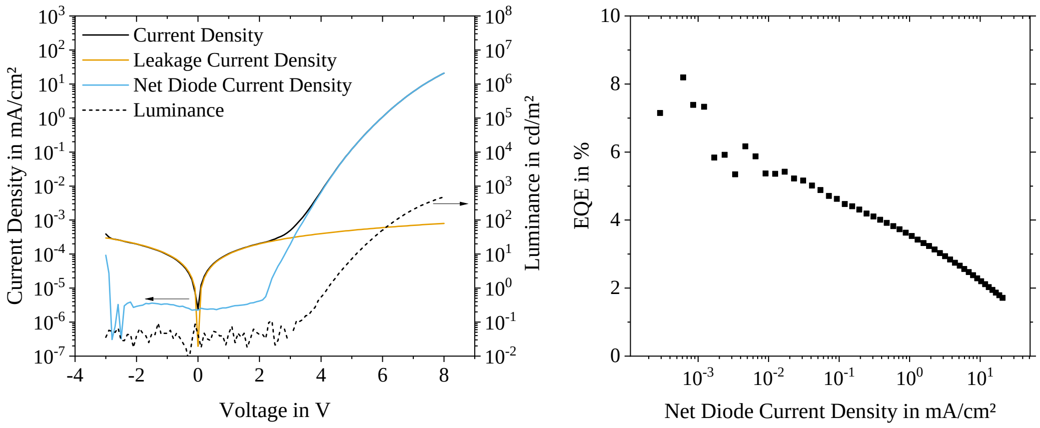

(a)

(b)

Figure 3.3.: Actual measurements of QD-samples processed in this work. jVL-characteristics (3.3a) and EQE-vs-j-plot (3.3b)

In figure 3.3a, exemplary jVL characteristics of a QD LED processed during the course of this work can be seen. The dashed black line indicates the Luminance which turns on at around 3 V while the solid lines represent different current densities. The black solid line is the measured device current density j, while the orange line was found by a linear fit of j below 1.3 V and represents the device leakage current density $j_{Leakage}$. Subtracting the two finally yields the blue net diode current density j_{nd} that can be used to gain more information about the device physics in the current turn on region. In this exemplary graph it can be seen, that j_{nd} has its turn on voltage at ca. 2.1 V while the luminance turns on at only 3.1 V. This clearly shows that this particular device stack would need further optimization and therefore clearly shows the importance of basic jVL characterization.

Figure 3.3b shows the calculated EQE according to equation 3.2 of the same device with the Electroluminescence (EL) spectrum of a red QD emitter as will be shown later in this work. This kind of data can then be further analysed and compared to different theoretical models explaining the efficiency loss of LEDs during operation described in the respective sections for organic- and QD LEDs of this work.

3.3. Impedance spectroscopy

One useful tool to investigate on electrical properties of organic semiconductor devices in general is impedance spectroscopy. It can be used to gain insights into, e.g., charge transport properties of different organic or inorganic-organic hybrid systems [59–61]. Studies on charge carrier dynamics including trap densities have furthermore proven the versatility of this characterization method [62–65].

The method used during this work was to apply a constant DC voltage at a sample device which is superimposed by a comparably small AC sinusoidal signal [66]. Then both the AC-frequency and the DC-Offset are varied while the current response of the sample is recorded. For measurements of the complex impedance, obviously the phase signal is of utmost importance. For all shown measurements, the Platform for All-In-One characterization of Solar cells and OLEDs (PAIOS) system by Fluxim was used including their comprehensive data analysis software *Characterization Suite*.

The most basic theoretical framework to explain the recorded data includes the definition of an equivalent circuit diagram, that is used to model the device under investigation. A simple, yet often reliable model can be to approximate any single layer in a device stack as a parallel circuit of a resistor and a capacitor. A complete device can therefore then consist of several of these units in serial connection. Depending on the type of device, additional resistors might then be necessary to fully describe the device behaviour. A more detailed description for the measurement technique and the theoretical modelling can be found in ref. [18, 29, 67, 68].

The main application point of impedance spectroscopy during the course of this work was to detect the onset of charge accumulation due to a GSP. As was described earlier in this thesis, the introduction of interface dipoles can lead to an accelerated or decelerated charge accumulation in parts of the device. By comparing the onset(s) of charge accumulation with other (e.g. optical) measurement methods (see e.g. section 3.5), insights into the emitter environment and the respective efficiency loss channels can be found. The reason why this is possible with the help of Capacitance-Voltage (CV) measurements is schematically depicted in figure 3.4.

As can be seen in the figure, the charge carrier densities in an idealized bilayer device are dependent on the applied bias. Starting from strongly negative biases below the transition voltage V_{tr}, no external charges can enter the device. The two layers act as two dielectrics and can be modelled as two connected RC-subunits. Upon reaching V_{tr} however, the HTL becomes a conductive layer and loses most of its capacitive properties, meaning the overall device capacitance is mainly due to the ETL capacitance. This is also accompanied by charge injection into the HTL and charge accumulation at the injection barrier at the HTL-ETL interface with a further increase in applied bias. This can be seen in the second to last sketch in figure 3.4. Finally exceeding the injection voltage $V_{injection}$, the external bias leads to injection of electrons as well as holes into the device, which leads to the breakdown of the device capacitance. The injected charge carriers can then - depending on the details of the specific stack design - recombine and form excitons or pass through the device. Both possibilities will be explored during the

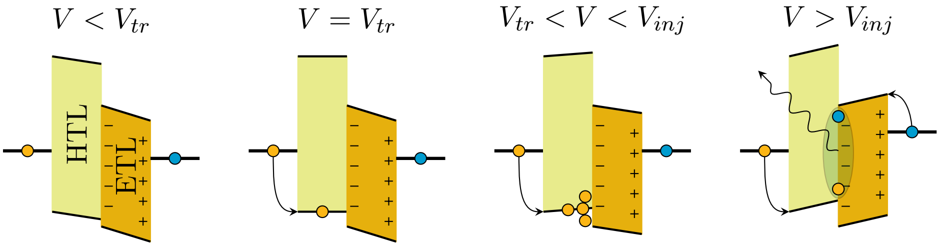

Figure 3.4.: Schematic view of charge accumulation in a hypothetic bilayer light emitting device, where the ETL shows a positive and larger GSP compared to the HTL illustrated by the + and − signs in the ETL. The applied voltage is increasing from left to right and leads to mobile holes (orange circles) in the HTL at V_{tr}. Further increasing the bias leads to charge accumulation at the HTL-ETL interface. Upon further increasing the voltage, electrons (blue circles) can be injected into the device and exciton formation with (radiative) recombination is enabled. Image adapted from [18, 69].

course of this work as different emitter classes will be applied in both unipolar (charges pass through the device) and bipolar devices (radiative recombination).

3.4. Time resolved photoluminescence spectroscopy

One of the most commonly used techniques in research with optical systems is the measurement of the Time Resolved Photoluminescence (TRPL) decay. This transient measurement enables insights into the physical processes involved when excited states relax under the emission of photons. There are different ways to achieve the measurement of a TRPL transient, however the resulting data looks similar independent of the choice of measurement setup. During the course of this work, a streak camera system was used to acquire the TRPL data, which is why only this method shall be explained here in detail. However, it shall also be mentioned that there are different methods to achieve this as well, like the use of (gated) iCCD cameras [70, 71] or time correlated single photon counting systems [72, 73].

The TRPL measurements during the course of this work were conducted with combination of a Hamamatsu C5680 streak camera with a Princeton Instruments Acton SpectraPro 2300i spectrograph. The sample excitation was done with a wavelength tunable picosecond pulsed PT400 laser system by EKSPLA. The laser additionally served as a trigger source for the camera setup, so that no external pulse driver was needed for the experiment. The pulse length was in the order of roughly 25 ps, which allowed the detection of fast fluorescent decays in the nanosecond regime as well as observation of any longer lifetimes.

The laser is, depending on the system under investigation, being set to a suitable wavelength and guided onto the sample. The Photoluminescence (PL) signal is then collected by a collimating lens and fed into the spectrograph through an optical fiber. In the spectrograph, the signal is then separated in the horizontal axis to reflect the (integrated) emission spectrum. These photons are then guided onto a photocathode which converts the optical signal beam into an electron beam. These electrons pass an acceleration system that is connected to a sawtooth-like sweeping voltage, which accelerates earlier and later electrons to a different degree and therefore separates the electrons in the vertical axis. These electrons will then pass a micro channel plate to potentially amplify the signal and will eventually be absorbed by a phosphor screen. The camera will finally take an image of this screen, which then has the spectral information in the horizontal axis combined with the transient information on the vertical axis. Integration over suitable regimes in the measurement data will then yield either transient decay curves (integration over wavelengths) or spectra (integration over time). For a more detailed description of the measurement setup, refer to [23, 31, 74, 75].

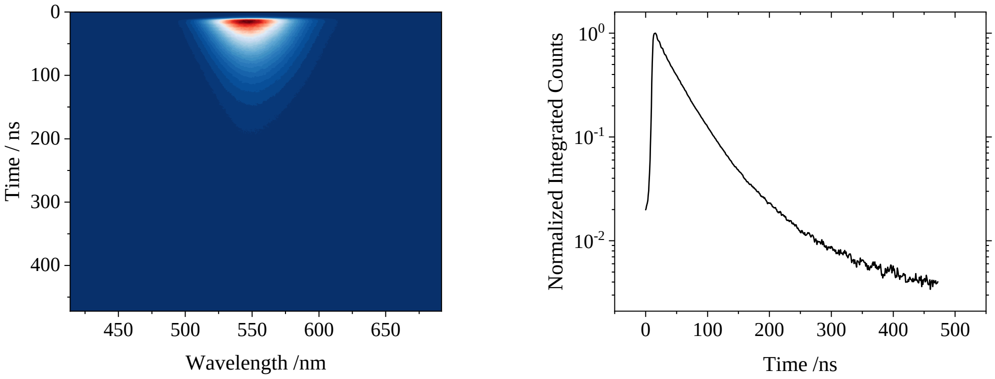

(a) (b)

Figure 3.5.: Streak camera image (3.5a) and transient decay derived by integrating between 440 and 780nm (3.5b) of a QD sample excited at 405nm. Note that the left image is plotted linearly in the color coding, while the right image is a logarithmic plot of the normalized integrated intensity. The laser beam hit the sample ca. 15 ns after the image recording started.

Figure 3.5 shows the TRPL measurement of an arbitrary QD sample excited at 405nm. Wavelength integration over the image yields the decay curve, that can be used to further analyze the excitonic processes in the QD layer. Starting point for this kind of evaluation is the rate equation including the relative change of exciton density per time interval $\dot{n}$:

$$\dot{n} = -k \cdot n(t) = -(k_r + k_{nr}) \cdot n(t) \tag{3.3}$$

This formula already includes the approximation that the overall decay rate k equals the sum of radiative and non radiative decay rates. Note that in reality, the theoretical modelling is more complex than that, however it shall serve as an example to illustrate the basic principles:

$$k = k_r + k_{nr} \tag{3.4}$$

Solving equation 3.3 for $n(t)$ with an exponential function approach yields

$$n(t) = A \cdot e^{-k \cdot t} + C \tag{3.5}$$

with a normalization constant A and a baseline constant C, which both are without physical meaning as they describe the sensitivity of the measurement setup (A) and the recorded background noise level (C).

Depending on the observed system, a monoexponential fit as described by equation 3.5 does not describe the measurement data well. For these cases, a multi-exponential fitting approach can be applied with an adapted fitting function:

$$n(t) = A \cdot e^{-k_1 \cdot t} + B \cdot e^{-k_2 \cdot t} + C \tag{3.6}$$

Note, that neither of these k_i-values equals the radiative recombination rate, even though the experiment only can detect radiatively decayed excitons. The calculated k_i-values always represent the overall decay rate defined by equation. 3.4. To further define the radiative and non radiative decay rates k_r and k_{nr}, additionally measurements of the absolute emitter quantum yield are necessary.

Futhermore, the necessity of a multiexponential fitting approach has to be considered carefully respecting the physical processes potentially involved in the decay dynamics. Multiple decay channels of a single exciton population can effectively not be distiguished in this proposed model. Therefore it is not directly possible to distinguish between e.g. different efficiency loss channels like Triplet-Triplet Annihilation (TTA) or Triplet-Polaron-Quenching (TPQ) solely by a single TRPL measurement. The need for a second exponential curve in the fitting procedure therefore has to be justified by an additional term in equation 3.3. One prominent example, that clearly justifies this additional term, is the field of TADF emitters. Here, the effective emissive state population is also depending on the process of Reverse Intersystem Crossing (rISC). This process increases the number of available singlet excitons by decreasing the number of non-emissive triplet states. As this process is not linked to the decay of singlet excitons, a secondary term emerges in the rate equation:

$$\dot{S}(t) = -(k_r + k_{nr})S(t) + k_{rISC}T(t) \tag{3.7}$$

Also note, that equation 3.7 is a strongly simplified result from the theoretical modelling concerning TADF emitters. It introduces the singlet and triplet state densities $S(t)$ and $T(t)$, respectively, where only the singlet state is considered to allow a radiative decay. The triplet state here solely leads to a delayed increase in radiatively available singlet states, while the intersystem crossing rate k_{ISC} is neglected in this formula. More details of the involved processes can be found in section 4.1.2 and [23, 76, 77].

3.5. PLQE measurements in thin film LEDs under operation

One major driving force of LED research has always been the need to optimize devices and improve device efficiencies. Investigating the efficiency of thin film light emitting devices, however, is a widely complex and multi faceted area of research. The first and most straightforward approach to learning about the scientific merit of, e.g., a specific emitter is to measure the electrical efficiency, meaning the EQE. However, as is shown in equation 2.22, the EQE is depending on both the physical properties of the emitter (q_{Exc}, q_{eff}) and the device stack (γ, η_{out}). Therefore, assuming the factor of q_{Exc} is known for the respective emitter, the only route to access the internal emitter quantum efficiency via an EQE measurement would be to fully optimize the stack. By doing so, γ can be brought to unity and the outcoupling factor η_{out} can be defined by careful optical simulations as described in section 2.4 of this work. Then the EQE should be proportional to the internal Quantum Efficiency (QE) and findings about the loss process during operation can be made. Note that for the following theoretical description, the Purcell factor will be considered constant. Therefore q is set proportional to q_{eff} in equation 2.22.

This, however, is of course relying on the assumption of γ, q_{Exc} and η_{out} being constant across the whole observed measurement range. This does not necessarily have to be true considering that the observed efficiency drop usually happens across several orders of magnitude of current density change, where especially the charge balance factor γ can definitely change, as will be shown in the experimental part of this work. Similarly, the recombination zone inside the emissive layer might change during the course of an electrical experiment, which in turn might, depending on the used stack, lead to a change in outcoupling efficiency η_{out}.

A more reliable way to access the internal quantum efficiency of a specific emitter would be to change from electrical to optical measurements. The first imminent advantage here is that, e.g., electrical properties of the CTLs do not play a role anymore. Also, for standard OLEDs with thin emissive layers, the recombination zone is considered to be the whole layer, as the optical excitation is usually too strong to be absorbed in only a fraction of the layer.

One possible way to detect optical efficiencies is to use the exciton lifetime via TRPL as the observable of choice to learn about the internal physical processes. This has been utilized in the past to investigate on the efficiency roll-off in phosphorescent OLEDs [74, 78–82]. However, as was shown in section 2.6 of this work, the comprehensive analysis of efficiency losses during electrical operation is a complex matter that requires considerable theoretical and mathematical input to gain the desired insights.

Therefore, another approach was introduced by the Bulovic group at Massachusetts Institute of Technology in order to quickly measure the field dependent PLQE drop that happens during operation of - in their case - CdSe-based Quantum Dot Light-Emitting Diodes (QDLEDs). The original publications can be found in references [3, 83, 84].

Their approach was to optically excite the emitter with a chopped continous wave light source while also powering the device with a (quasi-)constant bias. Additionally, the optical excitation was achieved through the use of a microscope objective, that allowed to selectively optically excite only a small area of the total pixel area. By doing so, they were able to measure the overall pixel emission - the electrically generated signal over the whole pixel area - as well as the optically generated signal through the objective only at the same time. Comparing the two allowed them to attribute the overall efficiency loss in their system mainly to the effect of the electric field across the QD layer.

This approach was adapted during the course of this work and realized into a new measurement setup for the bias dependendent determination of PLQEs. Note that the terms of *bias dependence* or *field dependence* will be used throughout this thesis to refer to this measurement setup, although the dominant efficiency limiting processes do not necessarily have to be directly caused by an electric field. For large parts of this work, much rather the charge carrier concentration induced by the applied bias is responsible for the efficiency losses instead of the applied field itself. The terminology for these two mentioned cases will however be the same, regardless. The experimental measurement setup can be seen in figure 3.6:

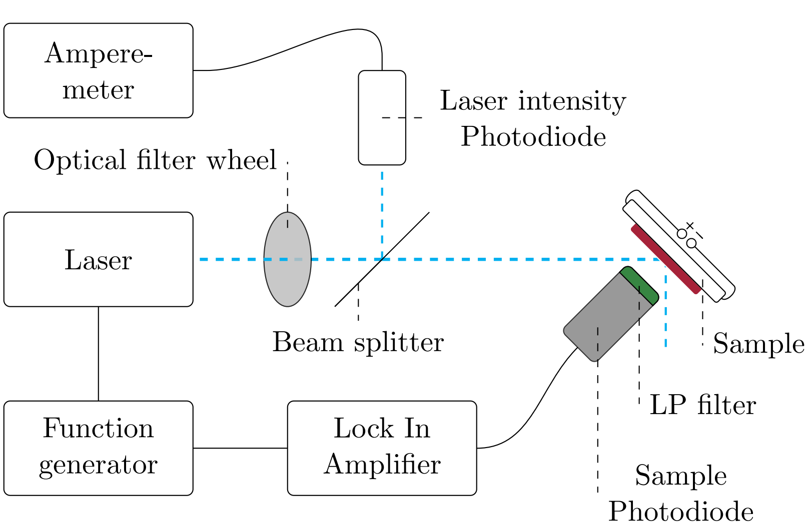

Figure 3.6.: Schematic drawing field dependent photoluminescence quantum efficiency setup. The two photodiodes translate the respective optical signals into electrical currents. The Amperemeter and the Lock-In Amplifier record the two signals. The AC function generator drives the modulation of the Laser and is fed into the Lock-In Amplifiers reference input.

The sample is biased by a SMU (indicated by the sample circuit) with a constant DC bias. This can, depending on the sample and the magnitude of the voltage, induce EL in the sample. Simultaneously, the pixel under investigation is hit by a laser beam which leads to PL as well. The photons emitted by the sample will then be collected by a photodiode after passing through a suitable longpass filter to cut off the laser stray light. The photodiode in turn is connected to a lock-in amplifier that records the PL signal j_{LockIn} and transfers it to the measurement PC.

The laser used for excitation is a modulated cw laser, meaning that the laser can be fed an electrical signal with which the cw laser beam then will be convoluted. This electrical signal is supplied by a function generator and was kept constant as a square wave with an amplitude of 2 V during the course of this work. The resulting laser beam therefore is similar to a physically chopped cw beam without the need for an actual hardware chopper. The same electrical square wave signal will also be fed into the aforementioned lock-in amplifier to serve as the reference signal.

Due to lock-in amplifiers' inherent property of phase and frequency sensitivity in general, the recorded signal corresponds solely to the optically excited PL emission from the sample [85]. The magnitude of EL signal caused by the electrical bias does not have any influence on the PL signal recorded this way. In principle, it is even possible to do these kind of measurements in room light without significantly declining signal-to-noise ratio in the resulting measurement as long as the measurement frequency is not equal to the line frequency of 50 Hz or a multiple of it.

Note that the arising EL signal is not recorded during these measurements. Although experiments with additional instrumentation and photodiodes were conducted to achieve exactly this simultaneous detection of EL- and PL signal, the resulting additionally gained EL data was always at the expense of signal quality in the PL signal path. As the EL signal could however better be measured at the jVL measurement setup described in 3.2, the focus in this optical setup was set to optimize the PL detection. Therefore all attempts to simultaneously measure the EL were reverted and no EL detection was included in the experiment.

The resulting recorded lock-in signal is depending on several parameters, as can be seen in equation 3.8:

$$j_{LockIn}(V) = \frac{P_{Laser} \cdot q(V)}{c_1 \cdot (1 - e^{-\alpha d}) \cdot \Phi_s} \tag{3.8}$$

P_{Laser} is the total emitted laser power and $q(V)$ equals the internal optical emitter efficiency. c_1 is a constant, accounting for optical losses of laser power between laser and sample as well as the photodiode alignment. The term $(1 - e^{-\alpha d})$ takes into account the assumption of sample absorption behaviour according to Beer's Law and the final term of Φ_s takes into account any spectral changes in the emission spectrum during the measurement according to:

$$\Phi_s = \int \Psi_s(\lambda) \cdot S(\lambda) d\lambda \tag{3.9}$$

with Ψ_s being the normalized spectral density of the emitter and $S(\lambda)$ being the respective photodiode sensitivity at a given wavelength λ.

Following the laser beam path in figure 3.6, an optical filter wheel was included in the setup to be able to quickly change the attenuation of the laser and change the PL excitation density. Note that the optically generated exciton density is supposed to be

small compared to its electrical counterpart, so that the additional optical excitation can be considered a small perturbation of the electrically generated excitonic properties in the emissive system. This allows to directly probe the optical efficiency under electrical operating conditions.
To check whether this condition was met during this work, the whole range of attenuation of the mentioned filter wheel (> 2 orders of magnitude) was used to repeatedly run an otherwise identical measurement. The results of these experiments can be seen in figure 3.7. Note that the measured datapoints at normalized laser intensities below 10^{-2} are not shown in this figure, since the error bars exceeded 100% and S/N-ratio therefore was even worse. Starting from the highest attenuation (not shown), the laser beam was

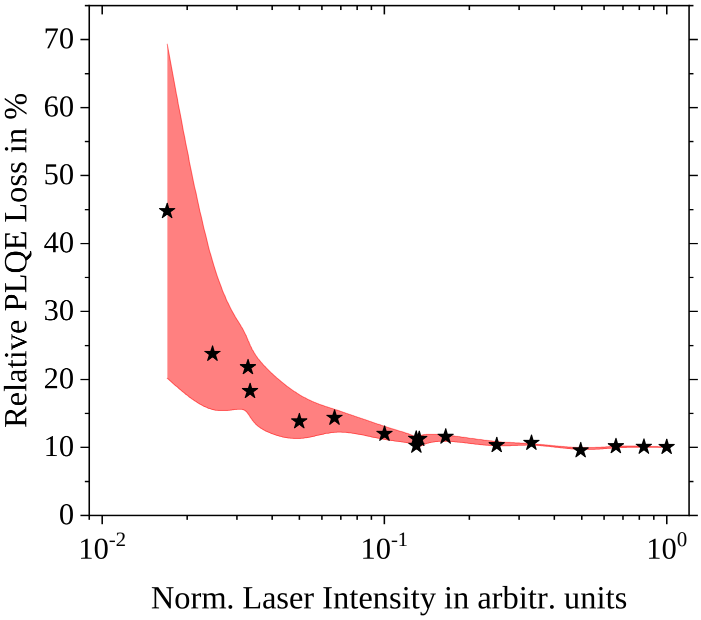

Figure 3.7.: Validification of the new measurement setup with OLED samples from [82]. The experiment was run multiple times up to a bias of only 4 V to make sure not to damage the sample. The relative PLQE was arbitrarily normalized at a current density of $10\,\mathrm{mA\,cm^{-2}}$ for each run. Then the recorded relative efficiency loss at $34\,\mathrm{mA\,cm^{-2}}$ for any single run was plotted in the graph in black against the respectivly applied laser intensity of the run. A laser intensity value of 10^0 corresponds to a measurement without laser attenuation. The respective measurement noise error is illustrated by the red shading. It can be seen, that the gained information of an efficiency loss of around 10 % does not depend on the excitation density as long as the laser is strong enough to ensure a reasonable signal-to-noise ratio. The current densities of the multiple runs (not shown) were identical to each other indicating no degradation by repeated device operation.

too weak to detect any optical signal with the lock-in system except for measurement noise. Then with decreasing attenuation, the signal to noise ratio increased significantly without changing the emerging PL signal shape. Therefore one can safely assume that the laser intensity is not high enough to induce nonlinearities in the samples and the forementioned precondition can be considered as fully met. Experimentally, the attenuation was kept rather high ($< 1 \times 10^{-1}$ norm. laser intensity in figure 3.7) for all shown experiments in order to keep the optical excitation density low.

After the filter wheel, the laser beam then goes through a beam splitter that reflects a constant amount of laser radiation while the main beam is transmitted towards the sample. The reflected beam will be detected by a second photodiode that tracks the laser intensity during an experiment. Although the ratio of reflected to transmitted light is not measured in this experiment, it can safely by considered constant so that any changes in laser output power will be tracked with this second photodiode. The recorded photocurrent of this second diode can be described as

$$j_{PD} = c_2 \cdot P_{Laser} \tag{3.10}$$

with the constant factor of c_2 accounting for the setup alignment, the constant fraction of reflected light from the beam splitter and the photodiode sensitivity at the given laser wavelength.
Substitution of P_{Laser} from equation 3.10 into equation 3.8 eventually yields

$$j_{LockIn}(V) = j_{PD} \cdot q(V) \cdot \frac{1}{c_1 c_2 (1 - e^{-\alpha d}) \Phi_s} \tag{3.11}$$

so that the bias dependent PLQE can be described as

$$PLQE(V) = q(V) = C \cdot \frac{j_{LockIn}(V)}{j_{PD}} \tag{3.12}$$

with $C = c_1 c_2 (1 - e^{-\alpha d}) \Phi_s$.

Normalization of this quantity therefore yields the relative PLQE in dependence of the applied electric field. Combining this measurement with an absolute PLQE measurement e.g. in an integrating sphere then yields the absolute bias dependence of the PLQE. This information can then in turn be used to explain the physical processes involved in the emissive system. Note however, that this implies C being constant over the whole measurement range. c_1 and c_2 can safely be considered constant as they depend on the setup alignment which does not change during measurements. Further room for future improvement of this setup is however given in simultaneously recording α and Φ_s as well. For the experimental data shown in this thesis, the assumption should however be valid anyhow. Although small changes in QD emission spectra are observed for the QDs in this work, the photodiode sensitivity $S(\lambda)$ is however essentially constant over these comparably small changes. Therefore, also the integral over the product of these two quantities Φ_s can therefore be considered approximately constant against the observed large changes in PLQE. Also, first experiments to track the sample absorption have not shown any reproducible change in $\alpha(V)$.

Upon finalization of the measurement setup, several tests to validate the setup's output data have been performed. In order to do so, the samples used in [82] - although already roughly eight years old - were measured and the results of the initial study shown in the publication were compared to the received measurement data. In this publication, one of the key messages was, that the analysis of the electrical OLED efficiency pointed towards triplet-triplet annihilation (TTA) as being the dominant quenching process in these phosphorescent devices, while their optical analysis via the exciton lifetime pointed towards triplet-polaron quenching (TPQ). Without going into detail of the discussion and the conclusions drawn in the publication, the measurement data could be reproduced nicely as can be seen in figure 3.8. The optically gained data also clearly shows the mismatch of TTA and suitability of TPQ to explain the measurement data, which in turn serves as validation of the experimental setup. More information on the mentioned efficiency loss processes can be found in section 4.2 of this thesis.

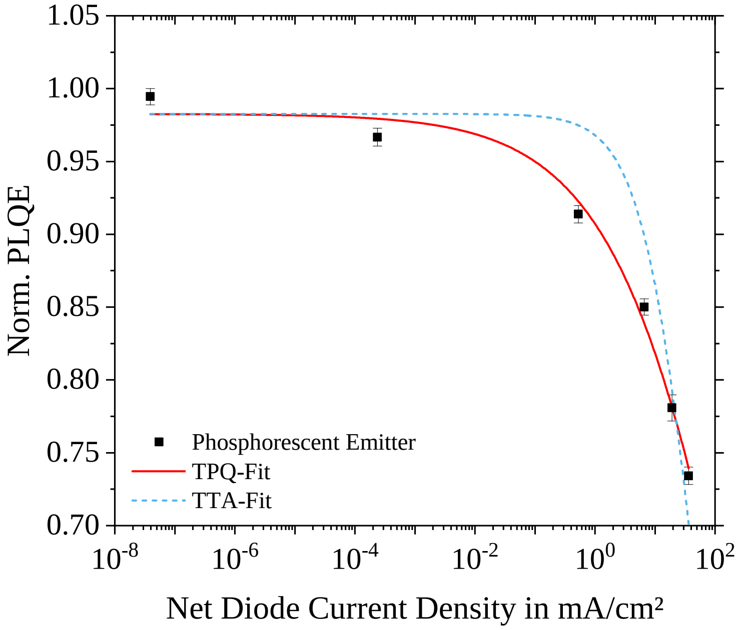

Figure 3.8.: Validation of the new measurement setup with samples from [82]. The key message of TPQ over TTA as dominant quenching process due to optical measurement techniques can be reproduced. The fit curves were calculated using the models described in [82].

The data shown in figure 3.8 was measured in the matter of minutes. This alone shows one great advantage of the bias dependent PLQE measurement setup compared to other analysis techniques. The optical efficiency is directly displayed even while the measure-

ment is running. No further post processing or calculations are needed besides averaging, normalizations and error estimations. Additionally, the setup is equally useful for a whole range of different sample types. With investigations on mainly QDLEDs in mind during the installation of the setup, it has proven to be a very versatile and valuable tool for research in different fields. During the course of this work alone, the setup has been applied to polar and unpolar phosphorescent OLEDs, unipolar devices, InP-based QDLEDs, Perovskite-based LEDs, Metal-Insulator-Semiconductor (MIS)-diode-like thin film devices involving phosphorescent emitters, NC based thin film solar cells and third generation TADF based OLEDs. Not all of these measurements are part of this thesis however, although their results will most likely be part of the future publications and theses of my colleagues in the group.
Note however, that with this setup, two crucial input parameters for the system are the laser wavelength λ and the modulation frequency f. It is imperative that these parameters are chosen suitably for the sample under investigation:

- Firstly, the modulation frequency f should be chosen far enough from the line frequency and any other common frequencies in a lab environment or their multiples to keep potential error sources through the frequency sensitive detection as low as possible. Additionally considering the excited state lifetimes of, for example, TADF emitters, which can be in the range of several μs, the frequency should not be chosen too high in order to let the system fully relax between optical excitations. Therefore, the chosen frequencies for experiments shown in this work were 1234 Hz for phosphorescent and TADF emitters and 12 345 Hz for any NC based LED system.

- And secondly, the laser wavelength has to be chosen in a way to enable the respective absorption of choice. For phosphorescent OLED samples it is common practise for optical experiments to excite the host material with a UV laser and generate an exciton there. Then in a second step, the exciton will be transferred to the guest where the emission occurs. In all measurements shown in this thesis however, this is not the case. In all shown measurements, the respective emitter was directly excited at a suitable wavelength, where all surrounding layers where transparent. In that way, it is possible to probe even more specifically towards the intrinsic emitter properties without other involved effects. While both strategies can be used in different experiments it is important to consider this fact to be able to properly interpret the measurement data. The choice of laser wavelength obviously then in turn also influences the choice of respective optical filter.

Experimentally, during this work, two different lasers by *Oxxius* were in use. One blue 405 nm laser *LBX-405* for excitations of green phosphorescent and TADF OLEDs and a green laser centered at 520 nm *LBC-520* for investigations on red QD devices. The lock-in amplifier is a *Stanford Research Systems SR830*, a *Keithley196 DMM* was used to measure the laser intensity, the sample was powered by a *Keithley2400* SMU that also recorded the sample current while a *HP3314A* function generator was used as a source for the modulation and reference frequency. The photodiodes *SM1PD1B* were supplied by Thorlabs as well as the optical filters at 450 nm and 550 nm, respectively, to separate the sample signal from the laser stray light.

Note that during the timeframe of this work (2017-2021), several groups in different research fields have also successfully adapted the approach initiated by [3, 83, 84] in a similar way compared to the here proposed experiment. It successfully has been used to investigate on polar phosphorescent OLED materials [50, 86] as well as perovskite LEDs [87] which again proves its flexibility regarding involved material classes. Similarly to the work shown in this thesis, a comparable setup has been used in studies investigating the PL properties of CdSe QD as well [88].

3.6. Device fabrication

During the course of this work, devices from different suppliers have been investigated. These samples were supplied in an already encapsulated state, which is why for these samples no more processing had to be applied. The author thanks all suppliers of samples including but not limited to Prakhar Sahay, Dinara Samigullina and Dr. Yohan Kim. For all other samples, which were prepared here in Augsburg, the following section will show the procedures and sample processing. All samples were processed both with solution based techniques as well as thermal evaporation.

Solution processing

All samples were processed on glass substrates with a precoated layer of 90 nm ITO. The substrates were cleaned in a cleanroom facility by three subsequent washing steps in an ultrasonic bath in technical acetone and isopropyl alcohol followed by UV-grade isopropyl alcohol. Each cleaning step lasted for 10 min and the samples were dried with a blow gun inbetween washing steps. An UV-Ozone surface pretreatment then was applied to the samples to improve the wetting behaviour of subsequent film deposition. Spincoating of Poly(3,4-ethylenedioxythiophene) polystyrene sulfonate (PEDOT:PSS) was also carried out in the cleanroom under ambient conditions. The coated layer was removed on top of the ITO contact pads with a cotton Q-Tip in wet state whereafter the substrates were heated on a hotplate at 120 °C for 20 min.
All samples from the OLED section of this work were then already prepared for thermal evaporation, while the QD samples underwent another step. They were transferred to a nitrogen filled glovebox system to minimize contamination of the layers with oxygen and water. Subsequently, the next layer was spincoated on top of the PEDOT:PSS, which was a polymeric HTL in most cases. As a last solution based processing step, the QD layer was deposited on top of the polymeric HTL. The devices then were transported into another glovebox system with an included thermal evaporation chamber under nitrogen atmosphere, where the remaining layers were evaporated without exposure to ambient conditions at any time.

The spincoater used in the glovebox system was manufactured by Ossila [89] with a custom chuck design specifically adapted to the sample dimensions used throughout this thesis. Spincoating duration for all deposited layers was 30 s, the spinning speed was fixed to 3000 rotations per minute. If necessary, the resulting film thickness could be chosen by changing the rotation speed and the concentration of the used solution.

High Vacuum Thermal Evaporation

After the solution based processing steps, the samples were brought into the deposition chamber under nitrogen atmosphere. The chamber contains six sources for organic materials with additional sources for metal deposition. Therefore a break of vacuum during the deposition process was never necessary for the investigated samples. The shadow masks' position in the chamber was fixed during every single deposition, however by changing the actual deposition position of the samples, a de facto change of evaporation

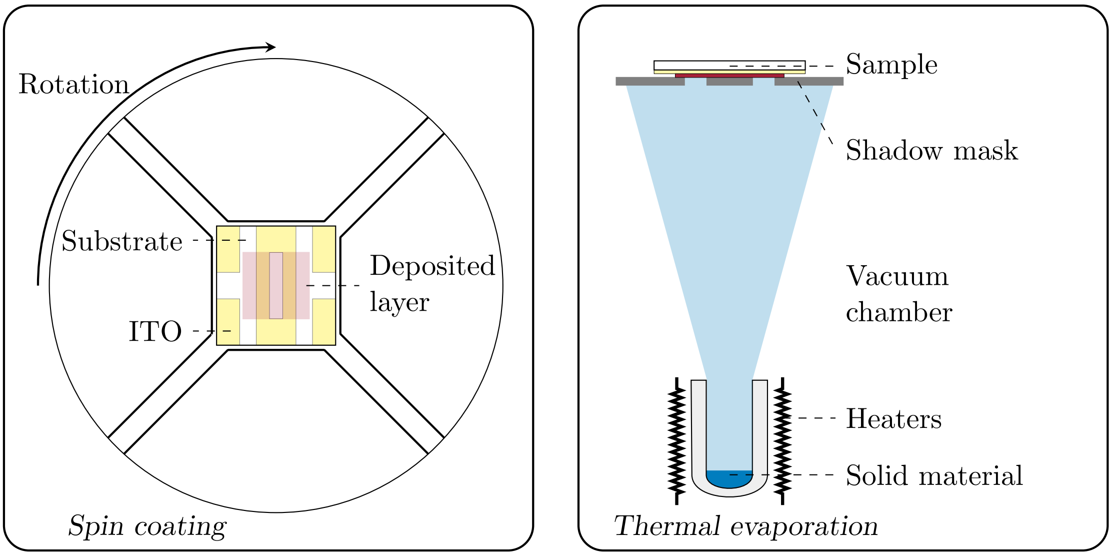

Figure 3.9.: Schematic depiction of the spincoating and thermal evaporation process. The yellow shaded areas represent the precoated ITO layout. The red shading represents the final spincoated layer after removing the material above the contact pads. The blue material is being evaporated / sublimed from solid phase to gas phase. The vapor forms a film on the substrate area which is not covered by a suitable shadow mask.

pattern was possible.

The depositon itself was carried out at a vacuum of around 10^{-7}mbar in order to keep the sample contamination of the deposited layers as low as possible. Unfortunately, the chamber is used by several members of the group working with different materials, so a certain degree of impurity can never be excluded during sample evaporation.

The samples were separated from the main part of the chamber by a mechanical shutter during evacuation and preheating of the materials. Once a desirable evaporation rate was achieved, the hardware shutter was opened and the material could start to grow films on the areas of the substrate which are not covered by the shadow mask. The layer thickness growth was monitored by a quartz crystal microbalance, which also allowed to close the hardware shutter as soon as the desired layer thickness was reached. Similarly, also co-deposition of two materials was possible from two different sources with two different microbalances. This allowed deposition of guest-host systems for e.g. phosphorescent OLEDs.

Part II.

Organic light-emitting diodes

CHAPTER 4

Theoretical description of organic light emission

Historically, OLEDs were initially based on organic molecules that emit light through the process of fluorescence [1]. These fluorescent devices are commonly labelled as *first generation OLEDs*. As was described earlier, the efficiency of these OLEDs was limited by several factors and over the years, a multitude of improvements was introduced in order to gain modern highly efficient devices. During the course of the work presented in this thesis, these fluorescent emitters were replaced by a phosphorescent as well as a TADF emitter. An overview over these two material classes will be given in the following section, followed by a short description of two efficiency limiting processes.

4.1. Organic emitters

4.1.1. Phosphorescent emitters

As was shown in section 2.2 of this work, the formation of an exciton can result in effectively four different spin states which are all equally likely to form during electrical excitation. This leads to a q_{Exc} of only 0.25 for fluorescent emitters, since the radiative decay of the three triplet states is spin forbidden.

Phosphorescent emitters have been found to circumvent this problem and realize a higher overall device efficiency through the enhancement of q_{Exc}. The theory behind this efficiency improvement can be understood looking at a schematic term diagram as shown in figure 4.1.

Starting from the left in the illustration, the process of absorption is drawn. There, a photon will be absorbed and excite the molecule from the ground state S_0 to a higher state S_1 or S_2. Note that there are vibronic sublevels for each state which can be reached, however the excess energy is typically quickly lost due to internal conversion with the rate k_{ic}. Absorption into the triplet state is an optical transition, which is spin-forbidden in fluorescent materials, the respective rate would therefore be very small which is why

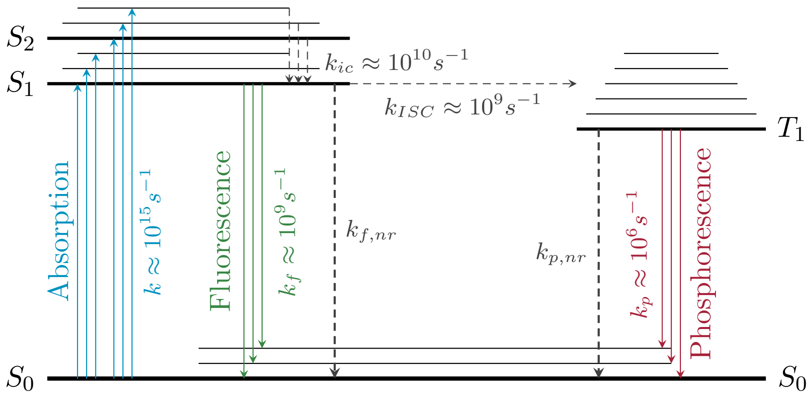

Figure 4.1.: Simplified Jablonski- or term diagram of possible electronic transitions in organic semiconductors. The processes of absorption, fluorescence and phosphorescence and their respective rates k, k_f and k_p are drawn to and from respective ground or vibrational substates. k_{ic} is the internal conversion rate, k_{ISC} the rate for intersystem crossing. Non-radiative processes are illustrated by dashed lines. More details can be found in the text. Redrawn from [15, 18].

it is not shown in this simplified graph. Note however, that it is not negligible for phosphorescent materials.

The excitons on the S_1 level can then decay radiatively or non-radiatively (k_f or $k_{f,nr}$) in fluorescent materials. Alternatively, they can be transferred to a triplet state via the process of Intersystem Crossing (ISC) (k_{ISC}), if enabled. This process is allowed in phosphorescent materials due to Spin-Orbit Coupling (SOC) in the presence of heavy metal ions in the organic material [90]. The spin states of singlet- and triplet states are hereby slightly mixed which allows the horizontal transfer in the illustration. This process typically generates a triplet in an elevated state which then decays nonradiatively to the T_1 state. [13, 91, 92]. As the T_1 triplet level is typically energetically lower than the respective singlet state S_1, all excitons are located in the mixed triplet state after the initial excitation. Similarly, during electrical operation, only 25% of excitons form in the singlet state, which then can be transferred to the triplet state as well.

Additionally to enabling the intersystem crossing, SOC in the presence of heavy metal atoms like Ir or Pt enables emission from the triplet T_1 state to the singlet ground state S_0. While the decay rates are still significantly slower for phosphorescence compared to fluorescence, they are fast enough to increase the overall device efficiency. Therefore the radiative exciton fraction q_{Exc} can reach unity with this class of emitters. Note however, that the slower radiative rate also means a longer exciton lifetime in the range of up to several μs. This can cause other efficiency losses during operation, as the triplets have comparably long times to diffuse and find positions or traps to quench and lose the excitation energy. Therefore the radiative quantum efficiency q_{eff} also needs to be considered carefully while designing these phosporescent, *second generation OLEDs*.

4.1.2. Thermally activated delayed fluorescence

Another big step in the development of modern and efficient OLEDs was taken with the introduction of TADF. The phenomenon of delayed fluorescence itself was initially found in uranyl salts in 1929, however was only comparably recently introduced into organic light emitting materials [93, 94]. Similarly to phosphorescent OLEDs, the approach to improve on the electrical efficiency is to increase the radiative exciton fraction q_{eff} as close as possible to unity. The mechanism behind it, however, is different.

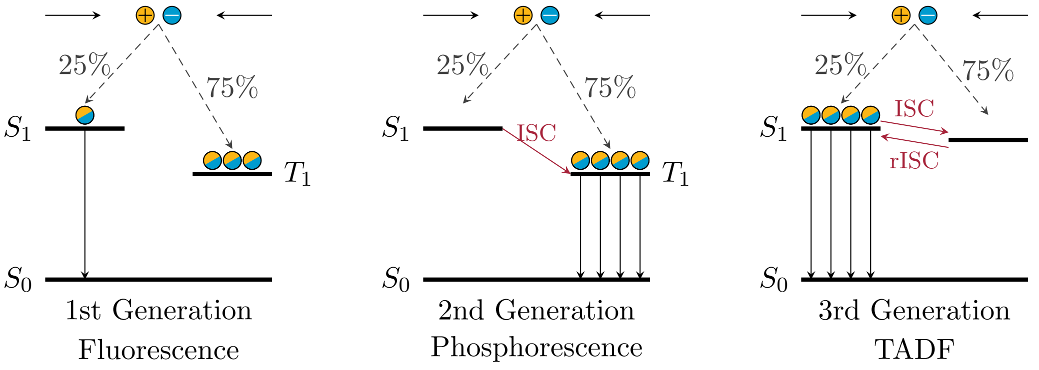

Figure 4.2.: Schematic comparison of the emission mechanisms for the three generations of OLEDs. TADF emitters rely on a small energetic difference between S_1 and T_1 levels so that eventually all electrically generated excitons can be harvested by prompt or delayed fluorescence. Black solid arrows indicate radiative exciton decay. Image redrawn from [95].

As can be seen in figure 4.2, the phosphorescent decay in second generation OLEDs orginates from the triplet state, where the respective decay rate is forbidden without SOC. Through the presence of heavy metal atoms, the phosphorescent decay rate is significantly increased which results in an excited state lifetime of phosphorescent emitters of around a few μs. The electrically formed singlet states are typically also transferred to the triplet state by ISC.

In TADF OLEDs, the radiatve decay originates from the singlet level and is thereby a fast (≈ ns) fluorescent decay. The efficiency improvement of TADF materials however stems from the highly increased rate of rISC, which enables the transfer of triplet states back to singlet states. With the minimization of non-radiative decay channels a high radiative exciton fraction q_{Exc} of over 90% can be reached [94]. This is made possible by only a small energetic difference ΔE_{ST} between S_1 and T_1 levels of typically below 0.1 eV. Then the thermal energy of the surrounding device is enough to enable efficient rISC. Typically, the dependence of rISC rate and energetic gap follows a Boltzmann distribution:

$$k_{rISC} \propto \exp\left(-\frac{\Delta E_{ST}}{k_B T}\right) \tag{4.1}$$

with the Boltzmann constant k_B and the absolute temperature T. Note however, that

elevated temperatures might also decrease the effective quantum efficiency q_{eff}, so that compromises need to be found in order to achieve optimal overall efficiency [96].
With the introduction of such TADF molecules into OLEDs, one big issue of phosphorescent emitters could be resolved: Efficient blue emitting molecules could be found while the phosphorescent emitters only achieved high efficiencies in red and green emitting complexes for a long time [97, 98]. Furthermore, TADF emitters are purely organic and do not need a heavy metal ion to form a complex. This in turn brings the advantage of in principle cheaper material costs and better environmental footprint.
The problem of TADF emitters, on the other hand, is that the working principle of the rISC is a highly complex field and the design rules for efficient molecular composition have not completely been understood yet. Note that the theoretical description of the exact processes would be too much to cover here, however, it shall be mentioned that the interplay between decay kinetics, electronic structure and spin-vibronic properties of the respective material needs to be considered [76]. Additionally, often different molecules indicate towards different working mechanisms of rISC so that a comprehensive (simulational) study of large numbers of molecules is even more difficult.
One common way to achieve a low ΔE_{ST} has been found to spatially separate the wavefunctions of HOMO and LUMO. Therefore, one could run Density Functional Theory (DFT)-calculations to identify the most promising candidates for efficient emitters from an arbitrary pool of molecules, however, the radiative rate of fluorescent decay is proportional to the wavefunction overlap of HOMO and LUMO as well. Completely separated frontier orbitals will result in low energy splitting and low radiative rates, which clearly emphasizes the importance of careful molecular design. Following from this, also the material synthesis can be rather complex which in turn increases the production costs again.

4.2. Efficiency loss mechanisms in organic light-emitting diodes

One of the most important points in modern technologies is the topic of overall efficiency. When talking about thin film LEDs, this mainly comes down to the figure of merit EQE, which was explained in detail in section 2.6 of this thesis. There it was shown, that the overall EQE was determined by mainly four components - the charge balance factor γ, the radiative exciton fraction q_{Exc}, the effective quantum efficiency q_{eff} and the outcoupling factor η_{out}. The first and last factor are mainly determined by the respective stack design involved in a LED while q_{Exc} can be assumed either 0.25 for fluorescent materials, or unity for phosphorescent materials and materials comprising TADF. The third factor q_{eff} however is dependent on the material property of the internal quantum efficiency q and the stack dependent Purcell-factor F as shown in equation 2.18. The following section will now cover the theoretical description of commonly seen efficiency loss mechanisms for both organic- and QD- LEDs, which will directly influence q.

4.2.1. Triplet-Triplet-Annihilation

It was already mentioned in the previous section that the illustration in figure 4.1 is only a simplified view of the reality. In this image, it is implied that electrically generated excitons will form both singlets and triplets and that, in particular, the triplet states can only emit a photon if the process of phosphorescence is enabled. However, even for materials with spin forbidden phosphorescence and hence low decay rates, the triplets can be used to increase the overall light emission [99]. This process is typically known as triplet fusion or TTA.

Due to allowed access to triplet states in phosphorescent OLEDs, the lifetime of these triplet states is significantly reduced. However, it still is several orders of magnitude longer than the lifetime of singlet states, which decay via fluorescence. Therefore, triplet excitons have a comparably long time to diffuse in an emissive layer before they eventually decay. Furthermore, the probability of two excitons diffusing in close proximity to each other is drasticly increased, which increases the probability of TTA related processes. If two triplets actually do meet, they can interact with each other in one of the following ways:

$$T_1 + T_1 \longrightarrow S_1 + S_0 \tag{4.2}$$

$$T_1 + T_1 \longrightarrow T_1 + S_0 \tag{4.3}$$

The first of the two cases will generate one excited state singlet exciton S_1, while one triplet state loses its energy and falls back to the ground state S_0. If this S_1 state then decays radiatively, two triplets effectively generated one photon via *delayed fluorescence*. In the second case, however, one triplet state's energy will be transferred to another triplet state, exciting it to a higher triplet level T_n $(n > 1)$. This state will then quickly relax nonradatively via internal conversion and the energy is effectively lost for light emission.

Note that the first case with the generation of a singlet exciton seems to be favourable in the case of fluorescent emitters, as some of the triplets can be harvested and turned into photons, however TTA is a massive problem in the case of phosphorescent materials and TADF emitters as it can lead to signficiant exciton quenching [14]. In both cases, even the favourably generated singlet state S_1 can be transferred into the triplet state via intersystem crossing, so that the secondary triplet state energy is effectively lost. The dominant process for these materials therefore is shown in equation 4.3.

Luckily however, the prerequisite for strong TTA was already mentioned above and can be circumvented quite easily. Since TTA relies on two triplet excitons diffusing in the emissive layer and eventually interacting with each other, the application of guest-host-systems with the respective emitter in a polymer or small molecule host can reduce the efficiency loss via TTA. By increasing the average emitter-emitter distance via a low concentration of dopant (typically 1-10% [14]), TTA can be successfully supressed. Furthermore, suitable energy band alignment of guest- and host- HOMO and LUMO levels will trap charge carriers on the respective emitter further impeding exciton diffusion and thereby TTA.

All OLEDs manufactured and presented in this work had a dye concentration of 8-10%, the amount of TTA is therefore expected to be low and only a minor factor in the efficiency analysis of second or third generation OLEDs. Therefore, only the final result of the theoretical description of TTA under electrical OLED operation given by Baldo *et al.* shall be given here [79].

$$\frac{dn}{dt} = -\frac{n}{\tau} - \frac{1}{2}k_{\mathrm{TTA}}n^2 + \frac{j}{ed} \tag{4.4}$$

Starting from the time dependence of exciton concentration dn/dt, all excitons can be lost via radiative or non-radiative processes besides TTA, represented by the first term of $-n/\tau$. Alternatively, they decay via TTA represented by the second term of $-\frac{1}{2}k_{TTA}n^2$. The third term of $+j/ed$ describes the electrical exciton generation at a current density j in the exciton generation zone with the thickness d. Solving this equation for the steady state condition of $dn/dt = 0$ eventually yields

$$q_{TTA}(j) = \frac{\eta_{ext,0}}{4}\frac{j_0}{j}\left(\sqrt{1 + 8\frac{j}{j_0}} - 1\right) \tag{4.5}$$

with the critical current density j_0 and the approximated EQE without applied current density $\eta_{ext,0}$. The details of this calculation can, as already mentioned, be found in the literature [74, 79]. This result however shall suffice for the analysis presented in this work, as equation 4.5 can be used to fit the measurement data shown in the experimental part of this thesis.

4.2.2. Triplet-Polaron Quenching

The introduction of second- and third generation OLEDs lead to a significant increase in potential device efficiency but leads to longer triplet lifetimes, as was mentioned already earlier. Another common quenching mechanism besides TTA is the so called TPQ.

If an electrical charge moves through an organic solid, the charge polarizes its environment which is commonly described as a quasiparticle, the *polaron*. This can, for example be a charged organic anion, that gained an additional electron in the LUMO. Triplets in the vicinity can then transfer their excited state energy to this electron/polaron, which will be excited to a higher state and immediately decay back through internal conversion. This effectively results in the transformation into thermal energy, potential chemical emitter degradation and, in general, optical energy loss [14]. This can be expressed by the following equation with an acceptor A:

$$T_1^* + A \longrightarrow S_0 + A^* \tag{4.6}$$

The theory of this bimolecular process has also been described in detail in the literature, so it again will suffice to focus on the main results here [74, 80]. Starting point for the description again is the rate equation for the exciton density in the emissive layer:

$$\frac{dn}{dt} = -\frac{n}{\tau} - k_{TPQ}\left[\frac{\rho_c(j)}{e}\right]n + \frac{j}{ed} \tag{4.7}$$

Similarly to the TTA rate equation, the first term in equation 4.7 resembles the radiative and nonradiative decay of excitons excluding TPQ, the last term represents the electrical exciton generation and the middle term describes the TPQ. The factor of $\rho_c(j)/e$ is the polaron density and is set equal to the charge carrier concentration. Note that this theoretical deduction is valid for the case of SCLC and constant charge carrier mobilities. Traps states, if present, are assumed to have an exponential distribution in the organic layer. This equation can then be solved for steady state conditions ($dn/dt = 0$) into:

$$q_{TPQ}(j) = \frac{\eta_{ext,0}}{1 + \tau C k_{TPQ} j^{\frac{1}{1+l}}} \tag{4.8}$$

Here, k_{TPQ} is the TPQ rate, C is a constant prefactor that exclusively depends on the material properties and does not change during device operation, τ is the excited state lifetime and l is a parameter defined by the energetic trap depth E_t with $l = E_t/k_B T$.

This expression can now again be used to fit the experimental data, however there are a few short points to note:

- In equation 4.8, the polaron density was set equal to the charge carrier concentration defined by the current density under operation. This however does not have to be the case as was shown in OLEDs with a significant GSP [50]. Here the GSP leads to charge accumulation below the turn on voltage, which increases the polaron density and thereby enables TPQ even before there is actual current flowing, which is not predicted by the formula.

- Equation 4.8 features a lifetime τ in the denominator. For the case of phosphorescent OLEDs, this is the combined radiative and nonradiative lifetime ($\tau^{-1} = k_r + k_{nr}$). For the case of third generation OLEDs however, quantitative application of equation 4.8 requires careful consideration about which value to use here. The emissive singlet state has only a short lifetime, while the accessible triplet lifetime is several orders of magnitude longer.

- Otherwise, equation 4.8 should be applicable for both phosphorescent as well as TADF OLEDs. C and l are dependent on the properties of organic semiconductors in general, which should be similar for both material classes. The TPQ-rate k_{TPQ} is dependent on the exact mechanism of the quenching process. Depending on the type of energy transfer, short range Dexter transfer via wavefunction overlap or longer range Förster transfer via dipole coupling can occur. This, in turn, is then again dependent on the distance between polaron and exciton and therefore relates to the molecular size. However, this is true for both second and third generation OLEDs, so that the formula should in theory be applicable for both material subclasses, as typical molecular sizes are comparable. Recent studies on the exciton quenching mechanisms in TADF OLEDs also have derived theoretical predicitons which qualitatively agree with these assumptions [100].

CHAPTER 5

Optical and electrical characterization of polar OLEDs

The main focus point of this part of the thesis will be to highlight different efficiency loss mechanisms in different thin film LEDs. The starting point for the research on efficiency loss mechanisms in OLEDs will be investigations with a second generation phosphorescent emitter. Tris[2-phenylpyridine]iridium(III) (Irppy$_3$) was used in different stack designs in samples built in Augsburg and the respective efficiency losses will be discussed with respect to the results of mainly jVL, CV and field dependent PLQE measurements. As a next step, devices comprising a third generation TADF OLED emitter were investigated and the results of second and third generation OLEDs will be compared and discussed. The TADF emitter used was 9,10-Dihydro-9,9-dimethyl-10-(4-(4,6-diphenyl-1,3,5-triazin-2-yl)phenyl)acridine (DMAC-TRZ). The OLEDs built in Augsburg will also make use of polar charge transporting materials and elucidate the effect of GSPs on the device performance.
After that, the second part of this chapter will revolve around samples received from the Technische Universität Dresden (TUD). The author is particularly grateful to Dinara Samigullina for the sample processing and jVL- as well as CV characterization. Here, the influence of polar electron transporting materials on the optical and electrical efficiency of phosphorescent OLEDs incorporating Irppy$_3$ will be investigated.

5.1. Investigations on polar hole transporting material OLEDs

5.1.1. Phosphorescent OLEDs

The phosphorescent emitter $Irppy_3$ was used in a number of different stack designs. An overview of these stacks can be found in figure A.1 in the appendix. These samples were all built at the University of Augsburg according to the methods described earlier in this thesis.

Unpolar OLEDs

As a starting point, unpolar OLEDs were processed. This means, that exclusively layers consisting of molecules with no or low PDMs were chosen to be incorporated into this stack. 2,4,6-tris(biphenyl-3-yl)-1,3,5-triazine (T2T), Tris(4-carbazoyl-9-ylphenyl)amine (TCTA) and 4,4-Bis(9-carbazolyl)-1,1-biphenyl (CBP) were therefore used as ETL, HTL and host for the emitter, respectively. The incorporated stack is shown in figure 5.1, the most basic jVL results are shown in figure 5.2.

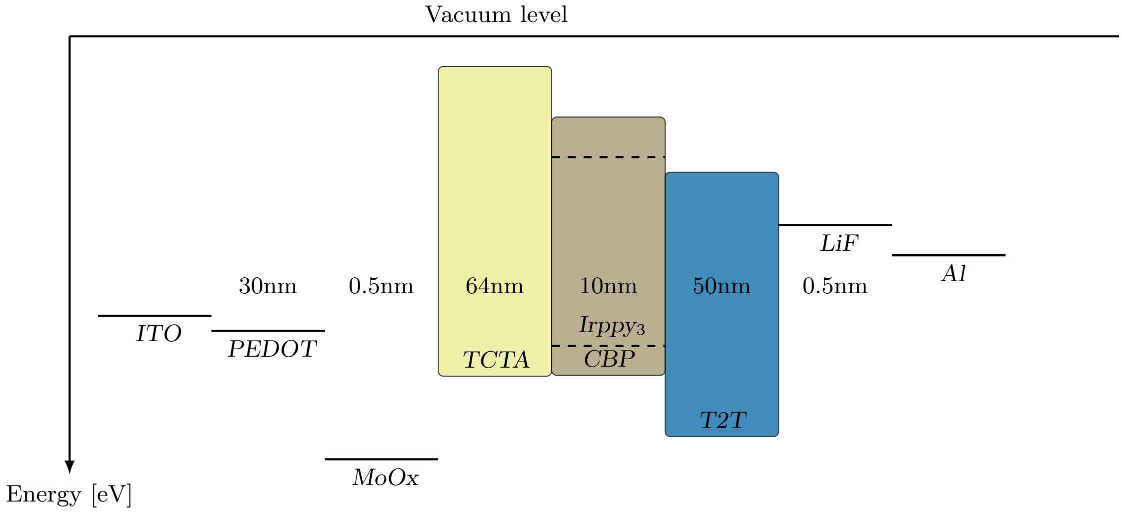

Figure 5.1.: Schematic energy diagram of the used unpolar OLED stack. Energy levels are drawn in scale, exact values can be found in the appendix in table A.1. The dashed lines mark the respective HOMO and LUMO levels of the $Irppy_3$ emitter.

The onset of luminance is detected at 2.3 V while the maximum EQE is not reached before ca. 3.3 V. As was already mentioned in the theoretical part of this thesis, this can happen if the device charge balance factor γ is not ideal in the onset region. This therefore is a hint towards one charge carrier type being injected better than the other. Furthermore, the EQE graph reveals a reproducible kink at a current density of around $4 \times 10^{-3}\,\mathrm{mA\,cm^{-2}}$. This feature can be seen at every individual measurement as well as in the shown average values and is therefore not a measurement or analysis artifact.

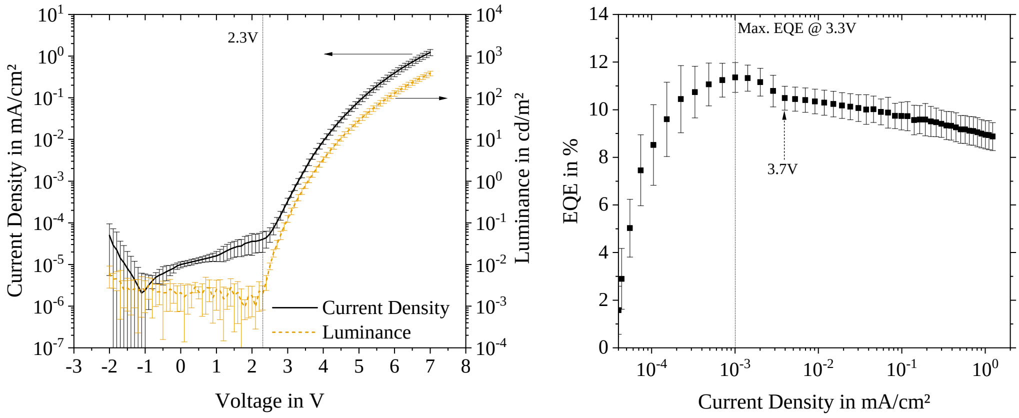

(a) (b)

Figure 5.2.: jVL measurement (5.2a) and calculated EQE (5.2b) of unpolar devices

The luminance graph at the equivalent voltage of 3.7 V however does not show any remarkable features.

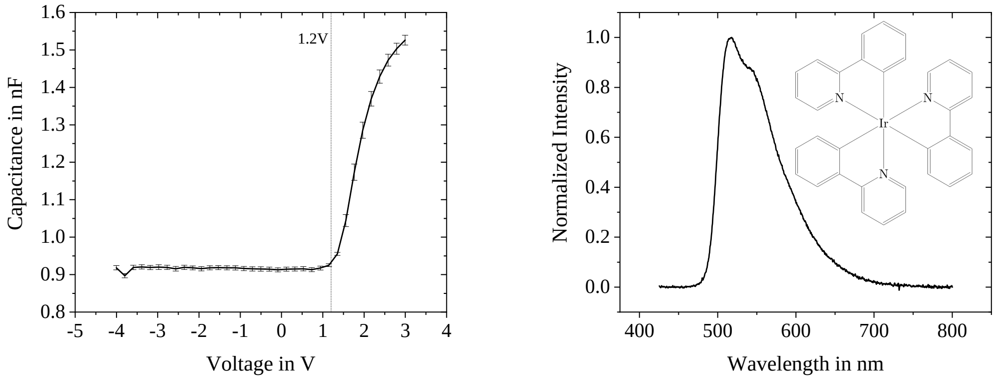

(a) (b)

Figure 5.3.: CV measurement (5.3a) and electroluminescence spectrum recorded at 7V (5.3b) of the unpolar Irppy$_3$ devices. The inset in the spectrum shows the chemical formula of the emitter.

Furthermore, the capacitance-voltage characteristics, recorded at a frequency of 133 Hz, reveals an increase of capacitance at 1.2 V, as can be seen in figure 5.3a. This is a clear indication for a fraction of the multilayered device becoming conductive. As was explained in the theoretical part, a typical OLED can be modelled by a series of parallel resistors and capacitors. Once the layer resistance of one layer drops due to enabled charge carrier injection, also the capacitive properties of this layer vanish. Therefore, the capacitance of the total device typically increases due to the reduced distance of the remaining modelled capacitive plates. Coming back to the measurement in figure 5.3a, we can therefore assume, that although the turn on voltage is at roughly 2.3 V, one type of charge carrier can already enter the device starting from 1.2 V. Considering the energy level alignment in the device stack seen in figure 5.1, it seems likely that the charge carrier injected are actually holes rather than electrons due to the quasi non existent HOMO injection barrier between EML and HTL compared to the larger energy difference in LUMOs of EML and ETL.

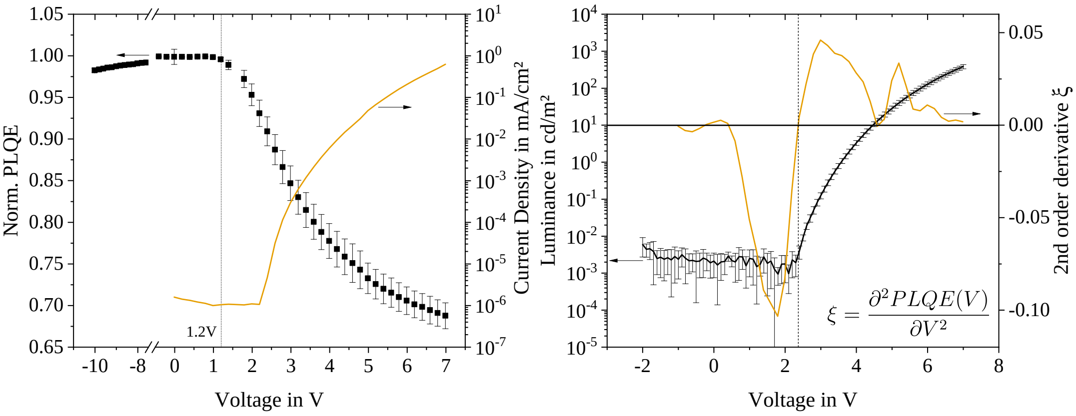

(a)

(b)

Figure 5.4.: Normalized field dependent PLQE (5.4a) and comparison of luminance and second order derivative of the PLQE (5.4b) of the unpolar light emitting diodes. Dashed lines are guides to the eye.

So far, the basic electrical characterization has yielded several hints towards the device physics during operation, which can be used to explain the optical PLQE measurement shown in figure 5.4a. Starting from negative biases, the normalized PLQE is close to unity as expected. Note, that no absolute Photoluminescence Quantum Yield (PLQY) measurement was performed at these samples, so no absolute efficiencies can be given. Only the relative change of efficiency during operation can be illustrated here.

At negative biases, a small amount of PLQE quenching can be seen. The relative PLQE at $-10\,\mathrm{V}$ is roughly 98.3%, so the overall amount of quenching is still lower than 2%. Studies on fluorescent dyes in guest-host systems have attributed this effect to electric field induced exciton dissociation [101, 102]. Assuming a homogeneous electric field distribution under reverse bias conditions and an estimated device thickness of 120 nm, the electric field present at the emissive site at $-10\,\mathrm{V}$ would be expected to be around $1 \times 10^{6}\,\mathrm{V\,cm^{-1}}$, which is a reasonable field strength to slowly overcome the exciton binding energy [18]. Note, that for this quick calculation, a built in potential of $\Phi_{bi} = +2.3\,\mathrm{eV}$

was assumed. The effective internal electric field at a bias of −10 V therefore corresponds to an external voltage of −12.3 V without Φ_{bi}.

Focussing on the forward bias now, expectations from the formerly mentioned internal field considerations would predict a maximum PLQE exactly at the built in voltage V_{bi}, where flat band conditions in the device are present. This is the point where the internal electric field is supposed to be minimal with no injected charge carriers which could act as additional quenching sources and would be expected to be, as mentioned above, at ca. 2.3 V. However, as can be seen, the PLQE already drops at ca. 1.2 V, which fits nicely into the image of injected charges suggested by the CV measurement in figure 5.4a. The strong drop in PLQE at forward biases can therefore be attributed to a process like the described triplet-polaron quenching, as injected charge carriers can dissipate excitonic energies. This process however notably happens before the exponential current and luminance onset at 2.3 V, so the crucial point for exciton quenching is not the device current itself but rather the accumulated charges in this case. This definitively needs to be accounted for when trying to analyze PLQE data with e.g. equations 4.5 or 4.8.
Proceeding further to higher biases in figure 5.4a, one would then however expect a change in trends at the luminance onset of 2.3 V. Here, the device current significantly rises by a few orders of magnitudes in the span of only a few volts, however the corresponding PLQE graph itself does not show any remarkable trend changes.
To continue in the argumentation, the second order derivative of the PLQE was calculated according to:

$$\xi(V) = \frac{\partial^2 PLQE(V)}{\partial V^2} \tag{5.1}$$

This second order derivative of the PLQE with respect to the voltage is plotted in figure 5.4b and shows a coinciding inflection point of ξ and the luminance onset at 2.3 V. An inflection point in the second order derivative of a mathematical function generally describes the position where the said function flips from concave up to concave down shape or vice versa. What this means for the physics of the unpolar OLED is, that the degree of PLQE reduction drops or, in other words, the PLQE decrease decelerates. This therefore means that the present effective charge carrier density at the emissive sites, since the optical measurement is selective to in this case Irppy$_3$ exclusively, is increased by a smaller amount per voltage increment with the luminance onset compared to a voltage increment before the luminance onset. This is not necessarily a straightforward result, as the current density increases exponentially (see figure 5.4a) together with the luminance onset and one would expect an even stronger increase of carrier concentration. Therefore this, in turn, leads to the conclusion that the charge carrier density present at the emissive site below 2.3V is already comparable with the carrier density during operation. Furthermore, since below V_{bi} only the majority carrier is present at the emitter, above this threshold, also the minority carrier type arrives at the site, reducing the majority carrier concentration by luminance generation .

Finally it was already mentioned, that there is a so far not explained kink in the EQE graph in figure 5.2b at 3.7 V. Plotting the optical and electrical efficiency simultaneously as shown in 5.5 now reveals that this mark is an interesting point.

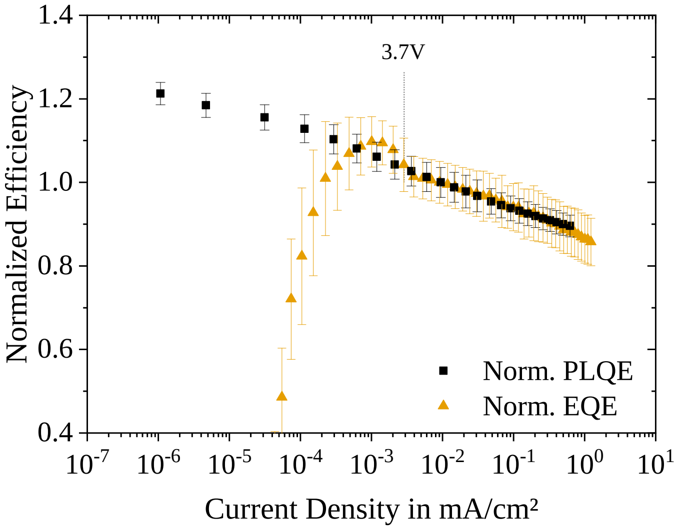

Figure 5.5.: Comparison of optical (PLQE) and electrical (EQE) efficiency of the unpolar OLED devices. Both efficiencies were normalized at their respective 10^{-2} mAcm^{-2} marks.

As can be seen in this figure, both efficiency graphs run in parallel to each other above this threshold voltage of 3.7 V. This means, that according to equation 2.22, the overall device efficiency η_{EQE} is exclusively governed by the effective quantum efficiency q_{eff}. As q_{Exc} and η_{out} are dependent on the device stack and the respective emitter and therefore considered constant during operation, this means that below 3.7 V, the charge balance factor γ has not yet reached its maximum value. This is a clear indication that the device stack needs more refining to achieve optimized efficiencies, which was not the goal of this work however.
Furthermore it can be seen that the optical emitter efficiency already is decreased from its maximum value at the luminance onset. More details on this effect will be presented later in this thesis.

Polar OLEDs

Later in this thesis, studies on third generation TADF OLEDs will be shown. The emitter in this TADF stack will be in a different stack compared to the formerly described rather unpolar stack. To enable a proper comparison between second- and third generation emitters, the same stack was also applied with Irppy3 as guest. The energy level diagram can be found in figure 5.6.

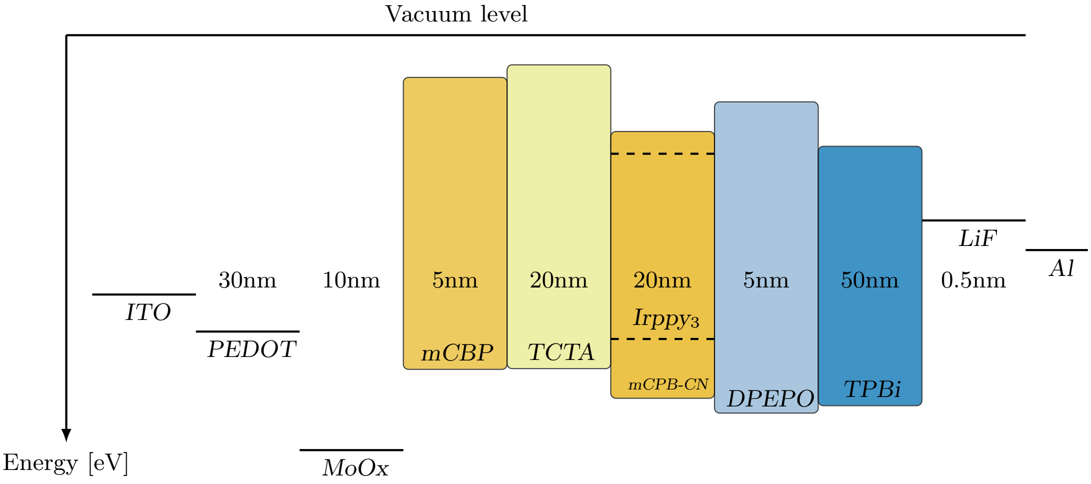

Figure 5.6.: Schematic energy diagram of the used (polar) OLED stack. Energy levels are drawn in scale, exact values can be found in the appendix in table A.1. The dashed lines mark the respective HOMO and LUMO levels of the Irppy3 emitter.

There are a few differences in the stack design, that have to be explained before interpreting the measurement data. Firstly, a thin layer of 3,3-Di(9H-carbazol-9-yl)-1,1-biphenyl (mCBP) was introduced beneath the TCTA to ensure fermi-level-pinning and thereby increase the hole injection into the HTL. Secondly, an interlayer of Bis[2-(diphenylphosphino)phenyl]ether oxide (DPEPO) was introduced on top of the EML to act as a dedicated Hole Blocking Layer (HBL). Most importantly, the host matrix of CBP was changed to 3,5-di(9H-carbazol-9-yl)-(1,1-biphenyl)-3-carbonitrile (mCBP-CN). These materials differ in, amongst others, their permanent dipole moments of 0 D (CBP, [49]) and 3.7 D (mCBP-CN, [43]). The mCBP-CN dipole moment leads to the formation of a GSP and therefore to a negative interfacial charge at the host-TCTA interface. This in turn leads to the possibility of increased hole accumulation far below V_{bi}.

As described in the theoretical part, impedance spectroscopy is a powerful tool to investigate on such effects. And indeed, as can be seen in figure 5.7a, the overall device capacitance starts increasing at roughly −1.8 V. This again is due to the fact, that the hole transporting side of the device becomes conductive and is therefore filled with holes. Note that at this measurement frequency, a slight increase in capacitance is already visible at even lower biases than −1.8 V. More on this small side effect can be found later in this work, it vanishes at higher frequencies.

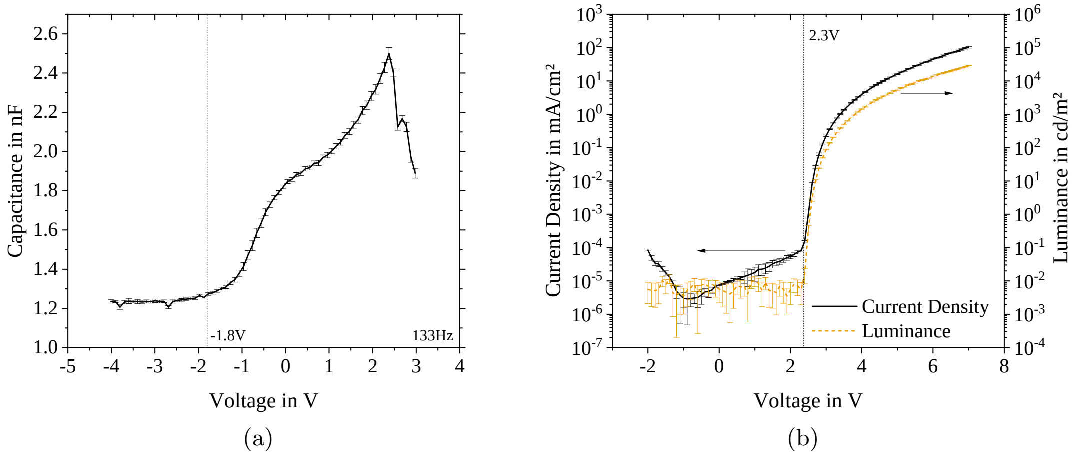

(a) (b)

Figure 5.7.: CV-(5.7a) and jVL- (5.7b) measurement of the polar devices. The capacitance was recorded at a frequency of 133Hz.

Similar to what was seen in the unpolar OLEDs, also their polar counterparts show a luminance onset at 2.3 V. A striking difference between figures 5.7b and 5.2a however is the increased current density due to the optimized stack layout. Also note, that together with the current density, the luminance increased by roughly the same factor as well. The peak EQE of the polar OLED reaches 10.5 % (not shown) and is therefore comparable to its non-polar counterpart. Although not part of the optical investigations that this thesis focusses on, this fact clearly emphasizes the importance of stack optimization. Through some minor modifications in the stack design, a similar efficiency could be reached at strongly increased luminances. It must be noted however, that this stack was taken from Mr. Prakhar Sahay's investigations on TADF OLEDs and not optimized by the author of this thesis himself.

As a next step, the field dependent PLQE of the polar OLED was recorded. The results are shown in figure 5.8a. Analogously to the the unpolar case, a small amount of reverse bias quenching can be observed at the most negative biases. The degree, again, is neglible and can be explained identically to the unpolar case by field induced exciton dissociation.

At increasing biases, the maximum PLQE is reached already at a voltage of roughly -1.8 V. This naturally was to be expected as the CV measurement already predicted charge accumulation in this bias regime. From this point on, charge carriers can enter the device and get to the vicinity of the emissive molecules. The photoexcited emitter can then dissipate the excitation energy via TPQ again and the optical efficiency is reduced. Note that this effect continously decreases the PLQE until V_{bi} is reached at ca. 2.3 V. The corresponding PLQE at this point is already below 0.7, so roughly one third of the excitons is quenched non-radiatively even before the luminance turn on. During the time

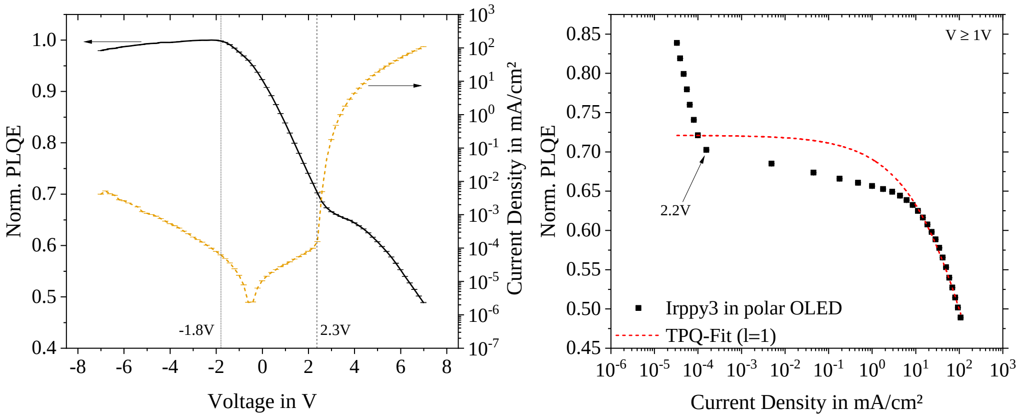

(a)

(b)

Figure 5.8.: PLQE in dependence on the applied bias (5.8a) and respective current density (5.8b) of the polar devices

span of this work, similar results have been published in phosphorescent OLEDs, where the sub-turn on quenching was also attributed to the presence of hole accumulation [50]. Starting from the luminance onset, the PLQE shows a noticable kink in shape corresponding to a significant deceleration of PLQE reduction. Again, this is attributed to the arrival of electrons at the emissive site, which reduces the hole density by recombination.

At even higher biases, the PLQE drop starts to accelerate again. This can be explained by the onset of TPQ according to equation 4.8, as is shown in figure 5.8b. Obviously however, the fit only represents the measurement data nicely in the high current regime above ca. $10\,\mathrm{mA\,cm^{-2}}$. The voltage region inbetween the luminance onset and this current mark is therefore a superposition of the two effects. TPQ happens due to both accumulated charges caused by the interfacial charge and due to the increased polaron density through the actual current flow.

In fact, the comparison of electrical and optical efficiency in figure 5.9 further proves this point. Here, both types of efficiencies were normalized at their respective maximum current value of roughly $10^2\,\mathrm{mA\,cm^{-2}}$. Then both graphs were rescaled with the same constant factor in order to match a maximum EQE of 1.

As can be seen, the normalized optical and electrical efficiencies are in fact identical in the high current regime above ca. $10\,\mathrm{mA\,cm^{-2}}$. Here, the device efficiency loss is therefore dominated by the internal emitter efficiency loss. Also, as can be seen, the TPQ fit already shown in figure 5.8b - also rescaled to match the different normalization but otherwise kept constant - nicely matches the EQE as well as the PLQE in this regime. Here, one can therefore safely assume TPQ due to the applied current density as dominant loss process.

Below that current density range however, the two efficiencies diverge. Reasons for this can be problems with the charge balance factor γ - as in the unpolar device case - and

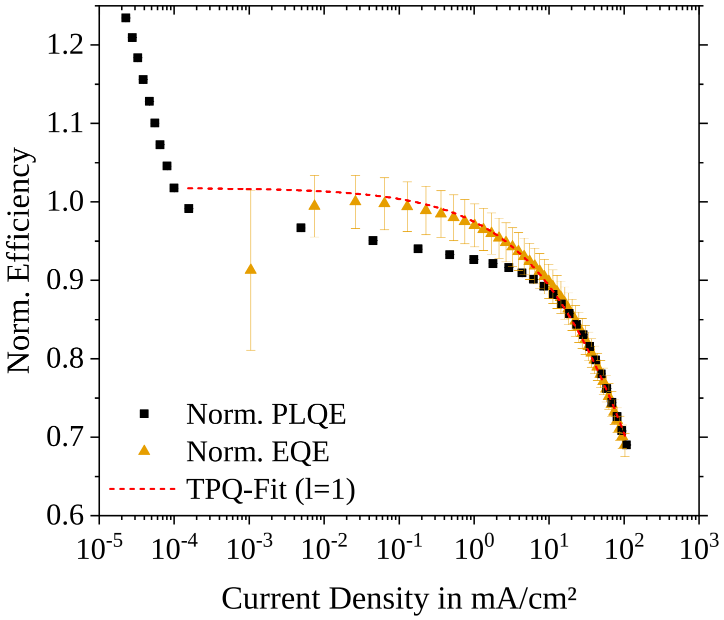

Figure 5.9.: Comparison of optical (PLQE) and electrical (EQE) efficiency of the polar OLED devices. Both efficiencies were first normalized at their respective 10^2 mA cm^{-2} marks and then scaled to a maximum EQE of 1. The TPQ fit was acomplished fitting the PLQE with equation 4.8 and a l-parameter of 1 suggesting trap free organic charge transport.

the still lasting effect of an interfacial charge. In fact, as the relative electrical efficiency appears to be higher at its maximum value compared to the respective optical efficiency, it seems, that the optical efficiency is residually quenched from the accumulated charges, which strongly decrease the optical efficiency at low biases. The interfacial charge therefore still increases the local charge carrier density in the emitter vicinity. Note that for this line of argumentation, the exciton recombination zone was considered to be constant, which not necessarily needs to be the case. Studies with thicker EMLs than in the here presented samples have shown, that a shift in recombination zone can influence the device efficiency as well [103]. However, the mentioned study utilized an EML of 35 nm thickness and the author's simulations showed a high exciton density over almost half of their EML thickness. During operation, the recombination zone then shifted from one end of the EML to the other end, however the overall recombination zone width always was close to the EML thickness presented here in this dissertation. Therefore it is reasonable to assume that this effect of recombination zone shift only plays a minor role in the here presented datasets and the forementioned assumption is justified.

Note furthermore, that the TPQ fit matches the EQE in a much broader range than it fits the PLQE data. An analysis of the electrical efficiency alone and subsequent fitting would therefore hint towards current induced TPQ being the sole efficiency limiting process prevalent until charge balance issues kick in at low luminances. Only with the help of optical analysis of the field dependent PLQE, a deeper understanding of the more complex physical processes could be gained. This clearly shows this measurement setup's importance in comprehensive studies of emitter efficiencies.

To shortly summarize, the data shows that at low operating voltages, the accumulated holes reduce the emitter PLQE. At higher biases, electrons from the ETL side reach the EML in significant quantities, so that these electrons and holes can recombine which reduces the overall charge carrier density. Thereby the PL quenching is slowed. Eventually, all accumulated holes are removed and the electrical and optical efficiencies coincide.

Unipolar hole only devices

As a next step to investigate on the photoluminescence quenching behaviour of phosphorescent OLEDs, unipolar Hole Only Devices (HODs) were manufactured and analysed. The energy level diagram can be found in figure 5.10.

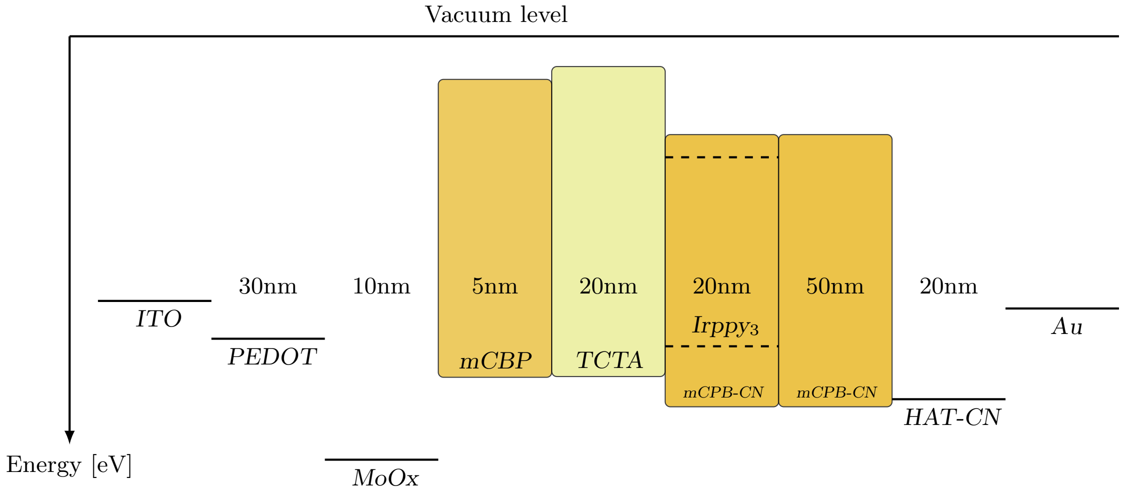

Figure 5.10.: Schematic energy diagram of the used HOD stack. Energy levels are drawn in scale, exact values can be found in the appendix in table A.1. The dashed lines mark the respective HOMO and LUMO levels of the Irppy_3 emitter.

In these types of devices, the injection of electrons was completely blocked by a 20nm thick 1,4,5,8,9,11-Hexaazatriphenylenehexacarbonitrile (HAT-CN) interlayer. As a result, the jVL curve in figure 5.11a did not feature any luminance in the experimental setting and the current can therefore be safely assumed to be of hole only character. Furthermore, without luminance there obviously is no EQE to report.
As can be seen in the same figure, the built-in voltage V_{bi} for this kind of device is lower than in the bipolar cases. Due to the small work function differences of the Gold (Au) and ITO electrodes, V_{bi} is assumed to be smaller than 0.5 V.
As can be seen in figure 5.11b, the charge accumulation visible in polar OLEDs is also present here in this HOD device. This is of course not surprising, as it is attributed to the PDM of the mCBP-CN layer and the resulting GSP. Note that in the graph, the -2.8 V mark is signed as the onset of capacitance rise, although there is some small contribution visible already below that voltage. The reason for this can be seen in the respective capacitance-frequency plot shown in the appendix in figure A.2. Both mCBP-CN containing devices show a multistepped capacitance rise at higher frequencies compared to the single step increase of the unpolar device. This is an indication for subsequent charge injection into different layers. The more complex hole transporting side of the respective polar stacks introduces this artifact, so that not all injected charges immediately accumulate close to the emitter.

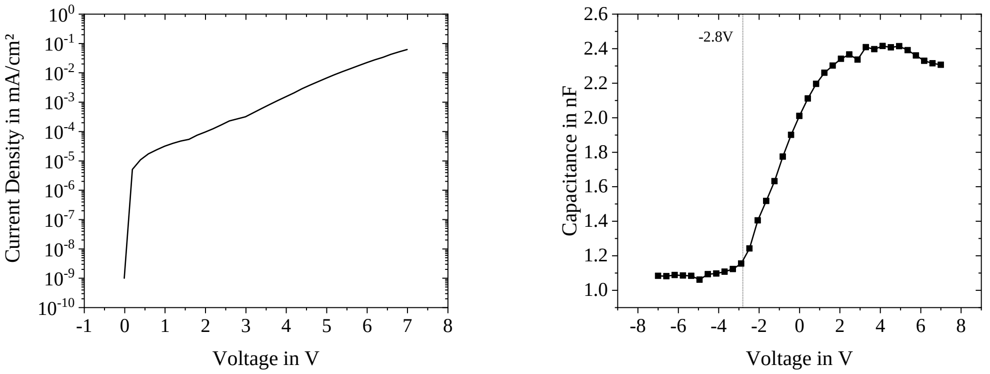

(a)

(b)

Figure 5.11.: jV- (5.11a) and CV- (5.11b) characteristics of the HOD devices. No luminance was detected during any of the measurements.

This claim is backed by the PLQE measurement shown in figure 5.12a, where the maximum PLQE also lies in the mentioned bias regime. Note, that in the HOD case, the PLQE maximum is at even lower voltages than in the bipolar case. The reason for this is however quickly found, as the overall layer thickness of mCBP-CN is a lot thicker in the unipolar case. Here, on top of the EML, an additional layer of 50nm of mCBP-CN was used before the top contacts of HAT-CN and Au were deposited. As the surface potential is proportional to the layer thickness of dipolar layers, also the accumulated charge density of thicker layers is expected to be higher for these devices as well as the onset of charge accumulation is expected to be at lower biases [49].

Qualitative analysis of the mentioned PLQE graph in figure 5.12a furthermore shows a few things. Firstly, the reverse bias quenching is again, analogously to the formerly mentioned device types, explained by electric field induced exciton dissociation. Furthermore, the forward bias quenching behaviour can be separated into three different regimes indicated by the colored dashed lines in the illustration. The respective transition points are to be found at roughly 1.6 V and 3.3 V. In both cases, a deceleration of PLQE decrease can be observed. In formerly described bipolar devices, this could have been due to the arrival of the minority charge carrier type and subsequent recombination, which leads to a charge carrier and therefore polaron density reduction. In this particular case however, the electron current is disabled by the stack design. Therefore, this can not be the explanation.

A doublelogarithmic plot of the current density against the voltage shown in figure 5.12b however quickly explains the PLQE line shape. The very same turning points of the PLQE graph are also turning points in the current density characteristics. According to the idealized theoretical description of current densities in thin film devices in section 2.3 of this work, at different voltages, the maximum current density is limited by different processes. Note that in this particular case, all three regimes follow a power

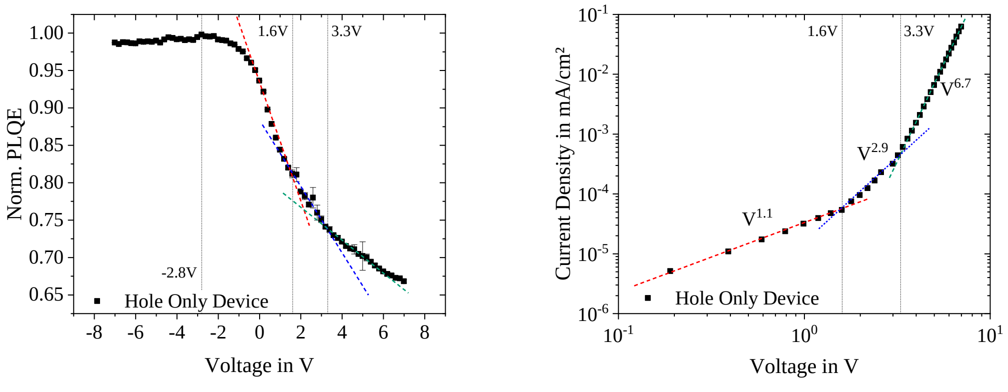

(a)

(b)

Figure 5.12.: Field dependent PLQE measurement (5.12a) and doublelogarithmic plot of the jV characteristics (5.12b). Colored dashed lines are guides to the eye and highlight the different current limited regimes.

law with different coefficients, from which none correspond to e.g. the case of SCLC. This observation can not be explained in satisfying depth at this point and needs further experimental research to comprehensively clarify the underlying charge transport processes. However, the illustration is sufficient to show that the PLQE drop in figure 5.12a follows the current density changes in figure 5.12b. Therefore, the emitter is not influenced by any additional quenching effects during operation in these devices, it's only the amount of current density - and therefore polaron density - that determines the amount of TPQ.

There's two more things to note with the findings of HOD devices with respect to their PLQE: Firstly, the PLQE in dependence of the current density does not follow the model describing TPQ in the theoretical part of this work. The data can therefore not be fitted with equation 4.8. This however is not surprising, as in an unipolar device with disabled electron injection, no electrical excitons can be formed. All excitons are thereby generated by the optical excitation and merely influenced by the polaron density. This is a striking difference to the model mentioned above, where the majority of excitons under electrical OLED operation form by electrical excitation and the optical excitation should be able to be considered negligible. Therefore, a basic requirement leading to the model and equation 4.8 is not fulfilled, so that the fit is not expected to work well in the first place. And secondly, the relation between turning points in the doublelogarithmic current-voltage plot was not mentioned in the case of bipolar light emitting devices in the two formerly described sections. The reason for that is simply, that for these bipolar cases, there is no concordance of PLQE and the jV plot. The respective turning points do explicitely not coincide, which leads to the conclusions drawn above.

5.1.2. TADF OLEDs

After the investigations on phosphorescent OLEDs with $Irppy_3$ as an emitter, similar experiments were conducted with identical stacks but a different emitter. Specifically, DMAC-TRZ was used as a representative for TADF based emitters and incorporated into the polar OLED and HOD stacks shown in the appendix in figure A.1.

DMAC-TRZ in polar OLEDs

Analogously to the investigations with phosphorescent emitters, DMAC-TRZ was used in the identical polar OLED stack shown in figure 5.13.

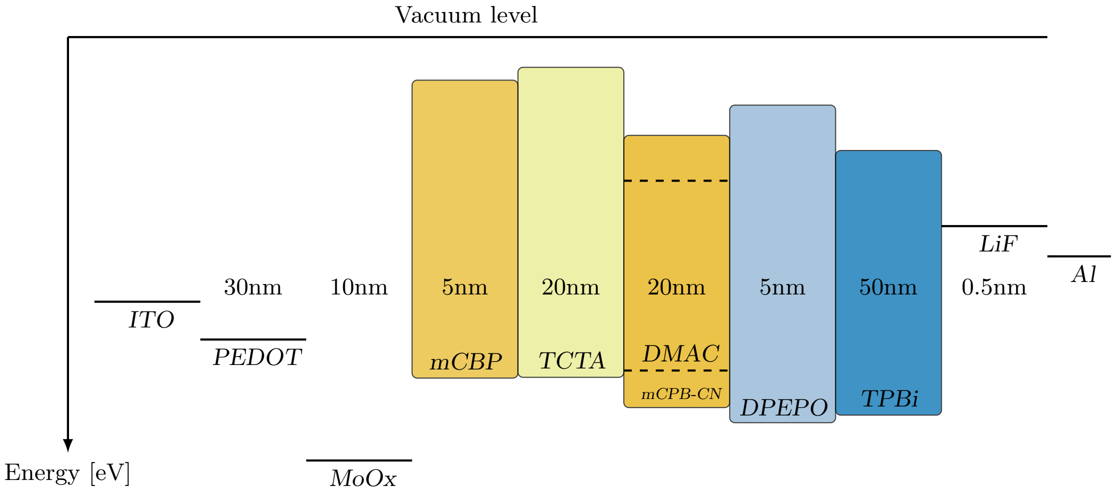

Figure 5.13.: Schematic energy diagram of the used (polar) OLED stack. Energy levels are drawn in scale, exact values can be found in the appendix in table A.1. The dashed lines mark the respective HOMO and LUMO levels of the DMAC-TRZ emitter.

The jVL characteristics as well as the calculated EQE of these devices can be seen in figure 5.14. The first thing to note is, that the device stability in this particular batch of samples was not as good as in the $Irppy_3$ case, so that the error bars in the low current regime are quite large. This is due to the fact, that the jVL measurements were not the chronologically first measurements and the samples potentially were damaged by other methods of investigation. Statements about the exact current density at low biases therefore are potentially unreliable. The high current and luminance regime however still show reproducible behaviour over several devices and can be considered reliable.
As can be seen, the luminance onset voltage is at 3.4 V, the EQE again indicates charge balance problems until the maximum EQE at around 10^{-2} mA cm^{-2} is reached. In figure 5.15, furthermore the CV measurement together with the electroluminescent spectrum can be seen. As is shown, the formerly used $Irppy_3$- and the DMAC-TRZ spectra are quite similar to each other, so that these two materials can be compared very well as

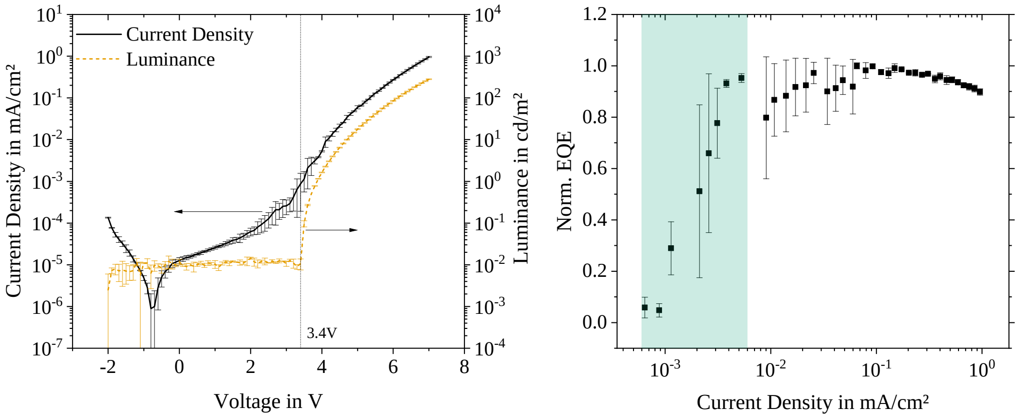

(a)

(b)

Figure 5.14.: jVL characteristics (5.14a) and calculated normalized EQE (5.14b) of the polar TADF OLEDs. Problems in the sample processing lead to less device stability and big differences especially in the low voltage region of the different pixels. Therefore the error bars in this regions are rather big. The highlighted area in figure 5.14b marks the luminance onset region before charge balance is reached.

emitters with the same function of emitting green light in e.g. industrial applications in displays. The CV measurement furthermore shows a step in capacitance at $-2.2\,\mathrm{V}$, which is similar to the polar Irppy$_3$-OLED case, as this step's position is more determined by the stack design and the surrounding layers than just by the choice of emitter itself. Again, it is caused by the non isotropic distribution of PDMs of the mCBP-CN molecules, which accounts for a GSP. This GSP leads to hole injection and accumulation below V_{bi}. Therefore the capacitance of the respective layers vanishes and the overall measured device capacitance increases due to a nominally thinner residual capacitive structure. Note, that the CV measurements of this particular set of OLED samples initially failed. Therefore, the here shown results are taken from a study of Mr. Prakhar Sahay, where a bilayer device structure of NPB and the same emitter-host combination was deposited between two electrodes. Statements about the GSP in the mCBP-CN layer can be made with this data, anything regarding additional processes like charge injection into other layers or the onset of light emission can obviosuly however not be made from this data set, as these layers were not present in this particular sample.

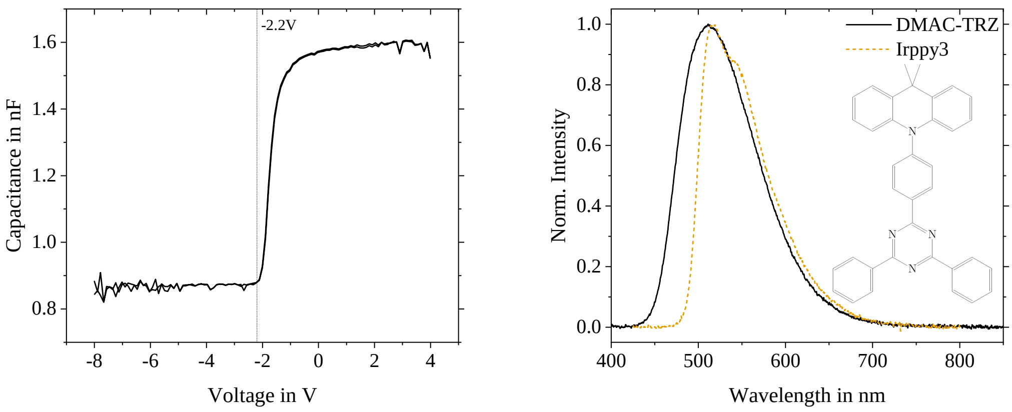

(a) (b)

Figure 5.15.: CV measurement of a doped mCBP-CN layer (5.15a) and electroluminescent spectrum (5.15b) of the polar TADF OLEDs. For reference, also the $Irppy_3$ spectrum is plotted here. Furthermore, the inset shows the chemical structure of emitter molecule DMAC-TRZ. The sample structure in figure 5.15a was different to all other devices, more details can be found in the text.

Now having a look at the optical efficiency to determine the internal device physics, there are a few things to note in the respective graph in figure 5.16a. The reverse bias behaviour again will not be covered in detail here, a small amount of quenching can be seen. Also, the CV onset and optical efficiency maximum do not perfectly coincide, however as mentioned earlier, the capacitance is sensitive to any layer in the stack becoming conductive while the optical experiment exclusively is sensitive to polarons in the emitter vicinity, assuming only TPQ once more. Small deviations are therefore possible. All in all, the quenching in reverse bias is negligible compared to the efficiency loss above the accumulation onset.

Above the charge accumulation onset, again a significant PLQE loss is observed prior to the electroluminescent device turn on at 3.4 V. A total of almost 10 % can be regarded as lost here already. This can again be attributed, analogously to the $Irppy_3$ case, to charge accumulation induced by the GSP and therefore by the molecular orientation of mCBP-CN. This regime is highlighted by a green dashed line in figure 5.16a.

From this low bias regime, we shall now focus on the higher bias part of the experiment shown in figure 5.16b. The optical efficiency here can be perfectly fitted by equation 4.8 again, which validates the formerly taken assumption of pure TPQ as dominant loss mechanism. This in itself is an interesting piece of information, as the equation was initially developed to explain the Roll-off of phosphorescent emitters. However, the quenching behaviour of this particular TADF emitter can also be nicely modelled by this formula. More details on this comparability can be found in section 5.1.3 of this thesis. Note, that the fitted part of figure 5.16b is also marked with a red dashed line in

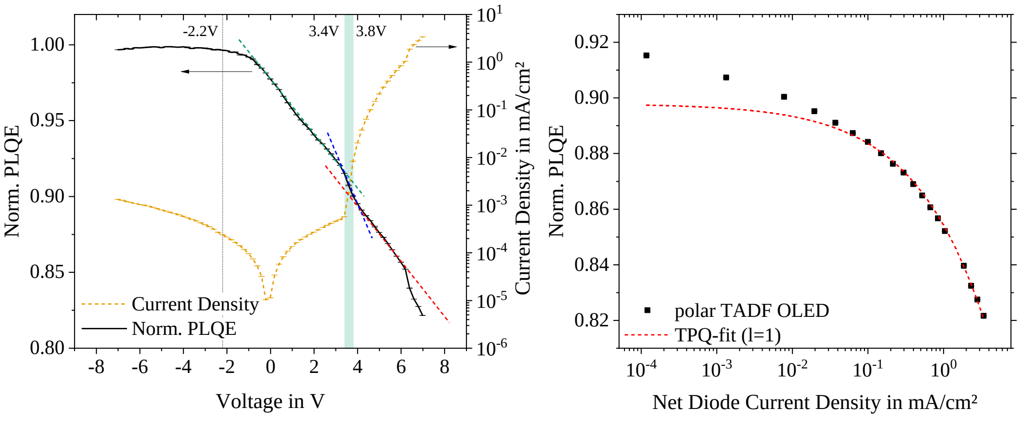

(a) (b)

Figure 5.16.: (Field -5.16a) and current density (5.16b) dependent illustration of the relative PLQE data of polar TADF OLEDs. These measurements were conducted before the jVL characteristics shown in figure 5.14a. The net diode current density was calculated according to the analysis shown in figure 3.3a.

figure 5.16a. Therefore, in this operating regime, the device efficiency is limited by the internal emitter efficiency.
Now, as can be seen in figure 5.16b as well, the TPQ fit does not at all match the experimental data in the low current regime below ca. $3 \times 10^{-2}\,\mathrm{mA\,cm^{-2}}$. This marks exactly the transition region between the two formerly mentioned regimes where either the flowing charges or the accumulated charges are responsible for the dominant quenching process. This region is marked by a blue dashed line and a green background color in figure 5.16a in order to better illustrate the following argumentation. As can be seen, exactly at the onset of exponential current increase, the slope of the PLQE also starts to decrease. This also marks the onset of luminance. Now, with the onset of luminance, also the first electrons can reach the emitter, which then recombine and create photons. This recombination then reduces the polaron density in the emitter vicinity, so that the expectation would actually be an increase in PLQE slope, while a decrease is observed. This means, that even though charge carrier recombination is enabled at this voltage, the polaron density still increases, which in turn means, that the arriving electron current is overcompensated by an even higher hole current. This is yet another clear indication for a non ideal charge balance in the device. Moreover, this explanation also fits perfectly to the EQE data shown in figure 5.14b, where charge balance issues are also apparent. Note, that the two regions highlighted by the green background color correspond to each other. As soon as charge balance is reached, the data can be explained by the TPQ model described in the theoretical part of this work. Device improvements could therefore be achieved by increasing the electron- or reducing the hole current densities during operation.

Unipolar hole only devices

Similar to the proceeding for phosphorescent OLEDs, also with the third generation TADF emitters, hole only devices have been manufactured and investigated. The energy level diagram can be seen in figure 5.17.

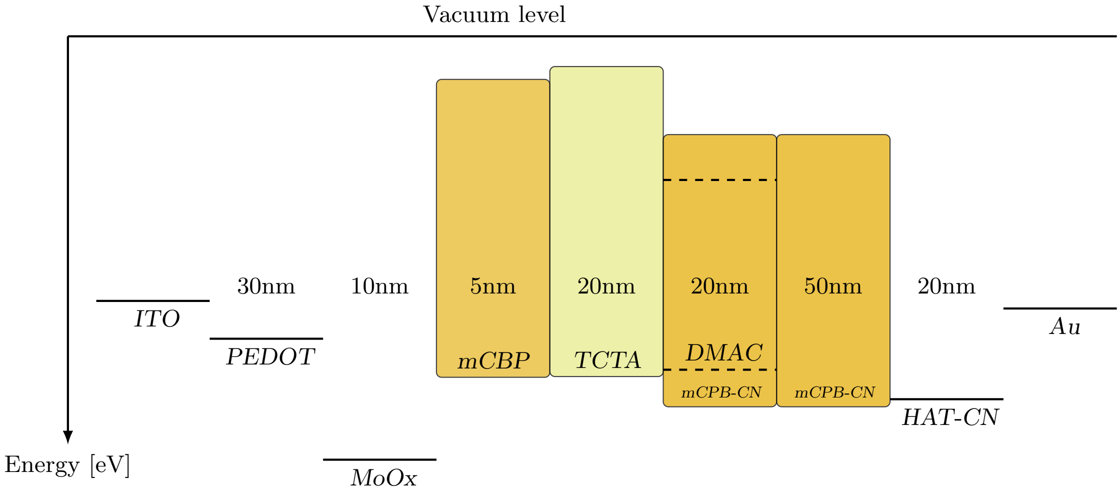

Figure 5.17.: Schematic energy diagram of the used HOD stack. Energy levels are drawn in scale, exact values can be found in the appendix in table A.1. The dashed lines mark the respective HOMO and LUMO levels of the DMAC-TRZ emitter.

Again, no luminance whatsoever was detected under electrical excitation, so electron injection can safely be excluded through the use of the HAT-CN interlayer. The corresponding jV- and CV-characteristics can be found in figure 5.18.

The double logarithmic jV plot reveals a striking change in current behavior at 0.7 V, which corresponds to V_{bi} and the onset of exponential current. The second trend change however can not be determined exactly with this method. An exemplary mark at 1.7 V is given in figure 5.18a, however this value is to be taken with caution. Good fits to the dataset can be found with various intersectioning points and therefore with different transition voltages. Figure 5.18b on the other hand again reveals a transition voltage of roughly -2.8 V and is thereby perfectly congruent with its respective phosphorescent counterpart. Note, that also here the transition voltage is marked not at the onset of the capacitance increase due to the multilayered stack design as was explained in the previous section.

The field dependent PLQE analysis is also very similar to the phosphorescent case. The reverse bias quenching is negligible, the maximum PLQE can be found at a plateau around -2.8 V, whereafter the PLQE starts to decrease. This, once more, is attributed to the build-up of accumulated charges in the emitter vicinity, which dissipate excitation energy via TPQ. With the onset of the exponential current, a slight kink is to be seen in the PLQE graph. The origin of this kink can be explained rather quickly, as it coincides

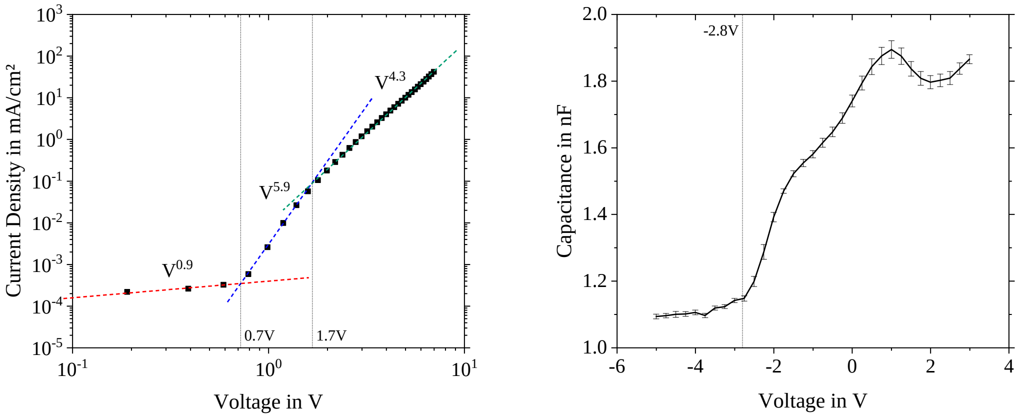

(a) (b)

Figure 5.18.: Double logarithmic jV- (5.18a) and CV- (5.18b) measurements of the 10% DMAC Hole dominated sample with a HAT-CN-Au top contact.

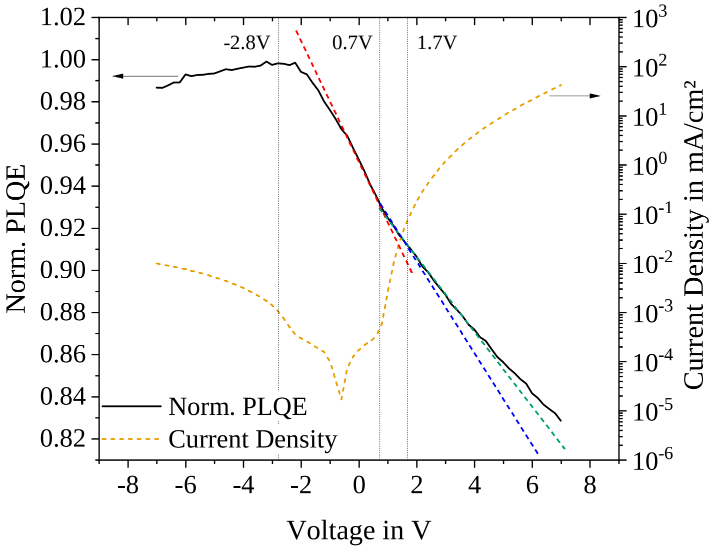

Figure 5.19.: Field dependent PLQE of the HOD incorporating DMAC-TRZ.

with the respective mark in figure 5.18a. The change in current limitation therefore leads to a change in PLQE trend.

Interestingly however, the PLQE drop again decelerates although the current density starts increasing over several orders of magnitude at this point. This must mean, that the respective polaron density based on charge accumulation below V_{bi} is at least similar to the polaron density caused by the electric current. Enabling the current flow above V_{bi} therefore allows the reduction of accumulated charge carrier density, which partially compensates for the additionally injected charges.

The second turning point labelled in figure 5.18a at 1.7 V is, analogous to the uncertainty of the exact value in this jV curve, not determinable exactly. This simple and purely empirical fitting with straight lines allows a multitude of exact turning points. What however can be stated is, that the PLQE quenching slope decreases. One potential reason for this could be, that with an increased current and thereby polaron flow, the interaction time of exciton and polaron is subsequently decreased. In other words, at elevated biases, a fraction of charge carriers potentially dwells in the emitter vicinity for too short times to actually interact with an optically generated exciton. This fraction of *passive* polarons should increase with increasing current, so that the relative quenching slope starts to flatten.

5.1.3. Discussion

In the previous sections, a number of different stack designs were investigated with respect to the relative optical emitter efficiency in comparison with other measurement techniques. Ultimately, the internal physical processes leading to efficiency losses under operation ought to be clarified. Both Irppy$_3$ and DMAC-TRZ were used as emissive molecules as representatives of second generation phosphorescent and third generation TADF emitters, respectively.
The investigations on non-polar Irppy$_3$ OLEDs have shown, how a combination of impedance spectroscopy, electrical efficiency analysis and field dependent optical efficiency measurements can shed light upon the charge carrier transport and recombination dynamics under operation. The dominant loss process at high luminances could be found to be TPQ, with coinciding optical and electrical efficiencies according to the theoretical models proposed in the respective literature [74, 78–80, 92]. At lower operating biases, the electrical efficiency reveals an imperfect charge carrier balance, while the internal emitter effiency is already reduced by injected charge carriers. Since the the PLQE in this model is dependent on the nearby polaron and thereby charge carrier density, the voltage value of achieved charge balance could be extracted from the optical measurement by analyzing the slope of the voltage dependent PLQE drop, which is congruent with the EQE data. One important result of the analysis of these non-polar OLEDs is again the importance of including optical measurement techniques into the measurement routine to gain comprehensive understanding of the device physics. The electrical EQE data alone shows great agreement with a theoretical fit of TPQ until issues with the charge balance become dominant. Only through optical measurements the sub-turn-on quenching could be resolved which still influences the device performance during electroluminescent operation.

With this non-polar OLED as a starting point for the further investigations on the influence of polar molecules on the performance of modern thin film LEDs, now the second batch of OLEDs was processed and investigated. Here, a non-isotropic distribution of molecular PDMs leads to a macroscopic surface potential, which in turn causes hole accumulation far below the turn-on voltage. These charge carriers accumulate in the vicinity of the respective emissive molecules, which can then lose their excitation energy by interacting with the so-created polarons. The optical PLQE measurement and the electrical capacitance measurement slightly disagree on the onset of this quenching process, as the onset signalled by the CV measurement is typically located at a few hundred mV lower operating biases than the onset signalled by the the maximum PLQE. This can be explained by two effects:
Firstly, the maximum PLQE is reached at the specific bias point, where the least amount of total efficiency quenching is present. Assuming exclusively TPQ as quenching process, this would mean that the maximum PLQE is reached at the minimum polaron density. Therefore the expectation would be to find the PLQE maximum in the reverse bias regime before charges are accumulated. At even lower biases, the PLQE would be constant. Including other types of quenching processes however, this does no longer hold

true. As can be seen in all voltage dependent PLQE plots so far, there is a secondary effect of field induced exciton dissociation present in these materials [101, 102, 104]. Pretending to exclusively focus on this field induced exciton dissociation as dominant quenching process would therefore lead to a maximum PLQE exactly at the built-in voltage V_{bi}, where flatband conditions are met and the effective electric field is zero.

In reality now, this secondary effect of exciton dissociation is rather small at the present biases of approximately $0\,\mathrm{V}$ to $-3\,\mathrm{V}$. Therefore, the PLQE maximum position will be dominated by the presence or absence of charge carriers with only a small disturbance caused by exciton dissociation.

And secondly, the discrepancy of optical and capacitive onset points can be explained by the nature of the respective measurement type. The optical measurement is exclusive to the respective emitter, as all other potential emission is disabled by the choice of excitation wavelength and optical filter. Therefore, the optical measurement exclusively probes the emitter efficiency - and thereby the polaron density - in the vicinity of the emitter. Charge accumulation far from the EML can not be detected in this measurement at all. The capacitive measurement however is sensitive to all layers in the device. Slight injection barriers between adjacent layers on the hole transporting side might as well lead to the mentioned capacitive effects. Therefore the discrepancy can also be explained by additional charge accumulation in the device, to which end the optical measurement is not sensitive. In fact, this is the most likely explanation of the observed shift, as the capacitive measurement shown in figure 5.15a coming from a non light emitting bilayer device has a way steeper onset compared to a multilayered OLED, where these additional charge accumulation sites are present.

Now comparing the two optical emitter efficiencies, a few things need to be noted. First of all, the measurements were run in the voltage range from $-7\,\mathrm{V}$ to $7\,\mathrm{V}$ in order to not damage the samples for both materials. Nevertheless, the maximum current densities differ drastically, where the $\mathrm{Irppy_3}$ current density is larger than the DMAC-TRZ value by a factor of approximately 30, as can be seen in figure 5.20a.

This however is not causing problems with respect to the overall achievable EQEs, since the differences here are rather small, as was mentioned in the previous sections. However, the higher current density should affect the internal PLQE due to the higher number of quenching sites. Therefore, it is not surprising to see a larger quenching with the $\mathrm{Irppy_3}$ samples compared to the DMAC-TRZ emitter. What however is in fact suprising is the amount of quenching, $\mathrm{Irppy_3}$ feels through the accumulated charges even below V_{bi}. The respective efficiency drops from its peak value down to approximately 66%, so that effectively one in three exciton is lost even prior to the luminance onset. This effect is also visible for DMAC-TRZ, however its PLQE at the luminance onset is roughly 92%, so that only one in ca. twelve excitons is lost. The difference between these emitters therefore comes down to a factor of 4 affecting the sub-turn on quenching.

The reason for this effect could be, that although the EL spectra and therefore the energy gaps of the two materials are similar to each other, the exact HOMO and LUMO levels differ from each other. This is schematically illustrated in figure 5.21.

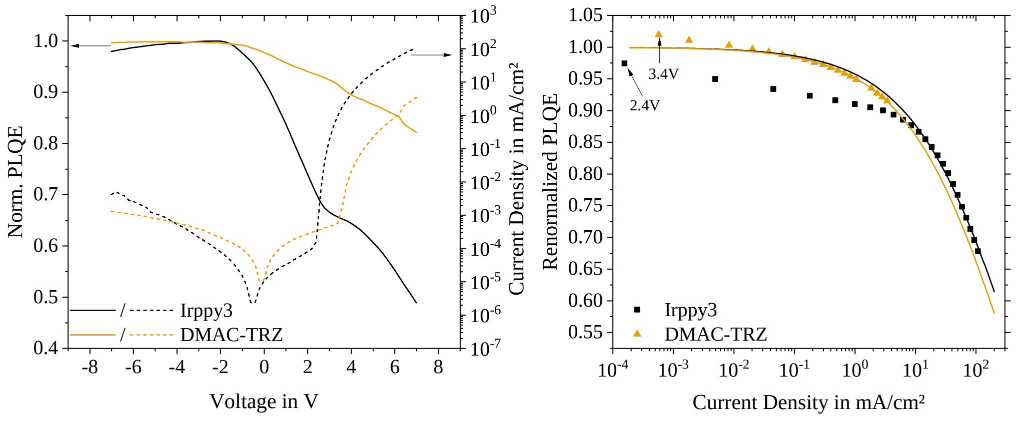

(a)

(b)

Figure 5.20.: Field dependent PLQE measurement results plotted against the applied voltage (5.20a) and the respective current density (5.20b) of both second and third generation OLEDs. Solid lines in figure 5.20b represent the formerly introduced TPQ fits. For clarity's sake, the datapoints as well as the fits were renormalized to match the normalization constants. The absolute PLQE shown in this subfigure therefore is without physical meaning.

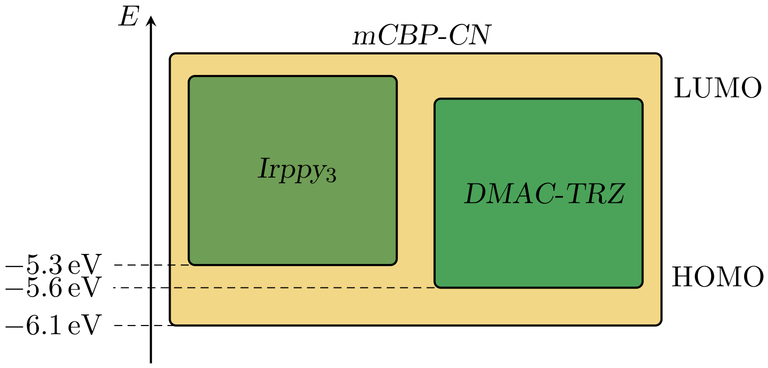

Figure 5.21.: Schematic energy diagram of the used emitter layers. HOMO/LUMO energy levels are drawn in scale with respect to each other, exact values for HOMO/LUMO levels can be found in the appendix in table A.1. The outer box represents the mCBP-CN host with the two inner green boxes representing Irppy3 and DMAC-TRZ, respectively.

It can be seen, that the HOMO energy level of Irppy3 lies energetically higher than the DMAC-TRZ HOMO. As was explained, the GSP of the mCBP-CN layer leads to charge accumulation in the vicinity of the emitter. To be precise, the majority charge carriers in this bias regime are holes. Therefore, the holes in vicinity to the emitter can be at least partially on the emitter molecules themselves. The difference in HOMOs now leads to the circumstance, that Irppy3 acts as a deeper hole trap. While holes in DMAC-TRZ can more easily leave the emitter molecule again and be transferred to an adjacent mCBP-CN molecule, this process is significantly hindered by the greater trap depth in the phosphorescent case. Therefore the amount of charged Irppy$_3$ molecules per volume at comparable biases is higher than the respective number of charged DMAC-TRZ sites in the TADF counterpart. These ionic species can then act as quenching centers for adjacent molecules and thereby reduce the overall efficiency, which can serve as an explanation for the increased quenching in the Irppy$_3$ devices.

Now focussing on the quenching behaviour above the turn on voltage, one has to keep in mind, that the data points shown in figure 5.20b have been renormalized and the absolute PLQEs shown in this graph therefore have no direct physical meaning. It is shown, that both emitters deviate from the TPQ fits made in previous sections of this work due to the sub turn on quenching. Fits with equation 4.8 do work in the high current operating regime. For clarity's sake, the equation is repeated here once more:

$$q_{TPQ}(j) = \frac{\eta_{ext,0}}{1 + \tau C k_{TPQ} j^{\frac{1}{1+l}}} \qquad \text{(4.8 revisited)}$$

Again, τ is the excitonic lifetime, C is a material constant dependent on, amongst others, the trap concentration, transport level density of states and charge carrier mobilities in the organic semiconductor, k_{TPQ} is the TPQ rate, while l is a parameter involved with the energetic depth of trap states by $l = E_t/k_BT$. More details on these parameters can again be found in the respective literature [80]. Experimentally, l was kept constant at 1 for these fits. Measurements of the phosphorescent excitonic lifetimes revealed a value for $\tau_{phos.}$ of approximately 0.7 µs. For the case of TADF emitters, the delayed fluorescence of DMAC-TRZ has a lifetime of ca. 1.9 µs while the prompt fluorescence is faster at ca. 20 ns [105]. The material constants C are not accessible and will therefore be set to 1 for the fits. The full parameter sets for the fits in figure 5.20b can therefore be found in table 5.1.

	Irppy$_3$	DMAC-TRZ
η_0 in arbitr. units	1	1
τ in µs	0.7	1.9
C in arbitr. units	1	1
k_{TPQ} in arbitr. units	36.47 ± 1.1	13.68 ± 1.7

Table 5.1.: Results for both Irppy$_3$ and DMAC-TRZ TPQ fits.

This result is an indication, that the third generation TADF molecule is the superior emitter in this respective stack with regards to TPQ. The respective quenching rates differ by a factor of ca. 2.7. This apparent result however has to be taken cautiously, as there are several factors to consider.

Firstly, the stack design was optimized for DMAC-TRZ. Therefore it is downright expected to be better suitable for this material. A more comprehensive study on the comparability would need to optimize the respective stack designs for both materials in order to quantitatively compare the two emitters. Secondly, it was assumed, that C is equal to 1 for both cases. This does not necessarily have to be the case. While no huge discrepancies are expected to occur between $C_{phos.}$ and C_{TADF}, a factor of roughly three seems at least possible, which would then invalidate the statement. Furthermore, the assumed excited state lifetimes also differ by a factor of roughly 2.7. The proper value to use for τ is rather straightforward in the phosphorescent case, since all excitons are transferred to triplet states via intersystem crossing and decay via phosphorescence. This resulted in the measurement value of 0.7 µs. For the more complex case of TADF emitters, however, the electrically generated triplets are converted back to singlets, where they then can decay radiatively. Even though the delayed fluorescence - and therefore the triplet state - in this material has a similar lifetime compared to the phosphorescent case, this interplay of ISC, rISC and thereby prompt and delayed lifetimes introduces potential error sources into the quantitative comparison shown in table 5.1. In fact, the influence of the prompt fluorescent lifetime has been completely neglected in this analysis, which raises the need for further theoretical modelling, simulations and more comprehensive experimental studies in the future. Lastly, the experimental data of the TADF samples unfortunately only shows the onset of TPQ quenching in figure 5.20b. Measurements to higher current densities could resolve this issue and further validate the theoretical fit, but then an increased device degradation comes into play, which needs to be accounted for again. Datasets which are not included in this thesis showed a more pronounced PLQE drop when measuring until 10 V instead of only 7 V, however the resulting device degradation was significant, which again invalidates the model of TPQ as single dominant efficiency loss mechanism.

As a next step, unipolar HODs were processed to investigate on the optical emitter efficiencies under exclusion of one charge carrier type. Through the application of a 20 nm thick HAT-CN layer, pure hole dominated current was ensured. As can be seen in figure 5.22a the device currents again do not match with the DMAC-TRZ sample supplying an increased current density. This can be attributed to the difference in energy levels again, as was already shown in figure 5.21.
While so far unpublished work at the group shows that doping of DMAC-TRZ into mCBP-CN in fact increases the conductivity of the total EML, Irppy$_3$ acts as a deep hole trap, which drastically decreases the charge carrier mobility and thereby conductivity. This effect has been known in blends of organic semiconductors for a long time and usually is strongly dependent on the dopant concentration [106]. If the concentration of dopant is too low to enable guest-to-guest hopping transport, the trapped charge carriers can not contribute to the overall conductivity. Furthermore in the here proposed stack design, the adjacent layer where the holes would be drawn into by the electric field consists of an undoped layer of mCBP-CN again. Therefore the trapping energy needs to be overcome without the help of potential beneficial energy level alignment which could increase the transport by an energetically more suitable subsequent transport layer.
Aside from the differences in current densities, the respective capacitive measurements

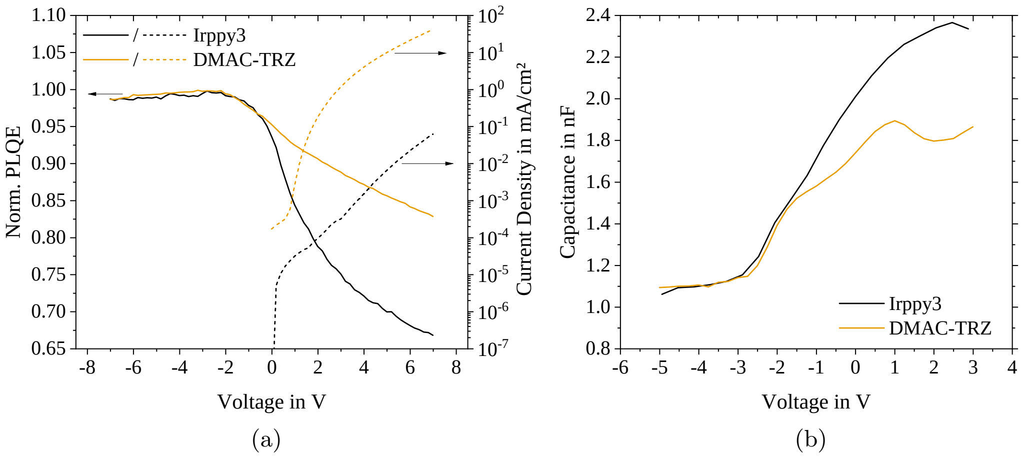

(a) (b)

Figure 5.22.: Field dependent PLQE measurement results plotted against the applied voltage (5.22a) and the respective CV data (5.22b) of both second and third generation unipolar HODs.

show good agreement of the onset of charge accumulation. The GSP of the 20 nm mCBP-CN host layer and additionally 50 nm thick transporting layer adjacent layer leads to a lower transition voltage compared to the bipolar case of LEDs. As was already explained in detail earlier, the CV onsets and PLQE maxima do not match perfectly due to the additional charge accumulation potential in additionally incorporated layers towards which the optical measurement is insensitive. Anyhow the major capacitance increase starts at a bias of approximately -3 V where also the PLQE maximum is located for both emitters. The quenching behaviour beyond that point is governed by the current densities as was shown in detail earlier in this section, so that the difference in PLQEs again can be attributed to the increased hole trap depth of Irppy3 over DMAC-TRZ.
Note that Irppy3 appears to be the by far inferior material in this particular sample setup. DMAC-TRZ samples can support a higher current density and still show significantly less quenching. This however does not automatically mean that Irppy3 is the inferior material in light emitting applications. As was mentioned earlier, the EQEs of both polar device types were comparable and well above 10%. This is due to the fact, that the apparently detrimental larger hole trapping capability of Irppy3 does not correspond to a worse device performance. In fact, the reduction of hole mobilities in Irppy3 containing devices seems to be more than compensated for in the polar OLED stacks, as the phosphorescent OLEDs reach higher luminances at lower operating voltages compared to their TADF counterparts, which would in fact mark Irppy3 as the superior material. This obvious ambiguity once more clearly emphasizes the need of matching the material properties and stack design to the respective application and therefore shows the importance of comprehensive electrical as well as optical analysis.

5.2. Investigations on polar electron transporting material OLEDs

The final part of this chapter will cover the experiments performed on samples received from TU Dresden. The stack design of these samples is shown in figure 5.23.

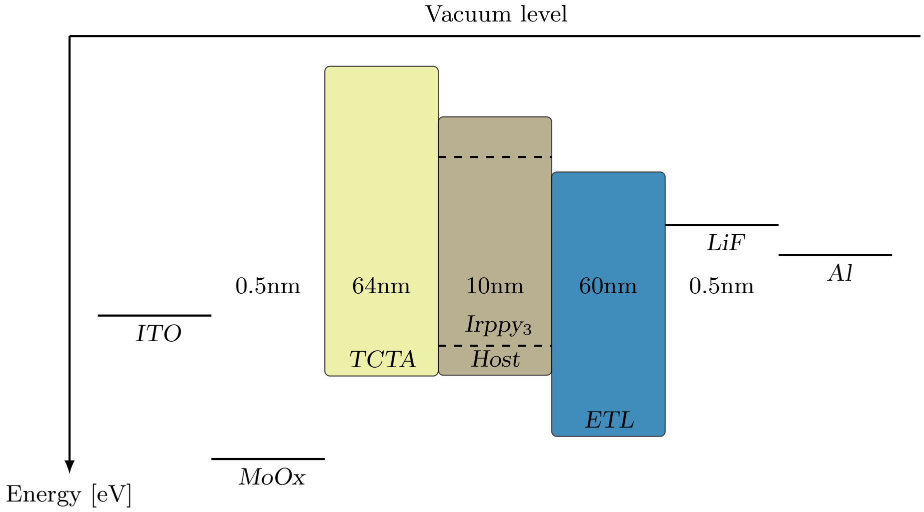

Figure 5.23.: Schematic energy diagram of the used TUD OLED stack. Energy levels are drawn in scale, exact values can be found in the appendix in table A.1. The dashed lines mark the respective HOMO and LUMO levels of the Irppy$_3$ emitter. CBP and 2,2',2"-(1,3,5-Benzinetriyl)-tris(1-phenyl-1-H-benzimidazole) (TPBi) were used as host materials, TPBi and 1,3,5-tri(m-pyridin-3-ylphenyl)benzene (TmPyPB) were used as ETL materials in different devices. Irppy$_3$ was doped into the host with a doping concentration of 8%.

The stack itself is rather similar to what has been used in the previous section. However, while so far the GSP was introduced into the device by means of the polar host of mCBP-CN, now the focus is set on the dipolar effect of an electron transporting material. To that end, the interplay of polar and unpolar layers was investigated in a systematic study. Both polar and unpolar host- and ETL layers were incorporated into samples, TPBi was used as a polar host and ETL, while CBP and TmPyPB were used as its unpolar counterparts. The applied emitter was again Irppy$_3$ for all samples shown in this section. Note, that the jVL- and CV-data was recorded in Dresden while the optical measurements were conducted in Augsburg. Therefore, slight differences can occur in e.g. the current density plots from optical and electrical measurements.

5.2.1. Unpolar host OLEDs

Starting point for the investigations are samples comprising the emitter Irppy$_3$ in the unpolar host material CBP similar to what was shown in section 5.1.1 of this work. With the EML consisting of Irppy$_3$ doped in CBP and an adjacent TmPyPB ETL, the least amount of polarity is introduced into the system. These samples will therefore serve as unpolar reference. Furthermore, in the first variation step, the ETL was changed to TPBi while keeping the EML unpolar. The jVL- and CV characteristics of these samples are shown in figure 5.24. In this sample set, the host material is identical with a variation in the ETL polarity. The positive effect of an incorporated GSP can be seen as the charge injection in the TPBi devices is improved with respect to their unpolar counterparts in figure 5.24a. This is reflected by the earlier onset voltage and overall higher current densities and luminances at given voltages. This difference in improved charge carrier injection can be attributed to the surface dipoles resulting in a net positive sheet charge at the interface between cathode side and ETL, which allows for enhanced electron injection. Furthermore, the respective counter charge is located towards the EML side, which also increases the hole accumulation potential. This phenomenon is known in the literature and has largely been expected [69, 107].

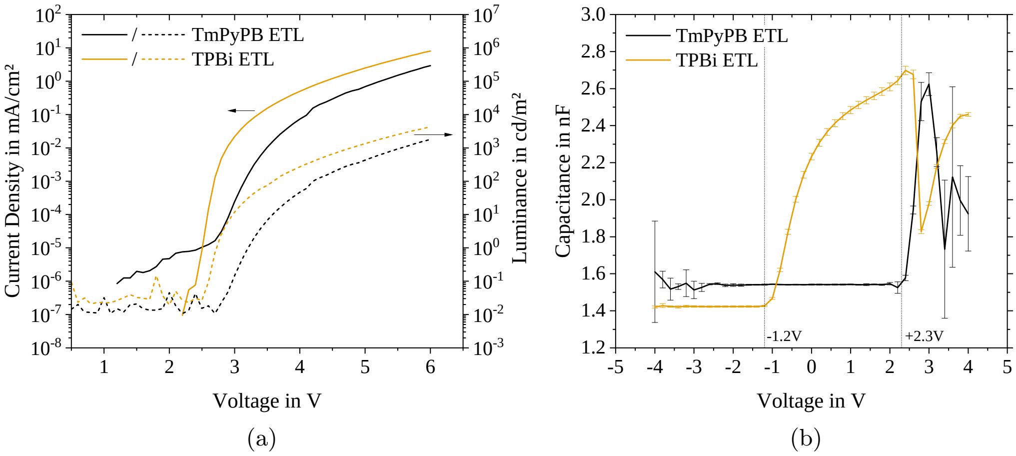

Figure 5.24.: jVL– (5.24a) and CV– (5.24b) characteristics of TUD OLEDs with CBP as host material

In fact, the TPBi samples show a reduced transition voltage in the CV data that clearly marks the onset of hole accumulation, as was just mentioned. While the TmPyPB devices show capacitive behaviour until ca. 2.3 V, hole accumulation in the TPBi stack already starts well below 0 V. These voltage marks also fit perfectly to the optical PLQE data shown in figure 5.25a.

The PLQE maxima for the two device types lie at -1.2 V and 2.3 V for the polar and unpolar sample, respectively. This backs up the claim of induced hole accumulation by the polar ETL layer similar to what was observed with polar hosts in previous sections

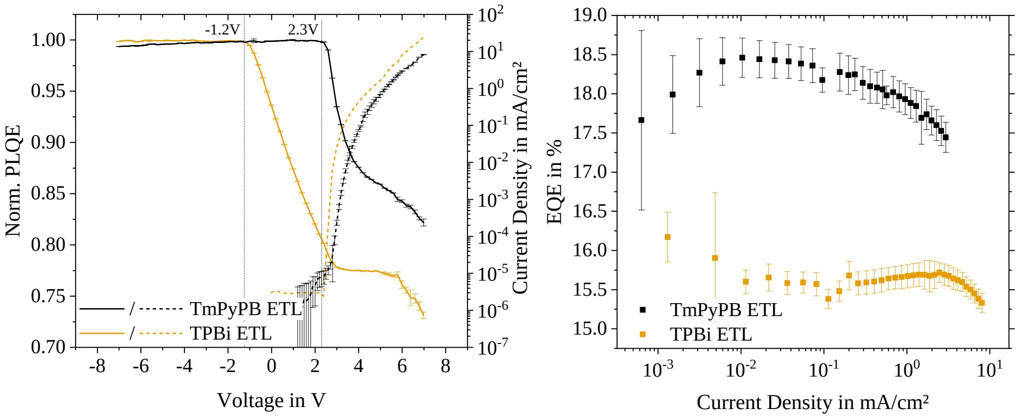

(a) (b)

Figure 5.25.: PLQE– (5.25a) and EQE– (5.25b) plots of TUD OLEDs with CBP as host material

of this work. Taking a look at the unpolar TmPyPB device data first, the PLQE shows a rather flat behaviour from negative biases to the aforementioned threshold voltage of 2.3 V. The small amount of efficiency loss can again be attributed to the onset of electric field induced exciton dissociation as in the previous sections. The PLQE starts to drop at 2.3 V which, as mentioned, fits to the respective CV data. Interestingly however, the device current density does not start to increase and transition into the exponential regime quite yet, as also is illustrated in figure 5.25a. This can now have several causes. Firstly, the emitter $Irppy_3$ itself has a considerable PDM of 6.4 D [108]. If these dipoles were anisotropically oriented, a small GSP could form even in the case of the so called unpolar OLED. This however is usually not the case, as $Irppy_3$ tends to show an isotropic distribution of molecular orientation [108]. Therefore, a GSP is not expected and the discrepancy between PLQE maximum and exponential current onset should not be attributed to it. In fact, the issue is much more likely due to imbalanced charge injection through non ideal energy level alignment in the stack. A schematical depiction of the quenching process responsible for this discrepancy of PLQE drop– and exponential current increase onsets can be found in figure 5.26. If one charge carrier type is already able to enter the device while the other can not, the charges in emitter vicinity reduce the optical efficiency. This is also backed up by the EQE data shown in figure 5.25b, which marks the maximum EQE at a current density of approximately $1 \times 10^{-2}\,\mathrm{mA\,cm^{-2}}$. This maximum EQE position is a compromise between efficiency loss through a decreasing PLQE and an improving charge balance factor γ.

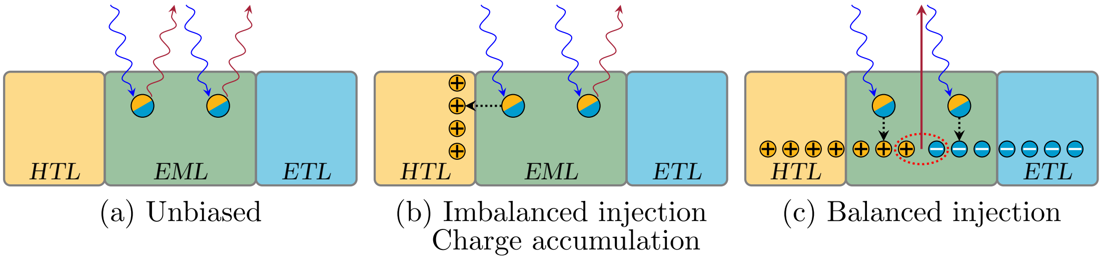

(a) Unbiased (b) Imbalanced injection Charge accumulation (c) Balanced injection

Figure 5.26.: Schematical depiction of quenching processes at different biases. Solid blue curved arrows represent the modulated optical excitation, red solid arrows represent the device emission from either photoexcitation (curved) or electrical excitation (straight). Dashed arrows represent non-radiative efficiency loss processes. Blue, orange and two-colored circles are electrons, holes and excitons, respectively.
(a) In the unbiased case, the intrinsic emitter efficiency determines the detected signal.
(b) In the presence of charge carriers, supplied by, for instance, imbalanced injection or accumulation caused by a GSP, the optically generated excitons can dissipate the excitation energy by TPQ. A significant PLQE reduction can be observed even without large amounts of current.
(c) At higher biases, efficient injection of electrons as well as holes leads to high currents. The excitons can still lose their energy via TPQ, the amount of quenching however is strongly dependent on the charge carrier density in emitter vicinity. Depending on the sample under investigation, the enabled electron injection in fact can reduce the hole density significantly, so that the PLQE decrease per voltage increment decreases. Simultaneously, electrical exciton generation is enabled as well, so that EL can be observed. This emission, however, does not falsify the recorded data, as the experimental setup is locked to the optical modulation frequency.

Now taking a look at the polar TPBi device results, there are a few apparent observations to make. Most notably, the PLQE maximum is located at the transition voltage deduced from the CV measurement due to the hole injection onset as was explained earlier. The magnitude of accumulated charges and therefore polaron density in emitter vicinity increases with the applied bias up until roughly 3 V. Notably, this mark is located at 3 V while the exponential current density onset is already at around 2.4 V. This means, that the majority charge carrier current (holes) is enabled sooner than the electron current. Only at biases above 2.6 V, electrons start being injected in significant numbers which corresponds to the luminance onset in figure 5.24a. Eventually at the PLQE threshold bias of just below 3 V, the electron current is large enough to compensate the hole current from the anode. Starting from this mark and increasing the voltage even further leads to a plateaulike feature in the PLQE plot up until ca. 6 V. At first, this seems to be rather counterintuitive, as the overall device current density increases over several orders of magnitude in this bias regime. However, the recorded PLQE signal is sensitive to the charge and therefore polaron density in the vicinity of the emissive molecules only. This includes both the EML as well as closeby interfaces. Therefore the plateau shows, that the net electron and hole currents above approximately 3 V are equal, as they compensate each other so that these charges do not sufficienctly alter the polaron density and hence the PLQE. At even higher biases, the elevated overall current then leads to an increased polaron density and therefore to further PLQE quenching. Due to this, the data in the high current regime of the graph can be fitted with the TPQ model described in equation 4.8. The respective graph can be found in the appendix in figure A.3a.

Similar results have been published recently in the literature, where the PLQE in fact even showed a second local maximum during operation, as the charge density caused by hole accumulation was overcompensated by the electron current and the net polaron density therefore decreased with increasing bias [50]. The difference between this secondary maximum from the literature and the plateau as observed in the data presented in this work can be explained by differences in the sample processing. The two sets of samples were built in different groups, with not identical machines under not identical conditions. Therefore slight differences are expected. Furthermore, similar results with an increasing PLQE at increasing bias have been reproduced also at the Augsburg group with purposely altered injection properties. Although this data is not shown in this thesis as it was not part of a systematic study, it helps to understand that even minor differences in the energetic landscape of the device stack can lead to a significantly changed device behaviour. In particular, for the case of accumulated holes, an improved electron injection would reduce the hole density at the emitter sooner and therefore lead to a reduced polaron density. Therefore the height of the second and relative PLQE maximum might serve as a figure of merit for the electron injection. The presence of a plateau in the here presented samples would then just be a sign for a not yet fully optimized device structure.

Even though further device optimizations might still increase the performance of the polar OLED stack incorporating TPBi as an ETL, both the absolute EQE and the relative PLQE show that the GSP induced by the polar ETL decreases the device efficiency. The only advantage of the polar ETL stack is the slightly reduced luminance turn on voltage due to the improved electron injection.

5.2.2. Polar host OLEDs

The second batch of samples received from TUD changed the host material with respect to the formerly described CBP devices. The host in all now described samples was kept constant to be the polar molecule TPBi, while the ETL layer was either a standard TPBi layer as well, a TPBi layer where the substrate was heated up to approximately 70 °C during film deposition or a TmPyPB layer. In the following part of this work, these three device types will therefore be labelled *Unheated TPBi ETL*, *Heated TPBi ETL* and *TmPyPB ETL*. Note that the TmPyPB ETL also was not heated during deposition.

The idea behind these three archetypes is to gradually alter the layer GSP. The unpolar

TmPyPB does not form a GSP, the unheated TPBi layer by contrast does show a strong influence of the molecular alignment. The heated TPBi layer system has been used to show efficiency improvements of phosphorescent OLEDs in the literature, however the exact reason for this efficiency improvement was not stated by the authors [109]. A range of effects were stated to potentially be responsible for the improvement, all attributed to the fact that heated TPBi forms an ultrastable glass layer with thereby increased the layer density. Specifically a reduction of excitonic trap states and a reduction of nonradiative exciton-phonon coupling were mentioned [109]. Empirically, both an improved device efficiency as well as lifetime was observed with the heated TPBi layer devices. The data presented here in this work now aims to elucidate the influence of the molecular orientation and the accompanied formation of a GSP on the device performance.

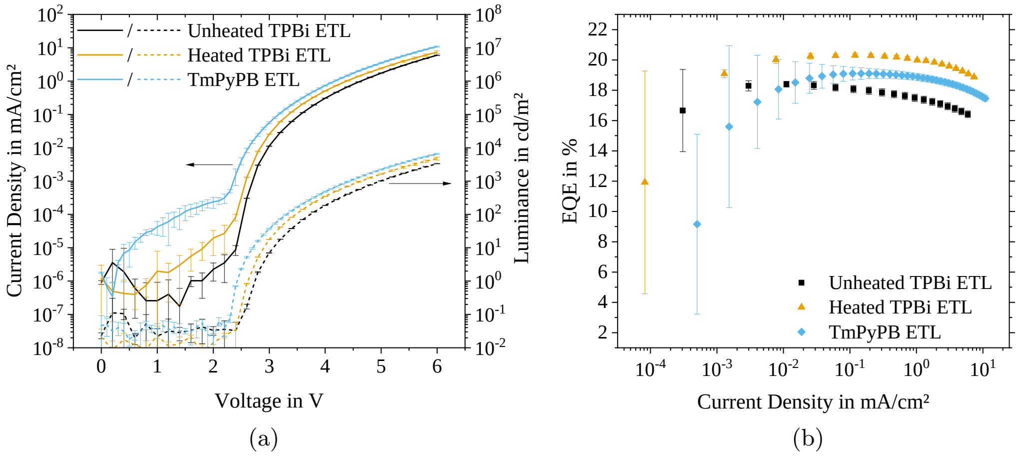

Figure 5.27.: Measured jVL– (5.27a) and calculated EQE– (5.27b) characteristics of TUD OLEDs with TPBi as host material

For these samples, the jVL curves look quite similar to each other although both the current densities as well as the luminances of the unpolar TmPyPB sample are highest at any given applied bias, as can be seen in figure 5.27a. Similarly, the luminance onset values are close to each other but slightly reduced for the unpolar OLED between 2.3 V and 2.5 V. The polar ETL therefore seems to introduce additional energy barriers for the charge carriers, which decrease the total current density at any given voltage and increase the turn on voltage. Notably, this is a contrary observation to what was shown for the unpolar host OLEDs in the previous section, where an unpolar ETL lead to lower currents and higher turn on voltages. Efficiency-wise, figure 5.27b shows, that the unpolar TmPyPB OLEDs performs better than the unheated TPBi batch. The best efficiency was achieved with the heated TPBi sample, which reproduces the efficiency improvement by ultrastable glass formation from the literature [109].

The optical PLQE measurement in figure 5.28a now shows three clearly distinct plots for

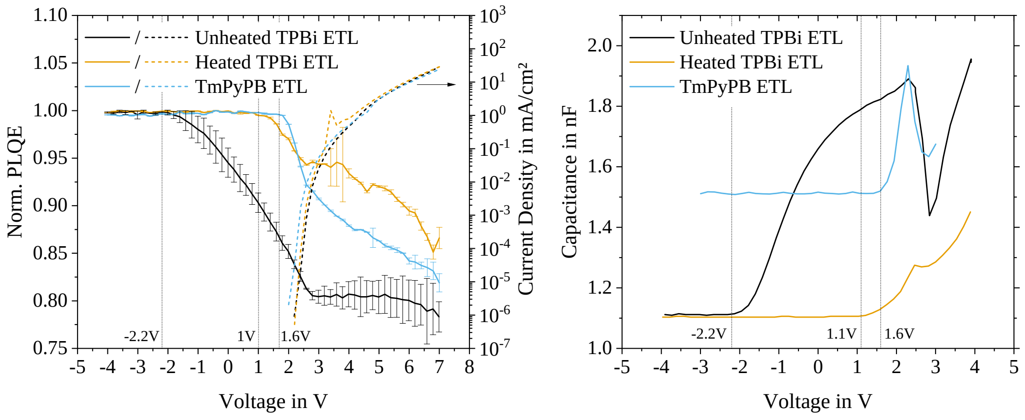

(a) (b)

Figure 5.28.: PLQE– (5.28a) and CV– (5.28b) plots of TUD OLEDs with TPBi as host material

the three device types. The unheated TPBi sample maintains its maximum value only until an applied voltage of -2.2 V, whereafter the PLQE starts to drop. This is expected and has been described in this thesis several times. The GSP enables hole accumulation at the interface between HTL and EML. These holes can act as quenching centers for excitons and thereby reduce the overall efficiency. A similar effect was observed for the unpolar host OLED counterpart in the previous section, however the threshold voltage decreased even lower to more negative values due to the accumulated effect of TPBi as both host and ETL. In general, these two samples are very much alike, as also their behaviour above this transition voltage of -2.2 V is quite similar to each other. The PLQE slope decreases as soon as the exponential current sets in. Unfortunately, the noisy leakage current measurement in figure 5.27a does not allow for a net current density determination as shown in figure 3.3a, however this current onset can be approximated to be at around 2.2 V. This fits nicely to the second order derivative analysis analogous to figure 5.4b, which shows that a PLQE deceleration starts at this threshold. The respective graph for the polar TUD sample can be found in the appendix in figure A.4. This again means, that starting at the exponential current onset, not every charge carrier that gets into the emitter vicinity increases the polaron density, as it is the case in the sub-turn on quenching regime. A fraction of carriers recombines with their countercharges and reduces the slope of the PLQE decrease. This eventually leads to a PLQE plateau at the threshold bias of 3 V, which is exactly the same value for the CBP host counterpart. Here, all arriving charge carriers recombine with each other so that the net polaron density and therefore also the emitter efficiency is constant. At higher currents, the onset of a further increase is observed due to the increased current density. The PLQE data of the TmPyPB samples also fit into the so far described findings. The maximum PLQE is maintained up until a voltage of 1.6 V, which is a lower value than observed in the CBP host case. This again is attributed to the TPBi host material, which builds up a GSP and in turn enables sub turn-on hole accumulation. As the magnitude of a GSP increases with the film thickness according to equation 2.20, the 10 nm thick host layer is expected to build up a significantly lower GSP than the 60 nm TPBi ETL or the 70 nm of combined TPBi layer thickness of EML and ETL. Taking the maximum PLQE position of the most unpolar, CBP host- and TmPyPB ETL device of 2.3 V as a reference point, the change of host material to polar TPBi leads to a shift of -0.7 V to the new PLQE maximum position of 1.6 V shown in figure 5.28a. The change of 10 nm of host material therefore leads to a shift of -0.7 V.

By contrast, exchanging the 60 nm of ETL from TmPyPB to TPBi leads to an additional shift from 1.6 V to -2.2 V, netting a shift of -3.8 V. This kind of analysis can be applied to all TUD samples measured so far, the results are summarized in table 5.2. Note, that here the unpolar sample type was used as a reference and the $\Delta\text{PLQE}_{\text{max}}$ values were calculated by subtraction of the reference position and the respective sample value. $\Delta\Phi$ was then calculated by dividing this difference in maximum PLQE positions by the total thickness of deposited TPBi d_{polar}.

Host (10 nm)	ETL (60 nm)	d_{polar} [nm]	PLQE_{max} [V]	$\Delta\text{PLQE}_{\text{max}}$ [V]	$\Delta\Phi$ [mV nm^{-1}]
CBP	TmPyPB	0	2.3	0	0
CBP	Unheated TPBi	60	-1.2	3.5	58
TPBi	TmPyPB	10	1.6	0.7	70
TPBi	Unheated TPBi	70	-2.2	4.5	64
TPBi	Heated TPBi	70	1.0	1.3	19

Table 5.2.: Correlation of PLQE maximum positions and polar materials used in the different device stacks processed by TUD. The PLQE_{max} positions extracted from the optical measurements nicely align with the threshold voltages from the CV measurements shown in figure 5.28b.

In this table, the last column shows the parameter of $\Delta\Phi$ which corresponds to the induced shift in PLQE maximum per nm of incorporated polar material. The dimension of this parameter mV nm^{-1} is identical to the dimension typically used to describe the size of a GSP. Note, that this parameter however is not necessarily related to the GSP and should therefore not be confused with it. Although the purely optical measurement traces the emitter efficiency locally in the device, it is also dependent on the rest of the stack. Attention has to be paid in cases where for instance a GSP close to the emitter is present, but charge carrier injection towards the EML is disabled. In this case, the optical measurement would not detect any shift, while the GSP obviously would still be present. Furthermore, samples where the emitter is far from the polar layers can not be investigated with this method.

Despite these apparent differences in measurement methods, the values of ca. 60 to 70 mV nm^{-1} match a literature reference value of 43 mV nm^{-1}, determined by Kelvin-probe measurements, reasonably well [49].

In this table, also the values for the last so far not described sample with a heated TPBi layer as both host and ETL are already given. As is shown in figure 5.28a, the maximum PLQE is between the values for the completely polar and unpolar stack at approximately 1 V. The plot shows a rather short decrease from 1 V to ca. 2.6 V, where the PLQE once again shows a plateau. Notably, this plateau is only stable until an applied bias of roundabout 3.8 V, whereafter the PLQE drops further. Still, the relative PLQE losses are smallest compared to the two other plots in the same graph. This could very well explain the improved EQE of these heated TPBi samples as is shown in figure 5.27b and was reported previously [109]. The overall device efficiency improvement could then be deduced to a higher emitter efficiency instead of, for example, improved charge carrier transport.

The reason for the comparably small shift in PLQE maximum, which is also represented by the low $\Delta\Phi$ of only $19\,\mathrm{mV\,nm^{-1}}$ in table 5.2, lies in the different arrangement of TPBi molecules in heated and unheated films. Starting from the unheated case, during film deposition, the first polar TPBi molecules deposited will lie flat on the substrate and thereby build up an electric field. Further molecules will then ideally align themselves in a way to minimize the dipole potential energy U, which scales with $p \cdot E$, where p and E are the magnitudes of molecular dipole moment and electric field, respectively. This leads to parallel alignment during the whole deposition, which then eventually results in the formation of the macroscopic GSP. At elevated temperatures however, the additional thermal energy leads to more molecular motion and the minimization of dipole energy effect is less dominant. Therefore, the overall built up electric field and GSP is reduced, which leads to the forementioned effects of less hole accumulation and PLQE maximum shift.

This can also be seen in Kelvin-Probe measurements shown in the appendix in figure A.5 [110]. These measurements were conducted and the data was graciously provided by Mr. Albin Cakaj, to whom the author is grateful. The GSP of a heated TPBi layer is significantly reduced in comparison to an unheated room temperature case. Note, that the glass transition temperature of TPBi is 122 °C, so that room temperature (unheated) conditions correspond to roughly 0.74 T_g [109]. Note furthermore, that the size of the GSP of the unheated TPBi layer shown in figure A.5a is $74\,\mathrm{mV\,nm^{-1}}$, which in fact fits rather well to the values determined by the optical measurement shown before. Since the maximum PLQE positions fit very well to the threshold voltages extracted from the CV data shown in figure 5.28b, the comparison of $\Delta\Phi$ and the electrical GSP seems reasonable for this particular set of samples. Again, this does not automatically mean, that the optical PLQE measurement is always a fitting tool for quantitative investigations on the GSP in dipole OLEDs due to the requirements mentioned above.

The overall message to be taken from the investigations on polar host OLEDs presented in this section is, that the layers containing polar molecules are not beneficial for the efficiency of electrical OLED performance on the first glance. The potentially induced GSP and correlated sub turn-on PLQE quenching caused by charge carrier accumulation at an interfacial charge reduces the emitter performance. This is reflected in the EQEs of the respective devices as well, according to equation 2.22. This however does not mean that devices containing layers of polar molecules are always inferior to unpolar OLEDs. As was shown in the CBP host devices, the GSP can still help inject charge carriers into the device and therefore lead to lower operating voltages. Furthermore, although the introduction of polar molecules leads to an earlier drop in PLQE, the plateau-like constant behaviour over a wide range of current densities can also be advantageous, for instance in applications where the operational bias stability is not necessarily given. Finally, the GSP can be manipulated by e.g. heating during deposition, so that even a better electrical performance of heated TPBi OLEDs – compared to its unheated counterpart or even an all-unpolar OLEDs – can be observed. Polar materials should therefore not in any case be disregarded for the development of high efficiency OLEDs, as they offer unique design possibilities which can be exploited. A future way to drive the research in this field even further is to combine polar and unpolar materials – or unheated and heated versions of a single matterial, for that matter – in device stacks to make use of the advantages of both material classes. This particular work is currently under investigation at the group in Augsburg, where the improved device stability of heated TPBi layers is combined with the supression of sub turn-on quenching by unpolar molecules.

As was shown during both the investigations on both samples made in Augsburg, containing polar hole transporting materials, as well as the polar electron transporting samples from TUD, the sub turn-on quenching is introduced into OLEDs through the introduction of a GSP and the consequential charge accumulation in the emitter vicinity. The model to explain TPQ, as is described in the theoretical part of this thesis, does not include the additional quenching due to polarons originating from other sources than the diode current density. Therefore, further theoretical and experimental work is necessary to adapt the mentioned model also to the regime of TPQ well below the turn on voltage. These studies should include a quantitative correlation between bias dependent charge accumulation and respective effective polaron density close to the emitter. Therefore, experiments and simulations with non conductive device types like for instance MIS diodes could help to elucidate the physical processes involved. Displacement current measurements could then determine the bias dependent amount of charge on the respective interface in the device, which can then be correlated to the optical efficiency. From this point on, the theoretical modelling explaining efficiency losses via TPQ could be extended to include several bias regimes with specifically dominant polaron sources. The quantitative information extracted from the MIS diode work would then describe the sub-turn on behaviour, while the high current density behaviour already can be well explained by the established model, as can be seen in the appendix in figure A.3.

Part III.

Quantum dot light-emitting diodes

CHAPTER 6

Basics of QD light-emitting diodes

6.1. Theoretical backgrounds of colloidal quantum dots

In chapter 2 of this thesis, the theoretical backgrounds of thin film LEDs were described. While so far, the case of organic LEDs was treated, the following part will cover the results from investigations on QDLEDs. In this kind of device type, colloidal Quantum Dots (QD) are sandwiched in a thin film device stack as was described earlier. The term *colloidal* refers to the fact, that these QDs are synthesized in and deposited from solution. Other sources of QDs like molecular beam expitaxy were not used in this work and will therefore not be covered.

Historically, the first nanocrystal LEDs were described in 1994 by the group of Armand Paul Alivisatos, who used CdSe QDs as emitter [111]. To this day, Cd-based emitters play an important role in the optical NC research community due to their superior optoelectronic properties. Due to their high undesired toxicity however, the experimental work presented in this chapter will exclusively revolve around their less toxic counterparts based on Indium Phosphide (InP).

6.1.1. Introduction to nanocrystal emitters

In a bulk semiconductor like silicon, the discrete energy levels, which are available to electrons and holes in single atoms, are smeared out due to the delocalization of electron wavefunctions in a periodic crystal lattice. Decreasing the interatomic distance of two infinitely distanced atoms will eventually lead to a splitting of the formerly identical energetic levels. Introducing more and more atoms into the system and into a periodic potential then leads to the well known image of electronic bands and the accompanied charge carrier transport – if possible – through the partially filled Valence Band (VB) and Conduction Band (CB) [112].
In an insulator, these two bands are separated by an energy gap and no charge carriers can be transported, hence the insulating properties. Semiconductors are similar to insulators, in a way that at lowest temperatures, the CB is typically empty with a completely filled VB, so that no transport can happen either. Since the semiconductor bandgap is low compared to insulating materials however, mobile charge carriers can be generated in either band through e.g. doping, photon absorption or thermal excitation already at room temperature. This leads to mobile charges in the periodic crystal and therefore a reasonable electrical conductivity.

The idea behind QDs is now, to split the energy bands gained in the band model by drastically decreasing the particle size from bulk. This is schematically illustrated in figure 6.1.

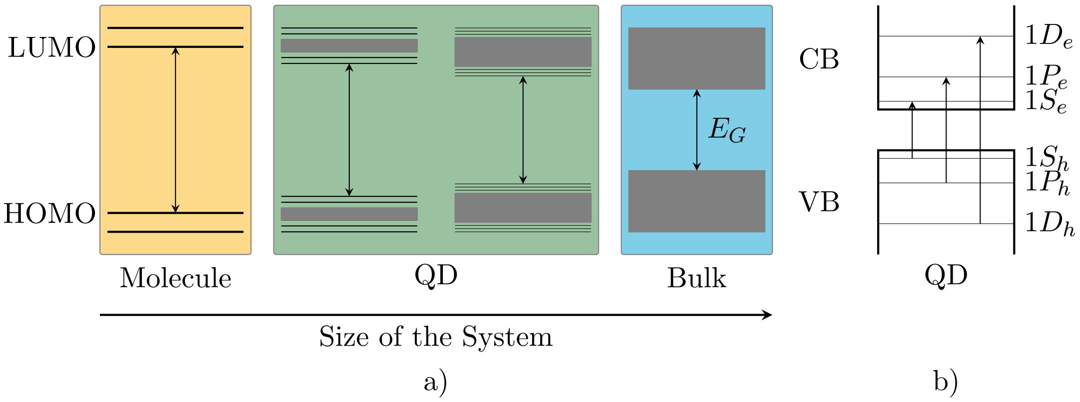

Figure 6.1.: a) Schematic energy diagram for semiconductors of different sizes. The band gap E_G decreases with increasing crystal size while the density of states increases from molecule to bulk.
b) Allowed optical transitions with respective level nomenclature for the quantum dot case. Images adapted from [113, 114].

With nanocrystal systems typically being in the range of a few to several tens of nm, they can be sorted inbetween purely atomic or molecular and bulk materials. This leads to the unique properties these QD systems possess. Note, that decreasing the NC size can be done in all dimensions. Therefore, different NC architectures can be realized starting from nanoplatelets with still quasi infinite periodicity in two dimensions, going to nanorods with decreased dimensionality in two directions followed by QD, where the size was reduced in all three dimensions to introduce the strongest carrier confinement effects. During the course of this work, exclusively QDs were used, therefore the terms of NC and QD can mostly be considered synonyms for this thesis.

Furthermore, the selection rules valid for optical transitions in QD structures are schematically depicted in figure 6.1b. The simplified illustration only shows transitions between CB and VB states where the quantum numbers n and L do not change for the involved charge carriers. Note that the nomenclature here is chosen analogously to the theoretical deduction leading to equation 2.6. This is due to the fact, that the transition probability k_{if} in these systems is a product of the transition dipole matrix element and the carrier envelope functions according to

$$k_{if} \propto \left| \langle \psi_f | \, e\hat{r} \, | \psi_i \rangle \right|^2 \cdot \left| \langle f_f | f_i \rangle \right|^2 = \left| \langle \psi_f | \, e\hat{r} \, | \psi_i \rangle \right|^2 \cdot \delta_{n_e,n_h} \delta_{L_e,L_h} \tag{6.1}$$

where f_f and f_i are the envelope functions and δ_{n_e,n_h} and δ_{L_e,L_h} are Dirac delta functions. Therefore, the transition rate k_{if} is only unequal to zero if $\Delta n = 0$ and $\Delta L = 0$, which is shown in figure 6.1b. Note that this is only an approximation and needs further refining to comprehensively describe the excitonic fine structure. This however is typically not relevant for studies on ensembles of QDs, as they were done during the course of this work in contrast to single crystal spectroscopy. Further theoretical descriptions can be found in the literature [113, 115, 116].

6.1.2. Quantum confinement effect

Understanding the electronic properties of NC requires a quantum-mechanical description of the available states in the respective system. This can traditionally be understood by either taking the *bottom-up* or the *top-down* approach. The former approach takes the molecular energy splitting of a two-body system and subsequently extends the system size. This requires immense calculational power, which is why this approach had commonly not been used to describe systems with thousands to hundreds of thousands of atoms in a cluster [113, 117].

On the other hand, the *top-down* approach can be used to describe the QD properties by starting from the semiconducting bulk material with subsequently reducing the system size. This will then lead to a theoretical problem similar to the classical *particle in a box* known from the description of the electron in a hydrogen atom. This approach will be described here – for more details the reader is referred to [113]. The theoretical description below largely follows this reference as well.

Note that both approaches can yield valuable insights for the comprehensive understanding of the QD properties. Both model descriptions have their limitations and reach their limits at some point, as QDs are settled inbetween the sizes of molecules and bulk. One therefore has to pay attention to effects coming from both worlds.

Similar to the mentioned *particle in a box* problem, QDs can often be assumed to be spherical in shape. Therefore the model to use is a *particle in a sphere*. Starting point for this kind of description is the energy of a free electron in a semiconductor, that has been lifted from the VB to the CB by for example photoexcitation, thermal excitation or doping

$$E_c = \frac{\hbar^2 k^2}{2m_e} + E_G \tag{6.2}$$

with the effective carrier mass m_e, the reduced Planck constant $\hbar$, the wavevector k and the band gap energy E_G.
As soon as the electron is put inside a spherically symmetrical potential $V(r)$

$$V(r) = \begin{cases} 0 & r < a_p \\ \infty & r \geq a_p \end{cases} \tag{6.3}$$

with the radius a_p, the boundary conditions state that the electron wavefunction at a_p needs to be zero. This in turn leads to discrete energy levels for electrons near the band edge. This can be expressed by the DOS $\rho(E)$ for particles in different dimensionalities d:

$$\rho(E) \propto E^{(d-2)/2} \tag{6.4}$$

For threedimensional materials (bulk, $d = 3$), the DOS follows the well known $\rho(E) \propto \sqrt{E}$ relation, while the zerodimensional case of QD results in a set of delta functions showing the comparability to molecules once more [118]. Due to these sharp energy levels, QD are sometimes also referred to as *Artificial Atoms* [119].

The formerly mentioned boundary conditions are of course only valid if the NC is so small, that the exciton Bohr radius, again in analogy to the electron Bohr radius in the hydrogen atom model, is similar to the NC size. This exciton Bohr radius a_{exc} is given by

$$a_{exc} = \frac{\epsilon \hbar^2}{\mu_0 e^2} \tag{6.5}$$

$$\mu_0 = \frac{m_e m_h}{m_e + m_h} \tag{6.6}$$

with the semiconductor permittivity ϵ, the elementary charge e and the effective electron and hole masses m_e and m_h [120], respectively.
The final result for allowed energy states in a potential as described by equation 6.3, assuming an identical effective charge carrier mass in bulk and NC, will then eventually yield [121–124]:

$$E \approx E_G + \frac{\hbar^2}{2a_p^2}\left[\frac{\beta^2_{n_e L_e}}{m_e} + \frac{\beta^2_{n_h L_h}}{m_h}\right] - \frac{1.765 e^2}{\epsilon a_p} \tag{6.7}$$

In this rather simple equation, the overall allowed excitation energy levels E for a quantum confined system are composed of three different terms. The first term is the bulk energy band gap E_G that will be the dominating term for large systems, meaning large values for a_p. The second term describes the energetic splitting due to the quantum mechanical spherical potential. This term is proportional to a_p^{-2}, meaning that a smaller a_p will result in a larger E and therefore a larger lowest possible transition from HOMO to LUMO or VB to CB. For the application of QD in e.g. optical fields of research, this means that the effective optical band gap can be directly influenced by the size of the NC. This is one of the major advantages of QD for optoelectronic applications, as will be described later. $\beta_{n_e L_e}$ and $\beta_{n_h L_h}$ are the n-th zeros of the L-th order spherical Bessel functions, where n is the index for different energy bands and L corresponds to the respective harmonic angular momentum quantum number [113]. The subscripts e and h refer to electrons and holes, respectively.

The third term in equation 6.7 finally resembles the Coulomb binding energy of electron and hole in the formed exciton, which reduces the excitonic energy value. This term is proportional to a_p^{-1}, which can play a significant role in not too small NC. Furthermore, the distinction of QDs into the *strong-* or *weak confinement* regimes can be deduced from this equation. Strong confinement means, that the second term with a_p^{-2} is dominant against the third term with a_p^{-1}. For theoretical considerations, the charge carriers forming an exciton can therefore be treated as free carriers with the Coulomb interaction being only a perturbation in the overall energy term [125].

Note that this relatively simple description of zerodimensional NC does not quantitatively describe all detectable optical transitions in real QD semiconductors. With the optical transition selection rules described in section 2.2, one would assume discrete transitions according to the respective changes in quantum numbers as shown in figure 6.1b, however the experimental data does not reproduce these theoretical expectations. The main reason here is that the bulk valence band orbitals in inorganic NC tend to mix, so that a more complex model for a comprehensive description is needed [114, 125]. This however also means, that the spin forbidden transitions of organic semiconductors are not a problem for inorganic NC emitters, so that the radiative exciton fraction q_{Exc} can safely be assumed to be unity. The strongly simplified result of theoretical considerations of valence band mixing in quantum confined systems is, that the selection rules of $\Delta n = 0$ and $\Delta L = 0$ as mentioned above are no longer strictly valid. The QD angular momentum (L) and underlying atomic orbitals forming the bulk valence bands (J) mix, therefore neither L nor J are *good quantum numbers* to describe the optical transitions. Much rather, the total angular momentum $F = J + L$ and the parity need to be conserved, which relaxes the strict selection rules given above. More details on the theoretical models for a more realistic description of QD can be found in the literature [113, 123, 125–128].

6.1.3. QD band structure engineering

The confinement of charge carriers in semiconducting QD leads to a wavelength tunable photon emission as was pointed out in the discussion of equation 6.7. However, this is a highly simplified and idealized model. In reality, semiconductor nanoparticles with only a few nanometers in size will have a huge surface to volume ratio, which is why the NC surface needs to be paid attention to as well. The major problem with QD, as they were described above, is that their PLQY is typically not too high and barely exceeds 10 to 50 % [113, 129]. Significant improvements were achieved with the introduction of an additional semiconducting layer, leading to the emergence of so called *Core-Shell* nanoparticles [130–132].

The idea behind these particles is to passivate the surface of the earlier described (optically) active core material with an additional inorganic layer, which would not change the energetic landscape of the core while passivating the surface atoms, which otherwise can act as quenching sites or charge carrier traps. One key factor to pay attention to here is of course the choice of a suitable semiconducting material, which can be grown epitaxically without introducing significant lattice mismatch between the two subspecies of semiconductors.

Commonly used material combinations and their respective field of application will be explained later in this thesis, however from a purely theoretical and conceptional point of view, the introduction of multiple adjacent materials in a single QD allows for tuning of desired optoelectronic properties even more. While the core material can for example determine the main optical emission wavelength by itself, the addition of a shell can introduce new properties into the system. Therefore, band structure engineering opens up new possibilites in QD design. A basic distinction of QD in different types is shown in figure 6.2.

As can be seen, the formerly mentioned example of a lower bandgap core compared to a high band gap shell material is called type-I QD and is represented by the CdSe/ZnS system. Here, both charge carriers are confined to the core and the optical transition is favoured due to the bigger wavefunction overlap of electron and hole. This setup is typically used in light emitting applications and is the only type of QD used in this thesis. Furthermore, this setup can be inverted to confine the charge carriers in the shell rather than the core, which can lead to better performances in photovoltaic devices [133].

By contrast in type-II QDs, the charge carriers are confined to different parts of the QD. The effective separation of electron and hole to core or shell (or vice versa) opens up e.g. photon emission or absorption at energies lower than either of the two involved materials' band gaps. This feature can be exploited in the design of highly efficient tandem solar cells again [134]. Furthermore, the band alignment of core and shell does not have to be symmetrical by any means. In fact, it is common to choose the energy values of the shell materials with respect to their application, so that e.g. a stronger hole confinement than electron confinement or improved electron or hole injection into the QD can become possible. This de facto tailoring of properties of inorganic NC emphasizes the versatility of QD and justifies the immense research interest in this type of material class.

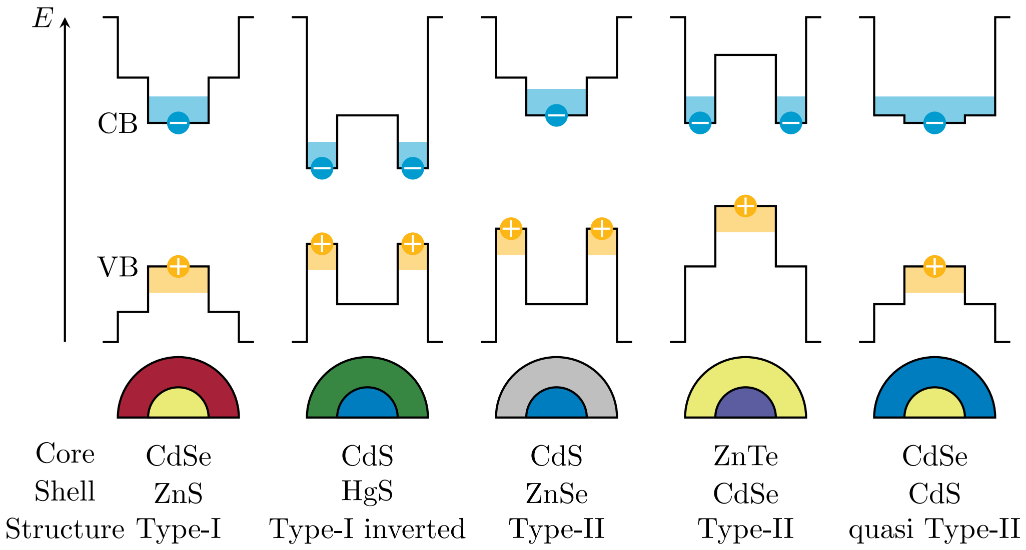

Figure 6.2.: Schematic representation of different band alignment configurations in Core-Shell QD. The respective charge carriers are represented in the lowest energy state in the respective band. Shaded areas represent the space where the respective charge carriers are confined to. Note that the absolute energy levels of the different semiconducting materials are not in scale. Illustration adapted from [123].

Finally, the rightmost plot in figure 6.2 shows additional possiblites in the band alignment design. In this exemplary *quasi-type II* case, the electron feels only a weaker confinement in the core compared to the hole and is thereby delocalized over a large fraction of the total QD. This can lead to an altered effective charge carrier density during electrical operation, which can have an impact on the device performance as will be described later on in this thesis.

6.1.4. Device architecture of QDLEDs

Tuning the energetic landscape of the emissive QD for optoelectronic applications is only the first step on the way to a QDLED. The next step after the theoretical material design and experimental synthesis is typically the material deposition. Here, all QD used in this work were deposited from solution, as was described in more detail earlier. However, the fact that the QD synthesis and deposition happen in a solvent brings several requirements for the further processing.

Firstly, the carefully synthesized QD can agglomerate in solution, so that their properties detoriate once again. To impede this process, the Core-Shell QD typically have an additional loosely bound organic ligand shell around them. These organic ligands bind to the open bonding sites on the NC surface and passivate them. Furthermore, these ligands typically are fairly long aliphatic molecular chains to maintain a certain minimum distance between two adjacent QD. This effectively supresses QD agglomeration, however due to the insulating nature of most commonly used ligand molecules, the electrical conductivity of QD films decreases and charge injection can be impeded. Therefore, another step called *ligand exchange* can be applied in order to replace the insulating ligands commonly used during QD synthesis to stabilize the dispersion by shorter, functionalized ligands. This will not be the case in the QD presented during this thesis, so no more details will be given about this process here. Note however, that this modification step can be exploited to additionally tune the thin film properties, so that higher efficiencies in both light emitting as well as photovoltaic applications can be reached, for more details see e.g. [135, 136]. During the course of this work, all QDs were capped with non conducting aliphatic organic ligands like oleic acid or octanethiol.

And secondly, the fact that QDs are deposited from solution requires stable underlying layers. As was described earlier, a typical standard thin film LED consists of several individual layers stacked on top of each other. If one layer is to be deposited from solution, the underlying layers must not take damage from this deposition. Different strategies to achieve this are the usage of polymeric, crosslinkable layers or application of orthogonal solvents for adjacent layers. Alternatively, inorganic metal oxides can be utilized as underlying layers.

During the course of this work, polymeric HTLs were used below the QDs as well as the latter mentioned inorganic layers. These strategies have also found broad usage in the QD community, so that the respective terms of *Type-I*, *Type-II* and *Type-III* QDLEDs have emerged [137], which should not be confused with the nomenclature of different core-shell QD architectures. *Type-I* hereby describes a QDLED where the emissive QD layer is sandwiched between two organic layers. By contrast, *Type-II* has the QD inbetween one organic and one inorganic layer while *Type-III* finally only incorporates inorganic adjacent layers to the QD. This work will cover both *Type-I* and *Type-II* devices, which will be labelled as *conventional* and *inverted* device stacks throughout this thesis. In the conventional stack, the QDs are deposited on top of a polymeric HTL while the inverted stack comprises an underlying Zinc oxide (ZnO) layer as ETL. Higher lying layers for both device types will be thermally evaporated organic layers.

As one big part of this thesis will cover these just mentioned *inverted* - or Type-II - devices, a short introduction of the physical properties of the incorporated ETL consisting of ZnO shall be given here. Although ZnO by far is no recently discovered material and has been investigated in the past with respect to its crystal structure, vibrational and optical properties, enhanced layer quality by improved deposition techniques have given rise to its application in, amongst others, optoelectronic applications [138, 139]. ZnO can crystallize in either rocksalt, zinc blende or wurtzite structure and can be processed from a number of different processing routes like chemical vapour deposition or solvent based sol-gel processes. In the latter case, huge impact of the processing conditions and precursor materials on the film formation have been reported [140]. Similarly, the electrical properties of said layers can be heavily influenced by the exact stochiometric chemical

composition and processing conditions, so that the reported values for - for instance - the electrical conductivity of single crystalline ZnO ranges over several orders of magnitude from roughly $10^{-3}\Omega\,\mathrm{cm}^{-1}$ to $10^{2}\Omega\,\mathrm{cm}^{-1}$ [141]. Additionally, doping of ZnO with other metal ions like Mg^{2+} or Al^{3+} can significantly alter the conductivity once again. Those manifold possiblities to tailor the properties of ZnO layer to match the requirements of the device explain the versatility of this particular material. A prominent example is the intentional reduction of the electronic conductivity of pristine ZnO with Mg^{2+} in order to reach a better charge balance during electrical QDLED operation [142].
All ZnO layers used in this work were not prepared by the author, but were received from a collaboration partner, details can be found in the respective discussion part of this thesis. Therefore, different doping concentrations or differently processed ZnO was not part of the presented investigations. In fact, all ZnO layers were deposited from a ZnO NC solution, which is commercially available. Therefore, the layer can be regarded as a constant factor for all compared devices. On the other hand however, even a homogenous layer of ZnO has a certain number of interstitial Zn^{2+}-ions and houses oxygen vacancies in the crystal lattice. These crystal defects are mobile and can change the device behaviour during operation, as was shown in the literature [143, 144]. This point is important when trying to explain the physical processes in QDLEDs containing a ZnO ETL. For example, the migration of mobile ions in ZnO can lead to the formation of interface dipoles in the respective layer. This in turn can then lead to a changed injection behaviour, as was explained in section 2.5 of this thesis. Therefore, also the concentration of said vacancies and interstitials will have huge impact on the layer properties, which is why ZnO layers from different sources or publications might show vastly different behaviour even though being a nominally identical material [141].

Furthermore, ZnO ETLs are reported to enable light emission of QDLEDs even below the built-in voltage V_{bi}. Although this should in theory be thermodynamically impossible, the high electron injection rates into ZnO can be followed up by an Auger assisted energy upconversion, so that in fact, photons can be emitted even below the actual turn on voltage [145, 146]. This process is proposed to happen via the formation of a charge-transfer exciton which transfers its energy to a secondary electron, which is thereby lifted above the injection barrier and can form a radiative exciton.
As was described, even though ZnO seems to be a fairly common and well known material, its application in QDLEDs can significantly influence the device performance. This is therefore to keep in mind when analyzing this kind of devices, as the mentioned effects do typically not occur in traditional OLEDs as described in section 2.

6.1.5. State of the art

As was shown in equation 6.7, the size of a QD system has massive influence on the (optical) band gap. Controlling the particle size during synthesis is therefore a crucial parameter to keep in mind. If executed well, the photon wavelength of an emissive QD can then however nicely be tuned over the whole visible electromagnetic spectrum. This is shown schematically in figure 6.3. A big advantage of solution processing in general is the overall easy scalability of the process. This primarily is of huge interest for industrial applications due to the low overall costs compared to other thin film deposition methods like thermal evaporation or lithography. Ideally, the synthesis of colloidal QDs produces a solution with uniform nanoparticles with only a single particle size. In reality however, every synthesis will be affected by a certain width of particle size distribution. This is already shown in 6.3 and will lead to non-monochrome PL emission with a certain distribution width, represented by the Full Width at Half Maximum (FWHM), of typically around 150 – 200 meV for the QDs used during this work. Although this is typically not a problem for industrial applications e.g. in the display industry, as the color purity of QDs is still better than that of other dyes, it opens up interactions of QDs with different sizes with each other. As the Stokes-shift in these materials usually is very low as well, emitted photons of a smaller QD might very well be absorbed by a larger QD which then of course can lead to an unwanted efficiency loss. In other words, with a larger Stokes-Shift, these reabsorption processes would not be possible with commonly

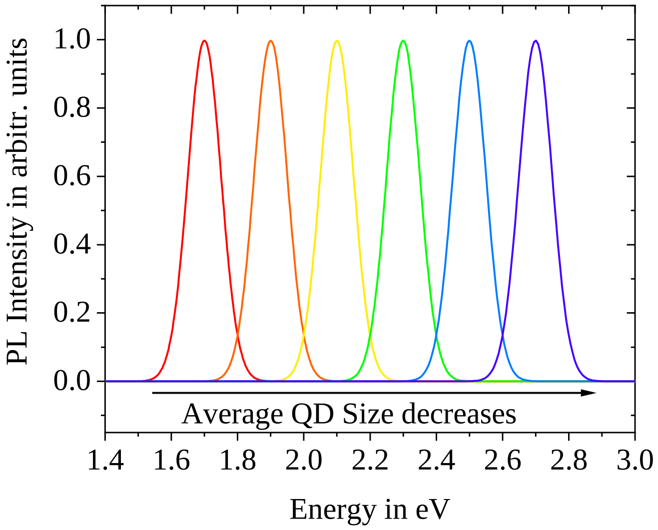

Figure 6.3.: Simulated emission of photoluminescence from QDs with different cores. Smaller cores relate to a lower emission wavelength, hence a larger energy value. All QD emission was approximated by monochrome emission from single particles with a gaussian size distribution of particle sizes in solution.

available high purity and small-FWHM QDs.

On the other hand however, studies on perovskite LEDs have shown, that the photon reabsorption, or photon recycling, can be a useful mechanism to exploit in order to increase the outcoupling factor η_{Out} with a sufficiently high internal quantum efficiency [147]. No comprehensive studies about this effect in colloidal QDLEDs have been published yet, so future respective research could enhance the understanding of optical processes here as well [148]. The quantum yields of QDs used in this thesis are generally not high enough for photon recycling to effectively play a major role, however the need for a well controlled synthesis of QD is still given to keep particle size distribution widths small.

The first thin film luminescent QDLED was prepared from CdSe already back in 1994 [111]. To this day, the combination of II-VI-semiconductors like present in the case of CdSe still is dominant in the field of electroluminescent QDLEDs. Their unique properties like the mentioned wavelength tunability, but also the high color purity through a low width of the emission peak, long operational stability and the overall high PL quantum yield clearly justify the immense research interest. Furthermore, they are, as also already mentioned, solution processable which emphasizes the technology's attractiveness especially for industrial applications.

Modern thin film LEDs featuring CdSe QDs comprise high quantum yields of close to unity and high peak EQEs of over 20% closing the gap to the theoretical limit for all red, green and blue emitting diodes [88, 149, 150]. Therefore for quite some time, the biggest challenges to solve were the efficiency Roll-off, meaning the reduction of luminance efficiency at high brightnesses, and the device operational lifetime. A breakthrough was achieved recently however with the introduction of *compositionally graded* QDs, where Klimov *et al.* essentially got rid of the Roll-off effect by careful QD structure engineering as described in section 6.2.4 [151]. More details on this particular study and their QD design will be given later in this work. With that, it seemed that the commercial application of QD was to be expected soon.

Unfortunately, however, CdSe based light sources can be, depending on the particle size, composition and ligand sphere, quite toxic for both humans and animals and are generally considered environmentally unfriendly. In fact, their application in consumer end products is regulated under the European Union's RoHS guideline, which emphasizes the importance of alternatives that accord to these environmental regulations.

The most prominent representative for environmentally more friendly light emitting applications is the subclass of InP QDs from the subclass of III-V-semiconductors [152]. The more covalent type of bonds between In and P compared to Cd and Se impedes complex formation of heavy metal ions with organic molecules to thereby impede ingestion into the human body. Studies showed, that the main toxic component from CdSe QD are in fact the Cd^{2+} ionic species, which can leach through several Cd-free shells and be absorbed in living cells while the toxicity of leaching In^{3+} was found to be smaller [152, 153].

The synthesis of these subspecies of QD, however, has proven itself to be more difficult compared to the CdSe counterpart and could only recently reach similar values as forementioned CdSe devices. An EQE of 21.4% for red emitting QDLEDs was reached together with a high quantum yield through careful synthesis of the QD and subsequent deposition on top of a polymeric HTL [154]. Key challenges however remain the unsatisfying device lifetimes and the efficiency Roll-off. Similarly, green InP-based QDs are slightly lagging behind their red counterparts in terms of efficiency. Recent studies showed EQEs of 16.3% with a high PLQY of 86% [155]. This again was achieved by carefully adapting the emissive QD layer to the surrounding layers by artificially attenuating electron and enhancing hole injection properties in an inverted device stack with a highly conductive ZnMgO ETL.

Finally, blue InP QDs are typically not seen in high efficiency LEDs. Recent studies reached an EQE of only 1-2% [156, 157] and were limited by a comparably low PLQY. Therefore, Cd-free research regarding blue emission has been focussed on ZnTeSe/ZnSe/ZnS Core-Shell-Shell QD, where recently the theoretical maximum was approached by an EQE of over 20% and PLQYs of almost unity [158]. Changing the emission wavlength was hereby achieved by tuning the doping concentration of Te in the Core.

During the course of this work, QDs were exclusively used as emissive materials in optoelectronic applications. Although this definitely is one huge field of application for QDs in general as both energy efficient lighting sources and high color puritiy displays will grow in importance in the future's economy, the general applicability of QD is still a lot bigger.

With CdSe and InP being the main candidates for light emission technologies, for example also PbS or CdTe QDs find application in photovoltaics [135, 159, 160]. Additionally, QDs can in general also be used in various biomedical or pharmaceutical fields for example for in-vivo drug tracing as optically active tracers or in form of a cancer cell-specific drug delivery treatment [161, 162].

Additionally, QDs are highly attractive in the field of sensors and sensing in general, as QDs with different sizes emit at different wavelengths, while the optical absorption of multiple species of QDs is possible at any low enough excitation wavelength. Therefore observation of complex systems is made possible with simple experimental techniques [163]. Furthermore, QDs could potentially be used in the near future in electrically pumped lasers with a wide range of accessible colors [164].

6.2. Efficiency loss mechanisms in quantum dot light emitting diodes

6.2.1. Trap assisted recombination

When Alivisatos *et al.* designed the first QDLED in 1994, they used a CdSe NC layer and a holeconducting polymer sandwiched between two electrodes to generate photons [111]. As was already mentioned, these *Core-Only* QD did not have very high optical efficiencies. The reason for this lies in the design of the QD themselves. Due to the small NC size, the surface-to-volume ratio in this material class is huge. Therefore, the surface needs to be accounted for and the *particle-in-a-sphere* model explained earlier with an infinite potential wall outside the QD does not hold anymore. Typically, the QD are coordinated with ligands to keep them in their colloidal solution. These ligands can attach themselves via a multitude of different chemical bonds to the QD surface, however incomplete coordination always results in non-ideally capped NCs.

These imperfectly capped QD therefore can introduce trap states for charge carriers which are located in the formerly unpopulated energy gap [165]. This effect is schematically shown in figure 6.4. Note that this process is also temperature dependent, so that charge carriers can reach a wider range of trap states at elevated temperatures and access thermally activated charge transfer states [84].

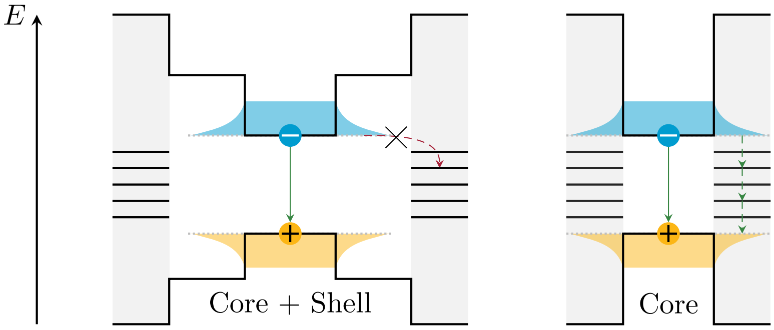

Figure 6.4.: Schematic representation of Core-Shell and Core-Only QD energetic landscapes. The QD-solution interface introduces trap states, which are accessible in case of pure Core-QD, as the charge carrier probability density function is unequal to zero close to the Core. With the introduction of a suitable shell, the traps states still are introduced into the system, however the charge carriers can not access them. Therefore this non-radiative loss channel is blocked. Green and red arrows indicate possible and blocked transitions, respectively. Dashed and solid arrows represent nonradiative and radiative transitions, respectively. Shaded areas represent the areas, where the respective charge carrier probability density function is unequal to zero. The style of illustration is adapted from [123].

As mentioned earlier, due to the fact that the potential well in real particles is not infinitely high at the surface of a core-only QD, there is a certain probability for charge carriers to be located there - their probability density function is unequal zero outside the core [166]. If the core is capped by ligands, then the formerly mentioned intragap states are available for the charge carriers to be taken and non-radiative decay is possible. Hence, the system's non-radiative decay rate k_{nr} is increased.
If however the core is capped by a suitable shell, there are no trap states available for the charges. This of course requires epitaxial shell growth without the introduction of too much strain in the crystal lattice. Otherwise the lattice mismatch can lead to unwanted effects like a lower QD stability and therefore lower device lifetimes or simply to lattice defects at the Core-Shell interface, which again act as charge carrier traps [131, 132].

Trap assisted recombination, or Shockley-Read-Hall (SRH) recombination, has been known already in organic semiconductors and does not necessarily have to be disadvantageous. Effective trapping of one charge carrier type and subsequent recombination with an opposite charge carrier actually can lead to the emission of photons, however the radiative recombination rate should generally be higher than the trapping rate in order to still enable efficient light generation. If however the trapping rate is not negligible or – in other words – the injected electrons and holes are trapped faster than the standard bimolecular Langevin recombination mechanism of organic semiconductors, the overall trapping process is proportional to the trap concentration [14]. In particular, it is not dependent on the product of electron and hole densities and thereby not a quadratic term. Much rather, SRH recombination is considered to be linear with the current density under device operation, as trap states are typically only accessible for one charge carrier type and therefore only dependent on the respective charge carrier type density [14].

6.2.2. Electric field quenching

So far, the loss mechanisms of triplet-quenching in organic– and the SRH recombination in QD-based thin film LEDs have been described. The crucial factors for the respective quenching processes were either the exciton-, charge carrier- or trap densities. In the case of QDs however, also an electric field F alone can play a major role in quenching the luminescence efficiency via e.g. the Quantum Confined Stark Effect (QCSE). Furthermore, for high electric fields, the process of exciton dissociation is possible, where the charge carriers overcome their coulomb binding energy and escape from the quantum well.

Quantum confined Stark effect

In contrast to the atomistic *Stark-Effect*, which describes the energy splitting of atomic levels in the presence of an electric field, the QCSE descibes the features seen in quantum well structures like QDs when an electric field is applied.
As was already implied in figure 2.3, an electric field leads to band bending during operation in a multilayer OLED or QDLED structure. This shift in energy, however, is also happening internally in single QDs, as can be seen in figure 6.5.

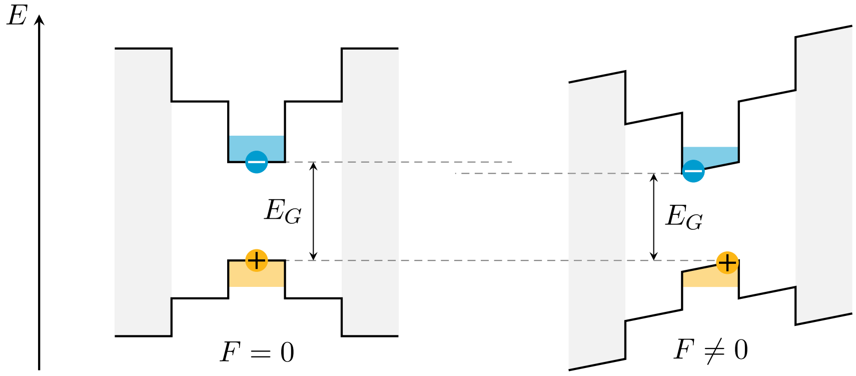

Figure 6.5.: Schematic representation of the electric field effect on charge carrier probability density functions in core-shell QD.
Left: No electric field ($F = 0$) applied, the charge carriers are delocalized in their respective potential wells.
Right: With an externally applied electric field ($F \neq 0$), the charge carriers shift towards the opposite ends of the wells. This spatial separation reduces the wavefunction overlap. Additionally, the lowest energy transition (E_G) decreases.
Note that for the sake of clarity, the energy levels of the Core VB maxima were drawn to be equal. Image adapted from [115]

The left image in figure 6.5 shows the energy landscape of a Core-Shell-QD in solution without any internal electric field. For the sake of simplicity, the image illustrates the case of a Type-I-QD, as was used throughout this work. The exciton is confined to the core and has a certain transition probability P to decay and generate a photon. In general, this probability P is expressed by

$$k_r \propto P = \left| \langle \psi_e | \vec{p} | \psi_h \rangle \right|^2 \tag{6.8}$$

with the electron and wavefunctions ψ_e and ψ_h and the momentum operator $\vec{p}$ [167]. Therefore, P is dependent on the transition dipole matrix element, which in turn is dependent on the square of the overlap of electron and hole wave functions [113].
Due to the applied field across the QD, the wavefunction overlap between electron and hole is reduced as indicated by the drifting apart of the two illustrated charges in figure

6.5 on the right. In consequence, the first effect of an electric field on the QD luminescence is a reduced optical efficiency through the reduction of wave function overlap, thereby transition probability and in turn the radiative rate k_r.

The second effect of an applied field is furthermore a potential spectral redshift in the emission wavelength. This occurs since the energy of the lowest possible energetic transition E_G, can change with the QCSE. Due to the electric field, both electrons in the CB and holes in the VB occupy states with lowered energies with respect to their unbiased counterparts. Therefore it is quite common to see a redshift in QD emission with the application of an electric field. Note however, that a redshift is not necessary to be seen, as this simple picture of a change in occupancy towards lower levels is not always the dominant effect of an electric field on the emission wavelength:

Excitons in CdSe QDs have been found to be slightly asymmetrical with respect to the respective electron and hole wave functions [2]. Single-Crystal spectroscopy revealed, that these QDs in fact form a dipole in the excited state with a non-negligible dipole moment. This was attributed to the excitons being partially of trap state character at the Core-Shell interface, as the modelled view of a trap-free and infinitely deep potential well is not given in reality. Application of an electric field to this dipole will then either induce reorientation of the QD or, in the case of QDs in a rigid environment with no possiblity to rotate the QD, an energetic change depending on the angle between external electric field and QD dipole moment. Considering the case of QD ensembles in a thin film now, the average dipole moment orientation will be zero, so that this energetic shift does not lead to a macroscopic emission shift. In fact, a fraction of dipoles will be oriented antiparallelly to the electric field and therefore have a larger E_G while another fraction of QD will be aligned in parallel to F and experience a redshift or smaller E_G. Detecting an ensemble of QDs therefore should result in a broadening of the emission peak with rising electric field.

If we now treat the formerly described spatial separation of electron and hole wave functions as the generation of an electric field induced dipole, the overall energetic shift ΔE_{SC} of the lowest state emission energy in a single emissive NC can be given as

$$\Delta E_{SC} = \mu F + \frac{1}{2}\alpha F^2 \tag{6.9}$$

with μ and α being the projections of dipole moment and polarizability onto the direction of the electric field F, respectively [168, 169].

For QD-ensembles, equation 6.9 yields $\mu_{ens.} = 0$ and the energetic shift barring the broadening is solely dependent on the electric field in a quadratic manner:

$$\Delta E_{ens.} = \mu_{ens} F + \frac{1}{2}\alpha F^2 = \frac{1}{2}\alpha F^2 \tag{6.10}$$

Deviations from this behaviour can then for instance indicate the presence of additional charges close to QDs, which screen the externally applied field [169]. This can also be used to probe for the concordance of externally applied and internally available electric fields.

Exciton Dissociation

Another effect that can occur in QD when exposed to an electric field is exciton dissociation. While generally considered favourable for the case of photovoltaic applications, this process opens up new non-radiative decay paths for excitons in LEDs. Thereby, the radiative rate k_r is not influenced by this effect while k_{nr} is increased, which distinguishes it from e.g. the efficiency loss via QCSE.
Exciton dissociation is typically utilized in photovoltaic applications by charge separation at a Donor-Acceptor Interface, where the respective energy levels are chosen in a way to efficienctly enable the charge carrier separation. Then, the separated charges will be transported through the CTLs towards the electrodes where the exctraction happens. For the case of emissive QD, this process is excluded without externally applied fields. Charge separation would require enough energy to both overcome the potential walls as well as the coulombic exciton binding forces as shown in equation 6.7. Thermal energy alone is typically too low to achieve this.
Sufficiently high electric fields can then however compensate for the exciton binding energy and even lead to charge carriers overcoming the confinement effect, which will then reduce the number of excitons available for radiative recombination. A new non-radiative pathway for excitons is therefore enabled and the non-radiative rate increases. Since this effect is highly dependent on the energetic landscape of the Core-Shell structure, it can be mitigated by careful QD design and synthesis [170, 171].

General considerations of electric field quenching in QDLEDs

With the two main factors influencing the QDLED efficiency via an electric field being the QCSE and exciton dissociation, one needs to consider the circumstances in real devices under operation. As was explained earlier in section 2.3 of this thesis, charge carriers in thin film light emitting diodes are usually injected from two electrodes with differing work functions. This leads to the formation of a built in potential V_{bi}, which needs to be overcome to generate photons. If the externally applied bias is just equal to V_{bi}, this device state is typically called *flatband* condition, as the band bending induced by V_{bi} is exactly compensated by the external bias. The internal effective electrical potential Φ_{int} is therefore given by

$$\Phi_{int} = \Phi_{ext} - \Phi_{bi} \Longleftrightarrow V_{int} = V_{ext} - V_{bi} \tag{6.11}$$

with the externally applied potential Φ_{ext} and the corresponding applied voltage V_{ext}. Therefore, one crucial point in analysing field effects on the QD efficiency is to keep in mind the effectively applied field rather than the externally applied field. As an example, for $V_{bi} = 2V$, the effective electric field in a QD structure would be identical in magnitude at 3 V and 1 V rather than at 1 V and −1 V. Therefore the respective effect of energy splitting and efficiency loss according to equation 6.10 are also considered identical at these voltages due to the second order dependence on F.

Similarly, interface dipoles need to be considered when trying to find the flatband conditions in a device. With polar layers, SOP can lead to the formation of a GSP. If the emissive NC species is close to such an interface, this might influence the internal QD effective field as well. However, one has to pay close attention to probing the internal quantum efficiency in presence of GSPs, since the accompanied charge accumulation can additionally increase the quenching, although this then obviously is no longer caused by the electric field.

6.2.3. Auger quenching

The final efficiency loss mechanism to be covered in this thesis is the case of Auger Quenching (AQ). The atomistic Auger effect describes a process, where electrons from outer atomic orbitals fall into an energetically lower inner shell electron vacancy while transferring their excess energy to a third particle. This electron can then be emitted and is typically called an Auger-electron.
Similar to this atomistic effect, AQ in QDs and other quantum well structures refers to an efficiency loss process with at least three particles involved. That is, if high excitation densities create so called positive or negative *Trions* from one electron and two holes (*ehh*, X^+) or two electrons and one hole (*eeh*, X^-), respectively, the excitonic energy can be transferred to the excess charge carrier. This third carrier will then be excited to a higher energetic state but will immediately non-radiatively decay. Therefore, effectively, two charge carriers are lost in this process and the non-radiative decay rate k_{nr} is increased [84, 172]. This is schematically illustrated in figure 6.6.

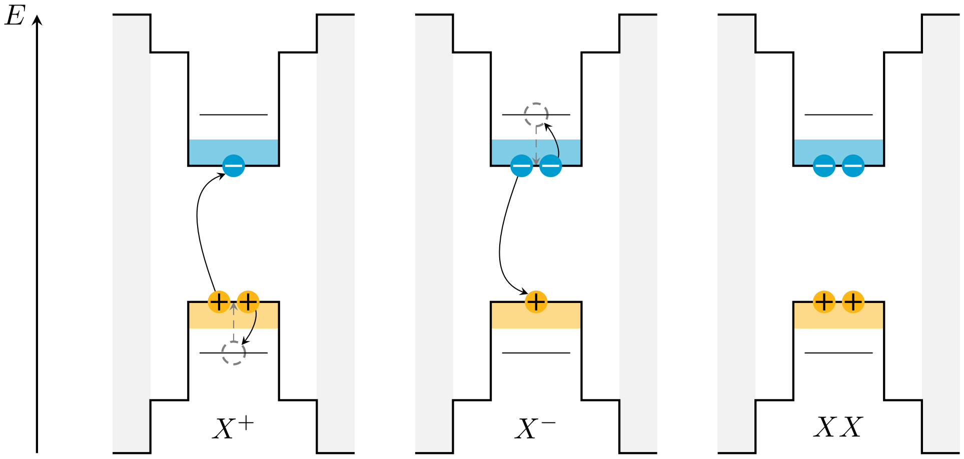

Figure 6.6.: Schematic depiction of charged excitons or trions (X^+, X^-) in quantum well structures. Fast three-particle processes can lead to an effective exciton loss. Photon emission from biexciton states (XX) is in principle possible, however competes with the forementioned Auger process and is therefore considered unfavourable for light emission [173]. Image adapted from [174].

For the case of positively or negatively charged excitons (X^+, X^-), the excitation energy is being transferred to the excess hole or electron, respectively. However, in QD

it is also common to see the formation of biexcitons (XX) or even higher numbers of excitons on a single QD. In fact, for photovoltaic applications, this can be advantageous since the absorption of a single high energy photon can lead to the generation of more than one exciton. This process is typically called Multi-Exciton Generation (MEG) and can be used to achieve photovoltaic EQEs higher than 100% [175]. One of the biggest challenges in these systems is however, to separate the charge carriers very quickly, as multiexcitons rapidly decay via the mentioned Auger quenching [176]. A potential way to overcome this issue is for instance the electronic coupling to suitable ligands attached to the NC surface, which stabilize the charge transfer state and enable efficienct charge extraction [177].
By contrast in QDLEDs, the generation of multiple excitons on a single QD is generally unfavourable. Although the direct transition from a biexciton to a single-exciton state can involve emission of a photon, this process has to compete with the aforementioned fast ($\tau_A \ll 1ns$) Auger process, so that the overall device efficiency is typically higher for single-excitonic emission only, where the typical radiative lifetimes are in the range of 1 to 10 ns.
Furthermore note, that additionally to the single charged trions X^+ or X^-, also multiply charged excitons (i.e. X^{n+}/X^{n-}) can exist. The decay of these states can however be treated as a cascade of single charge trion decays, i.e. $X^{n-} \to X^{(n-1)-} \to X^{(n-2)-} \to \dots$, where the respective lifetimes are shorter, the higher the charge carrier density in the NC [178, 179].

Coming back to the most basic case of the three-particle quenching process, the change in exciton density over time follows a cubic law [178]:

$$\frac{dn_{eh}}{dt} \propto -n_{eh}^3 \tag{6.12}$$

Interestingly, this relationship is true for both bulk and nanocrystal semiconductors, which shows that the quantum confinement potential depth in itself does not affect the process of AQ. Only the QD system size influences the degree of AQ by means of controlling the QD volume and the therefore available space for the charge carriers and by doing so in turn the charge carrier density. Furthermore, if the device current j is mostly dominated by an Auger current j_A, it can be expressed by

$$j \approx j_A = C_A \cdot n_{eh}^3 \tag{6.13}$$

with an Auger constant C_A [180]. Note however, that this constant C_A is not a material specific constant by any means. The Auger constant C_A is, for instance, strongly dependent on the sample temperature by $C_A(T) = C_0 \exp(-E_a/kT)$ with an activation energy E_a, but also depends on the quantum well structure itself [180]. Studies on CdSe QDs revealed a spatial R^3-dependence of $C_A(R)$ for comparably small QD. Therefore, the Auger constant is also dependent on the QD size [178].

6.2.4. The ABC-model of efficiency losses in QDLEDs

The three main loss channels in QDLEDs are SRH recombination, quenching due to the electric field and the Auger quenching induced by high charge carrier densities. These three processes can be adapted into the general equation of emitter efficiency from equation 2.16.

$$q = \frac{k_r}{k_r + k_{nr}} = \frac{k_r}{k_r + k_{SRH} + k_{Field} + k_{Auger}}$$

As was described earlier, the trap assisted SRH quenching is, even though two charge carriers recombine with each other, limited by the density of traps and the density of minority charge carriers. Therefore it is considered linear with the charge carrier density n, under the assumption of balanced charge injection [14]. By contrast, radiative recombination is a process with two charges involved, which is why the process is dependent on the charge carrier density squared. Similarly, the QCSE leads to a reduction in overlap of electron and hole wave functions, which reduces the radiative rate. Lastly, as was explained before, the Auger rate depends on the charge carrier density in a cubic relationship due to the three-particle nature of the quenching process. Therefore, it scales with n^3.

Combining the three dominant efficiency loss processes of SRH- and Auger quenching as well as the reduction of the radiative rate via the QCSE with equation 2.16 now leads to

$$q = \frac{k_r}{k_r + \sum\limits_i k_{nr,i}} = \frac{Bn^2}{An + Bn^2 + Cn^3} \tag{6.14}$$

with the SRH recombination coefficient A, the bimolecular radiative recombination coefficient B and the Auger constant C. This model is typically called the *ABC-model* and can be applied not only to colloidal QD but finds usage in a wide range of both bulk and quantum confined emitters [181–183]. Note, that the process of exciton dissociation was neglected here, as it is a process barely seen in emissive QD structures with an appropriate Core-Shell structure. Inclusion into equation 6.14 would introduce another nonradiative component.

Figure 6.7 shows simulated efficiency vs. carrier concentration plots with different values for A, B and C. The three values for the black reference plot are varied, one per subsequent plot, in order to clarify the influence of the different efficiency loss processes. First of all, the general shape of the plots increases from low n to a certain maximum. This is simply due to the fact, that the number of radiative recombinations Bn^2 is smaller than the number of trap-quenched events An for the case of small n. Furthermore, the high carrier density behaviour also drops down to zero, as the cubic term of Cn^3 becomes dominant and decreases the overall efficiency.

Increasing A, as shown in the orange plot, will increase the quenching - and thereby decrease q - in the low n regime. The overall curve is therefore shifted towards higher charge carrier concentrations and reduced in overall peak height. Similarly, a higher C (green graph) reduces the efficiency in the high-n-regime and thereby shifts the plot

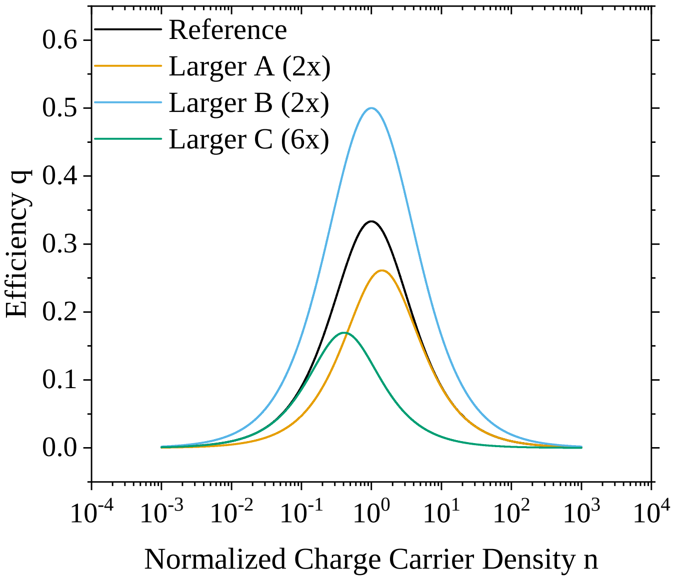

Figure 6.7.: Simulated predicted efficiency curves from the ABC-model for different parameters for A, B and C. The black reference plot features an arbitrary set of parameters, all other plots have only the parameter mentioned in the legend varied with respect to the reference.

towards lower n regions while also decreasing the peak height.
By contrast, increasing B will increase the overall peak height as the radiative decay pathway Bn^2 is increased. Additionally, the plot width increases, since the amount of quenching from A and C stay constant.

This theoretical model can help with the analysis of internal quantum efficiencies as will be shown in the experimental part of this thesis. Fitting the measurement data to this model can help understanding the bottlenecks of efficiency limiting processes which is a crucial step in improving device efficiencies.
Strategies to influence the three parameters A, B and C have partially already been mentioned in the preceeding sections.

- A is a figure of merit for the amount of trap assisted SRH recombination in the quantum well. Thereby, reducing the trap concentration in the QD will also reduce A and thereby improve the efficiency q. With the introduction of the discussed Core-Shell structures, a huge step was taken towards an internal quantum efficiency of one. Choosing a suitable shell material can minimize the trap concentrations, as long as the Core-Shell interface does not introduce strain into the system and the lattice mismatch is not too big.

- With B being linked to the radiative exciton decay, the goal would be to maximize it. Therefore, one would have to try to accelerate the exciton formation by a stronger charge carrier confinement and additionally also increasing the wave function overlap of electrons and holes, respectively. Since exciton dissociation and the reduction of overlap through the electric field during electrical operation also influence B, high degrees of confinement would be ideal. Therefore, for Type-I emissive Core-Shell-QDs, a comparably large difference in respective CBs and VBs of Core-and-Shell materials would be desirable, assuming a smaller band gap for the Core material.

- The detrimental Auger quenching, expressed by C, should be minimized to keep the high carrier density – and thereby high luminance – performance of the QDLED in an acceptable range. As was decribed earlier, Auger quenching is mainly caused by the local charge carrier density, therefore a rather low confinement of excitons in the system is desirable.

As can be seen in the last two points of B and C, ideal QD design has a lot of challenges, as the requirements for optimal efficiency at least partially contradict each other. Therefore a compromise has to be found to optimize the electronic structure for optical applications. This in turn emphasizes the importance of comprehensive efficiency loss analysis even more, as there is no simple rule valid for all QD systems. As an example, recently the design of so called *compositionally graded* CdSe-QDs has lead to essentially efficiency loss-free electrically operating QDLEDs [151]. Here, the authors applied the concept of a CdSe core with a ZnSe shell, while the transition from core to shell is smoothed out by gradually reducing the Cd- and increasing the Zn-content. This can be noted as a $\mathrm{CdSe/Cd}_x\mathrm{Zn}_{1-x}\mathrm{Se}$ structure. Furthermore, the authors applied an additional buffer layer of $\mathrm{ZnSe}_{1-y}\mathrm{S}_y$ as outmost shell, where they again changed y with increasing shell thickness in order to minimize lattice strain in the QD. With this sophisticated design of a $\mathrm{CdSe/Cd}_x\mathrm{Zn}_{1-x}\mathrm{Se/ZnSe}_{1-y}\mathrm{S}_y$ QD, it was possible to tune both the carrier confinement by variation of x and the electron injection and thereby the charge carrier density in the QD by varying y.

As was explained earlier, CdSe was one of the first materials used as luminescenct semiconducting NC. Due to its superior properties regarding stability and efficiency, still a lot of research is focussed on these structures. However, due to the inherent toxicity, also InP as Core material has been focussed on. However, a similar breakthrough would be necessary to introduce InP QDs into the broad consumer markets and is currently under investigation. Therefore, one of the main focal points also of this thesis will be to analyse the loss efficiency mechanisms in multishelled InP QDs.

6.3. Introduction to nanocrystal synthesis

The synthesis of the colloidal InP-QD used in this work was not carried out by the author of this thesis but the samples were provided by the Fraunhofer Institute for Applied Polymer Research (IAP). Even though the QD synthesis therefore was not part of the work presented here, its basic principles shall be given regardless. More information of the synthesis details and theoretical background can be found in the respective literature [184–188].

The synthesis of colloidal InP-QD originally was best carried out by the method of a dehalosilylation reaction where the precursor material Tris(trimethylsilyl)-phosphine ($P(SiMe_3)_3$) reacted with an Indium(III) halide like $InCl_3$. While the success of this method was already considerable, oxidation of both In and P surface sites decreased the quality of the final product [185]. Therefore a different synthesis route was needed, which was found by adding the aforementioned compounds into a non-coordinating solvent using both 1-octadecene as well as fatty acid type stabilizing ligands or other material groups during the synthesis. These chemical reactions usually take place at elevated temperatures up to 300°C and are nowadays used in most labs during the synthesis of colloidal InP QD.

The QD formation itself works via a nucleation and growth step, meaning that the starting point for any synthesis is a solution with a precisely controlled precursor concentration. The precursors form monomers, which then in turn build up the nanocrystals [189]. As the elevated temperature lead to considerable thermal energy in the solution, the thermodynamics and dynamics of this reaction have to be considered carefully as well:

$$Precursors \rightarrow Monomers \rightleftharpoons Nanocrystals \tag{6.15}$$

As NC start to form, they plainly have a small volume while comprising a comparably large surface. The surface energy will therefore work to dissolve NC below the size of a critical radius, while exceeding the radius will be energetically favourable. Nuclei already larger than this critical radius will therefore continue to grow through the process of *Ostwald ripening*. This is in principle an advantageous effect, as the NC growth is energetically favourable than the purely monomeric dispersion. A significant problem arises however considering the fact, that for optical application, a sharp NC size distribution is desired, which requires the careful control of synthesis parameters.

A milestone was reached with the introduction of the so called *Hot Injection Method*, where the room temperature precursor materials are quickly injected into a hot reaction solvent [190, 191]. This reduces the overall time needed for the nucleation and results in a more balanced growth period during which the already larger particles will grow slower than the smaller particles, which leads to size homogenization. Eventually, Ostwald ripening will again come into play and the small NC will decompose while the bigger NC grow further. By combining these two effects, the size homogeneity distribution can be significantly improved. In order to design more complex Core-Shell QD, the synthesis steps have to be repeated with suitable precursors and organic ligands in solution.

As already mentioned, during the course of this work, InP-QD processed by IAP were investigated. The author does not have any exact information on the synthesis of QD, however In-Acetate, Zn-Stearate, P(SiMe$_3$)$_3$, trioctylphosphine selenide and dodecanethiol were used as In-, Zn-, P-, Se- and S-precursors, respectively. The Core-Shell-design of the QD processed by IAP is schematically shown in figure 6.8. The InP-core is surrounded by a thin ZnSe layer to mitigate lattice mismatch and an outer, thicker ZnS layer. Subsequential charge carrier confinement for both electrons and holes is achieved by the illustrated energy level alignment. The total QD diameter is below 5nm, as will be shown in the experimental part of this work. Oleic acid was used as QD surface ligand.

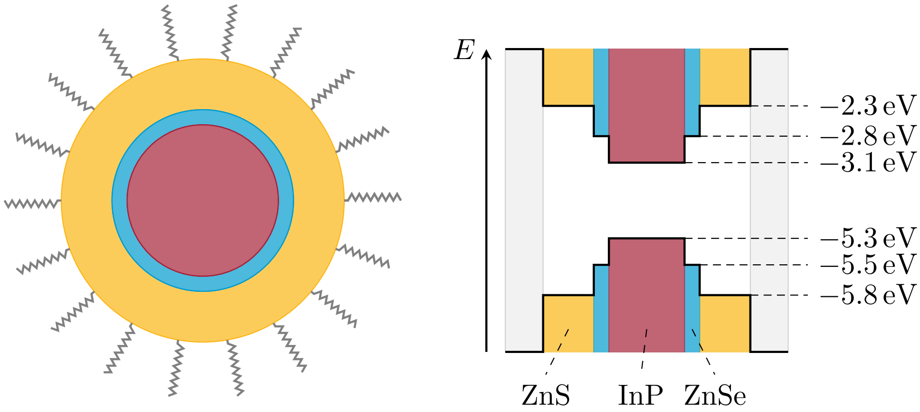

Figure 6.8.: Schematic depiction of the IAP QD organic ligand capped Core-Shell-Shell (InP/ZnSe/ZnS) cross section with the respective energy level alignment. Redrawn from personal correspondence with the manufacturer.

CHAPTER 7

Characterization of QDLEDs

As was already mentioned, the samples investigated in the QD part of this work were not fabricated by the author of this thesis. All samples from IAP were sent by Dr. Yohan Kim and the respective device stacks for both conventional and inverted stacks can be found in figures 7.1 and 7.2, respectively. The main difference between the two stacks is the use of Poly(4-butylphenyldiphenylamine) (pTPD) and Tris(2,4,6-trimethyl-3-(pyridin-3-yl)phenyl)borane (3TPYMB) or TCTA and ZnO as respective HTLs and ETLs in conventional and inverted devices, respectively. Furthermore, both the QD type as well as the QD layer thickness were varied across the sample set. In fact, samples with a single monolayer of QDs were used as a reference with a second batch of samples containing a thicker EML.

The following chapter is divided into three parts, where the latter two will focus on the PLQE quenching behaviour during electrical operation of the QDLED. The first part by contrast will cover properties of the used QD both in solution and thin films without an applied bias.

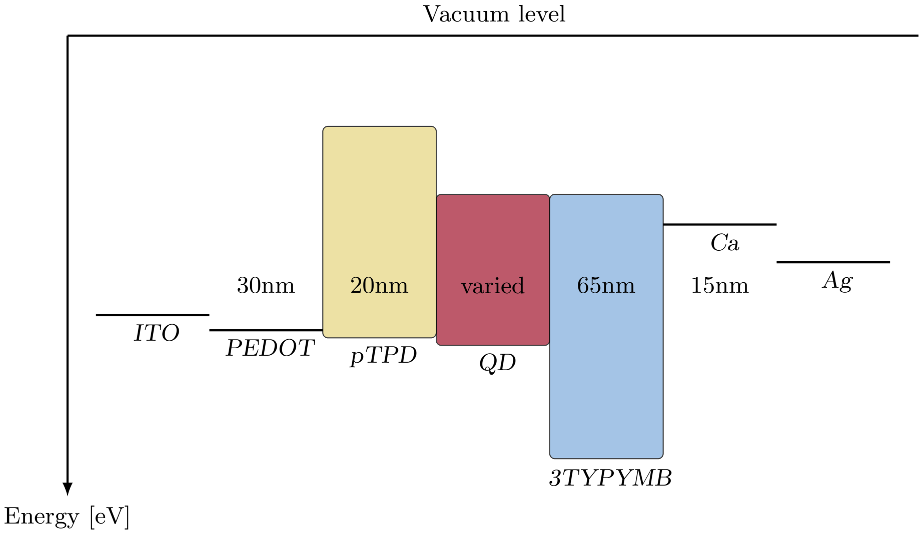

Figure 7.1.: Schematic energy diagram of the used IAP QDLED conventional stack. Energy levels are drawn in scale, exact values can be found in the appendix in table A.1. The QD layer thickness was varied.

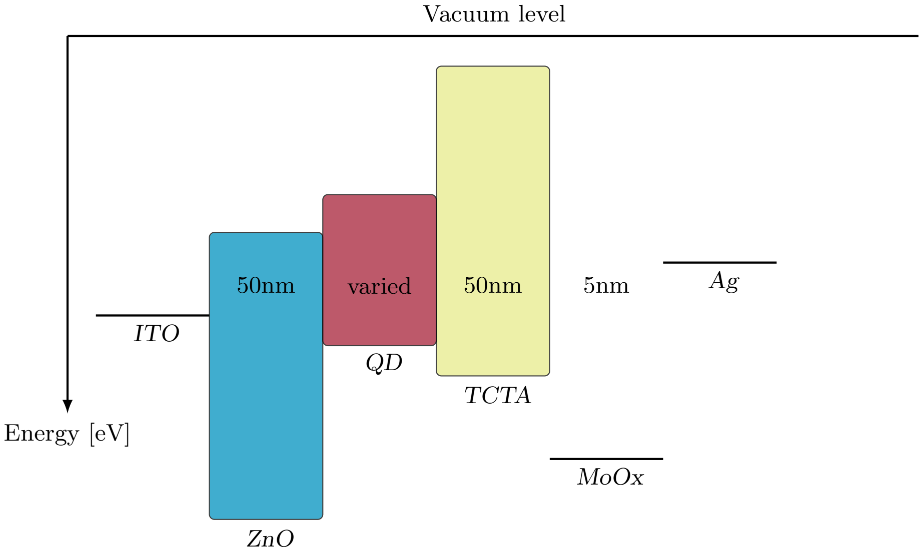

Figure 7.2.: Schematic energy diagram of the used IAP QDLED inverted stack. Energy levels are drawn in scale, exact values can be found in the appendix in table A.1. The QD layer thickness was varied.

7.1. Physical properties of QDs

During the course of this work, two types of IAP QDs were investigated. The two materials were labelled *HC100* and *HC103* and they are both based on an InP/ZnSe/ZnS Core-Shell-Shell structure as was shown in figure 6.8. The difference between the two materials is the shell thickness of the outer shell with only a single monolayer of ZnS for the case of HC100 and seven monolayers for HC103. The difference in total QD sizes therefore comes down to an additional set of six monolayers in the respective radii, corresponding to twelve monolayers in diameters. The system of exclusively changing the shells, in theory, should leave the core properties unchanged, so that the emission wavelengths should be comparable. Note that the information on the exact stochiometry of different QD substructure thicknesses was received from the manufacturer and was therefore taken as starting point for the investigations. No further information about how thick a monolayer is supposed to be or how a monolayer actually looks like is provided from the manufacturer. Note that both working QDLEDs and pure QD materials were received from the IAP.

7.1.1. Morphology of QD films and device stability

The theoretical description of QDs showed, that the energetic band gap of QDs can be tuned by varying the system size. A perfect NC synthesis would therefore then be a monodisperse QD solution with only a single QD size. Upon film deposition, these monodisperse QD would then form a film - assuming the deposition of a monolayer - where the film thickness equals the QD diameter.

This of course is a quite idealized picture and requires close attention in real world applications, as the film morphology can have a huge impact on the eventual device performance. Therefore, as a starting point, Transmission Electron Microscopy (TEM) images were taken to investigate on the QD shape. TEM images were taken for both HC100 and HC103 and the particle sizes were determined by averaging over more than 140 QDs on four images per QD type. The results of this analysis are shown in figure 7.3, while exemplary source TEM images can be found in the appendix in figure A.6.

As can be seen, the general statement of HC103 being the on average larger particles can be confirmed. The average QD diameter of HC100 is 4.26 nm while HC103 has a larger value of 4.97 nm. Assuming spherical QDs and the differences exclusively coming from the outer shell thickness, this would mean that the delta of average values of 0.71 nm corresponds to twelve monolayers of ZnS, as was explained above. Simple division would lead to a monolayer thickness of 0.6 Å, which would fit nicely to the ionic radius of Zn^{2+} ions at 0.74 Å [192]. Unfortunately however, the larger ionic radii of S^{2-} ions of 1.7 Å are not accounted for in this image [192]. Therefore, the assumption of six additional monolayers as difference between the two QD species has to be taken with caution.

Another important piece of information to extract from figure 7.3 is, that the size distribution of the QDs is not comparable. The size inhomogeneity of HC103 QDs is larger, which shows that the additional shell growth does not happen uniformly at all present

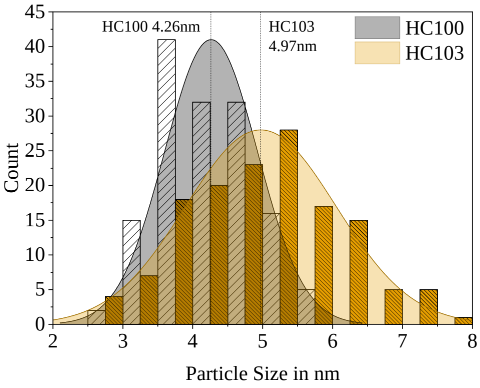

Figure 7.3.: Particle diameters of HC100 and HC103 QD. The author is grateful to Dr. Aladin Ullrich for the TEM measurements.

QDs. Since the optical properties mostly are determined by the core properties, which should be identical for both samples, this discrepancy does not necessarily mean that HC103 is an inferior material. One should however keep in mind, that the smallest QDs in both the nominally smaller and larger materials are approximately identical.

Following the TEM analysis of QDs in solution, the film formation of the respective emissive NCs was investigated on different substrates. As was already mentioned, the QDs were deposited from solution by spincoating. In these systems, the film formation of conductive materials plays a crucial role in the device performance of the emissive layer in the LED. Possible problems hereby include large agglomerations piercing through adjacent layers and therefore potentially leading to short circuits or a lack of full QD coverage on the underlying active pixel area, as this might lead to parasitic emission if the electron and hole recombine on e.g. one of the CTLs.
Luckily however, the QDs provided by IAP showed near perfect films on all investigated substrates being glass, ZnO and pTPD. Therefore also the QD layers in devices based on pTPD (conventional) and ZnO (inverted) are expected to be smooth. The respective AFM images can be found in the appendix in table A.2. It can be seen that all layers do show some small agglomerates or pin holes in the film, the overall difference between the peak height of an agglomeration and the mean thickness level of the total film however does not exceed a ca. 30 nm. With the top layers of TCTA or 3TPYMB in inverted or conventional devices being thicker than 50 nm, no problems are expected from this side.
The device stability of QDLEDs is still one of the biggest challenges requiring further research on InP based QDs. While however typically *device lifetime* is defined by so called L_{70} or L_{90} times, which characterize the amount of hours a LED can be operated under certain biases until they reach a fraction of 70 % or 90 % of the original luminance, in the context of this thesis, *device lifetime* is more related to the fact, that several measurement sweeps can be run consecutively without already drastically decreasing the LED EQE. The AFM images predict this to be the case, as e.g. agglomerates would lead to

leakage paths which would heat up during operation and thereby damage large parts of the QD layer. And indeed, the electrical performance of all device provided by IAP was stable in the forementioned definition of stability. To prove this, a measurement routine involving an initial jVL measurement, an Impedance Spectroscopy (IS) measurement routine over ca. 15 min and a subsequent repeated jVL measurement were conducted at all devices presented in this section. The exemplary result of a conventional device with HC103 as emissive layer is shown in figure 7.4.

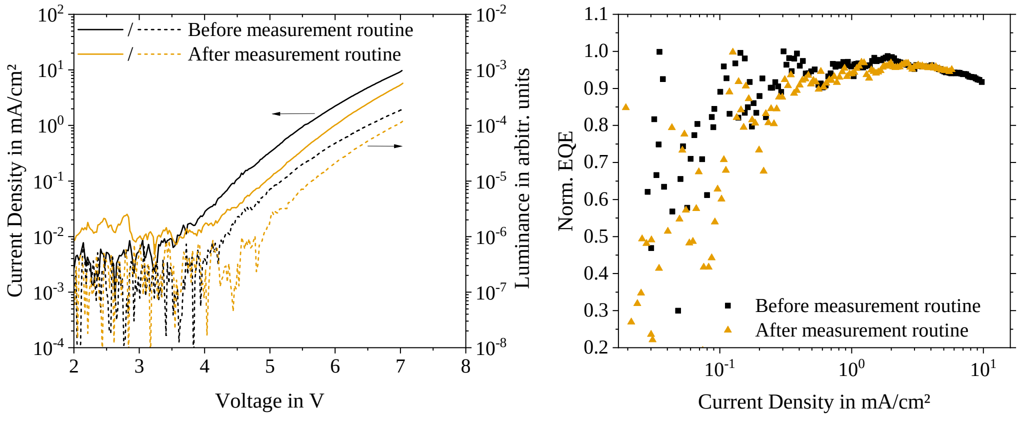

(a)

(b)

Figure 7.4.: jVl- (7.4a) measurements and calculated normalized EQE (7.4b) of a conventional IAP QDLED. The CTLs show degradation, the emitter performance is however unaffected by the previous measurement routine.

Here, a few things are to note. Firstly, from a purely experimental point of view, the jVL measurement setup described in section 3.2 could not be used for samples received from IAP due to the largely different sample layout. Therefore, all jVL measurements shown in this chapter were taken with PAIOS, which offered more flexibility in terms of measurable sample size. This firstly leads to the fact that the measurement of leakage currents at voltages below V_{bi} cannot properly be resolved as the system sensitivity was too low in this regime. Furthermore, the system's luminance detection was not calibrated and adapted to the specific IAP sample design as well. Therefore, the luminances and resulting EQEs can not be given in absolute units anymore. In fact, luminances and EQEs from different samples should no longer be compared - only luminances from several consecutive measurement runs without changing the sample alignment can be quantitatively compared to each other.

The mentioned measurement routine was done without changing any experimental alignment, so this latter precondition for the data shown in figure 7.4 is met. The jVL plot clearly shows, that the sample characteristics do in fact change through operation, as both the current density and the luminance are reduced after the prolonged routine. The efficiency shown in figure 7.4b however reveals, that this change in sample performance is not caused by emitter degradation, as the EQE stays constant. In fact, one big well known issue of device lifetimes - in the sense of L_{90} like explained above - is the degradation of the CTLs much rather than actual QD emitter degradation [193–196]. Although this is a crucial point for commercial applications of QDs, it will not be covered in detail in this thesis. Regardless, the IAP device performance can be considered stable over the course of electrical operation as was performed during this work.

7.1.2. Photoluminescence spectroscopy

TRPL is a powerful tool to investigate on the luminescent properties of different emitter classes. As a starting point, the pure QD material received from IAP was dissolved in toluene and deposited on precleaned glass substrates. After encapsulation under nitrogen atmosphere, these samples were excited at 405 nm and the transient PL data was recorded with the streak camera system described in the methods part of this thesis. Exemplary data for HC100 is shown in figure 7.5.

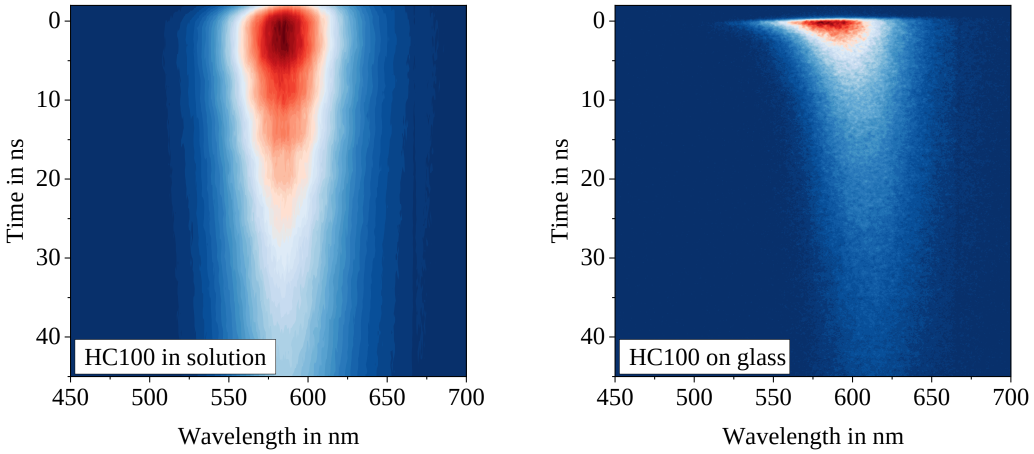

(a) (b)

Figure 7.5.: TRPL data of QD in solution(7.5a) and on a glass substrate (7.5b). Note that for the sake of clarity, a time range of approximately 50 ns is shown here, while the actual measurement range was close to 200 ns.

As can be seen, QDs behave quite differently in solutions and in thin films. Firstly, the lifetimes of QDs in thin films are significantly shorter compared to their solution counterparts. This is commonly seen in colloidal NC, as close proximity of QDs to each other opens up additional loss channels, which are only accessible in the closely packed solid film but not in the strongly diluted solution case. Furthermore, the solution data shows a uniform emission band between approximately 525 nm and 625 nm, while the emission in the thin film case shifts towards lower wavelengths at longer times. To further illustrate this effect, the data shown in figure 7.5b was split into 2 ns wide time windows and the resulting spectra are plotted in figure 7.6.

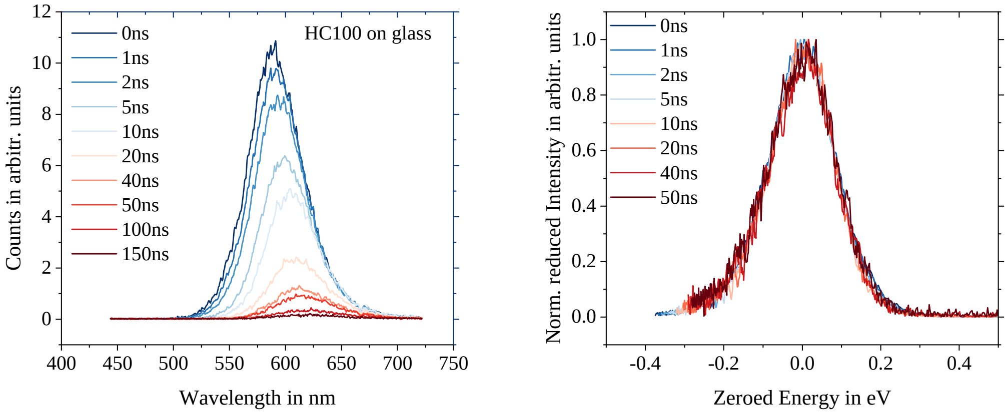

(a) (b)

Figure 7.6.: Integrated spectra over a 2 ns time span at different time marks (7.6a). For instance, the spectrum marked as 20 ns was integrated between 19 and 21 ns of the raw data shown in figure 7.5b. Gaussian fits of these spectra were conducted in the energy-space and the spectra were renormalized and shifted by their fitted central peak position in figure 7.6b. The emission profile does not broaden over time.

The spectral redshift can clearly be seen at longer times. Furthermore, the single spectra shown in figure 7.6a were normalized individually and wavelength shifted by their central peak position determined by a gaussian fit. Note that the gaussian fits were conducted with converted spectra, as the theory behind the gaussian fits requires intensity-vs.-energy $I(E)$ rather than intensity-vs.-wavelength data $I(\lambda)$. Therefore, $I(\lambda)$ was converted to $I(E)$ according to the description in the literature and the determined gaussian fit peak positions were used to generate the plot in figure 7.6b [197].

For the explanation of the observed redshift in emission during the first tens of ns, one has to consider the nature of the emitters. QD ensembles, as were used in these samples, have a non-uniform size distribution and therefore have a certain FWHM of the resulting emission. QDs with stronger charge carrier confinement, mostly smaller particles, will emit at lower wavelengths than their weaker confinement, larger counterparts. The observation of a redshift over time can either mean that the larger subspecies' emission is simply slower than the lower wavelength part or that the optical energy of the smaller QDs is transferred to their larger counterparts. If the former were the case, then the FWHM of the spectra in figure 7.6a would significantly decrease as the blue part of the spectrum would cease emitting quickly and the red part of the spectrum would emit for a longer time. However, figure 7.6b clearly shows that this is not the case. The FWHM of 0.171 ± 0.005 eV - representing the width of the single spectra - stays constant over the whole measurement range. Therefore, the transient redshift visible in the IAP QDs can be attributed to energy transfer between QDs. Additionally, this is backed up by the fact that the transient solution spectra do not show the redshift. Here, the interparticle distance is larger due to the dilution in toluene so that this effect does not come to play. Furthermore, this shows that the energy transfer has a short range so that for example also photon recycling processes cannot be the main cause of this effect while short range processes like for instance Förster Resonance Energy Transfer (FRET) are expected to be responsible for the shift.

So far, the data shown was exclusively gained from HC100 containing samples. Their respective HC103 counterparts however showed very similar results in all here presented methods. Therefore, only the final result in figure 7.7a is shown here, which illustrates the quasi identical redshift in both device types. This is however to be expected. As mentioned earlier, the cores of HC100 and HC103 are supposed to be identical, therefore the optical properties are supposed to be at least similar as well. Unfortunately, the TEM images in the previous section revealed, that although HC103 QDs are *on average* larger than HC100, the smaller fraction of QDs are in fact identical for the two batches. With the just mentioned presumption of a short range energy transfer like FRET being responsible for the shift, of course especially the small QDs are prone to lose their excitation energy. Large shells automatically ensure a Core-to-Core distance of adjacent QDs of at least twice the shell radius r. Förster-type energy transfer efficiency scales with r^6, so that the larger particles, which is where HC100 and HC103 strongly differ from each other, only play a minor role for this effect [198]. The smaller particles however, which are identical for the two materials, efficiently lose their energy in both sample types, which explains the observations being similar for the two materials.

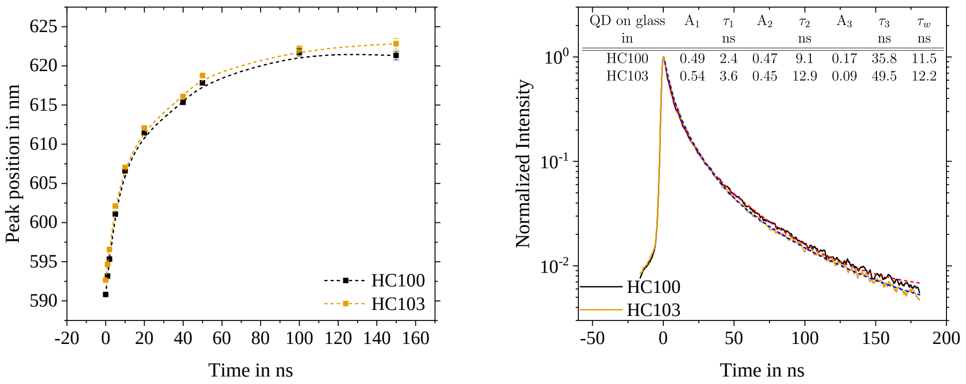

QD on glass in	A_1	τ_1 ns	A_2	τ_2 ns	A_3	τ_3 ns	τ_w ns
HC100	0.49	2.4	0.47	9.1	0.17	35.8	11.5
HC103	0.54	3.6	0.45	12.9	0.09	49.5	12.2

(a) (b)

Figure 7.7.: Redshift in IAP QD on glass TRPL spectra over the first 150 ns after the laser excitation (7.7a) Dashed lines serve as a guide to the eye.
Transient data of HC100 and HC103 integrated over the whole emission range (7.7b). Dashed lines are triexponential fits. The weighed lifetime τ_w was calculated as $\tau_w = \sum_i A_i \tau_i$.

7.2. PLQE determination of QDLEDs during electrical operation

As was described earlier, the PLQE is the optical efficiency of an emitter. A measurement setup was built during the course of this work to determine the PLQE during operation which allows to exclude efficiency losses originating from elsewhere in the device. As was described in more detail in section 3.5, this setup cannot record absolute quantum yields however. Therefore as a starting point, these absolute PLQY measurements without electrical bias were conducted in an integrating sphere. Note that in this thesis, the terms of *PLQY* and *PLQE* will be used to differentiate between absolute and relative PL efficiencies, respectively. Any PLQY data shown will originate from an integrating sphere, all PLQE data was recorded using the new measurement setup. Note furthermore, that this is not common practice in the literature, where the two terms are usually used synonymously [199].
The idea of the PLQY experiment is to optically excite an emitter while detecting all irradiated PL signal independent of the emission angle of the photons. The combination of the resulting dataset and a reference set without the emitter inserted into the sphere then allows to calculate the energy absorbed and emitted by the emitter. The ratio of these two values will then yield the PLQY. These measurements were conducted by Ms. Roshini Jayabalan and Mr. Tassilo Naujoks, to whom the author is grateful. Unfortunately however, the signal quality was rather poor for spin coated and drop cast thin films due to the low absorption and emission, so that the best results were obtained from QD solutions, as is shown below in figure 7.8a. The two types of QDs are both close to 20 % PLQY in an unbiased state.

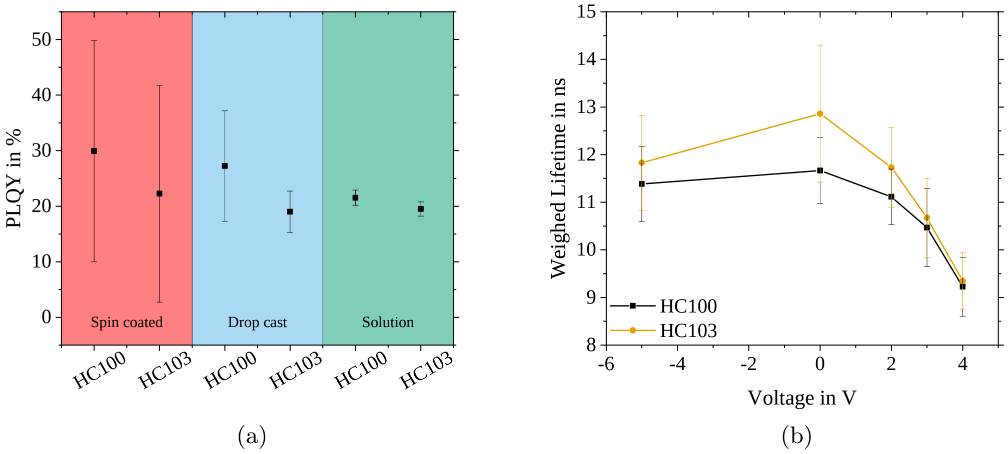

(a) (b)

Figure 7.8.: Steady state PLQY results (7.8b) and weighed excited state lifetimes at different operating biases 7.8b of inverted IAP QDLEDs.

Furthermore, the TRPL transient data shown in figure 7.7b can be fitted by exponential functions according to equation 3.5, although a tri-exponential approach is necessary to adequately describe the measurement data. This method of characterization has been used in the literature and the three decay times are usually attributed to charge transfer processes between the core and trap states, charge neutral emission from the core and slower trap emission, respectively [200]. The three lifetimes determined from the fits in figure 7.7b were weighted with their relative amplitude to generate an effective weighted lifetime value, which is shown in figure 7.8b. The combination of unbiased absolute PLQY measurement, biased relative PLQE measurement and lifetime determination allows to calculate radiative and nonradiative rates for the QDLEDs. These can be used to determine the dominant efficiency loss mechanisms during electrical operation present in those devices, which will be covered in this section. Firstly, the effects of an applied reverse bias will be studied, as here no diode currents are expected to influence the emitter efficiency and therefore the electric field alone can be assumed responsible for the emitter efficiency loss. Furthermore under reverse bias conditions, the electric field distribution can be considered uniform across the whole stack due to the absence of screening from free charge carriers. From that point on, investigations on forward biases will be demonstrated, which include the injection of charges into the device. The present charge carrier density therefore has to be additionally included in the PLQE loss considerations.

7.2.1. Electric field effects on the QD performance

As was described in the theoretical part of this work, the electric field can mainly have two effects on the QD performance. Exciton dissociation can occur, where the charge carriers forming an exciton in the QD core get separated and exctracted from the NC. This leads to an increase of the nonradiative rate in the transient lifetime measurement, since an additional nonradiative decay channel is enabled through the electric field. Additionally, the Quantum Confined Stark Effect (QCSE) can come into play. Here, the electron and hole wavefunction overlap is reduced due to the applied external electric field as is shown in figure 6.5. This leads to a reduced intensity in PL experiments and a redshift of the overall emission with a reduced radiative rate k_r. This section will cover the investigations on which of these two effects is the dominant efficiency loss mechanism in IAP QDLEDs.

To start the investigations, the QDs were embedded in 30 nm thick Poly (methyl methacrylate) (PMMA) layer, which in turn was sandwiched between two electrodes. That way, electrical currents through the device are blocked by the insulating polymer while the electric field can still affect the QD PL emission. Additionally, the dilution of QDs in the polymer matrix leads to a larger interparticle distance compared to pure QD films. Therefore, the short range energy transfer processes described previously do not play a significant role here.

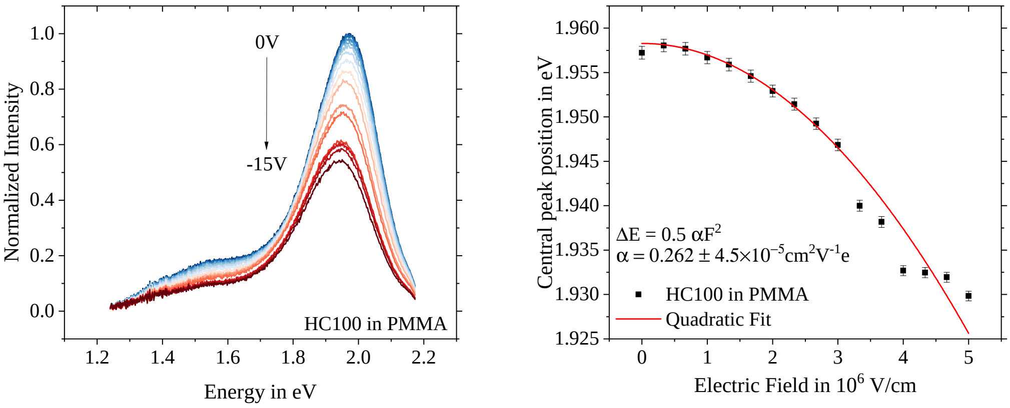

(a) (b)

Figure 7.9.: PL spectra of QD embedded in a PMMA matrix at applied biases between 0 V and −15 V (7.9a) and fitted central gaussian peak positions (7.9b). The red fit was calculated according to equation 6.10.

There are a few things to note in figure 7.9. Firstly, the QD emission at approximately 1.9 eV in figure 7.9a is accompanied by a low energetic parasitic emission tail. Therefore, the following analysis was only conducted between 1.8 and 2.2 eV. This data was approximated by gaussian fits and the central peak positions are plotted in figure 7.9b against the applied electric field F. As is illustrated, the data follows the expected quadratic behaviour predicted by the QCSE. Furthermore, the overall emission intensity decreases with increasing electric field as well. Therefore the IAP QDs can be considered susceptible to the QCSE, which reduces the PLQE with increasing electric field.

Subsequently, similar experiments were conducted with the QDLEDs received from IAP. Here, the QDs in films without any matrix material are used as EMLs, which reduces the interparticle distances. Furthermore, the QDs are in close contact to the CTLs. The results of the four samples containing HC100 are shown in figure 7.10.
In contrast to the formerly shown data from the PMMA device, in the QDLED devices all emission peaks shift towards higher energy values. Their respective PL spectra can be found in the appendix in table A.3.
The first way to explain the blueshift is to assume, that the single crystal emission of every QD itself is shifted towards the blue. This however is unreasonable, as it is contradicted by the expectations from the QCSE, which were confirmed previously. The cause of the blueshift therefore has to be in the QD ensemble or the CTLs.
As was explained earlier, the QD layer consists of an inhomogeneous mixture of smaller (*more blue*) and larger (*more red*) QDs. Keeping this in mind, the observed blueshift can be caused by either an enhancement of *blue QD* emission or a suppression of *red QD* emission. Given the overall loss of intensity with increasing bias, only the latter case makes sense - the red QDs somehow are subsequently quenched with increasing bias.

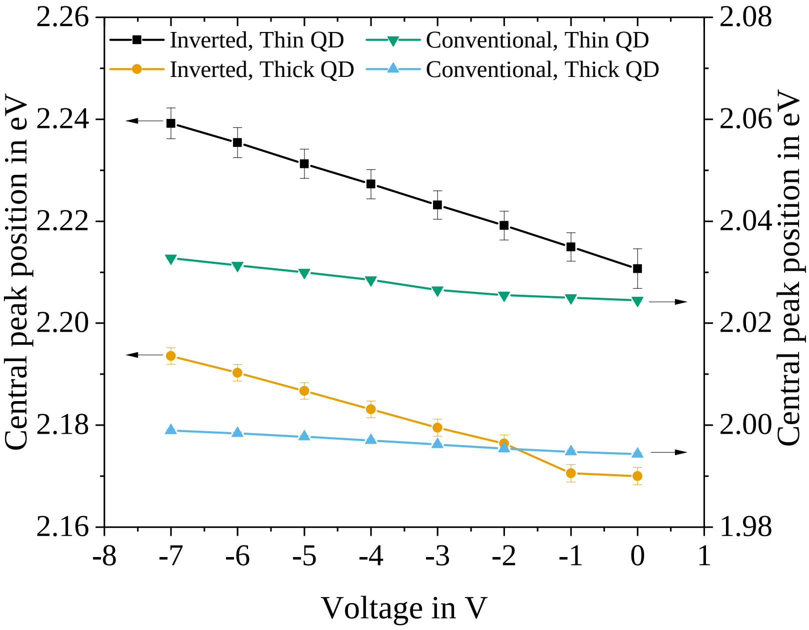

Figure 7.10.: Fitted peak positions of HC100 containing QDLEDs. Both inverted and conventional devices show an increase in emission energy upon application of an electric field.

A potential explanation for this quenching is the field induced QD ionization by exciton dissociation. Studies have shown that a sufficiently high applied bias can lead to mobile charge carriers in QDLEDs even without the injection of said particles [137, 171]. The idea here is that the electric field leads to charge transfer of a valence band electron of one QD to the conduction band of a neighbouring QD according to equation 7.1.

$$\mathrm{QD} + \mathrm{QD} \leftrightharpoons \mathrm{QD}^{+} + \mathrm{QD}^{-} \tag{7.1}$$

This field ionization can then lead to the formation of excitons and subsequent EL after several of these bipolar charge generation steps. While the electric fields are however too low to generate EL in the QDs studied during this thesis, a similar process might explain the observed spectral blueshift. Herein, photoexcitation leads to the formation of excitons on QDs. These electron-hole-pairs can be generated either in the respective QD core or at the core-shell interface, with one charge carrier on the core and the other on the shell material. Under these circumstances, even comparably low electric fields can suffice to transfer charges from one QD to another. Furthermore, this process can be accelerated by the presence of energetically lower trap states induced by e.g. insufficient coating of the core with the shell material. If at some point, exciton dissociation leads to two charged - or ionic - QDs, these QDs' efficiencies are reduced due to processes like Auger quenching.

In fact, this effect of charged QDs is a well known problem in QD single crystal spectroscopy and is typically referred to as *blinking*. The light emission of QDs here is being turned off and on repeatedly dependent on the presence or absence of additional charge carriers on the QDs [201]. Finally, the observed blueshift can then be explained by a process, where QDs are being turned dark by additional charge carriers. Since the formerly mentioned *red QDs* form a deeper energetic trap than their respective *blue* counterparts due to their smaller band gap, it is not surprising to see a disproportionately higher fraction of red QD being dark. Therefore the total QD ensemble emission is shifted towards the blue side of the electromagnetic spectrum.

With the cause of the observed overall blueshift seen in figure 7.10 determined, another significant observation can be made in this figure. The slopes of both inverted device stacks containing ZnO are much steeper than the slopes of the ZnO-free conventional stacks. Furthermore, the thin inverted device in turn shows a steeper slope than the thicker QD layer device. This however fits nicely into the argumentation presented above. Namely, the QDs are in close proximity to the ETL consisting of Zn^{2+} and O^{2-} ions. Therefore, charge transfer processes from or to QDs additionally occur and accelerate the formation of charged QDs according to equation 7.2.

$$\begin{aligned} \mathrm{Zn}^{2+} + \mathrm{QD} &\leftrightharpoons \mathrm{Zn}^{+} + \mathrm{QD}^{+} \\ \mathrm{O}^{2-} + \mathrm{QD} &\leftrightharpoons \mathrm{O}^{-} + \mathrm{QD}^{-} \end{aligned} \tag{7.2}$$

For the thin QD monolayer, every QD is located at the ZnO interface, while for thicker layers only a fraction of QDs is in contact to the ETL. Therefore this secondary charging effect is more pronounced, the thinner the QD layer. This then explains the steeper slope of the thin QD layer compared to its thicker counterpart.

Furthermore, this secondary source of ionization in general seems to significantly outweigh the field induced autoionization the conventional devices show. While this might be advantageous for e.g. optical sensing applications, the influence of the ZnO layer on the performance of a QDLED especially under forward bias needs further clarification. More on this topic can be found in the subsequent sections of this thesis.

So far, the dominant quenching mechanism under reverse bias conditions could not yet be clarified. The QDs clearly show signs of the QCSE when dispersed in a PMMA matrix. Therefore, the QDs themselves are susceptible for the effect.

The increasing blueshift at increasing negative bias in QDLEDs however can rather be explained by exciton dissociation and charged QDs. To solve this contradiction, another approach to distinguish between the two mechanisms was taken. As was described in more details in section 6.2, exciton dissociation increases the nonradiative decay rate k_{nr} since an additional nonradiative decay channel is available. Field quenching induced by the QCSE by contrast reduces the electron-hole wavefunction overlap, which reduces the radiative rate k_r. Calculation of k_r and k_{nr} should therefore determine the dominant loss process.

This can be achieved by the combination of absolute PLQY–, relative PLQE– and excited state lifetime τ measurements. These results were partially already shown in figure 7.8. The missing data of the relative PLQE is furthermore plotted in figure 7.11.

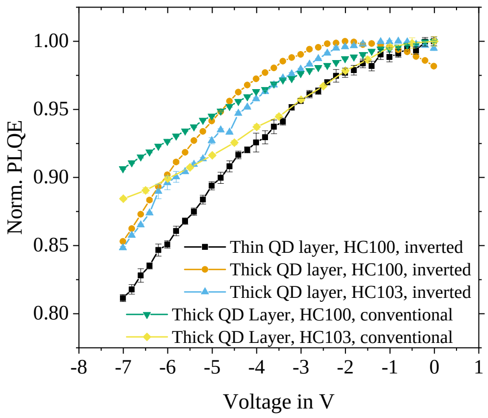

Figure 7.11.: Relative PLQE measurements of IAP QDLEDs under reverse bias conditions

Starting from equations 2.15 and 2.16, the two distinct rates can be expressed as

$$k_r = q \cdot \tau^{-1} \tag{7.3}$$

$$k_{nr} = (1 - q) \cdot \tau^{-1} \tag{7.4}$$

with the product of absolute PLQY and relative PLQE q from figures 7.8a and 7.11. Note that for this calculation, the absolute PLQYs from solution were used as the thin film PLQYs had problems with a bad signal-to-noise ratio due to the too thin layer thickness. Furthermore, the influence of the *Purcell-factor* F was neglected in this calculation. Since however the stacks of the inverted QDLEDs with thick QD layers are identical, the respective Purcell factors should also be very similar. This however leads to a not perfectly quantitative result for the radiative rates.

The result of the voltage dependent rate determination can be found in the appendix in figure A.7. Firstly, the assumptions made seem to hold as the radiative rates are in the range of 10^7 to 10^8 s^{-1}, which fits nicely to the literature [202]. Unfortunately however, the respective error bars are quite large. This can be explained by the comparatively large uncertainty in the excited state lifetime, which arises through the triexponential fit and subsequent weighing procedure. This error then propagates into figure A.7 and complicates the loss process determination. In fact, the radiative rates stay essentially constant under reverse bias, while the nonradiative rates slightly increase. This would serve as another indication for exciton dissociation present in both HC100 and HC103 containing inverted devices. However, as was just mentioned, the error bars significantly exceed both trends so that this statement has to be taken with caution. Note that the results of the analogous investigations on conventional devices are not shown, as the error bars also outweigh any physically safe statement to be made from this data set.

Eventually, therefore the question on the dominant loss mechanism in IAP QDLEDs under reverse bias can not be answered easily as there is no clearly dominant process. The QDs have shown to be susceptible to both the QCSE and exciton dissociation under different conditions. The spectral shifts in PMMA host devices clearly show the QCSE while the same QDs in LEDs show a spectral blueshift by charged QDs caused by exciton dissociation. This effect can occur if ionizable materials are in in close vicinity to the QDs and is therefore enhanced in inverted devices containing a ZnO ETL. Determination of radiative and nonradiative rates in principle points towards a dominant exciton dissociation, however the uncertainty of measurement data is too large to safely prove this.

7.2.2. Current induced quenching in QDLEDs

The previous section has shown the electric field effect on the performance of QDLEDs. This section, by contrast, shall elucidate the quenching processes under forward bias. This means that above the built-in voltage V_{bi} of around 2 V, charge carriers get injected into the QDs and ideally EL occurs. This emission can however be quenched by the charge carriers by processes like Auger quenching (AQ), as were described in section 6.2.3.

At first, the model proposed in the theoretical part of this work to describe the effiency losses during operation will be discussed, while the second part of this section will then compare the experimental data with the theoretical predictions.

Theoretical modelling of current induced efficiency losses in QDLEDs

Starting point for the modelling, which was in parts adapted from references [203, 204], is equation 6.14, which can be written the following way

$$q = \frac{k_r}{k_r + \sum\limits_i k_{nr,i}} = \frac{k_r}{k_r + k_{SRH} + k_{Field} + k_{Auger}} \tag{7.5}$$

with the nonradiative Auger-, field induced- and trap assisted quenching rates k_{Auger}, k_{Field} and k_{SRH}, respectively.

It was shown in the previous section, that the QD efficiency is significantly quenched at high electric fields. An applied voltage of -7 V leads to a relative loss of approximately 8 to 18 % depending on the device under investigation. However, similar to the argumentation made in the OLED part of this thesis in section 5.1.1, the effective internal field needs to be considered. Internal flat band conditions, and therefore the absence of an effective electric field, are reached at V_{bi} of approximately 2 V. Excluding the mobile charges' screening effect, the magnitude of the effective electric field V_{eff} can be expressed by $V_{eff} = |V_{applied} - V_{bi}|$, so that, for instance, the effective electric fields at applied biases of $+7$ V and -3 V are comparable. The amount of field quenching at -3 V is however only a few percent, while the amount of charge carrier induced quenching at 7 V is significantly higher as will be shown later in this section. Furthermore, as was already mentioned, mobile charge carriers furthermore screen the electric field effect from the QDs so that the effective field should be even lower. These considerations allow a first simplification of equation 7.5: k_{Field} can be considered negligible under forward bias operation.

The resulting formula can then be expressed by the ABC-model described in the theoretical part of this thesis:

$$q = \frac{k_r}{k_{SRH} + k_r + k_{Auger}} = \frac{Bn^2}{An + Bn^2 + Cn^3} \tag{7.6}$$

If we now consider the SRH process, we can furthermore simplify the theoretical model. SRH recombination dissipates the excitation energy via trap states at the InP core. Firstly, all QDs covered in this work had a Core-Shell-Shell structure so that the trap density at the Core interface is significantly reduced compared to Core-only QDs. And secondly, according to the simulations shown in figure 6.7, SRH typically plays a significant role at low charge carrier densities, while the higher current regimes are dominated by other processes.

These two assumptions allow to additionally neglect k_{SRH} in equation 7.6, which then simplifies to:

$$q(n) \approx \frac{k_r}{k_r + k_{Auger}} = \frac{Bn^2}{Bn^2 + Cn^3} = \frac{B}{B + Cn} \tag{7.7}$$

If we then furthermore use the rate equation defining the device current at high current densities according to equation 6.13

$$j_{total} \propto -\frac{dn}{dt} = C_{SRH} \cdot n + C_{Rad} \cdot n^2 + C_{Auger} \cdot n^3 \approx C_{Auger} \cdot n^3 \tag{7.8}$$

with the constants for SRH- , radiative and Auger recombination C_{SRH}, C_{Rad} and C_{Auger}, respectively, then the charge carrier density n is proportional to the device current j via:

$$n \propto j^{1/3} \tag{7.9}$$

Combination of equations 7.7 and 7.9 finally yields

$$\frac{q\,(j)}{q_0} = \frac{B}{B + Cn} = \frac{B}{B + Cj^{1/3}} = \frac{1}{1 + Dj^{1/3}} \tag{7.10}$$

with a normalization constant q_0 which resembles the PLQE where no current induced quenching occurs and a fitting parameter D without direct physical meaning.

This formula can now be used to fit experimental data gained from the bias dependent PLQE measurement setup. However, the model relies on the mentioned assumptions. Discrepancies between data and fit can therefore be caused by several factors:

- Equations 7.7 and 7.9 approximate both the device current and the overall dominant loss mechanism as governed by Auger processes. If this is not the case, the model can not be applied successfully to the data.
- This also includes the possibility, that the observed current density range is too low to be dominated by Auger quenching.

- Furthermore, other current limiting processes can cause problems for the applicability of this model. Especially field dependent charge carrier mobilities can be the origin of further challenges. In particular here, the focus should be put on the ZnO layers, as - additionally to the electronic currents - also ionic currents of, e.g., Oxygen vacancies in the crystal lattice can change the layer properties. This is not included in the model and would require more future research into this topic. Furthermore, the migration of ions in this layer can lead to interface dipoles as well as altered injection barriers, which furthermore complicate the data analysis [143, 144, 205].

- SRH recombination was completely neglected in this model. While this seems to be a reasonable approximation for the QDs presented during this work, other QDs structures might not fulfill this requirement.

Application to experimental data of QDLED

The QDs investigated in this work were intended to be used in QDLEDs. Therefore, the light emission is supposed to be generated by electrical excitation by the injection of charges into the devices. Here, the manufacturer's experience has shown, that the inverted device architecture yields better results with respect to both the device efficiency as well as the maximum luminance. Unfortunately, the samples do physically not fit into the calibrated measurement system at the group. Although the PAIOS system can be used to record basic jVL characteristics, the luminances and therefore EQEs cannot be quantitatively compared to each other due to the missing calibration. Although the data therefore will not be shown in this thesis, the luminance onset was slightly below 2 V for all inverted devices.
This agrees with the onset of the exponential current, which is measured simultaneously with the optical PLQE in the field dependent measurement setup. The result of the inverted HC100 sample with a thicker QD layer is shown in figure 7.12.
Figure 7.12a shows, that the PLQE slightly drops with increasing bias until approximately 1.8 V. Then, the PLQE drops more quickly as the charge carrier density increases exponentially. This PLQE decline then continues until the maximum voltage of 5 V, which was kept intentionally rather low in order to not degrade the samples.
Plotting the same data against the current density resulting from the applied voltage in figure 7.12b now allows to fit the data with the theoretical model described in equation 7.10. It clearly shows a great match between the experimental data and the theoretical fit. Therefore, also the assumptions made above can be considered reasonable and Auger quenching can be regarded mostly responsible for the efficiency drop under forward bias.

To further test this hypothesis, equation 7.8 was used to calculate the respective device currents, which can be attributed to SRH recombination, radiative recombination and Auger quenching.
A layer thickness of 10 nm was used to translate the charge carrier density flow dn/dt into a current density j and the total current was plotted together with the three sub-

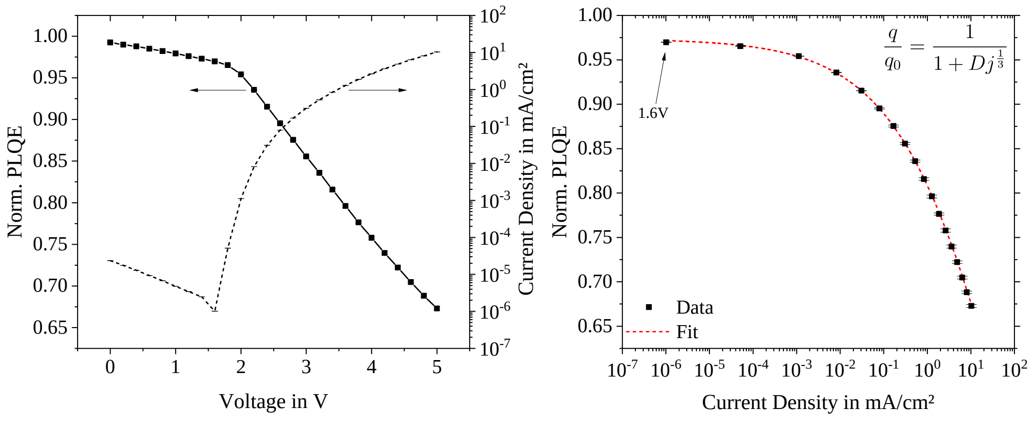

(a) (b)

Figure 7.12.: Field dependent PLQE of a thick HC100 QD sample in an inverted device stack. Plotted against applied voltage (7.12a) and concurrent current density (7.12b).

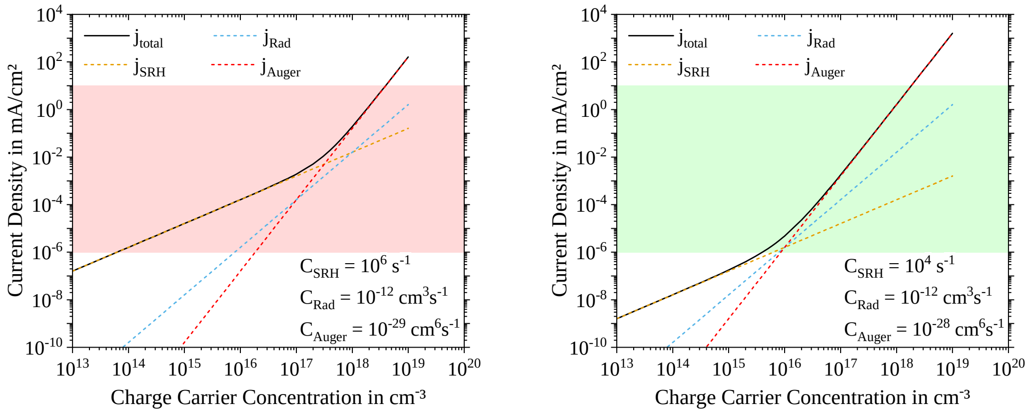

(a) (b)

Figure 7.13.: Simulated current density vs. charge carrier concentration plots. A layer thickness of 10 nm was used for calculations of the different partial and total currents. Simulation with perovskite reference (7.13a) and Core-Shell-QD adapted coefficients (7.13b) [203, 204, 206].

components it consists of. Both figures 7.13a as well as 7.13b feature a highlighted area, which marks the region where data points from figure 7.12b are available. The differences between the two subfigures lies in the C-parameters given in the lower right corners of the respective image. Figure 7.13a shows parameters typically used for perovskite based LEDs, where this analysis technique was adapted from [203, 204, 206]. The black total current density curve is mostly dominated by SRH recombination while only at carrier concentrations above approximately 10^{17}cm^{-3}, Auger currents become dominant. This would obviously contradict the assumptions made in the theoretical modelling described above, however as was already mentioned, the respective research leading to figure 7.13a is based on perovskite LEDs. Therefore, the constants need to be adjusted accordingly. One change in figure 7.13b was made to C_{SRH}. Since the dedicated Core-Shell structure is specifically designed to minimize the trap density in the NC, a reduction of approximately two orders of magnitude seems reasonable. Furthermore, the surface-to-volume ratio of the NC plays a significant role for the trap density in NCs [207]. With the spherical symmetry of the colloidal QDs with respect to the cubic perovskite NC, the trap density can safely be assumed to be smaller in the particles investigated. Furthermore, the Auger constant C_{Auger} was replaced by a typical value from respective colloidal QD literature of $10^{-28}\,\text{cm}^6\text{s}^{-1}$ [178]. Keep in mind however, that C_{Auger} is dependent on both the temperature and the QD size, as was explained in section 6.2.3. With this better fitting set of parameters, the total current density in figure 7.13b is mostly dominated by Auger currents in the observed range from figure 7.12b with only small deviations below 10^{-5} mA cm^{-2}. This furthermore proves the assumptions made earlier and the dominating loss mechanism during electrical operation in these devices is identified as Auger quenching.

Subsequently, the same measurements were conducted with both inverted and conventional stacks with either a thick HC100 or HC103 layer as EML. The results of the analysis can be found in figure 7.14.

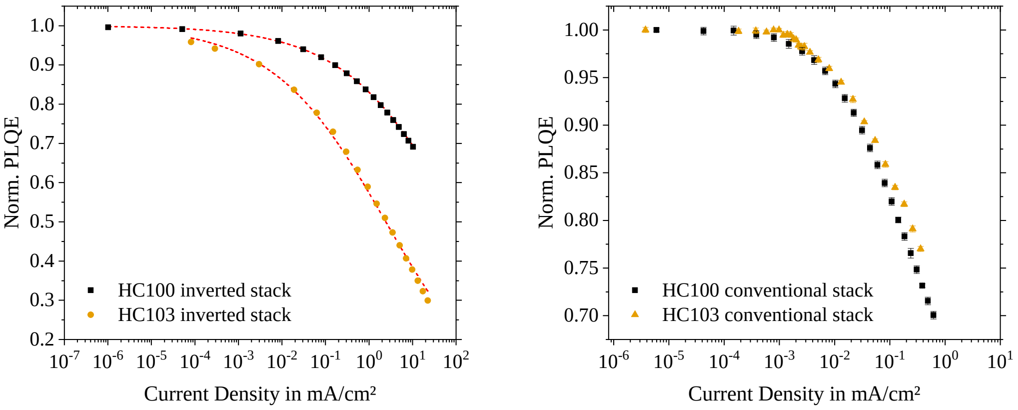

(a)

(b)

Figure 7.14.: Current dependent PLQE of thick HC100 and HC103 QD samples in inverted (7.14a) and conventional (7.14a) device stacks. Red dashed lines represent fits according to equation 7.10. The data and fits were renormalized in figure 7.14a to match a q_0 of exactly 1.

The theoretical model can be applied well to both inverted stacks, as is shown in figure 7.14a. Auger quenching is the dominant loss process in inverted devices, independent of the used QD material.

Unfortunately however, the same can not be said about the conventional stacks. Here, no fits are drawn, as the data cannot be represented well by equation 7.10. This shows, that the assumptions leading to the model can not be applied in this case. In particular, the Auger limited current is not given here and the quenching is therefore not mainly dominated by AQ.

Interestingly enough though, there is also not a statement to be made, on which type of QD performs better under electrical operation in general. While HC100 shows the better efficiencies in inverted devices, no real difference between the two species could be detected in conventional devices.

The difference between the two QDs is that the shell thickness *on average* is larger for HC103 than for HC100. The smallest particles present are identical for the two batches while the difference lies in the broader size distribution of HC103. If we now take into account, that the electronic confinement for electrons and holes is different in the core and shell, respectively, we can explain the difference in optical performance in different stacks [208].

According to this publication, holes are mostly confined to the core, while electron wave functions can spread into the shell more easily. Inverted devices are typically electron dominated, meaning that more electrons than holes are present at the EML. At sufficiently high biases, the electrons can acess the QDs and will therefore either be confined in the core or the shell. In the case of HC103 however, the shell is larger so that the probability of multiple electrons per QD is increased. This in turn enables nonradiative pathways over X^{n-} charged excitons as was described in section 6.2.3, so the efficiency decreases disproportionally faster in HC103 compared to HC100.

By contrast, the more balanced or even hole dominated conventional devices do not show this difference. Even if multiple holes are present in the QDs, there is no significant difference between the two subspecies of materials as the holes are strongly confined to the respective cores, which are identical in the two compared materials.

Regardless, this difference in QD performances in inverted and conventional devices shows a pathway to optimize QDLEDs for future work. The straightforward optimization of QDs alone is not sufficient to guarantee an improved device efficiency, as the device stack and QD properties need to be adjusted with respect to each other. One type of QD might be superior in one device stack, while being inferior in another. This opens up a multitude of combinations on how to obtain optimized efficiencies. A starting point for further research might for example be the investigation of different formulations of ZnO, potentially doped with other metal ions like Mg^{2+}. This is known to reduce the electron conductivity and might therefore suppress non-radiative recombination events [209].

7.3. Charging of QDLEDs

One of the biggest challenges while working with any kind of QDLED was the lack of quantitative reproducibility of measurement data. Previously in figure 7.4b, the normalized EQEs of two subsequent measurement runs were shown, which showed no major device degradation. Although this kind of reproducible behaviour in electrical efficiency measurements was observed independently of the device architecture and QD type, interestingly, all devices showed behaviour strongly dependent on the sample operation history in the optical efficiency.
The first point where this becomes clearly evident is a relative PLQE measurement without any applied bias. Results of exemplary experiments are shown in figure 7.15a.

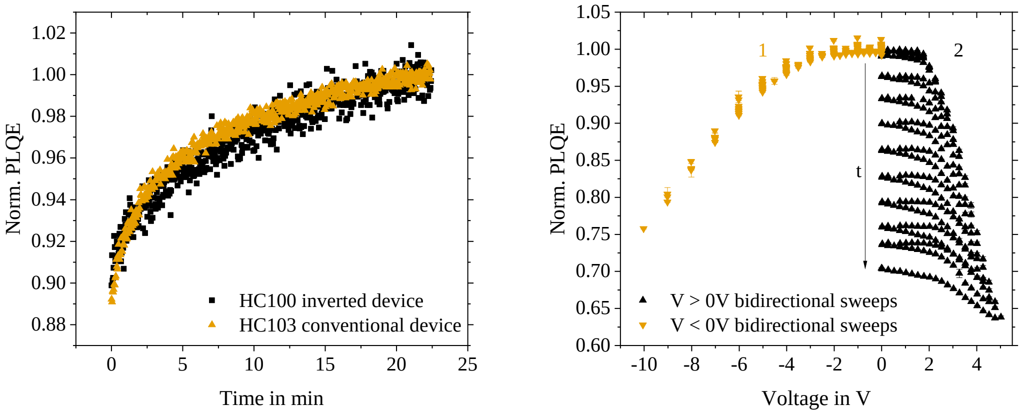

(a) (b)

Figure 7.15.: Initial PLQE increase with InP QDLEDs when turning on the laser without application of any bias (7.15a).
Multiple bidirectional sweeps starting and ending at 0 V with ascending maximum bias (7.15b) according to figure 7.16a.

The PLQE changes significantly over the course of minutes, which makes quantitative analysis of device PLQEs as it was shown in the previous sections difficult. This is due to the fact, that a standard PLQE characterization also takes place in the timespan of approximately 10 to 30 min depending on the respective experimental parameters. Therefore, the potential quenching due to the applied bias or current density is convoluted with the observed PLQE increase over time.
In order to circumvent this issue, all PLQE data from QDLEDs previously shown in this thesis was recorded after the sample had undergone a pretreatment similar to the unbiased experiment in figure 7.15a unless stated otherwise. The overall influence of this pretreatment effect can then be reduced and analyses like shown in the previous sections can be made. Notably, this effect of an initial PLQE increase is not to be confused with the term of *positive aging*, which has been reported in the literature and typically describes the EQE enhancement observed after several days of shelf-storage [210–212].

This effect is attributed to an anhancement of electron injection through a chemical reaction between ETL and electrode and is specifically not what will be described in this thesis.

In order to investigate on this initially increasing PLQE further, different experimental approaches were designed to illustrate the dependence on the device operation history. Firstly a measurement routine, which will be labelled *birectional* in the course of this thesis, should help shed light on the conditions under which the device operation history matters. It consists of measurement sweeps starting from 0 V to a maximum bias, after which the sweep direction is reversed and data points back to 0 V are collected. Subsequently, the formerly maximum voltage is increased and the procedure was repeated. A schematic depiction of this routine is shown in figure 7.16a.

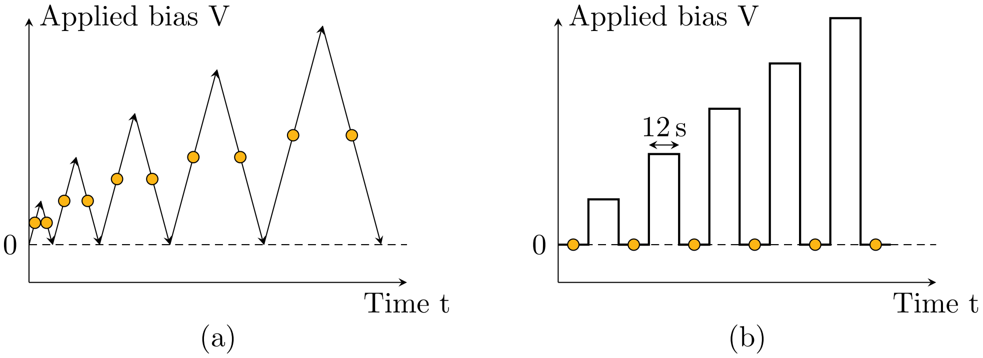

(a) (b)

Figure 7.16.: Schematic representation of different measurement procedures used at the field dependent PLQE setup. The orange circles represent the paths where measurement data was recorded.
Subfigure (a) shows the so called *bidirectional* measurement routine, where the maximum applied voltage is increased after each consecutive run. Note that every orange circle does therefore correspond to a multitude of data points between 0 V and the respective maximum bias.
Subfigure (b) shows the routine used to compare capacitive and optical data. Since all datapoints are collected at 0 V after a bias was applied, this measurement routine will be referred to as *preconditioning* measurements.

This birectional sweep measurement exemplarily was applied to an inverted HC100 QDLED and the result is shown above in figure 7.15b. It is important to note that at first, the bidirectional PLQE measurement was conducted in reverse bias direction until a maximum applied voltage of −10 V, only whereafter the positive biases were covered up until a peak bias of +5 V.

It is shown, that this bidirectional measurement method does not largely influence the PLQE under reverse bias conditions. The PLQE is rather stable with small deviations inbetween the consecutive runs which can be explained by the prolonged laser irradiation and the consequent PLQE increase over time according to the results shown in figure 7.15a. The PLQE drop therefore can be considered completely reversible under negative biases.

Coming to positive voltages in figure 7.15b, it is evident that the PLQE drops during electrical operation with increasing applied voltages. This is not surprising and has been covered in the previous section of this thesis. However, the sweeps from the respective maximum voltages back to 0 V show unexpected non-reversible behaviour. After crossing a threshold voltage, the PLQE cannot fully recover back to its maximum value and has a residually lowered value. Figure A.8 in the appendix shows four single bidirectional sweeps to further illustrate this point. In this case, the threshold voltage lies between 2.5 V and 3 V, so it can be assumed to be approximately 2.75 V. This explains the ladder-like graph under forward bias shown in figure 7.15b.

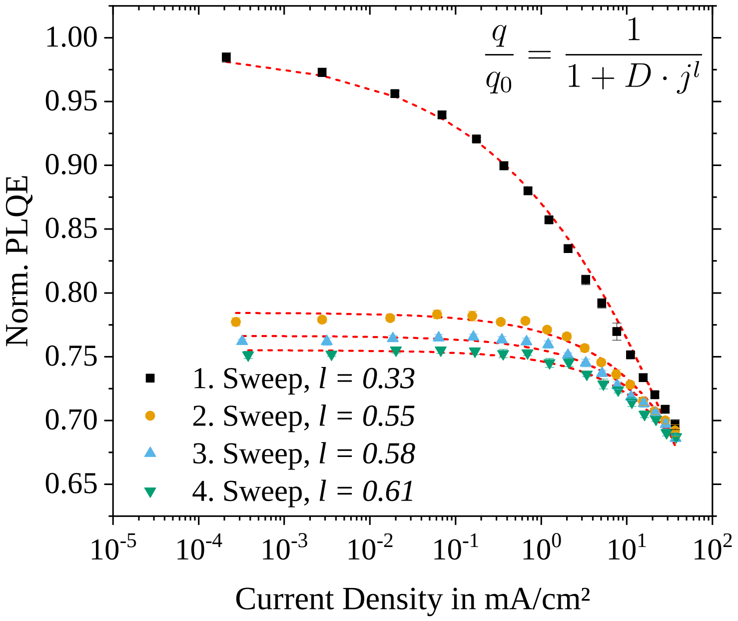

Figure 7.17.: Multiple consecutive PLQE sweeps from 0 V to 5 V of inverted HC100 QDLEDs. Red dashed lines are fits according to an adapted formula 7.10 given in the inset. The l- as well as the q_0- and D- parameters change over the course of the experiment, the changes in - for example - l should therefore not be directly attributed to any physical processes happening.

Similarly, also the current dependent plot of a different experiment shown in figure 7.17 shows the residual drop present after operation of the QDLEDs. Here, a sweep from 0 V to 5 V was run repeatedly and the resulting data was plotted against the resulting current density. Fitting according to equation 7.10 cannot work however, as the model does not include the residually reduced PLQE. A simple generalization however can help fitting the data according to

$$\frac{q}{q_0} = \frac{1}{1 + D \cdot j^l} \tag{7.11}$$

with an phenomenologically introduced fitting parameter l. Note that this parameter does not correspond to any physical quantity, however with $l = 1/3$ equations 7.10 and 7.11 are identical and AQ can be considered dominant once again.

Fitting the data from figure 7.17 clearly shows that the residual quenching heavily influences the PLQE of any measurement after the first. Four different subsequent measurements yield four different fitting parameters according to equation 7.11. While the first sweep can be nicely modelled by equation 7.10 with $l = 1/3$ indicating Auger quenching as described previously, all subsequent datasets show a superposition of Auger quenching and a convoluted effect. The model of exclusive Auger quenching by injected charge carriers therefore does not hold any longer.

For the explanation of these observations, another look at the theoretical description of loss mechanisms presented in section 6.2 can help:
Due to the nature of the measurement setup, excitons – bound electron-hole pairs – are generated exclusively in the EML, as the excitation energy is too low to be absorbed in the transport layers. If the PLQE is prolongedly reduced after electrical operation even in the LED off state at 0 V, then an additional quenching source must be present. SRH recombination and any kind of field induced quenching can however not be the cause of this effect as otherwise the PLQE would also have to non reversibly drop after applying negative biases, which it clearly does not. Therefore, Auger quenching has to be responsible for the efficiency loss again – even without further injection of charges. In the simplest case, AQ is a three particle process where charged excitons transfer excitation energy into heat. If the PLQE therefore is reduced in the off state, this leads to the conclusion, that a larger fraction of QDs in the EML are charged after operation compared to the prior state. Electrical charges injected into the EML at high bias would then be trapped with reduced voltages and remain on the QD to residually reduce the overall PLQE.

A powerful tool to investigate on charge carrier dynamics typically is impedance spectroscopy (IS) as it was done e.g. in chapter 5 of this work. Unfortunately however, the respective measurements did not yield reliable results during electrical operation. The devices did not show capacitive behaviour at negative biases with a phase shift between applied AC voltage and recorded AC current of far lower than the expected 90°. Furthermore, figure 7.15b shows that the onset of charging is at a higher bias than V_{bi} and the exponential current onset so the devices cannot be considered capacitive in this regime either.
Therefore, a second experimental routine labelled as *preconditioning experiment* was designed to investigate on this effect further despite no possiblity to measure CV characteristics directly.

Here, a reference measurement was taken without application of an electrical bias. Subsequently, the bias is increased for 12 s whereafter another reference measurement at 0 V was conducted. Following this, the bias is increased to a higher value followed by another reference 0 V measurement. These steps are then being repeated, a schematic illustration of the measurement routine can be found in figure 7.16b. The crucial point in this type of measurement is that the data is always recorded without an applied bias, which allows to specifically probe the residual changes in the device. In particular, this experiment was conducted with both CV- and relative PLQE measurements, which allows to correlate optical and electrical changes prior to and after operation.

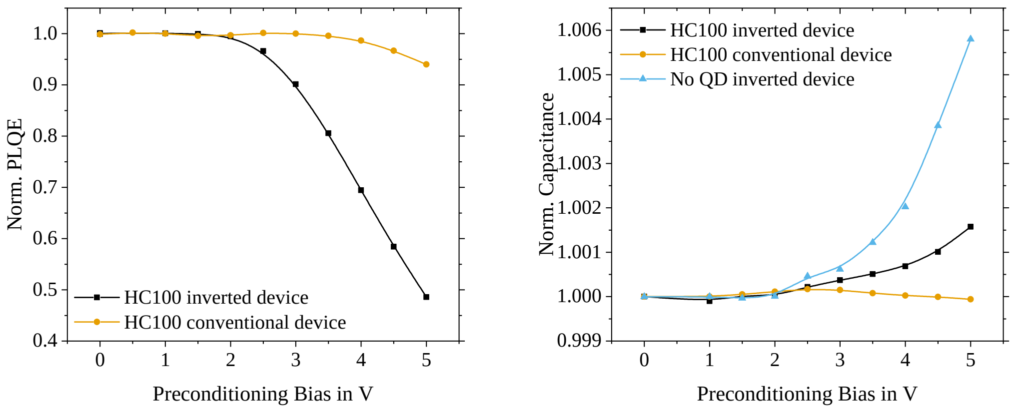

(a)

(b)

Figure 7.18.: Preconditioning measurements with the relative PLQE (7.18a) and Capacitance (7.18b) plotted against the formerly applied voltage. Again, note that all data points were recorded at 0 V with only a preconditioning bias applied prior to the measurement.

The PLQEs in figure 7.18a show the expected trend of a residual drop above V_{bi}. The threshold voltage for the inverted device is in fact lower than it was observed earlier in the previous measurements, which can be explained by the longer operation time per applied voltage. Regardless, the drop does only start well above the onset of the exponential current, which is at ca. 1.6 V according to figure 7.12a. The data from the conventional device shows a less pronounced drop with a larger threshold voltage of approximately 4 V, which is however not surprising as the current densities in general are lower in this device architecture. Also, the exponential current onset is only at approximately 3.5 to 4 V as is shown in figure 7.4a.

The capacitance measurements in figure 7.18b on the other hand show a quite different image. Firstly, the conventional device does not show any significant change after operation. This means, that a PLQE drop can also occur without the capacitance changing and the two observables can be independent from each other. The two inverted devices containing a ZnO ETL however show an increase in capacitance starting at the threshold voltage predicted by the PLQE measurement. This leads to the conclusion, that the capacitance change, if observed, enhances the PLQE decrease.

This can in parts be explained in analogy to the reverse bias quenching behaviour discussed in section 7.2.1. QDs in the vicinity of the ZnO ETL can more easily transfer charges from or to the transport layer according to equation 7.2. Together with the generally higher current densities in inverted devices, the stronger change in the respective *preconditioning* experiments can be expected to occur. The change in capacitance can then be qualitatively explained by the change of electronic transport properties in the EML and ETL.

Furthermore, the capacitance increase also occurs in the reference device without any QD EML. This means, that the processes leading to the capacitance increase are not necessarily coupled to the presence of QDs and happen in pure ZnO layers as well. One hypothesis would therefore be the migration of ions in the layer, which leads to interfacial charges. Figure 7.19 schematically sketches the outcome of this process.

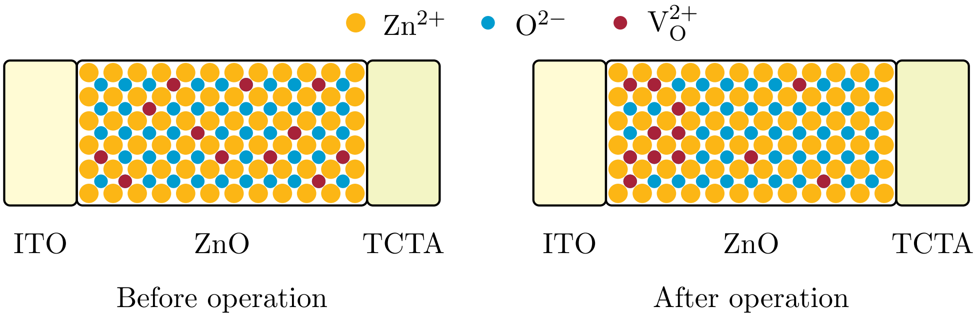

Figure 7.19.: Schematic representation of operation induced ion migration in ZnO ETLs. During electrical operation, the externally applied electric field causes migration of negatively charged oxygen ions away from the ITO-ZnO interface towards the neighbouring TCTA or QD layer. After turning the device off, the ions do not immediately migrate back to their original positions and form charging centers for adjacent QDs.

In this simplified figure, the case of the inverted device without QD EML is displayed. For the sake of clarity, the ZnO layer is represented by a rock salt crystal lattice type of zinc (Zn^{2+}) ions with either oxygen (O^{2-}) ions or oxygen vacancies V_O^{2+} inbetween the metal ions. Note that in reality ZnO typically has either a zinc-blende or wurtzite crystal structure [213].

Prior to operation, the oxygen vacancies are randomly distributed across the whole ZnO layer. During operation however, electrons get injected into the layer due to the externally applied electric field. This constant electric field then drives oxygen ions towards the TCTA HTL and, accordingly, the oxygen vacancies towards the ITO interface. Although an argument can be made, that the injected electrons would accumulate at the ZnO–TCTA interface due to the injection barrier, which would in turn attract V_O^{2+}, this effect would only reduce the amount of ion migration observed in the ZnO layer. Migration of oxygen vacancies towards the TCTA interface would however require electric field inversion in the layer, which can be excluded since under this conditions the electrical current would be changed as well. Eventually, after the electrical bias is removed, ions and vacancies move quite slowly compared to the biased case so that the increased O^{2-} density close to the HTL interface remains [143]. In the case of an actual QD containing device, these charged sites can then act as charge acceptors in turn charging the QDs. This way, the overall PLQE of the QDLED is reduced. Furthermore, the oxygen deprived part of the ZnO ETL has a more metallic character compared to the rest of the layer. The electrical conductivity across the ETL should therefore no longer be considered constant with the oxygen-poor area being more conductive. This can also be modelled by an in fact thinner semiconducting layer which explains the observed increase in capacitance according to formula 2.10.

Discussion and evaluation of the charging effect in QDLEDs

As was shown, PLQE measurements at InP-based QDLEDs lead to a strong dependence of the data on the sample operation history. The PLQE is dramatically reduced upon repeated operation. The EQE on the other hand does not change, so degradation of QDs as source of the effect can be excluded.

A physical model was proposed in figure 7.19 which can explain the observed optical and impedance data, however clearly more research is needed to test and confirm the hypothesized idea of oxygen vacancy migration in ZnO layers as main source of QD charging and subsequent PLQE reduction. Although no comprehensive study on the microscopic processes or the dependence of the residual charging on other experimental parameters could be performed during the course of this work, a starting point for these investigations is to test the overall reversibility of this procedure, as pure ion migration should be a completely reversible process. For this matter, the inverted HC100 sample was used as a reference stack. A pretreatment according to figure 7.15a was applied to the device, whereafter a voltage sweep was recorded. Subsequently, the bias was removed (0 V) and the PLQE was measured for a prolonged time. The result of this experiment can be seen in detail in the appendix in figure A.9a. It shows, that the formerly reached PLQE could not be regained for this sample even after a time span of close to 16 h, whereafter the measurement was manually aborted.

The data situation in this particular case does unfortunately not allow comprehensive conclusions. Firstly, even after the 16 h of constant measurement, a slight positive gradient in the PLQE was observed. One has to assume that 16 h are therefore not sufficient to recover the PLQE and a longer experimental duration would have yielded a different result. This however is highly impractible in a shared laboratory, so that a statistical study in this regard is barely possible. Furthermore, a different sample – fabricated and measured approximately one year earlier – underwent the same procedure of pretreatment, subsequent electrical operation and 0 V PLQE recovery, where a complete PLQE recovery was observed already after 1 h. These results are shown in figure A.9b.

The difference between the two presented samples lies exclusively in an altered ZnO ETL. This further proves the relevance of the exact ZnO composition and processing conditions. It was already described in the theoretical part of this work, that the macroscopic properties of ZnO, like for instance the electrical conductivity, can vary over several orders of magnitude depending on the processing conditions. This therefore strongly agrees with the data presented here, where also different ZnO formulations lead to varied performances. Unfortunately however, the author does not have any details about the microscopic differences between the two ZnO layers, so no further conclusions can be drawn except the fact that there is a strong dependence between ZnO and QD performance.

It is quite clear, that the understanding of involved processes is far from complete. In particular, a systematic future study with different well defined formulations of ZnO can help to elucidate the interplay of interfacial properties and QD performance. Furthermore, the dependence of ion migration on the surrounding temperature can potentially clarify the details of the microscopic processes. Cryogenic conditions should significantly slow down the transfer of oxygen vacancies in the ETL so that a lower degree of residual quenching after operation would be expected under these conditions. On the same note, soft annealing of the QDLED at elevated temperatures after operation could also be used to redistribute the oxygen vacancies in the ZnO. Both approaches of thermal experiments as well as ZnO compositionial variations should be covered in future works to comprehensively explain the observed data. Only then, more information about the proposed model can be gained and a deeper understanding of the effect of ZnO on the optical QD performance can be reached.

Coming back to the application of QDs in electrically operated LEDs, one important question to settle is the influence of the observed residual charges during operation. If the charged QDs stayed charged even after repeated operation, the overall efficiency would decrease with each run. Luckily however, this is not the case as was already shown in figures 7.4a, 7.15b and 7.17. Further proof can be found in the data recorded prior and after the 16 h recovery treatment mentioned earlier. This is plotted – dependent on both the applied voltage and the resulting current density – in figure 7.20.

Figure 7.20a once again shows the residually reduced PLQE at 0 V starting from 1 to approximately 0.81 after operation and the subsequent recovery over 16 h from 0.81 to 0.94. Figure 7.20b on the other hand illustrates that, plotted against the applied current density, the respective fits according to equation 7.11 in fact only differ in their normalization constant q_0. Therefore, it can safely be assumed, that the dominant quenching mechanism during operation – at high current densities and luminances – is not influenced by the residual charging effect observed here. Furthermore, this clearly shows that the operation at high current densities is independent of the residual charges priorly observed. This fits nicely into the image of charge carriers, which cannot escape their energetic trap on the QD, and therefore residually reduce the optical efficiency without bias. During operation however, the QDs are constantly being charged and discharged anyways, which leads to the dominant loss mechanism of Auger quenching, so that the residual charges from prior operations do not significantly reduce the overall performance. This then explains the reversibility of subsequent EQE measurements while the respective PLQEs strongly differ.

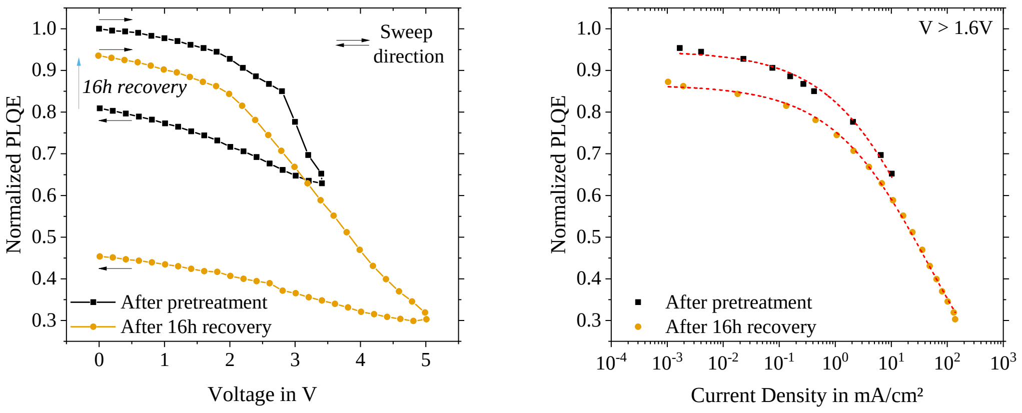

(a) (b)

Figure 7.20.: Voltage- (7.20a) and current density dependent (7.20b) plot of the PLQE data from an inverted HC100 device prior to and after a 16 h recovery routine. Figure 7.20b only shows the datapoints in forward sweep direction. Red dashed lines represent fits according to equation 7.11 with exclusively different q_0 parameters for the two data sets.

Summarizing, this on the hand means, that the charging issue can mostly be disregarded when using the QDs as light emitters in LEDs. The electrical efficiency is the most important figure of merit in this application field, which is not reduced by this effect. On the other hand however, the observed residual charging can be of crucial importance in other types of applications like for instance QDs in sensors or solar cells, where only low current densities are reached during operation. Under these conditions – if high current densities were applied priorly – the altered optical properties open up formerly unaccesible loss pathways, which can reduce the device performance.

Part IV.

Summary and Outlook

Summary

During the course of this work, a measurement setup was designed to determine the relative PLQE changes of thin film LEDs during electrical operation. This includes both reverse bias as well as forward bias conditions. While similar learnings can also be gained from bias dependent excited state lifetime measurements, the here proposed measurement routine has the advantage of a higher degree of automation and a significantly reduced experimental measurement time, which is crucial for samples susceptible for degradation. Also, the use of a lock-in amplifier leads to a very low noise level and well defined signals. Furthermore, the post-experimental data analysis does not need large computational power and the results can be viewed even during the measurement already. Disadvantages however also arise from the nature of the experiment. Due to the signal detection via a photodiode, only integral information of the emission spectrum is recorded while the wavelength resolution is lost. This would be particularly useful for samples, where spectral shifts at different operational conditions are expected. Furthermore, the resulting PLQE data is to be considered exclusively as relative, absolute efficiency measurements are not possible in the current state.

It was shown, how the setup can be used in various thin film LEDs to deepen the understanding of physical processes during operation and in the off-state.

Organic light-emitting diodes

In unpolar OLEDs, the setup was used to identify TPQ as dominant efficiency loss mechanism in Irppy$_3$ containing LEDs. At low current densities, additionally charge balance issues were found to reduce the EQE. The PLQE setup could however be used to optically determine the point of charge balance, which emphasizes the need of optical analysis for comprehensive descriptions of OLED efficiency loss processes.

Polar OLEDs additionally showed the influence of a GSP present in the device, which leads to hole accumulation below the luminance turn on. The charge carriers introduced into the emitter vicinity can act as quenching centers for excitons and thereby reduce the PLQE. This additional source of quenching could also be detected with the PLQE setup. The degree and onset of sub-turn on PLQE reduction coincides with the respective data from purely electrical impendance spectroscopy results. In the investigated stack design with a mCBP-CN host matrix, this sub-turn on quenching strongly distinguishes guest molecules of second generation phosphorescent (Irppy$_3$) and third generation TADF (DMAC-TRZ) molecules. The inferior performance of Irppy$_3$ can however be deduced from the energetically deeper HOMO levels with respect to the applied host material, which leads to a more efficient charge carrier trapping in Irppy$_3$ compared to DMAC-TRZ. These trapped charges then can dissipate excitation energy, so that the PLQE is reduced. However, these results should not be misinterpreted to prove the general superiority of DMAC-TRZ over Irppy$_3$ as emitter in OLEDs. Comparisons of the emitters in a different stack more optimized for Irppy$_3$ than DMAC-TRZ as it was done here might very well lead to contrary results. This is further backed up by the EQEs of the two devices during operation, which are very well comparable.

Additionally, the effect of polar layers and a resulting GSP on the PLQE of Irppy$_3$ was investigated with a set of samples received from TUD. Here it once more was shown how the PLQE setup can be used to reliably detect sub-turn on quenching, which is significantly increased with the introduction of a polar TPBi host compared to an unpolar reference. It was shown, that substrate heating during the deposition of polar molecules like TPBi reduces the overall layer GSP, which then reduces the sub-turn on quenching. The heating however could not fully remove the GSP, as the degree of sub-turn on quenching was still clearly larger than in unpolar samples.

Furthermore, the optical setup could be used to quantiatively determine the size of a GSP with respect to reference measurements with an unpolar sample. Here, both electrical Kelvin probe and optical PLQE data agree nicely. This however is strongly dependent on the mentioned unpolar reference sample. Therefore, absolute GSP measurements are not always possible at the current state – only shifts of the PLQE maximum can be used to quantitatively deduce the size of the GSP.

By analysing the bias dependent PLQE, the dominant loss mechanism in the Irppy$_3$ containing samples received from TUD could be determined to be TPQ as well. However, this is only true for large current densities. At lower current densities, the effect of current induced TPQ is convoluted with the effect of hole accumulation caused by the GSP. Therefore, the TPQ model proposed in the literature to exclusively describe the optical efficiency losses during operation should be extended to also respect charge carrier densities from other sources like e.g. the mentioned hole accumulation.

Quantum dot light-emitting diodes

Investigations on QDLEDs were conducted with samples received from IAP. Two different kinds of InP/ZnSe/ZnS QDs were used with nominal changes in the outer shell thicknesses. TEM images revealed that the thickness growth occurred inhomogenously so that the nominally larger shell QDs possess a slightly broader particle size distribution while the smallest particles for both batches are identical. Accordingly, hardly any differences in the optical and electrical performance could be detected throughout the thesis.

Investigations regarding their PLQE were conducted with the QDs under reverse bias conditions in both light-emitting devices as well as diluted in an insulating PMMA matrix. The polymer matrix experiments showed PLQE quenching by the QCSE with the characteristic spectral redshift and emission intensity drop with increasing electric field strength. However, all LED investigations showed contrary results with an observed blueshift accompanied by an intensity loss with increasing reverse bias. This apparent contradiciton can be ascribed to the higher QD density in the respective LED compared to the polymer-host device. Electric fields can induce exciton dissociation in closely packed QD ensembles where charge carriers are transferred between two adjacent QD leaving both of them in a charged and thereby optically less efficient dark state. Since the fraction of larger, more-red emitting QDs act as deeper energetic traps compared to their smaller, more-blue emitting counterparts in the ensemble, relatively speaking, the more-red emission is quenched stronger resulting in a net blue shift of the LED PL emission. This leaves the investigations regarding reverse bias efficiency losses in an ambiguous state where neither the QCSE nor exciton dissociation can be clearly identified as dominant efficiency loss mechanism. Furthermore, also deductions from calculated radiative and non-radiative rates only show a slight indication towards exciton dissociation being dominant, although the experimental uncertainty is too large to fully allow comprehensive conclusions.

The theoretical *ABC-model*, typically used to describe efficiency losses in inorganic emitters, could be used as a starting point to explain the dominant quenching mechanism under forward bias conditions. Comparisons between theoretical predictions and observed experimental data allowed to identify the three particle process of Auger quenching as dominant loss mechanism in inverted QDLEDs containing a ZnO ETL. Here, the results for the two types of QD in fact varied, as the larger shell QD showed a more pronounced quenching which corresponds to a worse performance. This is caused by an oversupply of electrons during operation due to the high electric conductivity of ZnO. Since electrons – in contrast to holes – can energetically spread into the respective shell comparatively easily, charging of QDs with one or multiple electrons is enhanced for larger shells. Therefore the efficiency is reduced compared to a smaller shell particle where less electrons can be available. This is backed up by the results of conventional devices without the inorganic ZnO layer, where the two types of QD show comparable performances.

One of the largest challenges while working with InP QDs was the lack of quantitative reproducibility of experimental data. While the electrical performance, the EQE, was constant upon repeated operation, the optical PLQE data turned out to be highly dependent on the sample operation history. Even prior to operation, ongoing unbiased measurements recorded a significant increase in PLQE so that every sample had to be pretreated in order to deconvolute this effect and potential bias dependent quenching processes as discussed above. Furthermore, repeated operation above a threshold voltage well above the luminance turn-on bias residually reduced the subsequent unbiased PLQE. This effect occurred in all investigated devices, however the ZnO containing inverted LEDs additionally showed a change in residual capacitance after electrical operation. A model was proposed to describe the experimental findings, which includes electric charges which are trapped on the QDs even after operation. Vicinity to inorganic layers without well defined stochiometry and with the potential of oxygen (vacancy) migration enhances the efficiency reduction. Oxygen vacancies migrate, driven by the electrical bias, towards the ITO cathode, which leaves more negatively oxygen ions at the interface to the EML. These charged sites can contribute to the charging of QDs and thereby stabilize dark energetic states, which residually reduces the PLQE.

In the context of applications in LEDs, this observed charging effect is not expected to play a major role. The amount of residually charged QDs is quickly outweighed by the charging and resulting Auger quenching during electrical operation, so that the charging effect of residually reduced PLQE should not impede QD applications in, for instance, smartphone displays. Attention has to be paid in other field of interest however, where only lower current densities are expected.

Outlook

Although the experimental PLQE setup has proven to be a valuable tool to investigate on the physical processes happening in thin film LEDs, it has not reached its full potential yet. For instance, an automated variation of the excitation intensity could be implemented to be able to investigate on non-linear effects or e.g. multiexcitons. Similarly, a simultaneous absorption measurement could be added to the recorded set of data in order to gain more information about the respective sample in a single measurement run. Lastly at its current state, the setup is only fit to measure samples under ambient conditions. Integration of a cryostat structure into the setup would then allow to remove the need for encapsulation and, more importantly, allow access to thermally controlled experimental conditions where processes like for instance the formerly described low temperature ion migration or the soft thermal annealing in ZnO layers can be investigated on further.

This is one crucial point regarding future work on QDLEDs. The interplay of inorganic metal-oxide layers and emissive nanocrystals should be elucidated in more detail to better understand the charging effect and the caused residual efficiency loss.

Additionally, the here presented experimental findings should be reproduced as simulations. This is especially true for the case of polar host OLEDs, where the observed plateaulike PLQE over a wide range of operational current densities should be connected to the macroscopic device performance. This is currently under investigation and soon to be published. Additionally, the literature model of TPQ in phosphorescent OLEDs should be extended to also pay respect to charge carriers which are present due to carrier accumulation rather than injection.

APPENDIX A

Appendix

List of abbreviations in alphabetical order

Materials

3TPYMB	Tris(2,4,6-trimethyl-3-(pyridin-3-yl)phenyl)borane
Al	Aluminium
Alq$_3$	Tris-(8-hydroxychinolin)-aluminium
Au	Gold
CBP	4,4-Bis(9-carbazolyl)-1,1-biphenyl
CdSe	Cadmium selenide
DMAC-TRZ	9,10-Dihydro-9,9-dimethyl-10-(4-(4,6-diphenyl-1,3,5-triazin-2-yl)phenyl)acridine
DPEPO	Bis[2-(diphenylphosphino)phenyl]ether oxide
HAT-CN	1,4,5,8,9,11-Hexaazatriphenylenehexacarbonitrile
InP	Indium Phosphide
Irppy$_3$	Tris[2-phenylpyridine]iridium(III)
ITO	Indium tin oxide
LiF	Lithium fluoride
mCBP	3,3-Di(9H-carbazol-9-yl)-1,1-biphenyl
mCBP-CN	3,5-di(9H-carbazol-9-yl)-(1,1-biphenyl)-3-carbonitrile
MoO$_x$	Molybdenum oxide
PEDOT:PSS	Poly(3,4-ethylenedioxythiophene) polystyrene sulfonate

PMMA	Poly (methyl methacrylate)
$P(SiMe_3)_3$	Tris(trimethylsilyl)-phosphine
pTPD	Poly(4-butylphenyldiphenylamine)
T2T	2,4,6-tris(biphenyl-3-yl)-1,3,5-triazine
TCTA	Tris(4-carbazoyl-9-ylphenyl)amine
TmPyPB	1,3,5-tri(m-pyridin-3-ylphenyl)benzene
TPBi	2,2',2"-(1,3,5-Benzinetriyl)-tris(1-phenyl-1-H-benzimidazole)
ZnO	Zinc oxide

Miscellaneous

AFM	Atomic Force Microscopy
AQ	Auger Quenching
CB	Conduction Band
CTL	Charge Transport Layer
CV	Capacitance-Voltage
DFT	Density Functional Theory
DOS	Density of States
EIL	Electron Injection Layer
EL	Electroluminescence
EML	Emitting Layer
EQE	External Quantum Efficiency
ETL	Electron transport layer
FRET	Förster Resonance Energy Transfer
FWHM	Full Width at Half Maximum
GSP	Giant Surface Potential
HBL	Hole Blocking Layer
HIL	Hole Injection Layer
HOD	Hole Only Device
HOMO	Highest Occupied Molecular Orbital
HTL	Hole Transport Layer
IAP	Fraunhofer Institute for Applied Polymer Research
IS	Impedance Spectroscopy
ISC	Intersystem Crossing

jVL	Current-Voltage-Luminance
LED	Light-Emitting Diode
LUMO	Lowest Unoccupied Molecular Orbital
MIS	Metal-Insulator-Semiconductor
NC	Nanocrystals
OLED	Organic Light-Emitting Diode
OSC	Organic Semiconductors
PAIOS	Platform for All-In-One characterization of Solar cells and OLEDs
PDM	Permanent Dipole Moment
PL	Photoluminescence
PLQE	Photoluminescence Quantum Efficiency
PLQY	Photoluminescence Quantum Yield
QCSE	Quantum Confined Stark Effect
QD	Quantum Dot
QDLED	Quantum Dot Light-Emitting Diode
QE	Quantum Efficiency
rISC	Reverse Intersystem Crossing
SCLC	Space Charge Limited Current
SMU	Source Measure Unit
SOC	Spin-Orbit Coupling
SOP	Spontaneous Orientation Polarization
SRH	Shockley-Read-Hall
TADF	Thermally Activated Delayed Fluorescence
TCLC	Trap Charge Limited Current
TDM	Transition Dipole Moment
TEM	Transmission Electron Microscopy
TPQ	Triplet-Polaron-Quenching
TRPL	Time Resolved Photoluminescence
TTA	Triplet-Triplet Annihilation
TUD	Technische Universität Dresden
VB	Valence Band

Energy levels of all used materials

Material	HOMO in eV	LUMO in eV	Workfunction in eV
Electrode materials			
Al			-4.1
Ag			-4.2
Au			-4.8
ITO			-4.9
PEDOT:PSS			-5.1
LiF			-3.7
MoO_x			-6.8
Ca			-2.87
Hole conductors			
HAT-CN	-9.9	-6.0	
TCTA	-5.7	-1.6	
mCBP	-5.71	-1.77	
mCBP-CN	-6.1	-2.5	
CBP	-5.69	-2.27	
HLX-026	-5.55	-2.69	
pTPD	-5.2	-2.4	
Electron conductors			
T2T	-6.5	-3.0	
TPBi	-6.2	-2.7	
DPEPO	-6.3	-2.1	
ETM-036	-6.46	-3.14	
3TPYMB	-6.8	-3.3	
TmPyPB	-6.75	2.75	
ZnO	-7.6	-3.8	
Emitters			
Irppy$_3$	-5.3	-2.8	
DMAC-TRZ	-5.61	-3.1	
QD (IAP)	-5.3	-3.3	

Table A.1.: HOMO / LUMO energies and workfunctions for all materials used in this thesis

Device Stacks and Energy level diagrams

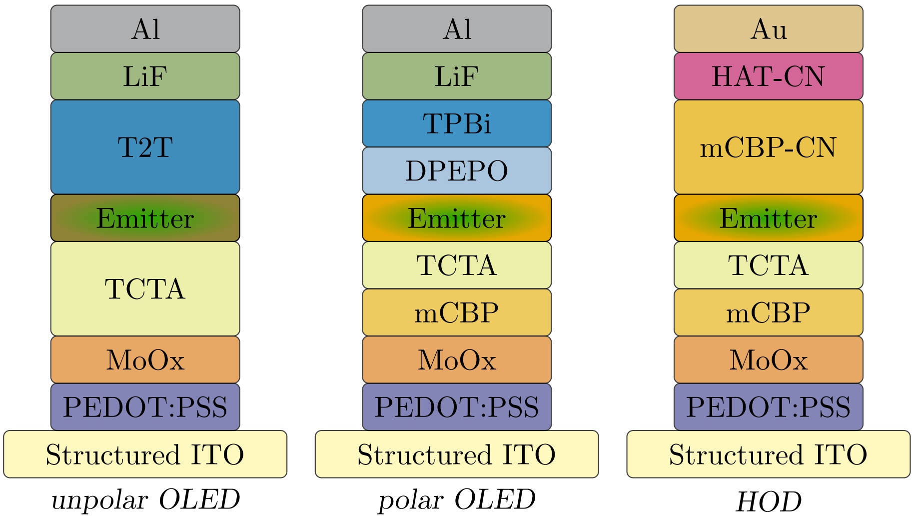

Figure A.1.: Stack designs of the various investigated device architectures. The three stacks are labelled *unpolar OLED*, *polar OLED* and *HOD*. The unpolar OLED comprises an emitter doped into CBP. All other devices had the emitter doped in mCBP-CN. The HOD device was designed to block electron injection, so that under operation, all present charge carriers are holes. All stacks were realized with Irppy$_3$ as emitter, identical polar OLEDs and HODs were built comprising DMAC-TRZ as emitter instead of Irppy$_3$ as well. The dopant concentration was left unchanged for all samples at 10wt%.

Additional graphs and experimental data

Polar OLEDs

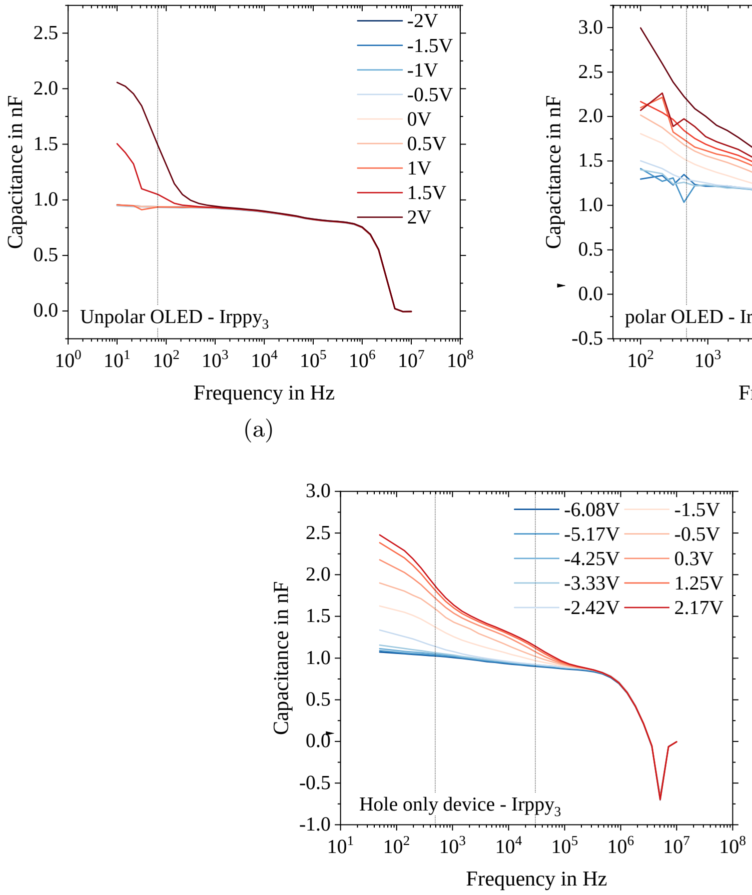

(a)

(b)

(c)

Figure A.2.: Capacitance-frequency measurements of phosphorescent OLEDs processed in Augsburg. Unpolar (A.2a), polar (A.2b) and HOD (A.2c) devices. Only the unpolar device shows a single capacitance steps while the other two samples, containing mCBP-CN, show multiple steps.

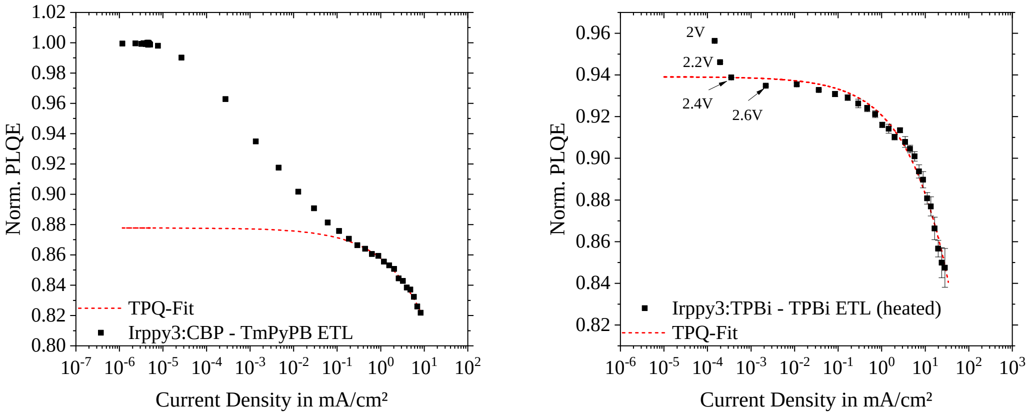

(a) (b)

Figure A.3.: A.3a: PLQE data from the CBP host TmPyPB ETL Irppy$_3$ OLEDs made by TUD. The fit was calculated according to equation 4.8. The data only matches the fit in the high current regime. Prior to that, the accumulated charges lead to deviations from the predicted efficiency curve. Note, that the currents in the lowest current regime are not actual diode currents but rather leakage currents. Therefore, here the device is not expected to be represented by the theoretical fit.
A.3b: PLQE vs. j-plot of the heated TPBi TUD OLED. The data can be modelled well by the TPQ fitting formalism described in equation 4.8 at high current densities. Low current deviations can by explained by the hole accumulation and thereby increased polaron density which is not accounted for in the theoretical model.

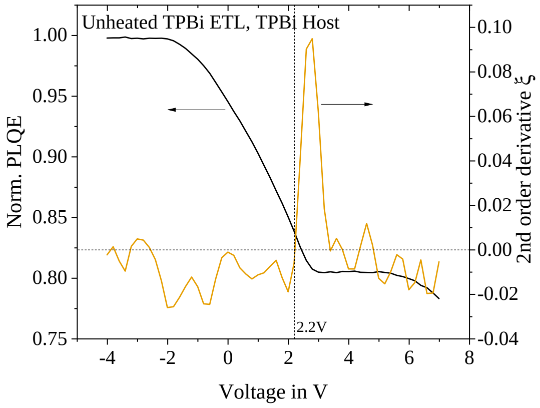

Figure A.4.: PLQE and second order derivative of the PLQE of the polar TUD samples with unheated TPBi as both host and ETL.

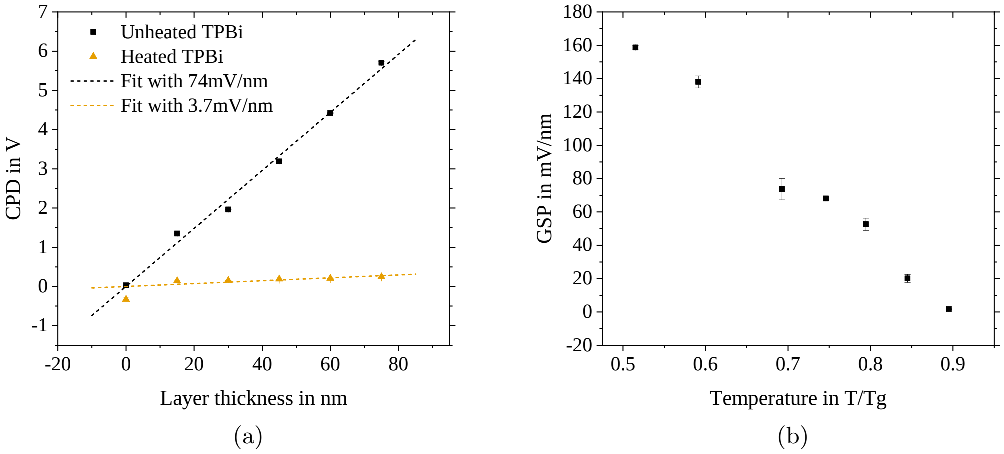

(a) (b)

Figure A.5.: Contact potential difference vs. deposited layer thickness (A.5a) and GSP vs. substrate temperature (A.5b) plots of pure TPBi films. The samples were processed and measured by Mr. Albin Cakaj. The effect of elevated substrate temperatures during film deposition can nicely be seen as the contact potential difference (CPD) and the GSP decline with increasing temperature.

InP Nanocrystal LEDs

TEM images

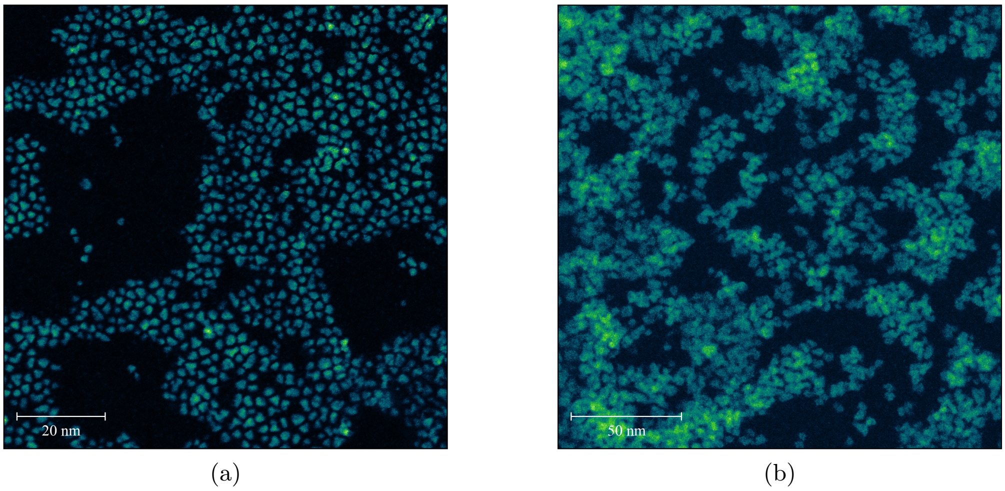

(a) (b)

Figure A.6.: Exemplary TEM images of HC100 (A.6a) and HC103 (A.6b) IAP QD. For the analysis, the diameters of 143 QDs per QD type were measured digitally on four images each. The result is shown in the text in figure 7.3.

AFM images

Substrate	HC100	HC103
Glass	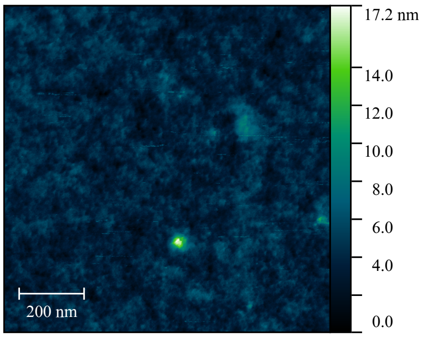	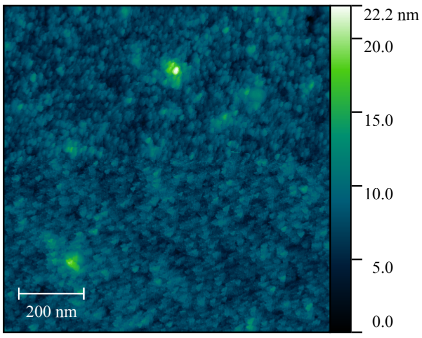
pTPD	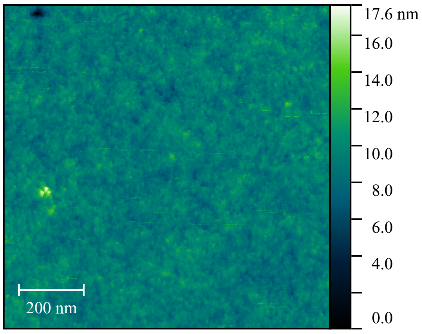	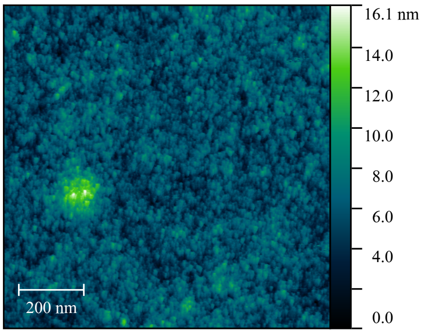
ZnO	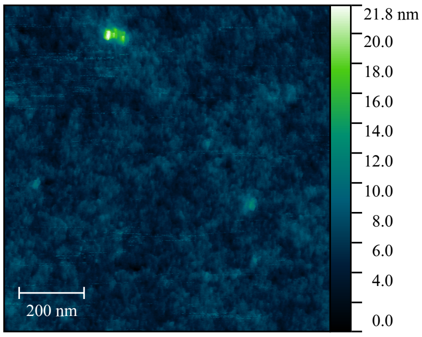	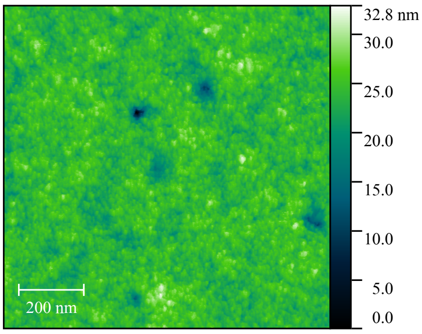

Table A.2.: AFM images of IAP QDs on different substrates.

PL spectra

Stack	thin QD EML	thicker QD EML
Inverted	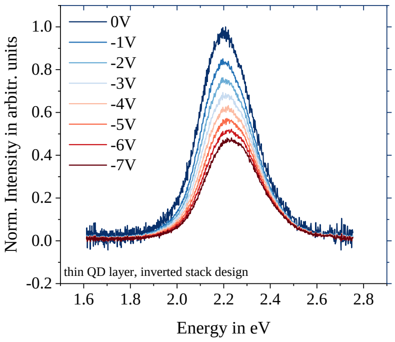	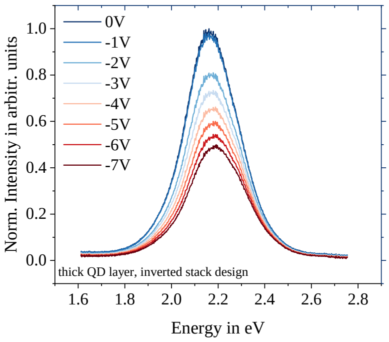
Conventional	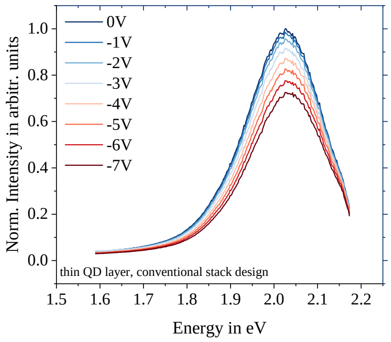	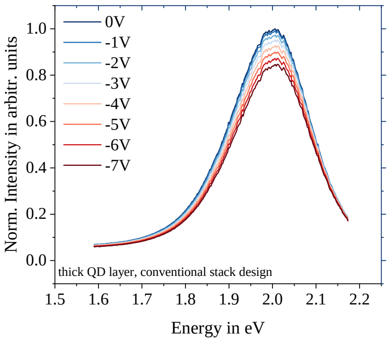

Table A.3.: Bias dependent PL spectra of IAP QDLEDs.

Rate determination of inverted IAP QDLEDs

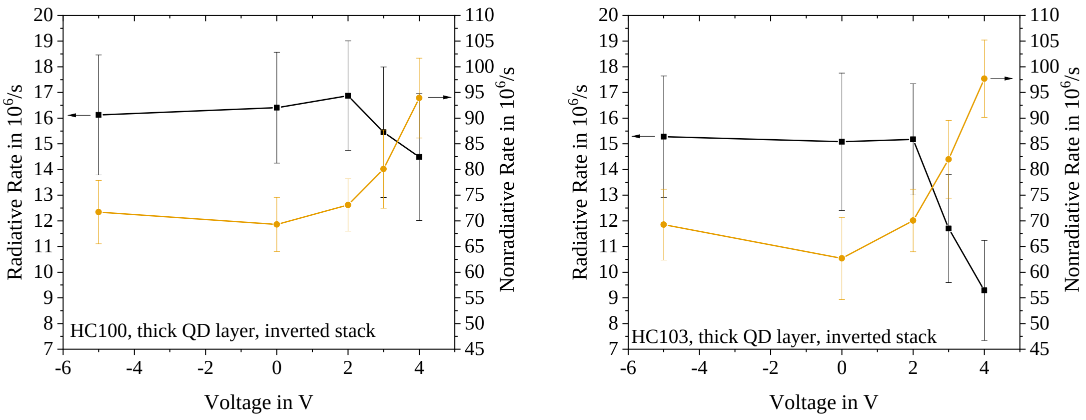

(a)

(b)

Figure A.7.: Applied bias dependent radiative and nonradiative rates of inverted IAP QDLEDs. The calculation was performed with absolute PLQY values from the respective solution measurement. The lifetime data as well as the respective PLQE data can be found in the text in figures 7.8 and 7.11.

Bidirectional sweeps of IAP QDLEDs

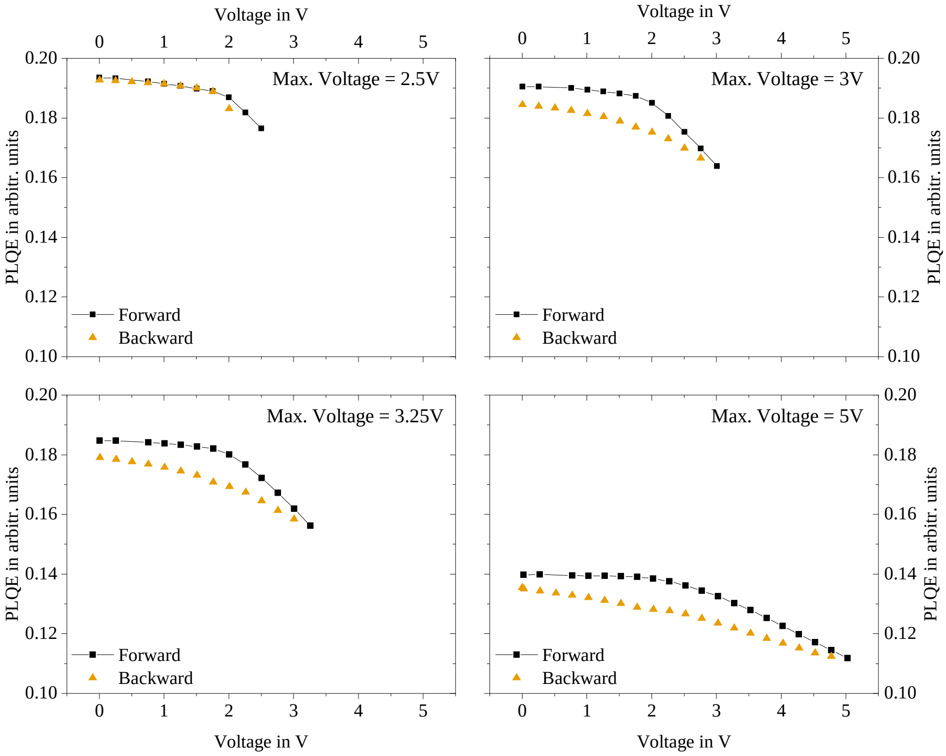

Figure A.8.: Bidirectional sweeps of an IAP QDLED according to the measurement routine schematically depicted in figure 7.16a. Black squares show the sweeps with increasing biases, orange triangles show the sweep-backs to 0 V. Note that for the sake of clarity, more measurement steps were conducted than are shown here. In particular, six additional bidirectional single sweeps were performed between the lower two panels, which explains the large drop between the PLQEs.
The PLQE behaviour is completely reversible in forward and backward sweeps until a maximum bias of 2.5 V. Higher voltages lead to not completely reversible PLQE drops.

Reversibility of QD charging

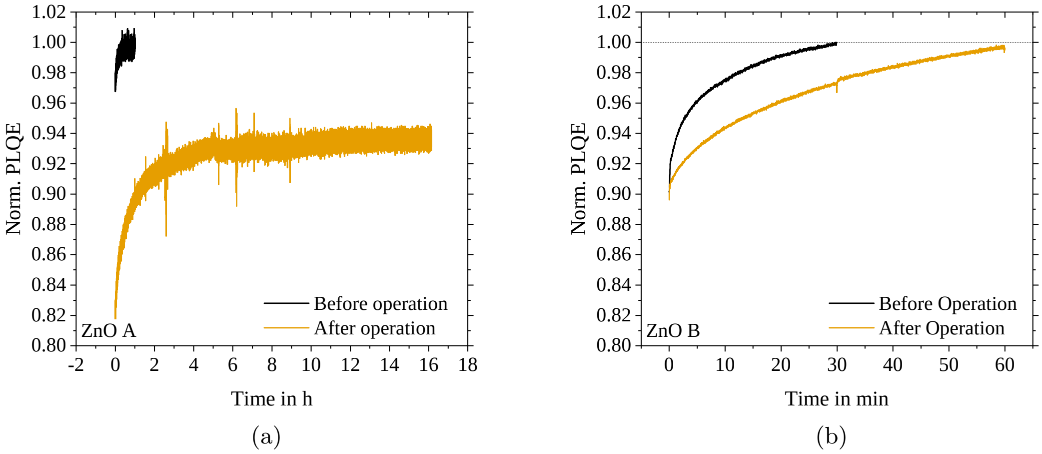

(a) (b)

Figure A.9.: Experimental data on the reversibility of QD charging. Both inverted HC100 samples are nominally identical with the single exception of a differently processed ZnO layer. *ZnO A* is the layer commonly used throughout this thesis, while *ZnO B* is an adapted version. Unfortunately, the author does not have any details about the microscopic differences between the two layers.

The PLQE of both samples were pretreated according to figure 7.15a for 20 min, whereafter a voltage sweep was run. Subsequently, another 0 V measurement was made for 16 h (A.9a) or 60 min (A.9b).

Bibliography

(1) Tang, C.; VanSlyke, S. A. *Applied Physics Letters* **1987**, *51*, 913–915.

(2) Colvin, V. L.; Alivisatos, A. P. *Journal of Chemical Physics* **1992**, *97*, 730–733.

(3) Shirasaki, Y.; Supran, G. J.; Tisdale, W. A.; Bulović, V. *Physical Review Letters* **2013**, *110*, 217403.

(4) Clayden, J.; Greeves, N.; Warren, S., *Organic Chemistry*; Oxford University Press: 2012; 1260 pp.

(5) Pope, M., *Electronic Processes in Organic Crystals and Polymers*; Oxford University Press: 1999; 1360 pp.

(6) Coropceanu, V.; Cornil, J.; da Silva Filho, D. A.; Olivier, Y.; Silbey, R.; Brédas, J.-L. *Chemical Reviews* **2007**, *107*, 926–952.

(7) Scher, H.; Lax, M. *Physical Review B* **1973**, *7*, 4491–4502.

(8) Scher, H.; Montroll, E. *Physical Review B* **1975**, *12*, 2455–2477.

(9) Haarer, D. *Macromolecular Materials and Engineering* **1990**, *183*, 197–220.

(10) Stoeckel, M.-A. et al. *Freeing electrons from extrinsic and intrinsic disorder yields band-like transport in n-type organic semiconductors, arXiv* **2019**.

(11) Fleming, I., *Molecular Orbitals and Organic Chemical Reactions*; John Wiley and Sons: 2009; 378 pp.

(12) Nakamura, K.; Hosokawa, Y.; Masuhara, H. *Crystal Growth & Design* **2007**, *7*, 885–889.

(13) *Physics of organic semiconductors*; Brütting, W., Ed.; Wiley-VCH: Weinheim, 2005.

(14) Köhler, A.; Bässler, H., *Electronic Processes in Organic Semiconductors*; John Wiley and Sons: 2015; 420 pp.

(15) Schwoerer, M.; Wolf, H., *Organic molecular solids*; Wiley-VCH: Weinheim, 2007.

(16) Pankow, R. M.; Thompson, B. C. *Polymer* **2020**, *207*, 122874.

(17) Duan, L.; Hou, L.; Lee, T.-W.; Qiao, J.; Zhang, D.; Dong, G.; Wang, L.; Qiu, Y. *Journal of Materials Chemistry* **2010**, *20*, 6392.

(18) Hofmann, A. J. L. The influence of dipolar doping on chargeinjection and transport in small molecularorganic semiconductors, Ph.D. Thesis, University of Augsburg, 2020.

(19) Haug, H.; Koch, S. W., *Quantum Theory of the Optical and Electronic Properties of Semiconductors (4th Edition)*; World Scientific Pub Co Inc: 2004; 468 pp.

(20) Liang, W. Y. *Physics Education* **1970**, *5*, 226–228.

(21) Wannier, G. H. *Physical review Journals archive* **1937**, *52*, 191–197.

(22) Fox, M., *Optical Properties of Solids*; OXFORD UNIV PR: 2010; 408 pp.

(23) Morgenstern, T. Preferential alignment of anisotropic transition dipole moments in organic and perovskite thin films, Ph.D. Thesis, University of Augsburg, 2019.

(24) Fowler, R. F.; Nordheim, L. *Proceedings of the royal society A* **1928**, *119*, 173–181.

(25) Adachi, C.; Tsutsui, T.; Saito, S. *Applied Physics Letters* **1990**, *57*, 531–533.

(26) Shockley, W. *Bell Labs Technical Journal* **1949**, *28*, 435–489.

(27) Würfel, P., *Physik der Solarzellen*; Spektrum Akademischer Verlag: 2000; 208 pp.

(28) Mott, N.; Gurney, R. *Oxford, Clarendon Press, 1940.* **1940**.

(29) Brütting, W.; Berleb, S.; Mückl, A. G. *Organic Electronics* **2001**, *2*, 1–36.

(30) Lampert, M. A.; Schilling, R. B. In *Injection Phenomena*, Willardson, R., Beer, A. C., Eds.; Semiconductors and Semimetals, Vol. 6; Elsevier: 1970, pp 1–96.

(31) Schmidt, T. D. Photophysics of organic light-emitting diodes–Device efficiency and degradation processes, Ph.D. Thesis, University of Augsburg, 2013.

(32) Nowy, S.; Krummacher, B. C.; Frischeisen, J.; Reinke, N. A.; Brütting, W. *Journal of Applied Physics* **2008**, *104*, 123109.

(33) Furno, M.; Meerheim, R.; Hofmann, S.; Lüssem, B.; Leo, K. *Physical Review B* **2012**, *85*, 115205.

(34) Schmidt, T. D.; Lampe, T.; M. R., D. S.; Djurovich, P. I.; Thompson, M. E.; Brütting, W. *Physical Review Applied* **2017**, *8*, 037001.

(35) Scholz, B. J.; Frischeisen, J.; Jaeger, A.; Setz, D. S.; g. Reusch, T. C.; Brütting, W. *Optical Society of America* **2012**, *20*, A205.

(36) Chen, S.; Kwok, H. S. *Optical Society of America* **2009**, *18*, 37.

(37) Riedel, B.; Kaiser, I.; Hauss, J.; Lemmer, U.; Gerken, M. *Optical Society of America* **2010**, *18*, A631.

(38) Bocksrocker, T.; Maier-Flaig, F.; Eschenbaum, C.; Lemmer, U. *Optical Society of America* **2012**, *20*, 6170.

(39) Heinrichsdobler, A.; Engelmayer, M.; Riedel, D.; Brabec, C.; Wehlus, T. *SPIE Proceedings* **2017**, *10362*, DOI: `10.1117/12.2272976`.

(40) Pitarke, J. M.; Silkin, V. M.; Chulkov, E. V.; Echenique, P. M. *Reports on Progress in Physics* **2006**, *70*, 1–87.

(41) Fuchs, C.; Schwab, T.; Wieczorek, M.; Gather, M. C.; Hofmann, S.; Leo, K.; Scholz, R. In *Organic Light Emitting Materials and Devices XVIII*, ed. by So, F.; Adachi, C., SPIE: 2014; Vol. 9183, pp 123–132.

(42) Brütting, W.; Frischeisen, J.; Schmidt, T. D.; Scholz, B. J.; Mayr, C. *physica status solidi* **2012**, *210*, 44–65.

(43) Naqvi, B. A.; Schmid, M.; Crovini, E.; Sahay, P.; Naujoks, T.; Rodella, F.; Zhang, Z.; Strohriegl, P.; Bräse, S.; Zysman-Colman, E.; Brütting, W. *frontiers in Chemistry* **2020**, *8*, DOI: `10.3389/fchem.2020.00750`.

(44) Morgenstern, T.; Schmid, M.; Hofmann, A.; Bierling, M.; Jäger, L.; Brütting, W. *ACS Applied Materials and Interfaces* **2018**, *10*, 31541–31551.

(45) Jurow, M. J.; Morgenstern, T.; Eisler, C.; Kang, J.; Penzo, E.; Do, M.; Engelmayer, M.; Osowiecki, W. T.; Bekenstein, Y.; Tassone, C.; Wang, L.-W.; Alivisatos, A. P.; Brütting, W.; Liu, Y. *Nano Letters* **2019**, *19*, 2489–2496.

(46) Noguchi, Y.; Brütting, W.; Ishii, H. *Japanese Journal of Applied Physics* **2019**, *58*, SF0801.

(47) Ito, E.; Washizu, Y.; Hayashi, N.; Ishii, H.; Matsuie, N.; Tsuboi, K.; Ouchi, Y.; Harima, Y.; Yamashita, K.; Seki, K. *Journal of Applied Physics* **2002**, *92*, 7306–7310.

(48) Friederich, P.; Rodin, V.; von Wrochem, F.; Wenzel, W. *ACS Applied Materials and Interfaces* **2018**, *10*, 1881–1887.

(49) Noguchi, Y.; Miyazaki, Y.; Tanaka, Y.; Sato, N.; Nakayama, Y.; Schmidt, T. D.; Brütting, W.; Ishii, H. *Journal of Applied Physics* **2012**, *111*, 114508.

(50) Bangsund, J. S.; Sambeek, J. R. V.; Concannon, N. M.; Holmes, R. J. *Science Advances* **2020**, *6*, eabb2659.

(51) Bansal, A.; Penzkofer, A. *Applied Physics B* **2008**, *91*, 559–569.

(52) Bruker Introduction to Bruker's ScanAsyst and PeakForce Tapping AFM Technology.

(53) Bruker ScanAsyst Exclusive, Self-Optimizing AFM Imaging, 2013.

(54) Naujoks, T. Polymeric hole injection layers for perovskite-based LEDs, MA thesis, University of Augsburg, 2018.

(55) Mccluney, W. R., *Introduction to Radiometry and Photometry*, 1994.

(56) Ronald W. Waynant, M. N. E. Electro-Optics Handbook, ISBN 9780070687165, 2000.

(57) Bass, M., *Handbook of Optics, Third Edition Volume II: Design, Fabrication and Testing, Sources and Detectors, Radiometry and Photometry*, 3rd ed.; McGraw-Hill Professional: 2009.

(58) Rea, M. S., *The IESNA lighting handbook : reference & application*, 9th ed.; of North America., I. E. S., Ed.; Illuminating Engineering Society of North America: 2000.

(59) Martens, H. C. F.; Brom, H. B.; Blom, P. W. M. *Physical Review B* **1999**, *60*, R8489–R8492.

(60) Tripathi, D. C.; Tripathi, A. K.; Mohapatra, Y. N. *Applied Physics Letters* **2011**, *98*, 033304.

(61) Chaudhary, S.; Yadav, V.; Negi, C. M. S.; Gupta, S. K. *Micro & Nano Letters* **2020**, *15*, 136–139.

(62) Fischer, J.; Ray, D.; Kleemann, H.; Pahner, P.; Schwarze, M.; Koerner, C.; Vandewal, K.; Leo, K. *Journal of Applied Physics* **2015**, *117*, 245501.

(63) Burtone, L.; Ray, D.; Leo, K.; Riede, M. *Journal of Applied Physics* **2012**, *111*, 064503.

(64) Pahner, P.; Kleemann, H.; Burtone, L.; Tietze, M. L.; Fischer, J.; Leo, K.; Lüssem, B. *Physical Review B* **2013**, *88*, 195205.

(65) Lin, J.; Weis, M.; Taguchi, D.; Manaka, T.; Iwamoto, M. *Japanese Journal of Applied Physics* **2010**, *49*, 01AE14.

(66) Barsoukov, E., *Impedance Spectroscopy: Theory, Experiment, and Applications*; WILEY: 2018; 560 pp.

(67) Jäger, L.; Schmidt, T. D.; Brütting, W. *AIP Advances* **2016**, *6*, 095220.

(68) Berleb, S.; Brütting, W. *Physical Review Letters* **2002**, *89*, 286601.

(69) Altazin, S.; Züfle, S.; Knapp, E.; Kirsch, C.; Schmidt, T.; Jäger, L.; Noguchi, Y.; Brütting, W.; Ruhstaller, B. *Organic Electronics* **2016**, *39*, 244–249.

(70) Li, W.; Li, Z.; Si, C.; Wong, M. Y.; Jinnai, K.; Gupta, A. K.; Kabe, R.; Adachi, C.; Huang, W.; Zysman-Colman, E.; Samuel, I. D. W. *Advanced Materials* **2020**, *32*, 2003911.

(71) Hinrichsen, T. F.; Chan, C. C. S.; Ma, C.; Paleček, D.; Gillett, A.; Chen, S.; Zou, X.; Zhang, G.; Yip, H.-L.; Wong, K. S.; Friend, R. H.; Yan, H.; Rao, A.; Chow, P. C. Y. *Nature Communications* **2020**, *11*, DOI: `10.1038/s41467-020-19332-5`.

(72) Rajamalli, P.; Chen, D.; Li, W.; Samuel, I. D. W.; Cordes, D. B.; Slawin, A. M. Z.; Zysman-Colman, E. *Journal of Materials Chemistry C* **2019**, *7*, 6664–6671.

(73) Mohanty, M. E.; Madhu, C.; Reddy, V. L.; Paramasivam, M.; Bangal, P. R.; Rao, V. J. *Physical Chemistry Chemical Physics* **2017**, *19*, 9118–9127.

(74) Wehrmeister, S. Zeitaufgelöste optische Spektroskopie zur Effizienzsteigerung organischer Leuchtdioden, Ph.D. Thesis, University of Augsburg, 2017.

(75) Hamamatsu Manual of Universal Streak Camera C5680 Series `https://cpb-us-w2.wpmucdn.com/sites.wustl.edu/dist/9/2407/files/2020/02/A1976-04.pdf`.

(76) Penfold, T. J.; Dias, F. B.; Monkman, A. P. *Chemical Communications* **2018**, *54*, 3926–3935.

(77) Yang, Z.; Mao, Z.; Xie, Z.; Zhang, Y.; Liu, S.; Zhao, J.; Xu, J.; Chi, Z.; Aldred, M. P. *Chemical Society Reviews* **2017**, *46*, 915–1016.

(78) Baldo, M. A.; Forrest, S. R. *Physical Review B* **2000**, *62*, 10958–10966.

(79) Baldo, M. A.; Adachi, C.; Forrest, S. R. *Physical Review B* **2000**, *62*, 10967–10977.

(80) Reineke, S.; Walzer, K.; Leo, K. *Physical Review B* **2007**, *75*, 125328.

(81) Murawski, C.; Liehm, P.; Leo, K.; Gather, M. C. *Advanced Functional Materials* **2013**, *24*, 1117–1124.

(82) Wehrmeister, S.; Jäger, L.; Wehlus, T.; Rausch, A. F.; Reusch, T. C.; Schmidt, T. D.; Brütting, W. *Physical Review Applied* **2015**, *3*, 024008.

(83) Shirasaki, Y. Efficiency Loss Mechanisms in Colloidal Quantum-Dot Light-Emitting Diodes, Ph.D. Thesis, Massachusetts Institute of Technology, 2013.

(84) Supran, G. J. S. Enhancing quantum-dot luminescence in visible and infrared light emitting devices, Ph.D. Thesis, Massachusetts Institute of Technology, 2016.

(85) Systems, S. R. About Lock-In Amplifiers - Application Note 3 `https://www.thinksrs.com/downloads/pdfs/applicationnotes/AboutLIAs.pdf`.

(86) Bangsund, J. S.; Holmes, R. J. In *Organic and Hybrid Light Emitting Materials and Devices XXIII*, ed. by So, F.; Adachi, C.; Kim, J.-J., SPIE: 2019.

(87) Zou, W. et al. *Nature Communications* **2018**, *9*, DOI: `10.1038/s41467-018-03049-7`.

(88) Pu, C.; Dai, X.; Shu, Y.; Zhu, M.; Deng, Y.; Jin, Y.; Peng, X. *Nature Communications* **2020**, *11*, DOI: `10.1038/s41467-020-14756-5`.

(89) Ossila Product page - Ossila Spincoaters `https://www.ossila.com/products/spin-coater?variant=37156979841`.

(90) Smith, A. R. G.; Burn, P. L.; Powell, B. J. *ChemPhysChem* **2011**, *12*, 2429–2438.

(91) Baldo, M. A.; O'Brien, D. F.; You, Y.; Shoustikov, A.; Sibley, S.; Thompson, M. E.; Forrest, S. R. *Nature* **1998**, *395*, 151–154.

(92) Baldo, M. A.; Thompson, M. E.; Forrest, S. R. *Nature* **2000**, *403*, 750–753.

(93) Delorme, R.; Perrin, F. *Le Journal de Physique* **1929**, *10*, 177–186.

(94) Uoyama, H.; Goushi, K.; Shizu, K.; Nomura, H.; Adachi, C. *Nature* **2012**, *492*, 234–238.

(95) Wong, M.; Zysman-Colman, E. *Advanced Materials* **2017**, *29*, 1605444.

(96) Tao, Y.; Yuan, K.; Chen, T.; Xu, P.; Li, H.; Chen, R.; Zheng, C.; Zhang, L.; Huang, W. *Advanced Materials* **2014**, *26*, 7931–7958.

(97) Brown, J.; Kwong, R.; Tung, Y.-J.; Adamovich, V.; Weaver, M.; Hack, M. *Society for Information Display* **2004**, *12*, 329.

(98) Liu, Z.; Zhang, S.-W.; Zhang, M.; Wu, C.; Li, W.; Wu, Y.; Yang, C.; Kang, F.; Meng, H.; Wei, G. *Frontiers in Chemistry* **2021**, *9*, DOI: `10.3389/fchem.2021.758357`.

(99) Wallikewitz, B. H.; Kabra, D.; Gélinas, S.; Friend, R. H. *Physical review B* **2012**, *85*, 045209.

(100) Zee, B.; Li, Y.; Wetzelaer, G.-J. A. H.; Blom, P. W. M. *Advanced Optical Materials* **2021**, *9*, 2100249.

(101) Luo, Y.; Aziz, H.; Popovic, Z. D.; Xu, G. *Applied Physics Letters* **2006**, *89*, 103505.

(102) Kalinowski, J.; Stampor, W.; Szmytkowski, J.; Virgili, D.; Cocchi, M.; Fattori, V.; Sabatini, C. *Physical Review B* **2006**, *74*, 085316.

(103) Regnat, M.; Pernstich, K. P.; Ruhstaller, B. *Organic Electronics* **2019**, *70*, 219–226.

(104) Mezyk, J.; Meinardi, F.; Tubino, R.; Cocchi, M. *Applied Physics Letters* **2008**, *93*, 093301.

(105) Tsai, W.-L.; Huang, M.-H.; Lee, W.-K.; Hsu, Y.-J.; Pan, K.-C.; Huang, Y.-H.; Ting, H.-C.; Sarma, M.; Ho, Y.-Y.; Hu, H.-C.; Chen, C.-C.; Lee, M.-T.; Wong, K.-T.; Wu, C.-C. *Chemical Communications* **2015**, *51*, 13662–13665.

(106) Pai, D. M.; Yanus, J. F.; Stolka, M. *The Journal of Physical Chemistry* **1984**, *88*, 4714–4717.

(107) Noguchi, Y.; Lim, H.; Isoshima, T.; Ito, E.; Hara, M.; Chin, W. W.; Han, J. W.; Kinjo, H.; Ozawa, Y.; Nakayama, Y.; Ishii, H. *Applied Physics Letters* **2013**, *102*, 203306.

(108) Graf, A.; Liehm, P.; Murawski, C.; Hofmann, S.; Leo, K.; Gather, M. C. *J. Mater. Chem. C* **2014**, *2*, 10298–10304.

(109) Rafols-Ribe, J.; Will, P.-A.; Haenisch, C.; Gonzalez-Silveira, M.; Lenk, S.; Rodriguez-Viejo, J.; Reineke, S. *Science Advances* **2018**, *4*, DOI: `10.1126/sciadv.aar8332`.

(110) Cakaj, A. Einfluss der Substrattemperatur und Dotierung auf die Orientierung organischer Moleküle, MA thesis, University of Augsburg, 2022.

(111) Colvin, V. L.; Schlamp, M. C.; Alivisatos, A. P. *Nature* **1994**, *370*, 354–357.

(112) Bloch, F. *Zeitschrift für Physik* **1929**, *52*, 555–600.

(113) Krauss, T. D.; Peterson, J. J. In *Colloidal Quantum Dot Optoelectronics and Photovoltaics*, Konstantatos, G., Sargent, E. H., Eds.; Cambridge University Press: 2013, pp 59–86.

(114) Klimov, V. I. *Annual Review of Physical Chemistry* **2007**, *58*, 635–673.

(115) Piprek, J., *Semiconductor Optoelectronic Devices*; Elsevier: 2003.

(116) Woggon, U., *Optical Properties of Semiconductor Quantum Dots*; Springer Berlin Heidelberg: 1997.

(117) Prezhdo, O. V. *Accounts of Chemical Research* **2009**, *42*, 2005–2016.

(118) Alivisatos, A. P. *Science* **1996**, *271*, 933–937.

(119) Ashoori, R. C. *Nature* **1996**, *379*, 413–419.

(120) Pokutnyi, S. I. *Semiconductors* **2007**, *41*, 1323–1328.

(121) Brus, L. E. *Journal of Chemical Physics* **1983**, *79*, 5566–5571.

(122) Brus, L. *Journal for Physical Chemistry* **1986**, *90*, 2555–2560.

(123) Pietryga, J. M.; Park, Y.-S.; Lim, J.; Fidler, A. F.; Bae, W. K.; Brovelli, S.; Klimov, V. I. *Chemical Reviews* **2016**, *116*, 10513–10622.

(124) Yoffe, A. *Advances in Physics* **1993**, *42*, 173–262.

(125) Norris, D. J.; Bawendi, M. G. *Physical Review B* **1996**, *53*, 16338–16346.

(126) Sercel, P. C.; Vahala, K. J. *Physical Review B* **1990**, *42*, 3690–3710.

(127) Ekimov, A. I.; Kudryavtsev, I. A.; Efros, A. L.; Yazeva, T. V.; Hache, F.; Schanne-Klein, M. C.; Rodina, A. V.; Ricard, D.; Flytzanis, C. *Physical Review B* **1993**, *10*, 100.

(128) Xia, J.-B. *Physical Review B* **1989**, *40*, 8500–8507.

(129) Grimaldi, G.; Geuchies, J. J.; van der Stam, W.; du Fossé, I.; Brynjarsson, B.; Kirkwood, N.; Kinge, S.; Siebbeles, L. D.; Houtepen, A. J. *Nano Letters* **2019**, *19*, 3002–3010.

(130) Hines, M. A.; Guyot-Sionnest, P. *Journal for Physical Chemistry* **1996**, *100*, 468–471.

(131) Reiss, P.; Protière, M.; Li, L. *Small* **2009**, *5*, 154–168.

(132) Yang, W.; Yang, Y.; Kaledin, A. L.; He, S.; Jin, T.; McBride, J. R.; Lian, T. *Chemical Science* **2020**, *11*, 5779–5789.

(133) Pan, Z.; Zhang, H.; Cheng, K.; Hou, Y.; Hua, J.; Zhong, X. *ACS Nano* **2012**, *6*, 3982–3991.

(134) Kim, S.; Fisher, B.; Eisler, H.-J.; Bawendi, M. *Journal of the American Chemical Society* **2003**, *125*, 11466–11467.

(135) Grassl, F.; Ullrich, A.; Mansour, A. E.; Abdalbaqi, S. M.; Koch, N.; Opitz, A.; Scheele, M.; Brütting, W. *ACS Applied Materials and Interfaces* **2021**, DOI: `10.1021/acsami.1c08614`.

(136) R, S.; Vishaka, H. V.; J, K.; Balakrishna, R. G. *ACS Applied Nano Materials* **2020**, *3*, 6089–6098.

(137) Yuan, Q.; Wang, T.; Yu, P.; Zhang, H.; Zhang, H.; Ji, W. *Organic Electronics* **2021**, *90*, 106086.

(138) Özgür, Ü.; Alivov, Y. I.; Liu, C.; Teke, A.; Reshchikov, M. A.; Doğan, S.; Avrutin, V.; Cho, S.-J.; Morkoç, H. *Journal of Applied Physics* **2005**, *98*, 041301.

(139) Treu, T. Untersuchung vonPrecursor - Zinkoxidschichten für dieVerwendung in organischen Bauteilen, Bachelor thesis - University of Augsburg, 2019.

(140) Gómez-Núñez, A.; López, C.; Alonso-Gil, S.; Roura, P.; Vilà, A. *Materials Chemistry and Physics* **2015**, *162*, 645–651.

(141) Utsch, B.; Hausmann, A. *Zeitschriften fuer Physik B Condensed Matter* **1975**, *21*, 27–31.

(142) Sun, Y.; Jiang, Y.; Peng, H.; Wei, J.; Zhang, S.; Chen, S. *Nanoscale* **2017**, *9*, 8962–8969.

(143) Li, C.; Vaynzof, Y.; Lakhwani, G.; Beirne, G. J.; Wang, J.; Greenham, N. C. *Journal of Applied Physics* **2017**, *121*, 144503.

(144) Deng, B.; da Rosa, A. L.; Frauenheim, T.; Xiao, J. P.; Shi, X. Q.; Zhang, R. Q.; Hove, M. A. V. *Nanoscale* **2014**, *6*, 11882–11886.

(145) Mashford, B. S.; Stevenson, M.; Popovic, Z.; Hamilton, C.; Zhou, Z.; Breen, C.; Steckel, J.; Bulovic, V.; Bawendi, M.; Coe-Sullivan, S.; Kazlas, P. T. *Nature Photonics* **2013**, *7*, 407–412.

(146) Qian, L.; Zheng, Y.; Choudhury, K. R.; Bera, D.; So, F.; Xue, J.; Holloway, P. H. *nanotoday* **2010**, *5*, 384–389.

(147) Cho, C.; Zhao, B.; Tainter, G. D.; Lee, J.-Y.; Friend, R. H.; Di, D.; Deschler, F.; Greenham, N. C. *Nature Communications* **2020**, *11*, DOI: `10.1038/s41467-020-14401-1`.

(148) Cheng, Z.; O'Carroll, D. M. *Advanced Science* **2021**, *8*, 2004076.

(149) Shen, H.; Gao, Q.; Zhang, Y.; Lin, Y.; Lin, Q.; Li, Z.; Chen, L.; Zeng, Z.; Li, X.; Jia, Y.; Wang, S.; Du, Z.; Li, L. S.; Zhang, Z. *Nature Photonics* **2019**, *13*, 192–197.

(150) Zhang, H.; Chen, S.; Sun, X. W. *ACS Nano* **2017**, *12*, 697–704.

(151) Lim, J.; Park, Y.-S.; Wu, K.; Yun, H. J.; Klimov, V. I. *Nano Letters* **2018**, *18*, 6645–6653.

(152) Brunetti, V.; Chibli, H.; Fiammengo, R.; Galeone, A.; Malvindi, M. A.; Vecchio, G.; Cingolani, R.; Nadeau, J. L.; Pompa, P. P. *Nanoscale* **2013**, *5*, 307–317.

(153) Tarantini, A.; Wegner, K. D.; Dussert, F.; Sarret, G.; Beal, D.; Mattera, L.; Lincheneau, C.; Proux, O.; Truffier-Boutry, D.; Moriscot, C.; Gallet, B.; Jouneau, P.-H.; Reiss, P.; Carrière, M. *NanoImpact* **2019**, *14*, 100168.

(154) Won, Y.-H.; Cho, O.; Kim, T.; Chung, D.-Y.; Kim, T.; Chung, H.; Jang, H.; Lee, J.; Kim, D.; Jang, E. *Nature* **2019**, *575*, 634–638.

(155) Chao, W.-C.; Chiang, T.-H.; Liu, Y.-C.; Huang, Z.-X.; Liao, C.-C.; Chu, C.-H.; Wang, C.-H.; Tseng, H.-W.; Hung, W.-Y.; Chou, P.-T. *Communications Materials* **2021**, *2*, DOI: `10.1038/s43246-021-00203-5`.

(156) Zhang, W.; Ding, S.; Zhuang, W.; Wu, D.; Liu, P.; Qu, X.; Liu, H.; Yang, H.; Wu, Z.; Wang, K.; Sun, X. W. *Advanced Functional Materials* **2020**, *30*, 2005303.

(157) Zhang, H.; Ma, X.; Lin, Q.; Zeng, Z.; Wang, H.; Li, L. S.; Shen, H.; Jia, Y.; Du, Z. *The Journal of Physical Chemistry Letters* **2020**, *11*, 960–967.

(158) Kim, T.; Kim, K.-H.; Kim, S.; Choi, S.-M.; Jang, H.; Seo, H.-K.; Lee, H.; Chung, D.-Y.; Jang, E. *Nature* **2020**, *586*, 385–389.

(159) Yu, X.-Y.; Lei, B.-X.; Kuang, D.-B.; Su, C.-Y. *Chemical Science* **2011**, *2*, 1396.

(160) Yang, J.; Zhong, X. *Journal of Materials Chemistry A* **2016**, *4*, 16553–16561.

(161) Manabe, N.; Hoshino, A.; Liang, Y.-q.; Goto, T.; Kato, N.; Yamamoto, K. *IEEE Transactions on Nanobioscience* **2006**, *5*, 263–267.

(162) Iannazzo, D.; Pistone, A.; Salamò, M.; Galvagno, S.; Romeo, R.; Giofré, S. V.; Branca, C.; Visalli, G.; Pietro, A. D. *International Journal of Pharmaceutics* **2017**, *518*, 185–192.

(163) Chern, M.; Kays, J. C.; Bhuckory, S.; Dennis, A. M. *Methods and Applications in Fluorescence* **2019**, *7*, 012005.

(164) Jung, H.; Ahn, N.; Klimov, V. I. *Nature Photonics* **2021**, *15*, 643–655.

(165) Giansante, C.; Infante, I. *Journal of Physical Chemistry Letters* **2017**, *8*, 5209–5215.

(166) Zenkevich, E. I.; Blaudeck, T.; Milekhin, A.; von Borczyskowski, C. *International Journal of Spectroscopy* **2012**, *2012*, 1–14.

(167) Bozyigit, D.; Yarema, O.; Wood, V. *Advanced Functional Materials* **2013**, *23*, 3024–3029.

(168) Empedocles, S. A.; Bawendi, M. G. *Science* **1997**, *278*, 2114–2117.

(169) Wood, V.; Panzer, M.; Sullivan, S.-C.; Bulovic, V. In *Colloidal Quantum Dot Optoelectronics and Photovoltaics*, Konstantatos, G., Sargent, E. H., Eds.; Cambridge University Press: 2013, pp 148–172.

(170) Jing, P.; Zheng, J.; Zeng, Q.; Zhang, Y.; Liu, X.; Liu, X.; Kong, X.; Zhao, J. *Journal of Applied Physics* **2009**, *105*, 044313.

(171) Bozyigit, D.; Wood, V.; Shirasaki, Y.; Bulovic, V. *Journal of Applied Physics* **2012**, *111*, 113701.

(172) Galland, C.; Ghosh, Y.; Steinbrück, A.; Sykora, M.; Hollingsworth, J. A.; Klimov, V. I.; Htoon, H. *Nature* **2011**, *479*, 203–207.

(173) Yan, C.; Weinberg, D.; Jasrasaria, D.; Kolaczkowski, M. A.; Liu, Z.-j.; Philbin, J. P.; Balan, A. D.; Liu, Y.; Schwartzberg, A. M.; Rabani, E.; Alivisatos, A. P. *ACS Nano* **2020**, *15*, 2281–2291.

(174) Park, J.; Won, Y.-H.; Kim, T.; Jang, E.; Kim, D. *Small* **2020**, *16*, 2003542.

(175) Davis, N. J. L. K.; Böhm, M. L.; Tabachnyk, M.; Wisnivesky-Rocca-Rivarola, F.; Jellicoe, T. C.; Ducati, C.; Ehrler, B.; Greenham, N. C. *nature communications* **2015**, *6*, DOI: `10.1038/ncomms9259`.

(176) Kagan, C. R.; Lifshitz, E.; Sargent, E. H.; Talapin, D. V. *Science* **2016**, *353*, DOI: `10.1126/science.aac5523`.

(177) Huang, J.; Huang, Z.; Yang, Y.; Zhu, H.; Lian, T. *Journal of the Americal Chemical Society* **2010**, *132*, 4858–4864.

(178) Klimov, V. I.; Mikhailovsky, A. A.; McBranch, D. W.; Leatherdale, C. A.; Bawendi, M. G. *Science* **2000**, *287*, 1011–1013.

(179) Wu, K.; Lim, J.; Klimov, V. I. *ACS Nano* **2017**, *11*, 8437–8447.

(180) *Semiconductor Lasers I*; Kapon, E., Ed.; Elsevier: 1999.

(181) Mott, N. *Solid-State Electronics* **1978**, *21*, 1275–1280.

(182) Weisbuch, C.; Piccardo, M.; Martinelli, L.; Iveland, J.; Peretti, J.; Speck, J. S. *Physica Status Solidi A* **2015**, *212*, 899–913.

(183) Hopkins, M. A.; Allsopp, D. W. E.; Kappers, M. J.; Oliver, R. A.; Humphreys, C. J. *Journal of Applied Physics* **2017**, *122*, 234505.

(184) Kim, Y. Design of High Performance Indium Phosphide (InP) - based Quantum Dot Light Emitting Diodes (QLEDs), Ph.D. Thesis, TU Berlin, 2018.

(185) Tamang, S.; Lincheneau, C.; Hermans, Y.; Jeong, S.; Reiss, P. *Chemistry of Materials* **2016**, *28*, 2491–2506.

(186) LaMer, V. K.; Dinegar, R. H. *Journal of the American Chemical Society* **1950**, *72*, 4847–4854.

(187) Nguyen, T.-D.; Do, T.-O. In *Nanocrystal*; InTech: 2011.

(188) Wu, Z.; Yang, S.; Wu, W. *Nanoscale* **2016**, *8*, 1237–1259.

(189) Liu, H.; Owen, J. S.; Alivisatos, A. P. *Journal of the American Chemical Society* **2006**, *129*, 305–312.

(190) Murray, C. B.; Norris, D. J.; Bawendi, M. G. *Journal of the American Chemical Society* **1993**, *115*, 8706–8715.

(191) Peng, X.; Wickham, J.; Alivisatos, A. P. *Journal of the American Chemical Society* **1998**, *120*, 5343–5344.

(192) Shannon, R. D. *Acta Crystallographica Section A* **1976**, *32*, 751–767.

(193) Lin, B.-Y.; Ding, W.-C.; Chen, C.-H.; Kuo, Y.-P.; Lee, J.-H.; Lee, C.-Y.; Chiu, T.-L. *RSC Advances* **2021**, *11*, 20884–20891.

(194) Xue, X.; Dong, J.; Wang, S.; Zhang, H.; Zhang, H.; Zhao, J.; Ji, W. *Journal of Materials Chemistry C* **2020**, *8*, 2014–2018.

(195) Chen, S.; Cao, W.; Liu, T.; Tsang, S.-W.; Yang, Y.; Yan, X.; Qian, L. *Nature Communications* **2019**, *10*, DOI: `10.1038/s41467-019-08749-2`.

(196) Davidson-Hall, T.; Aziz, H. *Nanoscale* **2018**, *10*, 2623–2631.

(197) Mooney, J.; Kambhampati, P. *The Journal of Physical Chemistry Letters* **2013**, *4*, 3316–3318.

(198) Förster, T. *Annalen der Physik* **1948**, *437*, 55–75.

(199) Jang, H. M.; Kim, J.-S.; Heo, J.-M.; Lee, T.-W. *APL Materials* **2020**, *8*, 020904.

(200) Kim, Y.; Ham, S.; Jang, H.; Min, J. H.; Chung, H.; Lee, J.; Kim, D.; Jang, E. *ACS Applied Nano Materials* **2019**, *2*, 1496–1504.

(201) Yuan, G.; Gómez, D. E.; Kirkwood, N.; Boldt, K.; Mulvaney, P. *ACS Nano* **2018**, *12*, 3397–3405.

(202) Kot, M.; Zdansky, K. *IEEE Journal of Quantum Electronics* **1992**, *28*, 1746–1750.

(203) Chen, Z.; Li, Z.; Zhang, C.; Jiang, X.-F.; Chen, D.; Xue, Q.; Liu, M.; Su, S.; Yip, H.-L.; Cao, Y. *Advanced Materials* **2018**, *30*, 1801370.

(204) Fakharuddin, A.; Qiu, W.; Croes, G.; Devižis, A.; Gegevičius, R.; Vakhnin, A.; Rolin, C.; Genoe, J.; Gehlhaar, R.; Kadashchuk, A.; Gulbinas, V.; Heremans, P. *Advanced Functional Materials* **2019**, *29*, 1904101.

(205) Chen, D.; Gao, F.; Dong, M.; Liu, B. *Journal of Materials Research* **2012**, *27*, 2241–2248.

(206) Cheng, Y.; Meleco, A. J.; Roeth, A. J.; Whiteside, V. R.; Debnath, M. C.; Santos, M. B.; Mishima, T. D.; Hatch, S.; Liu, H.; Sellers, I. R. In *2017 IEEE 44th Photovoltaic Specialist Conference (PVSC)*, IEEE: 2017.

(207) Nguyen, H. P. T.; Djavid, M.; Cui, K.; Mi, Z. *Nanotechnology* **2012**, *23*, 194012.

(208) Jang, E.; Kim, Y.; Won, Y.-H.; Jang, H.; Choi, S.-M. *ACS Energy Letters* **2020**, *5*, 1316–1327.

(209) Kara, R.; Mentar, L.; Azizi, A. *RSC Advances* **2020**, *10*, 40467–40479.

(210) Su, Q.; Sun, Y.; Zhang, H.; Chen, S. *Advanced Science* **2018**, *5*, 1800549.

(211) Su, Q.; Zhang, H.; Chen, S. *Applied Physics Letters* **2020**, *117*, 053502.

(212) Chen, D.; Chen, D.; Dai, X.; Zhang, Z.; Lin, J.; Deng, Y.; Hao, Y.; Zhang, C.; Zhu, H.; Gao, F.; Jin, Y. *Advanced Materials* **2020**, *32*, 2006178.

(213) Geurts, J. In *Zinc Oxide*; Springer Berlin Heidelberg: 2010, pp 7–37.

Acknowledgement - Danksagung

Zum Abschluss dieser Arbeit möchte ich mich noch bei einigen Personen bedanken, welche mir in den letzten Jahren mit Rat und Tat unterstützt haben und ohne die diese Arbeit nicht möglich gewesen wäre:

- Zuerst möchte ich mich herzlich bei *Prof. Dr. Wolfgang Brütting* bedanken. Für die Unterstützung während der Masterarbeit, für das Ermöglichen der Promotion, für die Aufnahme in die Arbeitsgruppe und natürlich auch für die unzähligen wertvollen Diskussionen, neuen Erkenntnisse und darausfolgenden Perspektivenwechsel.

- Weiterhin bedanke ich mich bei *Prof. Dr. Achim Wixforth*, der sich freundlicherweise bereit erklärt hat, trotz nahendem Ruhestand das Zweitgutachten dieser Arbeit zu erstellen.

- I am very grateful to *Dr. Yi Liu*, *Dr. Matthew Jurow* and *Dr. Monica Lorenzon* for the invaluable time I spent at the Lawrence Berkeley National Laboratory. Also I want to thank *BaCaTeC* for funding of the research trip.

- Ich möchte mich außerdem bei verschiedenen Projektträgern, hauptsächlich beim *Bundesministerium für Bildung und Forschung* sowie der *Deutschen Forschungsgesellschaft*, bedanken, von welchen die meisten Mittel für meine Arbeit in Augsburg gekommen sind.

- Furthermore, I'd like to greatly thank *Dr. Yohan Kim* and his colleagues from the IAP. Without them, this work would not have been possible. Also, I want to give my thanks for the great time I had in Potsdam at their labs and the many fruitful discussions we had on- and off-topic.

- Similarly, I want to thank *Dinara Samigullina* from TUD for supplying the samples and data for the respective part of this thesis.

- Unserer Stamm-Crew, bestehend aus Sekretariat und Techniker-Büro, gilt natürlich ebenso mein besonderer Dank. Vielen Dank für die jahrelange Unterstützung bei sowohl fachlichen als auch organisatorischen Problemen *Wolfgang Reiber*, *Birgit Knoblich*, *Bettina Schestak* und *Claudia Löflath*.

- Außerdem möchte ich mich natürlich bei den Kollegen am Lehrstuhl bedanken – für die tolle Zeit, die reichlichen Anregungen, den wertvollen Austausch von Erfahrungen und hilfreichen Tipps, das ein oder andere Freitagsbier und ganz allgemein das angenehme Miteinander. Allen voran möchte ich mich hier bei meinen Bierokollegen *Dr. Alexander Hofmann*, *Dr. Björn Gallheber*, *Markus Schmid* und *Eduard Meister* sowie den Mitgliedern der Organik-AG *Florian Graßl*, *Thomas Zechel*, *Dr. Thomas Morgenstern*, *Dr. Sebastian Wehrmeister*, *Dr. Mark Gruber*, *Tassilo Naujoks*, *Prakhar Sahay*, *Hongwon Kim* und allen Studierenden bedanken.

- Abschließend möchte ich mich noch bei meiner *Familie* und *Freundin Rita* bedanken. Ihr habt mich immer und in allen Belangen jederzeit bedingungslos unterstützt. Vielen Dank dafür, ohne euch wäre ich heute sicher nicht wo ich heute bin. Speziell bedanken möchte ich mich für die schier unendliche Geduld – gerade in letzter Zeit. Vielen Dank für Alles!